Development of PICOSEC-Micromegas for fast timing in high rate environments

Lukas Sohl

université
PARIS-SACLAY

Development of PICOSEC-Micromegas for fast timing in high rate environments

Thèse de doctorat de l'Université Paris-Saclay

École doctorale n° 576, Particules, Hadrons, Énergie, Noyau, Instrumentation, Imagerie, Cosmos et Simulation (PHENIICS)
Spécialité de doctorat: Physique des particules
Unité de recherche: Université Paris-Saclay, CEA, Département d'Electronique des Détecteurs et d'Informatique pour la Physique, 91191, Gif-sur-Yvette, France.
Référent: Faculté des sciences d'Orsay

Thèse présentée et soutenue à Gif-sur-Yvette, le 17.12.2020, par

Lukas SOHL

Composition du jury:

Patrick Puzo Professeur, Université Paris-Saclay	Président
Klaus Desch Professeur, Rheinische Friedrich-Wilhelms-Universität Bonn	Rapporteur & Examinateur
Theodoros Geralis Directeur de recherche, NCSR Demokritos	Rapporteur & Examinateur
Gloria Luzón Professeure, Universidad de Zaragoza	Examinatrice
Fulvio Tessarotto Directeur de recherche, INFN Trieste	Examinateur
Esther Ferrer-Ribas Ingénieure de recherche, CEA/IRFU/DEDIP	Directrice de thèse
Thomas Papaevangelou Ingénieur de recherche, CEA/IRFU/DEDIP	Co-encadrant de thèse

Thèse de doctorat

NNT: 2020UPASP084

[. . .]

Daß ich erkenne, was die Welt

Im Innersten zusammenhält

[. . .]

— Johann Wolfgang von Goethe (1749-1832),
***Faust I** (1808)*

"That I can see whatever holds, the world together in its inmost folds", Johann Wolfgang von Goethe (1749-1832), ***Faust I** (1808)*

Acknowledgements

First of all, I want to thank the thesis committee for the time and diligence spent assessing my thesis manuscript and for taking part in the unusual thesis defence under pandemic conditions. My biggest acknowledgement goes to my thesis supervisors Thomas Papaevangelou and Esther Ferrer-Ribas. Especially Thomas was not only scientific but also personally a great supervisor and friend over all the years. Without Esther and her unconditional support with all the french bureaucracy, finishing this PhD project would have been impossible for me.

In this context, I also want to thank for the important support from the CEA-PTC funding "RADIAMM" and the collaborating laboratories. Namely, Thomas Gustavsson from the LIDYL laser laboratories for providing us the laser set-up, which was an elementary building block for the different studies and measurements we performed over the last years, and Michal Pomorski together with Emmanuel Scorsone from the CEA-LIST diamond capture lab, who prepared the different carbon-based photocathodes and studied innovative methods in growing thin diamond films.

I also want to mention the international collaborators in the PICOSEC-Micromegas collaboration. First and foremost, the CERN gaseous detector development group lead by Leszek Ropelewski. I had my first contact with gaseous detectors and the PICOSEC-Micromegas project in the CERN group as a summer student of Eraldo Oliveri in 2017. The whole team introduced me to test beam measurements, and I learned major key competences for this PhD project from Eraldo.

Another main contributor in the PICOSEC-Micromegas collaboration is the research group from the Aristoteles University of Thessaloniki lead by Spyros Tzamarias. He taught me his incredible knowledge of data analysis and beyond. With the work on the modelling, he gave a perspective for 2020 when there were no measurements in the laboratory possible. Moreover, with all his wisdom, he was and is always a great mentor for me.

One individual who also had a remarkable impact on my PhD work is Paco Iguaz-Gutierrez. Together we spent countless hours by day and night at test beams and conferences, which were one of the best times during all the years of the PhD. Even after the measurements, he was still a great support with the detailed proofreading and corrections during the writing process of this manuscript. At this point, I do not want to forget the other groups and individual members of the PICOSEC-Collaboration. Mostly, Ioannis Giomataris, Sebastian White, Francisco Garcia Fuentes, Michele Gallinaro, Jona Bortfeldt, Michael Lupberger and the team from USTC around Yi Zhou. I want to thank all these people and all the unnamed from the collaboration for the countless discussion and interpretations of the results and the collective writing of many great publications during this time. Explicitly I want to mention Florian Brunbauer and Marta Lisowska from the

collaboration for the photocathode measurements in the ASSET chamber and the countless support during many stays at CERN.

I want to thank my intern Thomas Begey for his short but significant help with the measurements and analysis in summer 2020. Moreover, I want to thank all the colleagues at DEDIP for a great time we spend together. These are mainly Francesca Belloni, Laura Segui, Hector Gomez-Maluenda, Ioannis Katsioulas, Xavier-François Navick and all the others. Form DEDIP, I especially thank Fanny Jambon for sharing an office together.

I also want to thank my supervisors and colleagues during my bachelor and master studies at the institute for experimental hadron physics of the Ruhr-Universität Bochum. Namely, Matthias Steinke, Malte Albrecht, Fritz-Herbert Heinsius and Ulrich Wiedner. In my first years as a research assistant, I learned all the basics of detector operation and data analysis, which paved the way to this project's success.

Finally, I want to acknowledge all the new and old acquaintances and friends I made at conferences, stays at CERN, the doctoral school, and the summer school in Vietnam. Last but not least, I want to thank my family and my friends at home for moral support over all the years.

Contents

List of Figures

List of Tables

List of Physical Constants

The physical constants and their approximated values used in this manuscript.

Physical Constant	Symbol	Value	Unit
Archimedes' constant	π	3.1415	
Avogadro constant	N_A	$6{,}022 \cdot 10^{23}$	mol^{-1}
Electron charge	e	$-1.6 \cdot 10^{-19}$	C
Electron radius	r_e	$2.82 \cdot 10^{-15}$	m
Electron rest mass	m_e	0.511	MeV c^{-2}
Fine-structure constant	α	137^{-1}	
Muon rest mass	m_μ	105.66	MeV c^{-2}
Planck constant	h	$6.626 \cdot 10^{-34}$	J s
Speed of light	c	$2.99 \cdot 10^{8}$	m s^{-1}

List of Abbreviations

ADC Analog-to-Digital Converter
ALICE A Large Ion Collider Experiment
APD Avalanche Photodiode
ASIC Application-Specific Integrated Circuit
ATLAS A Toroidal LHC ApparatuS
AUTh Aristotle University of Thessaloniki

BBO Barium-Borate

CAD Computer-Aided Design
CAST CERN Axion Solar Telescope
CCD Charge Collection Distance
CCE Charge Collection Efficiency
CCQE Charged Current Quasi-Elastic
CEA Commissariat à l'énergie atomique
CENF CERN Neutrino Facility
CERN Conseil Européen pour la Recherche Nucléaire
CFD Constand Fraction Discrimination
CMS Compact Muon Solenoid
COMPASS Common Muon and Proton Apparatus for Structure and Spectroscopy
CVD Chemical Vaporised Diamond

DAQ Data Acquisition
DEDIP Département d'Électronique des Détecteurs et d'Informatique pour la Physique
DIRC Detection of Internally Reflected Cherenkov Light
DLC Diamond-Like Carbon
DNCD Boron-Doped Nanocrystalline Diamond
DUT Detector Under Test

EIC Electron-Ion Collider
EMC Electromagnetic Calorimeter
ENUBET Enhanced NeUtrino BEams from kaon Tagging
ESS European Spallation Source

FEC Front-End Card
FWHM Full Width at Half Maximum

GDD Gaseous Detector Development
GEM Gas Electron Multiplier
GIF++ Gamma Irradiation Facility

HDMI High-Definition Multimedia Interface
HEP High Energy Physics
HFS Hyper-Fast Silicone
HL-LHC High Luminosity-Large Hadron Collider
HV High Voltage

IBF Ion-Backflow
ILC International Linear Collider
IR Infrared
IRFU Institut de Recherche sur les lois Fondamentales de l'Univers

LCD Laboratoire Capteurs Diamant
LED Light-Emitting Diode
LEP Large Electron-Positron Collider
LGAD Low Gain Avalanche Detector
LHC Large Hadron Collider
LIDYL Laboratoire Interactions, Dynamiques et Lasers
LIST Laboratoire d'intégration des systèmes et des technologies

MAMMA Muon ATLAS MicroMegas Activity
MCA Multichannel Analyser
MCP–PMT Microchannel Plate – Photomultiplier Tube
Micromegas MICRO-MEsh GASeous detectors
MINOS Magical Numbers Of Shell

MIP Minimum Ionising Particle

MPGD Micro Pattern Gaseous Detector

MRPC Multi-gap Resistive Plate Chamber

MSGC MicroStrip Gas Chambers

MWPC Multi-Wire Proportional Chamber

nBLM neutron Beam Loss Monitor

NEA Negative Electron Affinity

NIM Nuclear Instrumentation Module

NSW New Small Weel

nTOF neutron Time-Of-Flight Facility

p.e. Photoelectron

PCB Printed Circuit Board

PDF Probability Density Function

PET Positron Emission Tomography

PID Particle Identification

PMT Photomultiplier Tube

PTC Programmes Transversaux de Compétences

QE Quantum Efficiency

R&D Research and Development

RADIAMM Radiation hard Diamond-based secondary emitter for delevopment of an ultra fast timing MicroMegas detector

RMS Root Mean Square

ROI Region Of Interest

RP Roman Pot

RPC Resistive Plate Chamber

S/N Signal-to-Noise Ratio

SAT Signal Arrival Time

scCVD Single Crystalline Chemical Vaporised Diamond

SEDI Service d'Electronique, des Détecteurs et d'Informatique

SHG Second-Harmonic Generation

SiPM Silicon Photomultiplier

SMA SubMiniature version A

SMC SubMiniature version C

SPAD Single-Photon Avalanche Diodes

SPS Super Positron Synchrotron

SRS Scalable Readout System

sTGC strip Thin Gap Chamber

T2K Tokai to Kamioka

TMAE Tetrakis(dimethylamine)ethylene

TOF Time-of-Flight

TOP Time-of-Propagation

TOT Time-over-Threshold

TPC Time Projection Chamber

USTC University of Science and Technology of China

UV UltraViolet

VPTT Vacuum Phototetrodes

WIMP Weakly Interacting Massive Particles

Prologue

Everything starts from a dot

— Wassily Kandinsky (1866-1944)

1 Motivation

Since the dawn of time humankind yearns for the understanding of what was, is, and will be. Various disciplines of academia are pursuing this quest. The subjects of humanities like Philosophy, Theology, and Psychology as well as the natural sciences like Biology, Chemistry and certainly Physics are sharing this virtuous hunt. All academic disciplines are driven by one fundamental question which can not be expressed more beautifully and accurately than by the words of the German writer Johann Wolfgang von Goethe. In his tragic play *Faust* the eponymous main character, a striving savant, is desperately seeking to answer his question of *"so that I may perceive whatever holds, the world together in its inmost folds"*[1].

Physics and more precisely, particle physics is interpreting this question as to the longing to explore the smallest building blocks and its interactions that make up all the known and unknown universe. One theory that can at least partly describe the composition of known matter and its interplay in the universe is the Standard Model. It is based on an accumulation of theories about different families of particles and their forces. Nowadays, ever-increasing experiments are required to study the last unknown of the Standard Model and beyond. In the past, smaller laboratory experiments were sufficient to gain new knowledge of the fundamental forces and particles. One example for this smaller experiments is the measurement of the elementary electric charge by R. A. Millikan [2].

One of the biggest facility to study particle interactions and to move the remaining frontiers of human knowledge is the Conseil Européen pour la Recherche Nucléaire (CERN). It hosts the, up-to-now, largest and most powerful particle accelerator in the world. The Large Hadron Collider (LHC) has a circumference of 27 km and centre-of-mass collision energy of 13 TeV for proton-proton collisions. Each high energetic collision generates a vast amount of particles scattered in all directions and with different remaining momenta. The underlying physical process that generates these particles is reconstructed with accurate identification of the particles and their energy and direction. Theories of the physical processes in the Standard Model and beyond can be verified or discarded from the reconstruction of the collision products. Each detector component needs to fulfil specific precision requirements in spatial, time and energy resolution to provide the needed accuracy in reconstructing all necessary information of the particles.

The four big LHC experiments, the additional experiments at CERN, and countless other earth and space-bound experiments have already collected a sheer amount of data. All these experiments have contributed to our understanding of the world and its underlying physical processes. However, there are still open questions and processes not yet fully understood like the neutrino oscillation mechanism, dark matter, CP violation and many more. New experiments must be conceived and built to address these questions. An already planned LHC upgrade will raise its nominal luminosity (HL-LHC) to detect the footprint of even more rare physical processes and long-term

projects of future linear and circular colliders are being proposed. Those colliders will significantly raise the centre-of-mass collision energy to enable the study of countless new physical phenomena. Not only large scale experiments are planned to address the remaining questions in particle physics. Smaller, but very specialised, (astro)particle experiments are planed all over the world to detect very rare events to complete the puzzle from all sides.

These new experiments are demanding a new generation of particle detectors with ever-increasing accuracy. Not only the performance need to evolve, but even the robustness has to improve as the detectors need to withstand several years to decades in an environment with persistent radiation and a strong flux of particles. For the HL-LHC upgrade a time resolution of the inner tracking detectors of 20-30 ps is needed for an accurate vertex separation, while the luminosity is expected to increase towards $\sim$5-10 x 10^{34} $cm^{-2}s^{-1}$ [3]. This first estimation directs the development of future tracking systems towards a regime of radiation hard detectors with few tens of picosecond time resolution that reduce the pileup and improves the vertex separation of different particles. Fast-timing detectors can be moreover useful for other sub-systems of particle physics experiments. The background rejection efficiency in calorimeters and the maximal momentum for time-of-flight particle identification can be improved.

The PICOSEC-Micromegas detection concept is one possible answer to the demands of detector systems in future particle physics experiments. It is the first Micro-Pattern Gaseous Detector (MPGD) that reaches a time resolution in the required range for future fast-timing detectors [4, 5]. This manuscript gives a detailed description of the PICOSEC-Micromegas concept. It explains the detection principle and describes the tested prototypes. An extensive series of characterisation measurements have been carried out to understand the impact of each detector component on detector timing and robustness. The bouquet of characterisation methods ranges from Monte-Carlo simulation over precision measurements with a laser facility up to large scale measurements in a particle beam. Based on this characterisations, new detector modules are presented and tested that lead the PICOSEC-Micromegas concept towards a versatile tracking detector for high-rate environments.

All in all, a comprehensive view of this new detector technology is given. Moreover, its possible applications in future particle physics experiments are elaborated. This work shows the different steps required in the development of a new cutting edge detector technology. In future physics experiments, PICOSEC-Micromegas might help humankind to understand piece by piece *"whatever holds, the world together in its inmost folds"*.

2 State-of-the-Art Fast-timing Detectors

Contents

In the following, a brief overview of the different current state-of-the-art detectors suitable for fast-timing applications is given. This chapter begins with an introduction into the virtue of fast-timing detectors, explaining the main parameters limiting the timing performance of a detector. At the end of this section, a table summarises the discussed technologies, applications, and typical time resolutions. This detector overview and its current applications are not exhaustive as the fast-timing detector development is rapidly growing, but it will help to sort the development and results of the PICOSEC-Micromegas into a broader context. MicroPattern Gaseous Detectors (MPGDs) for fast timing applications are not discussed in this section as the PICOSEC-Micromegas concept is currently the only successful development of MPGD as a fast-timing detector.

2.1 Introduction to Fast-Timing Detectors

Real detectors will always have limited accuracy when detecting particle energy, position and timepoint. These limited accuracies are manifested in jitter of the signal charge; the charge spread on the read-out anodes; and jitter in the signal arrival time (SAT). These three characteristic properties are affected by different components of a detector and can be improved individually in the development process of a detector. Anyhow, the improvement of one property can also affect another, like the improvement of spatial resolution with an improved time

resolution. This work focuses mainly on the time resolution and thus the reduction of the SAT jitter, which is an interplay of many physical effects taking place in the detector and the read-out electronics. The rising edge of a signal determines the SAT, and the main distortion to the rising edge is added by electronic noise. Hence, a first-order approximation of the detector time resolution (σ_{tot}) is calculated by the signal rise time (t_{rise}) divided by the signal-to-noise ration (S/N) as

$$\sigma_{\text{tot}} \approx \frac{t_{\text{rise}}}{S/N} \, . \tag{2.1}$$

This approximation is commonly used in the domain of communication engineering as a rule of thumb. For example, the PICOSEC-Micromegas has a rise time of $\sim$1 ns and needs, therefore, a signal-to-noise ratio of $\sim$50 to reach a time resolution in the order of $\sim$20 ps.

Different components contribute to the total time resolution in a detector set-up separately and the total time resolution is defined by the sum of the variances for each of these contributions. The total time resolution can be expressed on a macroscopic level as

$$\sigma_{\text{tot}}^2 = \sigma_{\text{elec.}}^2 + \left(\frac{\sigma_{\text{TTS}}}{\sqrt{N_{\text{p.e.}}}} \right)^2 + \sigma_{\text{t0}}^2 + \sigma_{\text{track}}^2 + \dots \, , \tag{2.2}$$

where $\sigma_{\text{elec.}}$ is the electronic noise of the signal, $\sigma_{\text{TTS}}/\sqrt{N_{\text{p.e.}}}$ is the single-electron transit time spread divided by the number of photoelectrons in a photodetector, σ_{t0} is the time resolution of the trigger system in a measurement set-up, and σ_{track} is the contribution of tracking effects depending on the track geometry [3]. Depending on the composition and the actual application of the detector, not all of these components contribute significantly to the time resolution, and even other components may become important. For the study of the PICOSEC-Micromegas detector, we will see that the main parameters are the electronic noise, the transit time spread and the number of photoelectrons.

2.2 MCP-PMT

The first presented fast-timing detection concept is the Microchannel Plate - Photomultiplier Tube (MCP-PMT). It is a derivation of classical PMTs with an advanced time response. In a classical PMT an inevitable time jitter is caused by different path lengths of the electrons between the dynode amplification stages. In the MCP-PMT technology, thick ceramic plates with several micro holes are substituting those dynodes. The microchannels plates are placed into a vacuum tube, and an intense electric field is created inside of the microchannels with metallic electrodes on both sides of the plates.

A photocathode in front of the microchannel plates emits electrons. The electric field inside the microchannels accelerates those electrons, which extract more electrons when interacting at sufficient energy with the microchannel walls. Figure 2.1 shows a sketch of the electron amplification inside one microchannel. With $\sim$10 µm diameter, the travel distance of the electrons from one wall to the other is significantly smaller compared to the distance between the dynodes

of several centimetre in a classical PMT. This shorter drift distance reduces the time jitter. Several microchannel plates can be stacked over each other inside of one vacuum tube for a multi-stage amplification [6, p. 188].

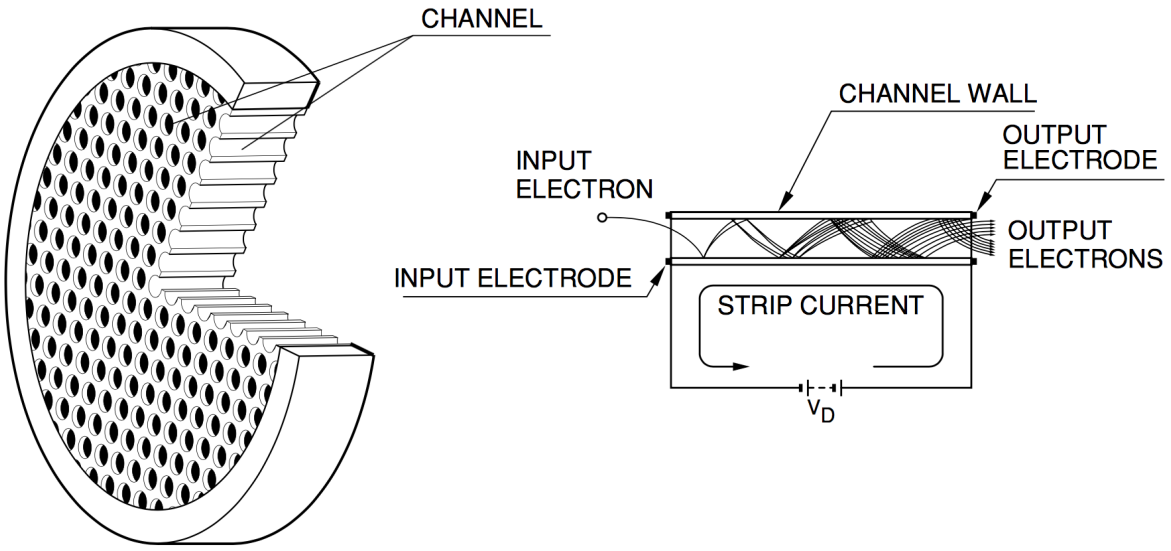

Figure 2.1: Left: Single microchannel plate. Right: Electrons are amplified in each microchannel when interacting along the channel walls. Image extracted from reference [6, p. 188].

MCP-PMTs are one of the available detector technologies with the best time resolution. However, they are not suitable to cover large detection areas due to its production cost. They are not suitable as vertex detector in a LHC experiment (i.e., near the interaction point) due to its larger amount of material compared to other technologies and more critical the rather low robustness of the photocathodes [7]. MCP-PMTs are used for applications where a small active area is sufficient like, for example, for beam monitoring devices of the European spallation source (ESS) proton beam. This application favours MCP-PMTs more for their gain characteristics than for the time performance [8]. MCP-PMTs are additionally used as a time reference detector for the PICOSEC-Micromegas beam measurements. Section 9.2 in this manuscript gives a characterisation of two MCP-PMTs with a combined time resolution measured as low as 7.2 ± 0.1 ps [9].

Large particle physics experiments use MCP-PMTs for particle identification detectors (P-IDs) detecting the internally reflected Cherenkov light (DIRC). One example is the Belle-II time of propagation (TOP) detector, which is a ring imaging Cherenkov detector placed as a barrel between the tracking detector and the calorimeters. It consists of long quartz radiators that are read out at one end by small MCP-PMTs. It is used for particle identification (PID) and is especially effective in the discrimination between pions ($m_0(\pi\pm) = 139.57\,\mathrm{MeV/c^2}$) and kaons ($m_0(K\pm) = 439.68\,\mathrm{MeV/c^2}$), because the Cherenkov cone opening angle variates for these particles due to their different momentum at the same energy. The light radiated at different Cherenkov angles propagates in different paths through the radiator and reaches the MCP-PMTs on different areas and at different times. A fast-timing detector like MCP-PMTs is a sensitive detector for these small propagation differences [10]. Belle-II MCP-PMTs are reaching a time resolution as low as 6.2 ps for time of flight measurements of 3 GeV/c pions [11].

2.3 Photodiodes

Semiconductor photodiodes with a band-gap between the conduction and the valence band of 1-1.5 eV are the second presented technology. The most prominent semiconductor in this range is Silicon with a band-gap of 1.12 eV at room temperature [12], but there are many others used in particle detectors like germanium or compounds like GaAs or InGaAs. One of the first use of semiconductors in HEP was as a precise tracking detector in the late 1970s [13].

Photodiodes are built up of several differently doped layers of semiconductors. One layer consists of a silicon crystal lattice, and each layer can be doped by adding different other elements to the lattice. A surplus of electrons is generated in the valence band when phosphor is added to the lattice. Those layers are called n-doped and phosphor acts as an electron donor. Aluminium can be added on the contrary to phosphor to generate electron holes in the valence band. In this way, added aluminium forms p-layers as an electron acceptor. The ratio of doping material to silicone can be variated to generate n- and p-layers with different intensity. A + or - can be used as indices to symbolise layers with different doping ratio. It is also possible to build photodiodes on other semiconductor bases instead of silicone (like GaAs or InGaAs photodiodes). The choice of doping material changes in this case, according to the different substrate material.

A typical photodiode is constructed with an intrinsic layer without any donation between a pn-junction ($p^+ - i - n^+$). It is used as a spatial boundary between the different doped layers, and it absorbs photons. Photons reaching the intrinsic layer with sufficient energy generate electron-hole pairs by the extrinsic photoelectric effect.

Photodiodes can be operated in three different modes depending on the bias voltage applied. Without additional voltage, a photodiode operates in zero biased mode. The generated photoelectrons create an electric field in the diode until the photocurrent can overcome the impedance of the electric circuit. This mode is mainly used for photovoltaic cells as the electric current is efficiently drained from the photodiode.

The second mode is the photoconductive mode. The photodiode is reverse biased with a negative voltage applied to the p^+-layer on the anode. The intrinsic zone gets widen by the bias voltage and a stronger electric field forms between the cathode and the anode. The electrical potential of the diode rises with the additional electrons created in the intrinsic zone. This mode is commonly used to measure light intensities, as the current flowing from the diode is linear correlated with the initial photon energy. The electric field and the reduced capacity due to the biased voltage improve the detector time resolution [14]. A photodiode operated in photoconductive mode is used as a t_0 reference and trigger detector in the laser set-up described in section 8.1. The laser provides enought light to generate large signals in the photodiode leading to adequate time resolution as a reference detector.

The third mode is the avalanche photodiode (APD) mode, with even increased reverse bias voltage. It provides the best time resolution with the highest gain, and different silicon detector technologies in HEP are based on APDs.

2.3.1 APDs

APDs are operated with a reverse bias higher than the breakdown voltage, which creates a strong electric field that accelerates the free-moving electrons. They have moreover a slightly different structure than classical PIN-diodes with the following layer structure: $p^+ - i - p - n^+$. More free electrons are formed by interactions of the electrons in the transition zone between the p and the n^+ layer. This zone is referred to as multiplication zone. The free-moving electrons will form an electron avalanche in the diode, and the diode will be conducive for a short time.

A resistor quenches the occurring current after the anode. In this way, the photodiode is a digital counter which gives a uniform signal every time photons hitting the active area. These signals do not contain any energy information, but even single photons can be precisely detected. This operation mode of a photodiode is called Geiger mode, as it behaves like a Geiger-counter. The electron avalanches can propagate faster than the free moving electrons through the diode, which results in a time resolution of 20 ps (FWHM) [15].

Large area APDs are used in the antiproton annihilation experiment $\overline{\text{P}}$anda in Darmstadt in the forward endcap of the electromagnetic calorimeter (EMC). The APDs have an active area of 14 x 6.8 mm^2 and two APDs are used to read out one square PbWO-II scintillator crystal. The $\overline{\text{P}}$anda experiment hosts a magnetic solenoid that generates a magnetic field of up to 2 T at the EMC. APDs are preferred over conventional PMTs for its operation independent of magnetic fields. They are moreover selected for the EMC due to its quantum efficiency and gain characteristics. An operation in a cooled down environment of $T = -25\,°C$ additionally increases the gain of the APDs. The particle flux and expected radiation damage in the inner parts of the endcap EMC are too high for a long term operation of APDs. Vacuum phototetrodes (VPTTs), a small PMT derivation, are developed for this region with inferior detection performance but increased durability under higher particle flux [16].

One of the most widespread detectors is silicon photomultiplier (SiPM), which has found an excellent reputation outside of HEP in medical imaging applications. The use of fast timing silicon detectors in future HEP experiments is challenging, as semiconductor-based devices are by default not very radiation hard. A highly energetic or heavy particle can create defects in the semiconductor lattice, which leads to space charge effects or even leakage current. One of the most promising developments of more radiation hard fast-timing silicon detectors are the low gain avalanche detectors (LGAD). An overview of the SiPM and LGAD detection concepts are given in the following.

2.3.2 SiPMs

Multiple APDs can be parallel interconnected to form a SiPM. Each of the APD microcells has a size of a few µm whereas SiPM sensors can reach up to several mm and contain hundreds of APDs. The SiPM signal is a superposition of all APD signals, and the amplitude is correlated with the number of activated APDs in one SiPM sensor. SiPMs are therefore suitable for calorimetry measurements as information on the amount of light is extracted from the signal, and the fast-timing properties of the APDs are preserved [17].

The overall performance of silicon detectors strongly depends on the surrounding temperature. A higher gain can be achieved at lower temperatures. For test measurements and operation the usual target temperature lies between $-25\,^{\circ}\mathrm{C}$ and $-20\,^{\circ}\mathrm{C}$. A higher detector gain improves the signal-to-noise ratio and thus the time resolution of any detector. The time resolution of SiPMs has been measured to 35 ps in a proton beam with a Cherenkov radiator in the front and $\sim$15 photoelectrons [18], while the time resolution for single photoelectron ranges between 176 ps and 330 ps (FWHM). An advanced type of SiPM based on single-photon avalanche diodes (SPADs) instead of APDs is further developed. These are quenched microcells that need only one photon to generate an avalanche. The time jitter contribution of a SPAD to a SiPM signal in a single photoelectron measurement is estimated to $\sim$20 ps (FWHM) after subtraction of the electronic noise [19].

SiPMs are in a rather mature development stage compared to the other presented fast-timing detector technologies and are used in various applications in physics and industry. However, they are likely to suffer from radiation damage. Therefore, they are mainly placed in outer parts of a HEP experiment. SiPMs are very suitable to read out calorimeter scintillators as their quantum efficiency is an advantage, and the timing information can be further used for particle discrimination.

SiPMs are considered as one option for the calorimeter upgrades of the HL-LHC detectors and other HEP experiments in design phase, like the international linear collider (ILC). The ILC is planned to be constructed in Japan, and it will be the first large-scale linear e^+-e^- collider with a centre of mass energy of 200 - 500 GeV in the first expansion stage [20].

A primary application domain of SiPMs lies outside of fundamental research. Medical imaging in the positron emission tomography (PET) is widely using SiPMs. This is a medical imaging procedure where a β^+ radiating substance is injected in a living organism. This substance accumulates in parts of the body with cancer cells. The β^+ decay radiates positrons, which annihilate with surrounding electrons and two photons with an energy of 511 keV each are then radiated diametrical. Those photons can be detected outside of the body, and the origin of the annihilation can be extrapolated from the photon detection positions. The time of flight (TOF) of these photons is additionally measured for background reduction. Advanced PET scanner usually consists of circular aligned fast scintillators like doped CsI or L(Y)SO to detect the annihilation photons and SiPMs to detect the scintillator light. The short decay time of the scintillator and the fast time response of the SiPM improves the spatial and TOF accuracy [21]. Industrial available PET scanners are reaching a TOF time resolution of 210 ps (FWHM) [22].

SiPMs can only detect photons directly. They need an additional photon converter like a scintillator to detect massive particles as required in HEP experiments. Another semiconductor fast-timing detector suitable to measure particles directly like MIPs is the Low Gain Avalanche Detector (LGAD) presented in the following.

2.3.3 LGAD

LGADs are a rather newly developed detector concept driven by the needs of HL-LHC experiments, with the aim to develop fast and small APDs withstanding the prospected particle fluences after the upgrade.

LGADs have a similar structure to APDs except for the intrinsic layer, which is replaced by a positive doped p-layer next to a highly negative doped n^+-layer. Figure 2.2 shows a schematic cross-section of the differently doped layers from one LGAD pad. The high charge gradient between the n^+/p junction creates a strong electric field, where electrons from the n^+ cathode are directly multiplied. This configuration reaches a gain of up to 10. The purity of the doping and the uniformity of the electric field defines the gain and operation stability. A specific junction termination extension consisting of n-doped walls helps to make the electric field uniform until the end of the detector [23].

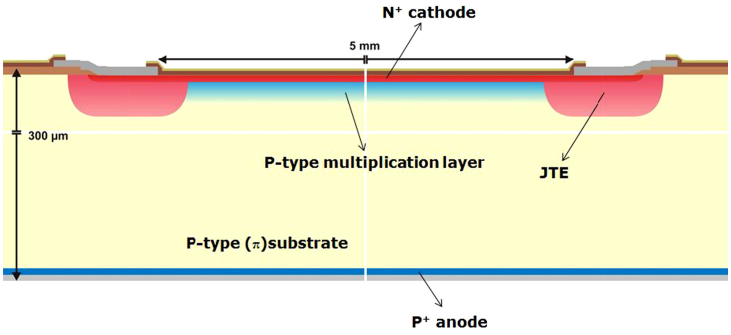

Figure 2.2: Schematic cross section of an LGAD with a p-layer directly under the n^+ cathode and n-doped junction termination extensions (JTE) on the sides. Image extracted from reference [23].

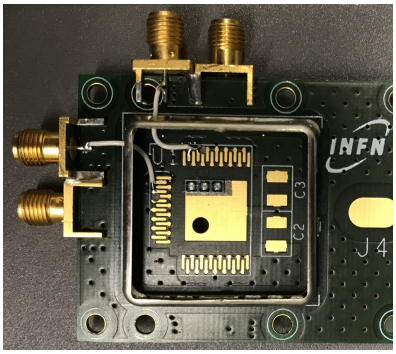

Figure 2.3: Photograph of three LGAD detector pads for the CMS upgrade on a testboard. Each pad is $1 \times 1\,\mathrm{mm}^2$ large and contains 9 cells with a size of $50 \times 50\,\mu\mathrm{m}^2$.

First radiation studies of LGADs have shown a lower gain after radiation exposure. Measurements have been conducted with samples before and after radiation of neutron, protons and hadrons up to an 1 MeV neutron equivalent fluence of $\Phi_{\mathrm{eq.}} = 10^{16}\,\mathrm{cm}^{-2}$. Mainly the charge collection efficiency degrades over time in a high-flux environment as more and more boron is removed from the p-layer. The degeneration of the p-layer diminishes the amplification field between the n^+/p junction and thus reduces the signal multiplication. The lower gain moderates the linear increase of the leakage current at increasing generation current under high fluence. A higher electric field can be applied to the detector after irradiation to recover (partly) from the gain loss. This procedure allows the operation of LGADs at higher fluence compared to $p - i - n$ diodes [24].

The first generation of LGAD detectors with a thickness of 300 µm were tested in a 170 GeV pion beam at CERN and a time resolution as low as 120 ps was reached and 65 ps was measured in an IR Laser set-up [25]. The time resolution in the Laser measurement is significantly

better as only the intrinsic time jitter of the detector is contributing to the time resolution. The energy transfer from the particle to the semiconductor follows a Landau fluctuation, while the time walk due to this fluctuation has to be included for beam measurements. Furthermore, the time resolution depends on the detector capacitance and the general detector noise [25]. Thinner LGADs with a lower capacity have been developed. Prototypes with a thickness of 45 µm are tested in a particle beam before and after irradiation. Figure 2.3 shows a photograph of an LGAD test board for the CMS experiment. The tested LGAD chips are 1 mm square containing nine cells of 50 µm square, which corresponds to a filling factor of 2.25 %. Before irradiation a time resolution of less than 30 ps has been reached at $-20\,^{\circ}\mathrm{C}$ at the maximum stable voltage. An increase of the surrounding temperature to $-6\,^{\circ}\mathrm{C}$ shows degeneration of the time resolution of 8 ps at the same voltage. This behaviour is expected due to the lower impact ionisation coefficient at higher operation temperature and thus lower gain. After irradiation with $\Phi_{\mathrm{eq.}} = 10^{15}\,\mathrm{cm}^{-2}$ the gain-loss could not be fully compensated by a higher bias voltage and a best time resolution of 57 ps was measured [26].

The CMS collaboration chooses LGADs as a high granularity timing detector for the high luminosity upgrade. The actual CMS calorimeter will not provide sufficient precision to reconstruct the vertices of low energetic MIPs in the HL-LHC phase. This limitation will be eliminated by an extra detection layer of precise timing detectors to the barrel and endcap structures. The barrel will be equipped with SiPMs and LYSO:Ce scintillators, as the radiation is expected to be maximum 25 kGy with a particle flux of $2 \cdot 10^{14}\,\mathrm{cm}^{-2}$ (1 MeV $\mathrm{n_{eq}}$) at $\eta = 1.45$. The SiPM-LYSO:Ce combination reaches a time resolution of 21 ps (σ) with MIPs and a pixel size of 6 x 6 mm^2 on a 3 mm thick crystal. The endcaps (1.6 <$|\eta|$ <3.0) will face a magnitude higher particle flux with $1.7 \cdot 10^{15}\,\mathrm{cm}^{-2}$ (1 MeV $\mathrm{n_{eq}}$) corresponding to 690 kGy at an integrated luminosity of 4000 fb^{-1}. LGADs are one option for the endcaps to reach a time resolution in the order of 30 ps with sufficient robustness [27]. A similar detector concept is proposed and studied for the ATLAS Phase-II upgrade [28].

2.4 Wide-gap Semiconductors

Diamond, as carbon in a crystalline lattice, has a band-gap between the valence and the conductive band of 5.48 eV [12]. Such materials are placed between insulators and classical semiconductors and are called wide-gap semiconductors. Charged particles and photons passing through a diamond detector ionise atoms like in a silicon detector. The main difference to a standard semiconductor is the lack of an intrinsic layer between a p-n-junction. In a wide-gap semiconductor, the whole detector volume is sensible for electron-hole-pair creation. The number of initially generated electrons is linear to the deposed energy of the detected particle. Diamond detectors can be produced as thin detectors with an exceptional radiation hardness and high atom density. These kind of detectors are well suitable for radiation detection [29] and dose monitoring [30, 31] and are mostly used for beam monitoring and medical applications.

Diamond detectors are moreover capable of providing an intrinsic time resolution better than 29 ps (σ) with a detector thickness of 100 µm [32]. Due to the higher band-gap, a higher electric field can be applied to the diamond without reaching the breakdown voltage. The electric

field moves the ionised electrons in the conductive band along the diamond lattice. The high electric field can bring the electrons to a higher thermal state than the lattice, and the electron can scatter between energy bands by transferring energy to the lattice. The possibility of electron scattering from higher energetic bands to lower ones depends on the field orientation related to the lattice structure. This effect leads to an anisotropy of the drift velocity, and the saturated carrier velocity of the electrons in strong electric fields is higher in diamonds than in silicon-like semiconductors.

The charge transportation in a semiconductor is sensitive to lattice defects causing recombination and charge trapping. As diamonds are wide-gap semiconductors, the direct recombination between two bands is negligible. Trapping of electrons in lattice defects and trap induced recombination is instead a severe concern for diamond detectors. The impact of defects on the charge mobility is expressed with two values: the charge collection distance (CCD) and the charge collection efficiency (CCE). The CCD gives the mean drift distance of a moving charge in the detector before it gets trapped, and it should be much higher than the detector thickness for an efficient detector. The second value, the CCE, is directly related to the CCD and the thickness, as it gives the fraction of collected charges to the generated charges. The trapping of space charges can cause irregularities in the detector behaviour. When many charges are generated in a small area, e.g. due to an α-particle, lattice defects can be all filled in that area by fixed space charges, polarising it. This polarised area generates an own field in the detector, deteriorating the pulse height. A second effect is the priming when defects are filled regionally over a longer distance, and the CCD can improve in that area. The regional defects cause an inhomogeneous behaviour of the detector.

Reproducible and regular diamond lattices with few defects are required for stable operating fast-timing detectors. These diamond lattices can be artificially produced with the single crystalline chemical vaporised diamond (scCVD) method. In this method, carbon atoms are vaporised to a gas state, and a clean substrate surface is coated with these diamonds. As carbon cannot be evaporated as a pure element, it is done as part of a precursor molecule. A typical precursor gas for CVD production is methane (CH_4). The methane is highly diluted with hydrogen (1-1.5 % vol. methane) and the gas mixture is heated above 700 °C. The hydrogen reacts with the methane and reactive methylium cations (CH_3^+ are formed. Under the right pressure and temperature, the cations can react on a substrate surface, and carbons can form a single crystalline diamond lattice [33].

One application of scCVDs with a need for fast-timing properties is the detector upgrade of the Totem experiment at CERN. The Totem detector is placed at the same interaction point of the LHC as the CMS experiment. It is designed to study elastic and diffractive scattering with a focus on precision measurements of the total cross-section of proton-proton scattering. The core detectors of Totem are two, so-called, roman pots (RPs) at each side of the interaction point. These are vacuum vessels (pots) containing precise tracking detectors to detect the scattered particles under a low angle close to the interaction point. The first version of the RPs has used silicon strip detectors [34].

The increasing luminosity of the LHC demands a more robust solution as a tracking detector close to the beamline. The additional capability of TOF measurements with fast-timing detectors allows the vertex reconstruction in the z-direction and matching with the CMS tracker data. ScCVDs are fulfilling all RP upgrade criteria, as they provide proper tracking and timing

capability on a small size detector with improved radiation hardness compared to silicon detectors. Measurements with two complete scCVD detector units have shown a time resolution per strip of down to 80 ps, which is below the required design performance of 100 ps [35].

2.5 Resistive Plate Chambers

The last presented detector type for fast-timing applications is the resistive plate chamber (RPC) and recent development called multi-gap resistive plate chamber (MRPC). RPCs are gaseous ionisation detectors with two parallel plates as electrodes. The plates have a typical distance of some millimetres, and a uniform electric field of $\sim$1KV/cm is created between the plates. Particles ionise the gas atoms, typically a noble gas like argon, and free-moving electrons are created. Electrons are then accelerated along the electric field towards the anode plate and can create further electrons in an avalanche. The electrode plates are coated with bulk resistive material, e.g. bakelite, so that a discharge of the gas due to the ionisation is spatial limited, and the surrounding sensitivity stays unaffected. The moving electrons induce an electric signal in the electrode plates while drifting towards the resistive coating.

Because of the high resistivity, RPCs can be operated under high particle flux. Large area detectors are built as the cost and material budged is rather low compared to scintillators, and a strip segmentation of the read-out plane preserves the spatial information of the passing particle. A time resolution of the order of nanoseconds can be reached [36].

MRPCs are a recent development of RPCs for a better timing performance. Several electrically floating resistive plates placed in a larger drift gap between the electrode plates that generates a strong electric field. The segmentation of the volume limits the spatial distribution of ionisations inside one gaseous volume and the drift distance of the generated electron. The signal for each detected particle is fully induced in the electrodes when the electrons are reaching the next resistive plate. They do not need to travel the whole distance until the anode plate, which improves the time resolution of the detector to sub nanoseconds [37].

Figure 2.4 shows the schematic of an MRPC with four independent electric fields and each of them separated in six gaps by additional floating resistive plates (light green). The differential signals from the anode and cathode are read out and processed by dedicated front-end electronic. One particle can create several signals in the detector, and the flight path can be reconstructed by the position and the time of each signal. The construction scheme of the MRPC reaching the best time resolutions is shown in figure 2.4. The distance between each resistive plate is 160 µm for this detector and it was operated with a gas mixture of $C_2F_4H_2$ (95 %) - SF_6 (5 %). A time resolution with two of these chambers in a 5 GeV/c secondary particle beam has been measured to $30/\sqrt{2} = 21.2$ ps (σ). A further increase of the time resolution is limited by the front-end electronics, and the signal propagation along the 2.45 x 7.4 cm^2 read-out strips [38].

One application of MRPCs in HEP is the TOF upgrade of the ALICE detector at CERN. Time of flight measurement is used to identify charged particles. A time resolution of less than 100 ps is required for a 3σ separation between π/K in the momentum range of 0.5-2.5 GeV/c. MRPCs are chosen to cover a large area with detector elements of 120 cm length in an environment

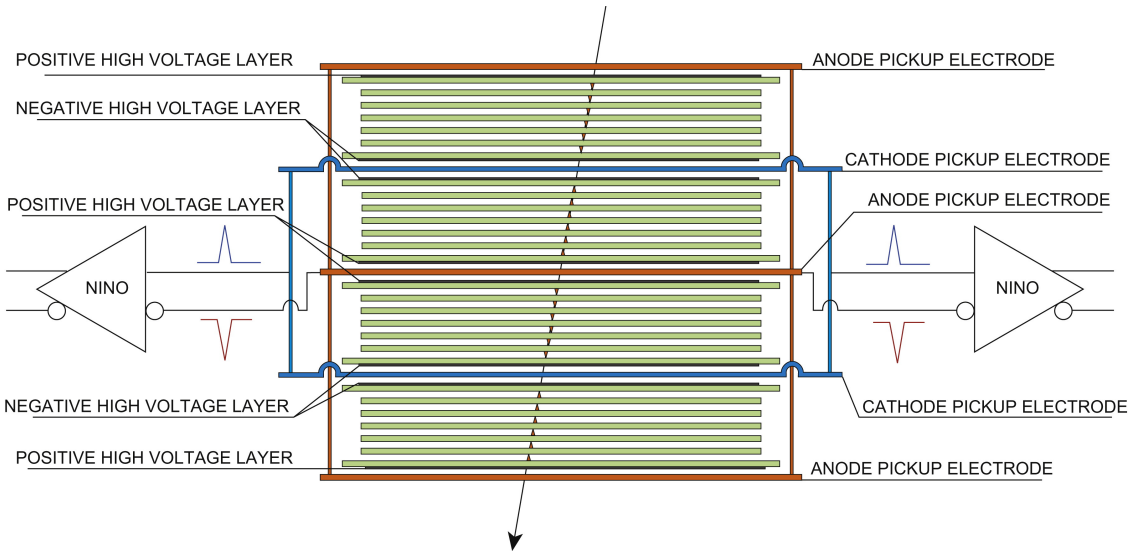

Figure 2.4: Schematic sketch of an MRPC with 24 gaps (160 µm each) in four separate electric fields. Image extracted from reference [38].

with particle fluxes of 50 Hz/cm^2 from Pb-Pb collisions. Detectors with two stacks of electric fields and five gaps in each field are used. The gap distance is 250 µm and a time resolution of 48 ps after slewing correction has been measured [39].

2.6 Summary of Fast-Timing Detector Technologies

An overview of the state-of-are of fast-timing detectors is made in table 2.1. The presented detector technologies have advantages and disadvantages, which makes them suitable for different applications. Some of the presented technologies are not only used for fast-timing applications. The PICOSEC-Micromegas, results presented in this manuscript, will be compared to the existing technologies, and it will show its own advantages defining new application modes. In general, a direct comparison of the measured values is difficult as the detectors are tested in different conditions and the time resolution is extracted in different ways. A comparison of the maximum particle rate is not possible, as these data are not available for all detector types.

Table 2.1: Overview of fast-timing detector technologies. The typical field of application and the achievable time resolution of the technologies are listed. Some entries have a short comment underlining its (dis)advantage or giving further information of the time resolution.

Detector Type	Application	Project	σ (ps)	Ref.
MCP-PMT	TOP PID	BELLE-II	6.2	[10, 11]
MCP-PMT	t_0-reference	PICOSEC-Micromegas	<7.2	[9]
	combined resolution of two MCP-PMTs			
PIN Photodiode	t_0-reference	PICOSEC-Micromegas	<4.7	
	upper limit for laser tests			
APD	EMC	$\overline{\text{P}}$anda	$\sim$8.5[1]	[15, 16]
	not radiation hard, but unaffected by magnetic fields			
SiPM	R&D	ILC	35	[18]
SiPM	Calorimeter	CMS	21	[27]
SiPM	PET TOF	Medical Imaging	$\sim$90[2]	[22]
	small size			
LGAD	Calorimeter	Atlas, CMS	57	[26, 27, 28]
	better radiation hardness compared to SiPMs			
scCVD	R&D		29	[32]
scCVD	Tracker	TOTEM (RP)	80	[35]
	radiation hard and small sized			
MRPC	R&D		21.2	[38]
MRPC	TOF PID	ALICE	48	[39]
	large area coverage			
PICOSEC	R&D		24	[5]

[1] 20 ps (FWHM)
[2] 210 ps (FWHM)

Part I

Gaseous Detectors

Poca favilla gran fiamma seconda:

— Dante Alighieri (1265-1321), ***Divina Commedia: Paradiso I*** *(1320)*

"A little spark is followed by great flame", Dante Alighieri (1265-1321), ***Divine Comedy: Paradise I*** *(1320)*

3 Working Principle of Gaseous Detectors

Contents

Gaseous detectors are particle detectors that generate a measurable electric signal from the interaction of particles with a gas. Gas atoms inside the detector chamber are ionised and form free-moving charges. In the ionisation process, a part of the particle energy is transferred into the gas atom and, if sufficient, an electron can be separated from the atom. The ionisation processes are varying depending on the particle and gas type. An electric field applied to the gaseous volume accelerates the free-moving charges. More electron-ion pairs can be created

after reaching sufficient kinetic energy, and many electrons can be formed in this way by only one initial particle interaction. A detectable current can be induced on the electrodes when the flux of free-moving electrons is large enough.

The different physical processes of gas ionisation and the transport of electrons in an electric field are described in the following sections. Then, the possible operation modes of gaseous ionisation detectors, based on these physical processes, are presented. At the end of this chapter, a historical overview of the principal types of gaseous detectors is given.

3.1 Gas Ionisation

In order to ionise the gas, particles need to have a certain kinetic energy. Different types of particles undergo different physical mechanisms when transferring energy to the gas atoms. The goal of an ionisation detector is to generate free-moving electron-ion pairs in the gaseous medium. Particles detected with the PICOSEC-Micromegas are not directly ionising the gas. A first free-moving electron is emitted by a photocathode (see chapter 5.2) and needs to be multiplied in the detector. The free-moving electrons are ionising further atoms while multiplying with the physical processes described in section 3.1.2. For completeness, the ionisation mechanism for most particle types are presented in the following sections.

The W-value (W_i) is a characteristic value for every gas, giving the mean energy transfer needed to generate an electron-ion pair. The W-value becomes proportional to the minimal ionisation energy (I_0) at higher particle energies with

$$W_\mathrm{i} \approx a \cdot I_0 \ , \tag{3.1}$$

where

$$a \approx [1.8, 2] \ . \tag{3.2}$$

The W-value and minimal ionisation energy for common gases used in gaseous ionisation detectors are listed in table 3.1. A gas with low W-value is used as a base gas of the detector to enhance the detection efficiency. The base gas is usually mixed with other gases, named quenchers, to absorb photons produced during the amplification process and to preserve the proportionality of the amplification process. These additional quenching gases are presented in section 3.2.4.

Most applications use noble gases as a base gas. Noble gases do not form chemical molecules, as they consist of atoms with full valence shells. Noble gases have fewer degrees of freedom without additional vibration modes than molecules, and they allow sharp discrete ionisation energies. The energy is directly transferred from an ionising particle to the electron without losing energy to different molecular orbital states and vibrating modes. One of the most widely used noble gases in gaseous detectors is argon. Its W-value is significantly lower than that of helium or neon, and it is more abundant than higher-order noble gases. Moreover, the mean energy loss of a charged particle in the gas ($\mathrm{d}E/\mathrm{d}x$) is high enough to obtain a sufficient detection efficiency. For these reasons, argon is commonly used in HEP tracking detectors.

Table 3.1: Density at standard temperature and pressure (ρ_{STP}), minimum ionization energy per atomic number (I_0/Z), and the W-value for common gases used in gaseous detectors. Values taken from reference [40].

Gas	ρ_{STP} $\left(\frac{\text{g}}{\text{cm}^3}\right)$	I_0/Z (eV)	W_{i} (eV)
H_2	$8.38 \cdot 10^{-5}$	15.4	37
He	$1.66 \cdot 10^{-4}$	24.6	41
N_2	$1.17 \cdot 10^{-3}$	15.5	35
Ne	$8.39 \cdot 10^{-4}$	21.6	36
Ar	$1.66 \cdot 10^{-3}$	15.8	26
Kr	$3.49 \cdot 10^{-3}$	14.0	24
Xe	$5.49 \cdot 10^{-3}$	12.1	22
CO_2	$1.86 \cdot 10^{-3}$	13.7	33
CH_4	$6.70 \cdot 10^{-4}$	13.1	28
C_4H_{10}	$2.42 \cdot 10^{-3}$	10.8	23

3.1.1 Charged Heavy Particles

Charged particles with a mass higher than electrons interact with matter mainly by collisions with energy transfer. The momentum of the incoming particle and the target material density and nucleus composition determine the collision cross-section and the amount of transferred energy. The stopping power ($\text{d}E/\text{d}x$) describes the energy loss of a particle per penetration depth and density of the target. The stopping power varies for the same target along with the particle momentum. Figure 3.1 gives an overview of the stopping power of a positive muon particle on a Copper target relative to its momentum range.

At low energy, the particle interacts mainly by scattering with the nuclei and bound electrons of the target material and the stopping power increases with the particle momentum. The stopping power reaches a maximum for non-relativistic particle energies and decreases with increasing momentum until a minimum is reached. Most relativistic massive particles detected in HEP with ionisation detectors are minimum ionising particles (MIP). The Bethe-Bloch formula describes the relationship between the particle momentum and the stopping power in a detector.

The Bethe-Bloch equation describes the mean energy loss per unit lenght ($\langle \text{d}E/\text{d}x \rangle$) of charged particles with moderate momentum as

$$-\left\langle \frac{\text{d}E}{\text{d}x} \right\rangle = kz^2 \frac{Z}{A} \frac{1}{\beta^2} \left(\frac{1}{2} ln \left(\frac{2\text{m}_\text{e}\text{c}^2(\beta\gamma)^2 T_{\text{max}}}{I^2} \right) - \beta^2 - \frac{\delta(\beta\gamma)}{2} \right) , \tag{3.3}$$

where Z and A are the proton and nucleon number of the target material; I is the mean ionisation energy of the target material; z is the charge number of the projectile; γ and β are the Lorentz factor and the relative velocity ($v = \beta\text{c}$) of the projectil; T_{max} represents the maximum energy transfer of the incident particle to a electron; $m_\text{e}\text{c}^2 = 0.511\,\text{MeV}$ is the electron energy at rest and

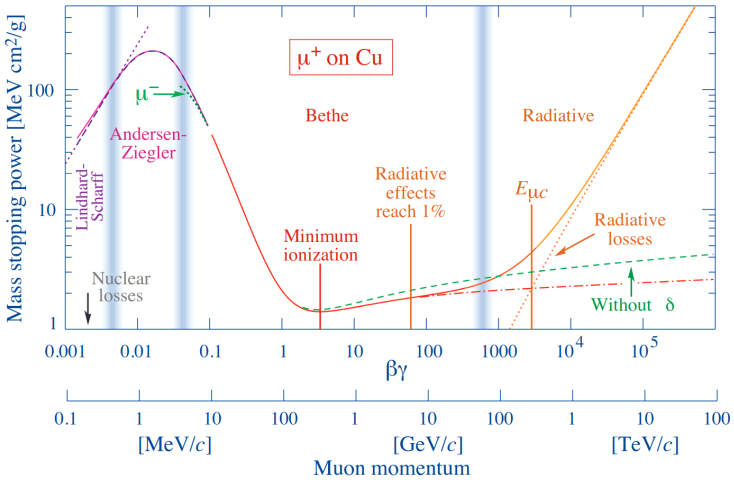

Figure 3.1: The stopping power of a muon in Copper relative to the muon momentum is shown. The Bethe-Bloch function describes the stopping power of charged particle heavier than an electron at moderate relativistic energy on a target. Figure extracted from reference [41].

$k = 4\pi\,N_A\,r_e^2\,m_e c^2 = 0.307\,\text{MeV mol}^{-1}\,\text{cm}^2$ is a constant coefficient. The linear stopping power can be calculated from this formula by multiplying the mass density (ρ) of the target material.

For particles with $\beta\gamma < 1$ the stopping power decreases with increasing energy as the term $(1/\beta^2)$ is dominant. The minimum is reached for MIPs with a stopping power of typically $1-2\,\text{MeV cm}^2\,\text{g}^{-1}$. For $\beta\gamma > 1000$, the stopping power increases by the logarithmic contribution of the Lorentz factor. For these higher energies, the equation needs to be corrected for density effects with $\delta(\beta\gamma)$. The electric field of fast-moving charged particles can polarise material depending on its density. This polarisation reduces the logarithmic rise of the stopping power. At higher relativistic energies, radiative losses become dominant, and the stopping power increases with the particle momentum. Radiative losses, like bremsstrahlung, are more important for the detection of lighter charged particles like electrons.

3.1.2 Electrons

Electrons are the lightest naturally occurring charged particles with a rest mass of $m_e = 0.511\ \text{MeV/c}^2$. The mean stopping power of an electron in a Lead target versus the kinetic energy of the electron is shown in figure 3.2. The stopping power value and the contribution of different processes depend on the kinetic energy and the atomic number of the target material. Electrons need lower energy to reach relativistic momentum compared to heavy particles, and radiation effects become more prominent at interactions with matter.

At low momentum, the energy transfer is still dominated by ionisation. The stopping power in a target can be calculated for electrons analogue to more massive particles by the Bethe-Bloch equation. The projectile electrons will collide with bound electrons in the target material atoms.

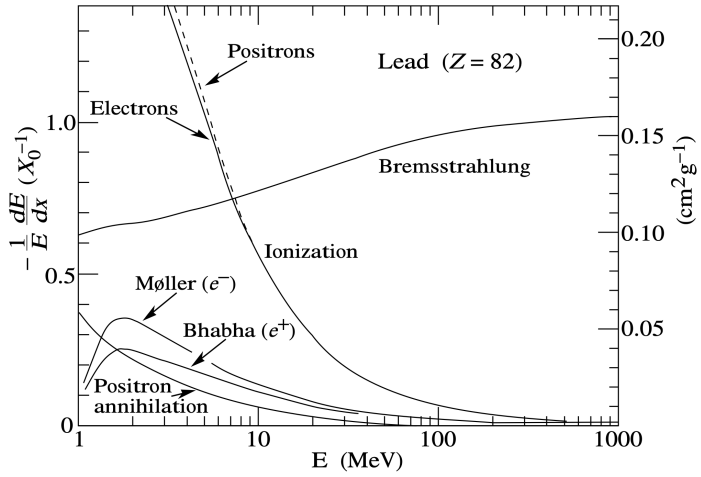

Figure 3.2: Light leptons, like electrons, can interact in different ways with matter. Ionisation is dominant at lower energies, while bremsstrahlung becomes more dominant at higher energies. Figure extracted from reference [41].

Both collision partners are indistinguishable, and the maximum energy transfer (T_{max}) is equal to half of the kinetic energy. Ionisation through an electron-electron collision may only happen in the amplification process of electrons. Other effects like annihilation and scattering of e^-e^- and e^-e^+ pairs occur at low electron energies, but these effects are playing a minor role for particle detection.

At high electron momentum (> 10 MeV for Lead with $Z = 82$), the dominant interaction process is bremsstrahlung. It is radiated when electrons decelerate while passing through the Coulomb field of a target atom. The deceleration changes the electric field induced by the moving charge, and the energy difference is emitted as a photon. Bremsstrahlung also happens at lateral deflection, like in a magnetic field of a synchrotron accelerator. For more massive particles like muons, bremsstrahlung becomes dominant at hundreds of GeV.

3.1.3 Photons

Photons have no mass at rest and can travel a significant distance through matter without interacting. Photons perform different interactions with bound state electrons when travelling through matter. A total or partial energy transfer from the photons to the electrons occurs, and the intensity of a photon beam reduces after passing through a target. The reduction of the beam intensity (I_x) is defined by the mean free path length ($\lambda = 1/(\rho\mu)$) of the photons in the target material as

$$I_x = I_0 \, \mathrm{e}^{-x/\lambda} \, , \tag{3.4}$$

where x is the thickness of the target; I_0 is the intensity of the beam before the target; and ρ and μ are the density and the mass attenuation coefficient (in cm^2g^{-1}) of the material.

Three main processes can happen between a photon and an atom that transfer enough energy to ionise the atom. These are the photoelectric effect, Compton scattering and pair production.

The cross-section of these three processes depends on the photon energy and the composition of the atoms, mainly the atomic number (Z). Figure 3.3 shows the individual and cumulative cross-section for the primary processes for two different materials (Carbon $Z = 6$ and Lead $Z = 82$)). Another effect, occurring for low energetic photons, is Rayleigh scattering. It is an elastic scattering of the light at atoms and molecules smaller than the photon wavelength. The energy transfer by this process is negligible for ionisation processes.

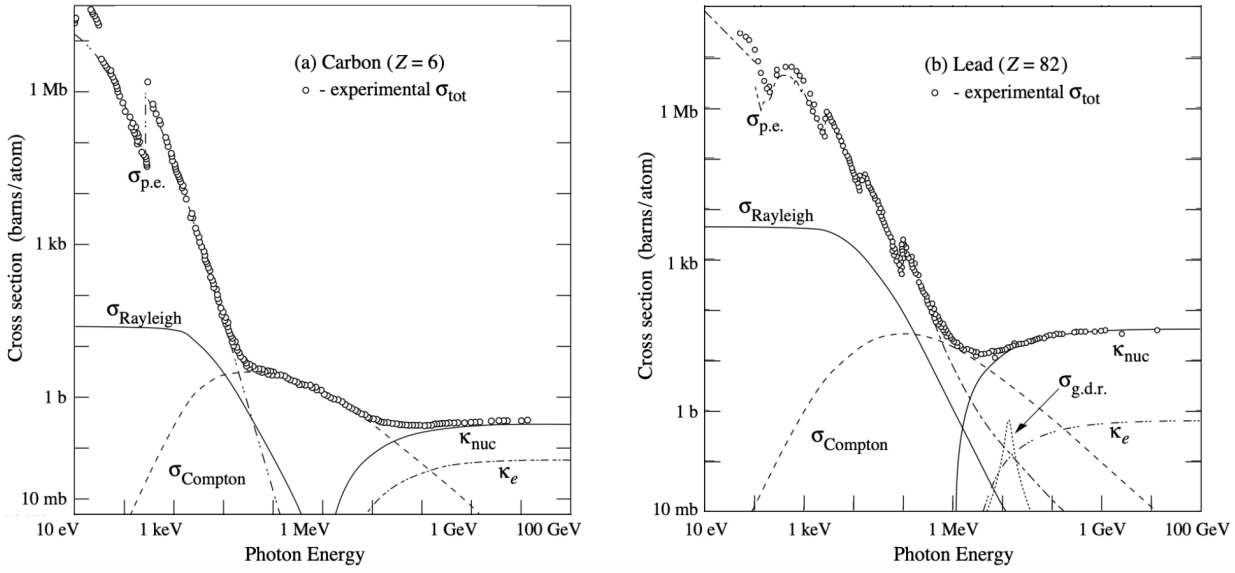

Figure 3.3: Dependence of the cross-section of different interaction processes on the photon energy for a light material (Carbon) and a heavy one (Lead). Figure extracted from reference [41].

At low photon energy, the dominant ionisation effect is the photoelectric effect. The photoelectric effect was first explained by A. Einstein, for which he received the Nobel prize in 1921 [42]. The photon transmits its total energy when interacting with an electron in an atomic bound state. After transfering the energy, the photon vanishes due to its lacking of rest mass. When the energy is sufficient, the electron can leave the bound state, and the atom gets ionised. This case is known as the external photoelectric effect. The second possibility is the internal photoelectric effect. In this case, the transmitted energy brings the electron in an excited bound state. The excited electron leaves a vacancy in the inner shell of the atom. The vacancy is filled afterwards by moving electrons down from the higher shells. These electrons emit photons equal to the energy difference of the bound-states. The photons can be directly emitted from the atom as secondary X-ray emission, or they can ionise a second electron in an outer shell. Electrons emitted by this second process are called Auger electrons.

Secondary emission of Auger electrons can be observed in argon-filled gaseous detectors. Figure 3.4 shows the pulse-height spectrum of a radioactive iron source measured with a GEM detector operated with an argon-based mixture. The iron isotope ^{55}Fe decays with electron capture to manganese ^{55}Mn with excited electrons in the shells. While deexcitation, the free spot in the K-shell of the manganese is filled with a higher shell electron and the energy difference can be

emitted by an Auger electron with 5.19 keV or a γ-ray of 5.89 keV. The emitted photon's energy is sufficient to extract a K-shell electron from an argon atom with a binding energy of 3.2 keV. These electrons are emitted with an energy of 2.7 keV. The vacancy in the K_α shell of the argon is filled in 86.5 % by the emission of one or several lower-energetic Auger electrons. In the remaining cases, a 2.9 keV photon is emitted instead. The combined energy of the K_α electron and the Auger electrons or photons deposited in the detector forms signals with a peak corresponding to channel 867 in the spectrum in figure 3.4. In some cases, the extracted photons escape from the detector and ~ 3 keV less energy is deposited. These smaller signals are forming the second peak, the argon escape peak. The energy difference of ~ 3 keV between the argon escape peak and the 5.89 keV peak can be used to calibrate the pulse-height distribution to the corresponding energy for different detector gains.

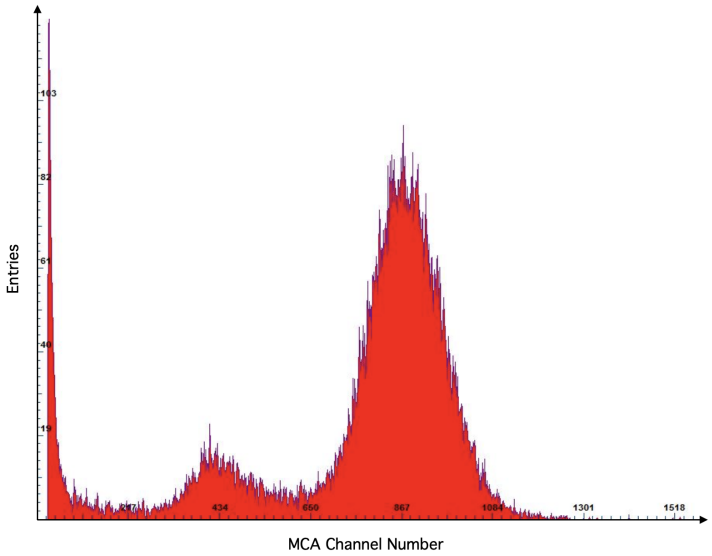

Figure 3.4: MCA pulse-height spectrum of a ^{55}Fe source in an argon (90 %) - CO_2 (10 %) filled triple-GEM detector. The triple-GEM is operated with a voltage divider as explained in section 9.1.3. The voltage divider is biased with $U = 4$ kV, and the detector operates with a gain of $\sim 1.6 \cdot 10^3$. The smaller peak at channel 434 is the argon escape peak.

At higher energies, the photon can scatter at electrons without transmitting all its energy. This scattering process is called Compton scattering. The photon transfers only a fraction of its energy and gets scattered under an angle from the electron. The transferred energy excites or ionises the atom analogue to the photoelectric effect. The increased wavelength (λ) of the scattered photon, and thus the transferred energy, can be calculated by the initial wavelength (λ_0) and the scattering angle (θ) as

$$\lambda = \lambda_0 + \frac{h}{m_e c} \left(1 - \cos(\theta)\right) \ , \tag{3.5}$$

where h is the Planck constant. The highest energy transfer is achieved when the photon is backscattered ($\theta = 180\,^\circ$).

The third physical process of a photon generating free-moving electrons in a material is the pair-production. In this process, the photon spontaneously generates an electron-positron pair. This pair directly annihilates in a vacuum, but close to the electric field of a nucleus (κ_{nuc}) or an electron (κ_{e}), the electron-ion pair can be separated before annihilation. Pair-production generates a free-moving electron and positron. The positron annihilates with an electron in the atom-shell generating two γ's of 511 keV. The photon energy for this process needs to be at least the rest mass of the electron-positron pair ($E_\gamma \geq E_{\text{e}^-} + E_{\text{e}^+} \approx 1\,\text{MeV}$). At high energy, the pair production is the dominant photon ionisation process. Higher charged nuclei, like Lead, show a higher cross-section for the higher-energetic pair-production, while Compton scattering is more dominant for photons up to several 10 MeV in lighter material like Carbon and few MeV for Lead (see figure 3.3).

3.1.4 Heavy Neutral Particles

The last class of particles are chargeless particles with a remaining rest mass. These particles need to undergo an indirect process to generate ions in the gas. Neutrons are the most common particles of this kind that need to be detected by ionisation detectors. One example of neutron detectors is neutron beam monitoring, described in section 4.2.3. Other members of this class are exotic particles like weakly interacting massive particles (WIMPs) predicted by physics beyond the Standard Model. Neutral particles are not affected by the electric field generated by the electrons and nuclei of the target material, and the strong nuclear force remains the main interacting force for neutral particles with matter.

Neutrons mostly interact by scattering with the target material nuclei. The recoil nucleus can then further ionise the gas. A target material with light nuclei like hydrogen or helium is preferred, as the rest mass is lower and the recoil stronger. Depending on the neutron energy, the scattering can be elastic or inelastic. Both participants, the nucleus and the neutron, remains in the same state at elastic scattering and the total kinetic energy is conserved. At inelastic scattering, the nucleus and neutron merge and emits a new neutron with lower kinetic energy. The remaining nucleus reaches an excited state and radiates γ-radiation while returning to the ground state. The emitted photon can further ionise atoms and generate the primary ionisation electrons.

Another detection process of neutrons is the transmutation and radiative capture. These cases are similar to the inelastic scattering. The neutron merges with the target nucleus, but instead of directly emitting another neutron, it forms a new isotope. The newly formed exited isotope needs to reach an energetic ground state either by emitting lighter nuclei (like an α-particle or Deuteron) and changing into another isotope (transmutation), or by emitting γ-radiation (radiative capture).

The last typical interaction process of a neutron with an atom is fission or spallation. Fission is the process used to gain energy in a nuclear power plant. A heavy nucleus captures a neutron, and the nucleus separates into two smaller nuclei. Fission products can further decay, and the emitted radiation ionises surrounding atoms. The second process, the spallation, uses high energetic neutrons or protons. These projectil particles are fragmenting the target nucleus in several smaller products. Spallation occurs naturally from cosmic neutrons, and the effect is used artificially in proton spallation sources for material studies.

3.2 Electron Transport and Amplification in the Gas

Primary electrons generated in the medium of a gaseous detector need to travel through the gas-filled volume towards the anode to induce an electric signal. This chapter discusses the transport mechanism of free-moving electrons in a gaseous medium. The dominant factors in electron transport are the electric field and the gas mixture. The electric field suppresses the recombination of electron-ion pairs and directs the electrons toward the anode. Multiplication of the free-moving electrons is necessary for most applications to generate a detectable signal. About the gas mixture, additives to the base gas can further improve the performance, as shown in section 3.2.4. An understanding and optimisation of the different electron transportation and multiplication processes are crucial for improvements of the time resolution of the PICOSEC-Micromegas.

3.2.1 Drift

Electron-ion pairs, generated by ionisation processes presented in chapter 3.1, need to be separated by an electric field to prevent recombination. Electrons are accelerated along the field line towards the anode and ions towards the cathode. The momentum of both particles increases and they gain velocity according to their mass and the transferred energy from the electric field.

An understanding of the electron drift velocity and the resulting signal arrival time (SAT) is essential for the development of fast-timing detectors, like PICOSEC-Micromegas. In a gas, electrons are not accelerated like in vacuum. The accelerated electrons get deviated from the straight path towards the anode, and the velocity is reduced each time when scattering with surrounding atoms. Higher amounts of kinetic energies are transferred at elastic scattering. More significant recoils increase the drift path, and the mean instantaneous velocity is reduced. A lower kinetic energy transfer is achieved with inelastic scattering between the electron and the gas.

The mean drift velocity (v_d) describes the mean velocity of the electrons towards the anode including collision effects. It can be described as

$$v_\mathrm{d} = \frac{e}{\mathrm{m_e}} \frac{1}{N \sigma_\mathrm{s} u} E \,, \tag{3.6}$$

where e and $\mathrm{m_e}$ are the charge and rest mass of an electron; E is the electric field; N and σ_s are the molar density and the scattering cross-section of the gas; and u is the mean instantaneous velocity of the electron between successive collisions [43].

The term $(N \sigma_\mathrm{s} u)^{-1}$ of the mean drift velocity describes the mean time between two collisions of the electron with gas atoms and is mainly affected by the density and composition of the gas molecules. Gaseous detectors mainly use noble gases as a base. The scattering cross-section of the electrons with the noble gas atoms is low, and mainly elastic scatterings are performed. Additional quenching gas can be added to the noble gas to increase the percentage of inelastic scattering and to reduce the diffusion of the drift path. The quenching gas molecules have additional vibration modes compared to noble gases and electrons inelastically scatter with these molecules reducing

the recoil moment. The acceleration of the particles in the electric field becomes more pronounced when a lower recoil moment has to be overcome after each scattering reducing the diffusion coefficient.

The drift velocity and total drift time of the electrons and ions can be improved with the right quenching gas. A higher drift velocity of the electrons improves the time response of the detector. The time resolution of PICOSEC-Micromegas improves with different types and amounts of quenching gas (see chapter 8.3). The shortening of the ions drift time is also essential, as it leads to a shorter signal. A short ion tail of a gaseous detector reduces the time-over-threshold without affecting the rising edge of the signal. Applications in high-rate environments are profiting from shorter signals and dead times of the detector.

3.2.2 Diffusion

Without an applied electric field, the electrons and ions move isotropically through the gas by diffusion. The diffusion of a single electron without external force is a statistical process without preferred direction. The position probability ($P[x_i, t]$) of the electron follows a Boltzmann distribution. The probability of the electron in one differential element ($\mathrm{d}x$) in each direction is

$$\mathrm{d}P[x_i, t] = \frac{1}{\sqrt{4\pi D t}}\, \mathrm{e}^{\left(\frac{x^2}{4Dt}\right)\mathrm{d}x}\,, \tag{3.7}$$

where x_i is the distance from the origin of the electron in each dimension; t is the time; and D is the diffusion coefficient. The diffusion coefficient is characteristic for each gas and pressure, and is experimentally determined. The standard deviation (σ) of the Gaussian describes the spread of the diffusion over time as

$$\sigma = \sqrt{2Dt}\,. \tag{3.8}$$

Diffusion loses its isotropic behaviour in an electric field. Electrons are additionally accelerated along the drift field lines and the diffusion coefficient is split in an transversal diffusion (D_T) in perpendicular direction (x,y) to the field and in a longitudinal diffusion (D_L) in parallel direction (z). The three dimensional position probability $P[x, y, z, t]$ can be expressed in this case as

$$P[x, y, z, t] = \left(\frac{1}{\sqrt{4\pi D_\mathrm{T} t}}\right)^2 \frac{1}{\sqrt{4\pi D_\mathrm{L} t}}\, \mathrm{e}^{\frac{-(x+y)^2}{4D_\mathrm{T}t} - \frac{-(z+v_\mathrm{d}t)^2}{4D_\mathrm{L}t}}\,, \tag{3.9}$$

where v_d is the drift velocity of the electron.

The transversal diffusion coefficient D_T defines the electron cloud spread projected on the anode plane. A small transversal diffusion minimises the signal spread. Some applications like tracking detectors are aiming for a higher spread over several read-out pads to improve the tracking precision. Other applications, like double beta decay experiments, require a smaller signal spread to record the topology of two signal separately. The longitudinal diffusion coefficient of a gas mixture needs to be reduced to minimise the SAT jitter for fast-timing detectors [43].

3.2.3 Avalanche Multiplication

In most cases, the primary electrons need to be multiplied inside the detector to induce sufficient current in the read-out. Free-moving electrons accelerate in the electric field and gain kinetic energy. Supplementary gas atoms can be ionised when the kinetic energy is above the W-value of the gas. Additional kinetic energy is accumulated at stronger electric fields, and at longer mean free path. The mean free path depends on the gas mixture and the density of the gas mixture. The gas amplification of different gases under specific conditions is experimentally described by the Townsend discharge coefficient as

$$\frac{I}{I_0} = \mathrm{e}^{\int \alpha \mathrm{d}x} \,, \tag{3.10}$$

where I is the current measured on the anode and I_0 is the current of the primary ionisation electrons; α is the first Townsend coefficient; and $\int \mathrm{d}x$ is the amplification lenght.

The first Townsend coefficient describes the number of electrons generated per lenght unit. The mean free path of the electrons is decribed in the fist Townsend coefficient by the ionisation cross section (σ_i) and the molar volume (V_m) as

$$\alpha = \sigma_\mathrm{i} \frac{\mathrm{N_A}}{V_\mathrm{m}} \,, \tag{3.11}$$

where $\mathrm{N_A}$ is the Avogadro constant. The first Townsend coefficient can be understood as the spatial propagation velocity of the electron multiplication in a gaseous detector [43].

With a high enough electric field, typically $>\mathrm{keV\,cm^{-1}}$, the electron acceleration is high enough to start a chain-reaction of multiplications. Each generated electron can produce multiple electrons on the way to the anode and an electron avalanche forms. The PICOSEC-Micromegas is one of the few detector, that reaches avalanche multiplication in the drift region. By this way, the single-electron drift path is reduced and thus the longitudinal diffusion of the drift electron. The number of new ionisation ($\mathrm{d}n$) per distance ($\mathrm{d}x$) is defined by the Townsend coefficient as

$$\mathrm{d}n = n_0 \alpha_E \, \mathrm{d}x \,, \tag{3.12}$$

where n_0 is the number of electrons at the beginning of the finite space element; and α_E the Townsend coefficient depending on the electric field strength. The electron avalanche propagates faster through a gaseous medium than the drift velocity of individual electrons, as the emission of new electrons is faster than the recovery from the recoil of the scattered electrons.

Most gaseous detectors have local areas with an electric field high enough to create avalanche multiplication. The gain of a detector G is defined as the ratio of electrons after (n) and before amplification (n_0). Each newly generated electron-ion pair alternates locally the electric field. This alternation is called space charge effect, and limits the maximal amplification of a gaseous detector. The limitation is reached when the multiplication saturates, and the detector starts to spark. These sparks can harm the detector structure and should be avoided. The Raether limit [44] is the maximal possible multiplication at a gain of $G \approx 10^8$, which corresponds to $\alpha x \approx 20$.

3.2.4 Quenching Gas

Atoms are ionised continuously, when an electron avalanche is formed in the amplification region of the detector. The energy transfer of some electrons in an avalanche is too low to ionise further atoms. These atoms only reach an excited energy state instead of becoming ionised. Afterwards, new photons are emitted from the excited atoms when rearranging to the ground state. These photons can again ionise and generate new free-moving electrons in the detector. These photons, emitted during the avalanche, generate spurious signals in the detector. The signals can not be assigned to real events caused by new particles passing through the detector.

A fraction of quenching gas added to the base gas of the detector can omit these spurious signals. The quenching gas absorbs the photons produced during the avalanche. This absorption avoids the creation of additional secondary avalanches after detecting one particle. Gases with complex molecules like organic or alcoholic gases are suitable as quenching gas. The photons can be absorbed by forming higher-order vibration modes and dissociations of the quenching gas molecules. The vibration modes of the molecules get excited without ionising the molecules and generating new electrons. The quenching gas can de-excite after absorption of the photon. It reduces the dead time, and the spurious signals after an electron avalanche have generated a signal in the detector.

The quenching gas itself may also enhance the avalanche multiplication. The Penning effect [45] occurs with small fractions of quenching gas in an inert gas. An excited inert gas atom can transfer its energy to a quenching gas molecule, and the transferred energy may be sufficient to ionise the quenching gas. A common use of Penning gas mixtures are neon lamps, where a small fraction $\sim$1 % of xenon is mixed to the neon to reduce the striking voltage [46]. The Penning transfer rate (r) is a characteristic probability factor for Penning mixtures giving the probability of an energy transfer for each excited inert gas atom. The ionisation probability can be expressed as

$$\alpha_r = \alpha_0 + r \cdot \beta \,, \tag{3.13}$$

where β is the increase of the Townsend coefficient per unit length for $r = 1$; α_0 is the Townsend coefficient without and α_r with Penning transfer. An electron drifting through a Noble gas is constantly losing energy to excitation processes by the factor β. The probability that the first ionisation occurs by the Penning effect is therefore

$$\frac{r \cdot \beta}{\alpha_0 + r \cdot \beta} \,. \tag{3.14}$$

3.3 Operation Modes of Ionisation Detectors

The intensity of the amplification electric field applied in a gaseous ionisation chamber defines its operation mode. The different operation modes define the amount of collected charge per detected particle. Figure 3.5 gives a schematic overview of the collected charge and the electric field of each operation mode. Only three of them are useful in a particle detector: the ion chamber region, the proportional region and the Geiger-Müller region.

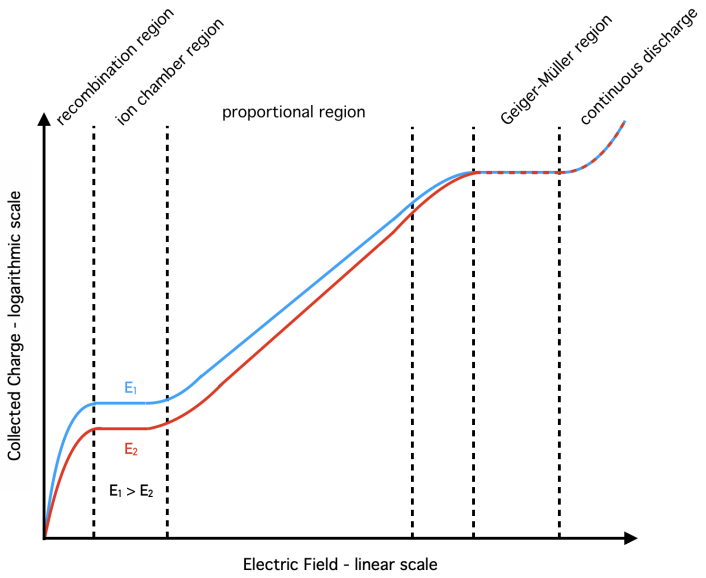

Figure 3.5: The operation modes of a gaseous ionisation chamber are depending on the applied electric field. At low electric fields, collected charge depends on the electric field and the ionising particle energy (E_1, E_2).

Low electric fields under a certain threshold will not be able to transfer enough energy in the electron to separate the electron-ion pairs. The electrons and ions recombine after ionisation, and only a small fraction of the generated charge is collected in the anode. The amount of collected charge increases with the electric field. At electric fields higher than a given value, the detector reaches the ion chamber region. Such recombination regions can also appear at radial symmetric detectors in the outermost radii when the electric field get weaker.

Ionisation Chamber Mode

The first usable operation mode of gaseous detectors is the ionisation chamber mode. The electric field is strong enough to separate each primary electron-ion pair, and all charge is collected. On the other hand, the electric field does not transmit enough energy to electrons to further ionise atoms. The collected charge is equal to the charge of the primary ionisation electrons and thus to the energy deposited by the incident particle. This operation mode is useful to separate different energetic particle, like α and β radiation. The collected charge is the same for a given particle energy over the whole electric field range of the ion chamber region.

Ionisation chambers are commonly used in nuclear physics experiments for fission studies and in heavy mass spectrometers. These experiments require the detection of heavy ions with precise energy resolution. As ions deposit enough energy to create a lot of primary charges, no further multiplication is required and the energy resolution is only defined by ionisation. For experiments with particles depositing smaller amounts of charge in the detector, the signal can be

buried in detector noise. An operation mode with charge multiplication like the proportional mode is preferred in that case.

Proportional Mode

When the kinetic energy of the accelerated electrons is high enough, the detector starts operating in the proportional region. Each electron can multiply, and the collected charge is proportional to the initial energy of the particle. Separation of different particle energies is still possible, as the total amount of collected charge is still proportional to the primary ionisation electrons. The proportional region covers the largest dynamic-range of applied electric fields to the detector, and all MPGDs operate in this mode, like the PICOSEC-Micromegas. At higher electric fields the electron multiplication loses its proportionality, as too many electrons and ions are formed, and the electric field loses its homogeneity.

Geiger-Müller Mode

With a further increased electric field, the Geiger-Müller region is reached. The electric field is high enough that each particle stimulates an ionisation avalanche going through the entire gaseous volume of the detector. The detector becomes conductive for a short time, and the smallest particle energies can be detected without additional signal amplification. Separation of different energetic particles is not possible, and the generated avalanche needs to be quenched to avoid continuous discharges of the gas. This operation mode was used in the very first gaseous detectors, the Geiger-Müller-counter, and is still used for radiation monitoring.

When the electric field overcomes the Geiger-Müller plateau, the gas starts discharging continuously, and the detector becomes insensitive to particles. Operation of the detector at such a high electric field is not possible, and the continuous discharges can harm the detector structure. The exact value of the electric field needed for each operation mode depends on the gas mixture.

3.3.1 Brief Overview of Gaseous Detectors

Geiger-Müller-counter

Ionisation of gas atoms was first used in the Geiger-Müller-counter to detect radiation particles [47]. It consists of a metallic cylindrical volume typically filled with a noble gas and a separated metallic wire stretched along the central axis of the cylinder. A voltage, applied between the cylinder and the wire, creates a radial electric field. Ionising radiation, like α-particles, can ionise gas atoms in the cylinder and the produced electrons are drifting along the electric field to the anode wire. The electric field strength increases due to the radial field, and more electrons are formed near the anode. The whole gas gets ionised, and the chamber discharges when enough electrons are formed in a strong electric field. The induced signal is therefore not proportional to the deposited energy (see figure 3.5). The electric signal from the detector can be further processed, and the discharge is quenched by a small amount of alcohol added in the mixture. The dead-time of the

detector due to the quenching process limits its counting rate. Geiger-Müller-counter are built as small portable detectors and are still today used for radiation monitoring.

MWPC

The first gaseous ionisation detector used in high energy physics (HEP) experiments is the multi-wire proportional chamber (MWPC) [48]. G. Charpak developed the MWPC concept in 1968. It consists of two parallel metallic plates and one layer of parallel conductive wires between the plates. The volume between the plates and the wires is the detection volume. It is filled with a mixture based on a noble gas for the ionisation and a smaller fraction of an organic gas as a quencher. A high voltage is applied between the plates (cathode) and the wires (anode), resulting in a radially increasing electric field around the wires. Figure 3.6a shows a sketch of the field lines in an MWPC. Particles passing through the volume can ionise gas atoms, and the primary electrons drift towards the wires, where they are multiplied in the strong electric field close to the wires. When a particle passes through the chamber, currents will be only induced at those wires close to the particle, allowing the reconstruction of its trajectory.

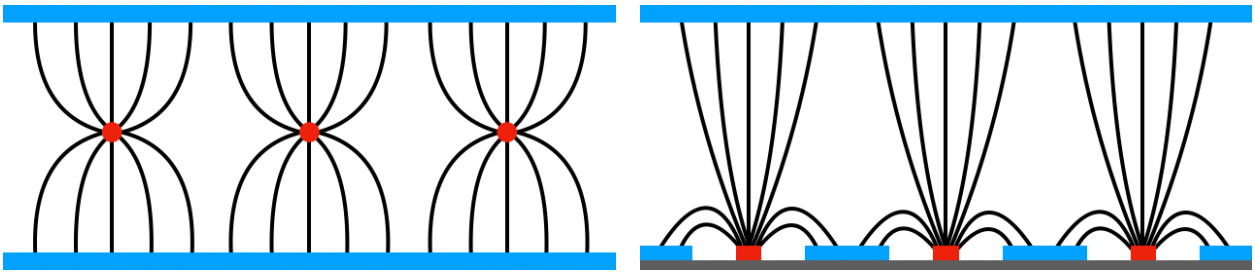

(a) MWPC (b) MSGC

Figure 3.6: Sketch of the electric field lines (black) in a) MWPCs and b) MSGCs. The cathodes are coloured in red and the anodes in blue. The field line density increases in both cases towards the anodes.

MSGC

A linking technology between MWPCs and Micro-pattern gaseous detectors (MPGDs) are MicroStrip Gas Chambers (MSGCs). A. Oed presented the first development of MSGCs in 1988 [49]. The advent and progress of Printed Circuit Board (PCB) technology allowed the replacement of MWPCs wires by cathode and anode microstrips coated on one read-out plane. A parallel drift field region is defined in front of the read-out plane by a cathode plate to define the detection volume. The microstrip pitch is reduced to some hundreds of micrometres, compared to the millimetre size of MWPC wires pitch. Field lines between the microstrips form the same pattern as MWPCs field lines, but at a different scale allowing an improved spatial resolution and the operation in stronger magnetic fields. Figure 3.6b shows a sketch of the field lines in an MSGC. MSGCs are the first example of MPGD. The new types of MPGD that appeared in the following years are considered descendants of MSGCs.

MPGDs

MPGDs [50] were developed during the last decades for modern HEP experiments. Examples of experiments using MPGDs are given in section 4.2. MPGDs are gaseous ionisation detectors with a detection volume thickness of few millimetres to several tens of centimetres and in general with a good spatial resolution due to their fine segmented read-out patterns. MPGDs are constructed with a clear separation between an ionisation (drift) region and an amplification region and the different MPGD concepts can be divided into two main categories. The first one is composed of a thin hole-like structure, that defines the detection volume, and a readout-plane. A high electric field is defined inside the holes, applying a moderate voltage difference between the two sides of the structure. Electrons are multiplied by the intense hole field and are then collected at the read-out plane. The main representative of this category is the gas-electron multiplier (GEM), introduced by F. Sauli in 1997 [51]. The detection principle of GEMs is futher described in section 3.3.2. The second type of MPGDs is composed of a metallic mesh, situated at hundreds of microns from the read-out plane. This region is the amplification gap, where an intense electric field is defined applying a moderate voltage difference between the mesh and the read-out plane. As the electric field is much more intense than the drift field, all primary electrons cross mesh holes and are then amplified. This detector concept is the MICRO-MEsh GASeous detector (Micromegas), introduced in 1996 by I. Giomataris [52]. The PICOSEC-Micromegas presented in this manuscript is a fast-timing MPGD based on the Micromegas concept.

3.3.2 GEMs

The GEM detectors follows the same principle as other MPGDs by generating locally high electric fields that accelerate primary electrons and stimulates further ionisations. GEMs are using isolating foils with a thickness of 50 µm and a conductive coating on both sides of the foil. The foil is manipulated with small holes of 50-70 µm diameter [53], so that a high electric field can be reached in the holes by applying a voltage of some hundred volts between both sides of the foil. The shape of the electric field inside of a GEM hole is illustrated in figure 3.7.

Multiple GEM foils can be stacked over each other in a single gaseous volume. Each GEM stage can further amplify electrons generated in the previous foil. The detector gain and stability can be improved when the amplification is conducted in several stages compared to a single GEM detector, without risking too high field and discharges in a single foil. A lower field in each foil minimises the discharge probability and improves the stability of the detector as discharges can damage the fragile structure of the foils [53]. The number of stages and voltage applied to each stage has to be set to find an equilibrium between a stable operation and a sufficiently high gain of the detector [51].

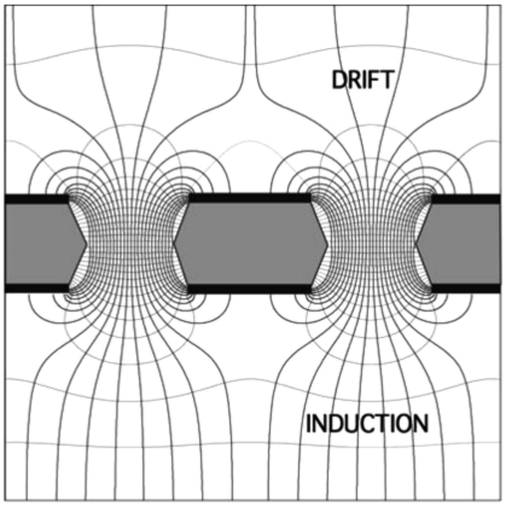

Figure 3.7: Electrons are amplified in the strong electric field in the holes between the conductive layers. Figure extracted from [51].

4 Micromegas Detectors

Contents

Micromegas (MICRO-MEsh GAseous Structure) is a modern gaseous detector concept introduced in 1996 [52] by the group of I. Giomataris and G. Charpak. A Micromegas consists of one gaseous volume with two electric fields separated by a conductive mesh. Figure 4.1 shows a sketch of the Micromegas working principle. The volume between the cathode and the mesh is the conversion volume or drift region, while the volume between the mesh and the

anode is the amplification region. The detection volume is at least one order of magnitude larger than the amplification volume in most applications.

The detector works either as a tracker or a time projection chamber (TPC). The drift region is some millimetres thick in the case of a tracker, long enough so that MIPs deposit the required energy to get clear signals. The detection volume can reach up to hundreds of centimetres in the case of a TPC. The electric field needs to be high enough to secure a drift of these electrons through the mesh to the second stage of the detector. The drift field has typical values of several 100 V/cm.

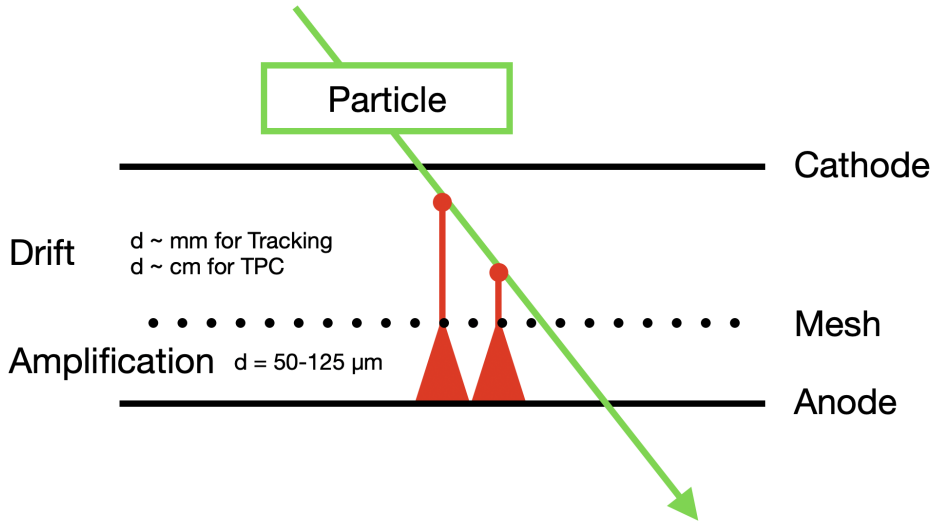

Figure 4.1: When a particle passes through the detector, it ionises several atoms in the detection volume, and the primary electrons drift to the amplification region. In the amplification region, an electron avalanche is formed.

The electrons are multiplied in the amplification region, with a typical thickness of 50-125 µm. The short gap allows applying an electric field of several kV/cm with moderated voltages of some ∼100 V between mesh and anode. The low voltages needed to generate a high electric field is one of the main advantage of Micromegas compared to its predecessors. Micromegas are operated without the obligation of using high-voltage supply units in the range of ∼kV that may create additional electric noise. The electron transmission through the mesh depends on the asymmetry between drift and amplification fields. A high amplification-to-drift ratio improves the transmission and reduces the ion backflow towards the cathode.

4.1 Micromegas Detector Technologies

Different technologies have been developed to attach the mesh structure to the anode plane. The different technologies aim to form a homogeneous amplification gap in order to get a constant field. PICOSEC-Micromegas detectors are mainly made with woven meshes produced in bulk technology. Additional tests with electroformed thin-meshes and microbulk sensors have been

performed. Their timing performance is presented in section 10. The robustness of the different Micromegas technologies against sparks and the durability at high detection rate is improved by different resistive read-out technologies. The resistive Micromegas read-outs used in PICOSEC-Micromegas prototypes are presented in chapter 11. The technologies have different advantages and disadvantages. The different mesh structures and Micromegas technologies are presented in the following.

Mesh Structures

Standard and bulk Micromegas technologies use separated meshes that are mechanically attached to an anode pillar structure. Different mesh types are available for this technology. One type is the mechanically woven mesh made of stainless-steel wires. Figure 4.2a shows a microscopic image of a woven mesh. The typical wire thickness is of 18 µm and a maximum mesh thickness of around 30 µm is achieved by flattening the crosspoints of the wires in the mesh. As the Micromegas amplification gap is short, a uniform electric field is essential to get a uniform detector response. The woven structure causes variances in the amplification gap length larger than 10 %. This variation creates irregularities in the amplification field, which degrade the energy resolution of the detector.

A second mesh type used for the PICOSEC-Micromegas is thin-mesh. It consists of one uniform metal sheet, where holes are produced by micro-machining procedures (e.g. electroforming, chemical etching, vaporisation, ...). A microscopic image is given in figure 4.2b. The hole size and the pitch of this mesh can be adjusted. The main advantage of the thin mesh compared to woven mesh is its uniform flatness, which improves the uniformity of the mesh transparency.

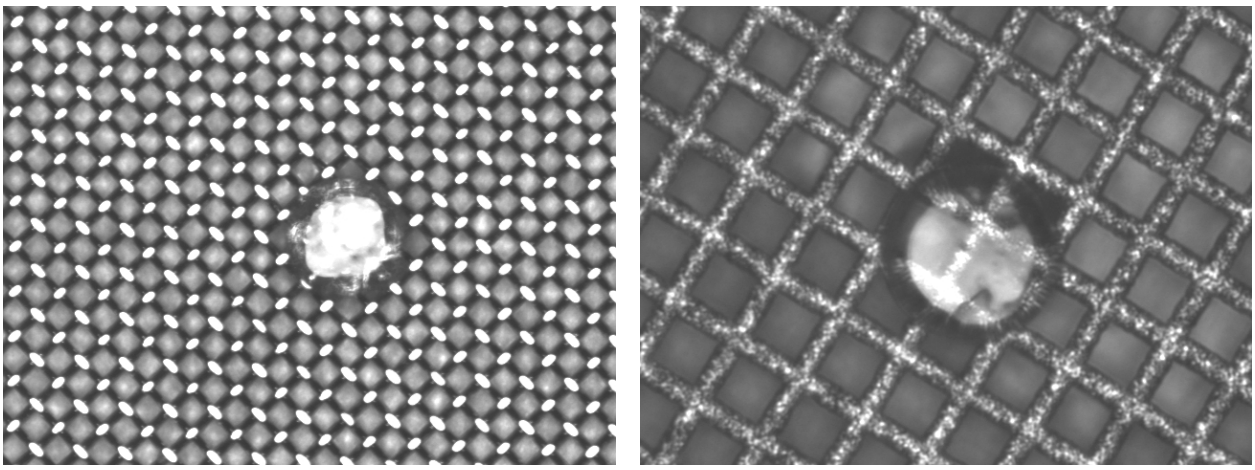

(a) Woven mesh (b) Electroformed mesh

Figure 4.2: Microscopic pictures of a) woven inox mesh and b) electroformed “thinmesh”. Both Micromegas are produced in the bulk technique and a pillar is shown in the centre of the picture.

Standard Micromegas

The first Micromegas detectors were built with an electroformed or fine woven mesh separated from the anode. The mesh is stretched on a mechanical frame, which is then screwed to the detector anode plane. Kapton pillars, attached either to the mesh or to the anode, keep a uniform amplification gap. Robust meshes, like woven stainless steel, are suitable for stronger stretching. The most significant advantage of this technology is the fast and easy replacement of the mesh. The first Micromegas prototypes were built in this way [54]. The replaceable mesh is useful for general detector studies, as the chosen mesh transparency impacts the energy resolution of a Micromegas.

This technology is still used for large scale detectors and mass production, as the frames can be built in large sizes and secure a uniform stretching over the whole surface. One example of larger area coverage is the ATLAS NSW detector (see section 4.2.1). The mesh of the detector tiles is stretched up to a surface of 3 m^2 [55]. One disadvantage of the loose mesh is the inability to produce curve-shaped detectors, normally used in HEP to cover high solid angles around a particle collision interaction point.

Bulk Micromegas

Most detectors are currently manufactured as bulk Micromegas [56]. A specific procedure encapsulates the mesh inside the pillars that are connected to the anode. The mesh and the anode form one single entity. Figure 4.3 shows the four main steps in the production of a bulk Micromegas. The base component for these detectors is a printed circuit board (PCB) with a printed conductive anode pattern. In the first step, the PCB is laminated with an insulating Polyimide material, like Pyralux®[1]. The thickness of this layer defines the amplification region of the detector. As the Polyimide layer thickness is of 64 µm, two layers are used to define an amplification region of 128 µm.

In the second step, the mesh is placed on top of the thick Polyimide layer. An additional laminated thin layer of the same Polyimide material fixes the mesh afterwards. In the last step, the Polyimide layers around the mesh are removed by a photolithographic process. A black mask with a hole pattern is used in this process. The mask is illuminated by UV light and the Polyimide under the holes becomes resistive to acid. The surrounding Polyimide is washed away by acid and only the cylindric pillars and a support frame around the active zone remain. This process allows to produce robust large area detectors. The detectors can be segmented and locally repaired after defects. The fixed mesh on each pillar allows moreover non-planar detector designs. The bulk method is the most reliable and standard manufacturing method. Very robust and spark resistant detectors can be produced. The meshes can stand mechanical stress during assembly and several sparks before being damaged.

[1] Pyralux® is a trademark owned by affiliates of DuPont de Nemours, Inc.

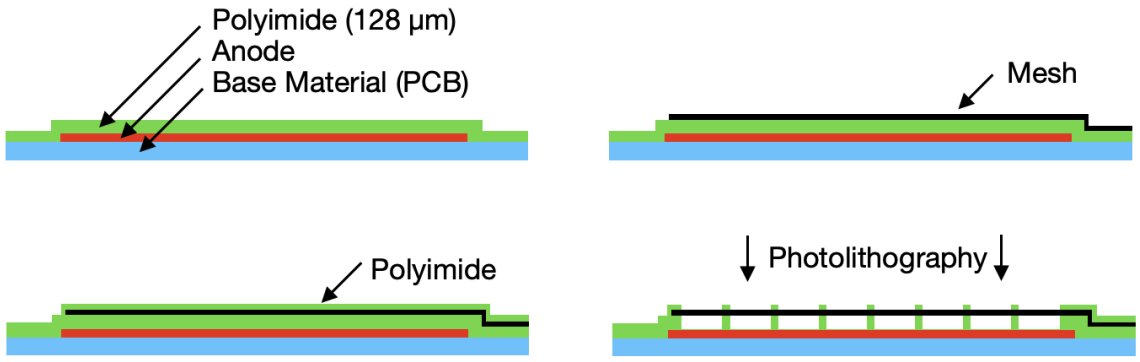

Figure 4.3: Main production steps of a bulk Micromegas. The mesh is laminated between Polyimide layers. The material between the mesh and the anode is removed with a lithographic process, and only the supporting pillar and frame structures remain.

Microbulk Micromegas

In Microbulk Micromegas the mesh, the pillars, and the readout structure are produced in one single structure. It was invented by Ionnis Giomataris (CEA Saclay) and Rui de Oliveira (CERN) [57].

The base component of this technique is a Kapton foil covered on both sides by a copper layer. The Kapton foil defines the thickness of the amplification gap. One side of the foil is used for the anode and the other for the mesh. The mesh and the read-out segmentation is produced by photochemical etching inspired by the foils of a GEM detector [51]. Typically, the hole opening on the mesh side is selected to be smaller than the gap thickness, which is production-wise limited to $\sim$40 µm. The optimum gap to get the maximum gain in a Micromegas detector depends on the type of gas. Light gas like neon or argon requires gaps of 50-100 µm, while heavy ones like krypton or xenon require gaps of 12.5-25 µm [58, 59]. The Kapton is partly removed around the holes after the etching of the mesh while most Kapton remains for mechanical support of the mesh.

Applications with requirements for low material budget, excellent energy resolution, and high radiopurity of the materials commonly use microbulk detectors. Microbulk detectors are, for example, used in the CAST experiment due to their energy resolution and radiopurity to enhance the background rejection [60]. The amplification gap of microbulk detectors is more homogeneous than that of other types of Micromegas and an energy resolution better than 12 % FWHM at 5.9 keV can be achieved[61]. Microbulk detectors find also use in neutron experiments like n_TOF [62] to minimise the γ production by the detector material.

Other Technologies

Further developments of the Micromegas detectors technology have been made. One example is the Piggyback Micromegas [63]. For this type, the segmented read-out is decoupled from the amplification region and the mesh by a ceramic layer. The signal is induced from the resistive anode through a dielectric on a (segmented) read-out electrode. Robustness and higher spark protection without significant signal loss can be achieved. This concept also improves the outgassing properties of the detector and makes it more suitable for a sealed detector construction without continuous gas exchange.

Micromegas technologies also benefit from advancing technics in manipulating silicon wafers. One example is the inGrid Micromegas [64]. This technology further improves the granularity of the Micromegas by growing a conductive grid with some distance onto a silicon wafer with a pixelated read-out. This technique uses a lithographic process similar to the microbulk procedure. This procedure allows exact alignment of the read-out pixels to the grid hole so that every hole has one dedicated pixel.

4.2 Typical Applications of Micromegas Detectors

Micromegas detectors find common use in different applications since its development in 1996. The following chapter presents examples of Micromegas sub-detectors in different physics experiments.

Micromegas are commonly used for tracking applications. Their low material budget due to their small anode thickness and the gaseous medium compared to solid-state detectors is an advantage. A segmentation of the anode in strips or pads is necessary to preserve position information of the crossing particles. Micromegas can be used for larger area coverage, and they can be placed in front of a calorimeter due to its relatively small material budged.

Other typical applications are time projection chambers (TPCs) [65]. These are detectors with a larger drift region that reconstruct the whole trajectory of a passing particle. They are equipped with a highly granular segmented read-out. Three-dimensional reconstruction of the flight path for each particle is possible by using the time differences of the signal at each read-out segment. TPCs are especially helpful for the identification of charged particles deviated in magnetic fields. Micromegas are excellent for TPCs as they provide a suitable spatial resolution and very low ion backflow in the drift region.

Micromegas can be additionally used as neutron detectors for beam profiling and flux monitoring, and as UV detectors. These applications profit from the high gain and small material budget of the Micromegas. Examples for this use of a Micromegas will be also given in the following.

4.2.1 Micromegas as Tracking Detectors

COMPASS

Micromegas are used as large-area tracking detectors in the COMPASS experiment at CERN [66]. The COMPASS experiment is a fixed target experiment with 200 GeV muons from the SPS beam. It is designed to perform hadron spectroscopy and especially for spin structure investigations using the Drell-Yan process [67]. Micromegas are used as a small angle tracker for particles in the beam direction. The mesh of the first detectors was stretched and glued to a replaceable frame. The detector unit had 12 sectors of 40 x 40 cm^2 with a strip read-out and a pitch of 400 µm. The tracker reached a spatial resolution of less than 100 µm and operated under a maximal particle rate of 90 kHz per strip [68]. Micromegas are an ideal detector for these conditions, as it has a low material budged to minimise additional particle scattering compared to solid-state tracking detectors.

An upgraded version of the COMPASS experiment was launched in 2012. New Micromegas produced with the bulk technology and with a pixelated read-out were developed. The bulk Micromegas improved the robustness and the detectors were designed for a high gas tightness. A pixelated read-out with 2x0.5 mm^2 pixels in the centre and 4×0.5 mm^2 pixels outside of the beam area was chosen to reduce the particle-flux per read-out channel. Former strip read-out could face fluxes of up to 500 kHz/channel near the interaction point, while the new smaller pixels only face 200 kHz/channel [69].

COMPASS Micromegas uses a gas mixture of neon (80 %) - ethane (10 %) - CF_4 (10 %). The addition of CF_4 increases the drift velocity, reducing the collection time of all charges and, per definition, the Time-Over-Threshold (TOT). A short TOT is important to reduce the detector occupancy and to improve the operation in higher particle fluxes [68]. The same gas mixture is tested with the PICOSEC-Micromegas (see section 8.3).

ATLAS NSW

Mircomegas detectors will be also used in the upgrade of the ATLAS detector for the HL-LHC era, where detectors will face an increased particle flux during operation. Micromegas is a well-suited detector technology for large-area applications with higher particle fluxes due to its rapid evacuation of positive ions. Micromegas will be installed in the New Small Wheel (NSW) of the ATLAS detector [55]. The purpose of the NSW is to track muons and to provide a Level 1 trigger in the endcaps. They are placed behind the calorimeters and in front of the magnetic toroid and has a total size similar to the current ATLAS muon spectrometer [70] with a diameter of $\sim$10 m and a thickness of $\sim$110 cm. This region will reach background radiation up to 15 kHz/cm^2 after the HL-LHC upgrade.

The NSW consists of 16 wedge-shaped sectors with each sector consisting of multiple detection layers with strip Thin Gap Chamber (sTGC) and Micromegas detectors. sTGCs are thin wire chambers with a total thickness of 2.8 mm between two resistive coated cathodes [71]. sTGC-Micromegas-Micromegas-sTGC is the stacking order of the layers in the z-direction. The

primary function of the sTGCs is to provide a trigger for the online trigger system and Micromegas detectors function mainly as the precise muon tracking, while both detection modules provide trigger and tracking information. The 16 sectors are constructed in two different sizes with eight sectors of each side adding up to form a full circle. Both discs of eight sectors are placed next to each other and slightly shifted in φ for a full coverage of all the active area.

The ATLAS NSW Micromegas has a resistive strip anode to prevent sparks and discharges while operating in high particle fluxes. The strip resistive Micromegas technology used in the NSW is similar to the resistive PICOSEC-Micromegas prototype that is presented in section 11.1. Resistive strips of carbon loaded epoxy with a resistivity of 10-20 MΩ/cm are coated on top of the copper read-out strips with an isolator layer of 64 µm thick in between to allow operation at higher flux. A resistive spark-protection diminishes the signal amplitude as trade-off for a stable operation [72].

The amplification region has a thickness of 128 µm, kept uniform by pillars produced in a photolithographic process on top of the anode. The woven mesh is stretched over the pillars and fixated by an outer frame. The frames with uniformly stretched meshes reach an area of up to 3 m^2 for the different sub-modules. Additionally, the frames contain the cathode and define a precise 5 mm thick drift region. The read-out strips have a pitch of less than 0.5 mm. A resolution of 73 µm was measured during a 120 GeV protons beam test with eight detector planes along the beamline. Each operated with argon (93 %) - CO_2 (7 %) gas, a drift field of 600 V/cm and an amplification voltage of 500 V applied to the mesh [55].

ScanPyramids

The last example for the use of a Micromegas as a tracking detector is away from classical HEP experiments. The ScanPyramids project [73] is a scan of the great pyramids in Egypt using cosmic muons. Cosmic muons are highly energetic and have $\sim$200 times the mass of an electron at rest, resulting in long radiation length in dense material like concrete. Muon tomography uses cosmic muons to make non-invasive images from the interior of larger structures like buildings, mountains or pyramids. A part of the muons passing through thick material, like several meters of concrete, interacts causing a reduction of the particle flux after the object. As structures of different density affect the flux differently, a muon detector can map the density distribution of an object. A three-dimensional image can be produced measuring the same object from different angles.

A portable telescope consisting of four resistive bulk Micromegas with an active area of 50 x 50 cm^2 each and an XY-strip read-out is used for the ScanPyramids project. The read-out strips are multiplexed to reduce the number of electronic channels and to build a more compact detector unit. A compact and lightweight detector with the given active area was built with Micromegas. Moreover, bulk Micromegas are robust, and they can operate autonomously for long time periods, even months, as long as a small gas flow maintains the gas quality [74]. For the ScanPyramids project, the Micromegas detectors took data continuously during around 100 days to accumulate $\sim$10 million of recorded tracks. A previously unknown void inside of Khufu's Pyramid was detected by the ScanPyramids project [73]. The muon tomography of the pyramids uses a scintillator hodoscope and nuclear emulsion additionally.

4.2.2 Micromegas as Time Projection Chambers

CAST

One of the first experiments using Micromegas with a drift region of the order of few centimetres was the CAST experiment [60], an experiment at CERN to detect solar axions. Micromegas were used as X-ray detectors placed at both ends of a 9 T dipole magnet. Axions, traveling traversal to the magnetic field, are converted into photons, detected by a Micromegas with an active area of 6 cm x 6 cm and a 3 cm thick drift region. A longer conversion region compared to tracking detectors is typical for TPCs to have several points from particle, like muons, and to reconstruct the track. In this case, X-ray photons detected in the CAST experiment will only create a "point-like" electron cloud in the conversion region, while muons will induce several signals. Micromegas are in this case a power tool to reject background events in the range of interest of the signal.

The detection of solar axions requires a low background and a good energy resolution for X-ray energies of up to 10 keV. Micromegas were built with microbulk technology, as they provide an energy resolution of 11.5 % FWHM at 6 keV (^{55}Fe), operated with an argon (95 %) - iC_4H_{10} (5 %) gas mixture [75]. Moreover, materials with low intrinsic radioactivity are used like Kapton and Copper. Both materials are available in high radiopurity.

T2K

The first experiment using Micromegas as a TPC with a 3D reconstruction of the particle trajectory inside of the detector is the Tokai to Kamioka (T2K) experiment. It is an experiment in Japan to study neutrino oscillation from artificially emitted neutrinos. The composition of a neutrino beam is measured near the accelerator in Tokai and again in a distance of 295 km at Kamioka. The goal of this experiment is the measurement of the mixing parameters between different lepton flavours, which may lead to new insights of leptonic CP-violation [76].

The neutrino spectra and interaction kinematics are measured near the source with a detector system. The system consists of scintillators as active neutrino targets and TPCs contained within a dipole magnet of 0.2 T. The TPC is additionally surrounded by electromagnetic calorimeters to measure the muon range. The neutrinos are performing charged current quasi-elastic (CCQE)[77] interactions in the scintillators. In this interaction, an (anti-)neutron scatters with a nucleus, and a charged lepton is emitted as

$$\nu_l + n \rightarrow l^- + p \,, \tag{4.1}$$

or

$$\bar{\nu_l} + p \rightarrow l^+ + n \,. \tag{4.2}$$

The momentum of the charged lepton is then measured in the TPC.

The TPC used in the T2K experiment has to fulfil certain criteria. The main requirement is an homogenous electric field. The space point resolution should be 0.7 mm with a reconstruction distortion smaller than 0.2 mm due to distortions of the electric field. The modules need to be

sufficient gas-tight to maintain a constant high gas purity level of the gas mixture argon (95 %) - CF_4 (3 %) - iC_4H_{10} (2 %) to reach the required performance. The detector modules have to fit inside the magnets, which limits the drift region to an effective sampling length of 700 mm. The detector consists of three TPC planes with a total active area of 9 m^2. Each detection plane is divided into twelve Micromegas sub-modules using bulk Micromegas with a pad segmentation of 70 mm^2 [78].

MINOS

Another example of the use of Micromegas as a TPC was the nuclear experiment for MagIcal Numbers Of Shell (MINOS) vertex tracking detector. In nuclear physics, magic numbers are a certain configuration of nucleons on one shell that allows an extraordinary stable nuclear shell. These magic numbers allow forming very heavy and stable nuclei outside the valley of stability. MINOS uses a source of radioactive nuclei and a liquid hydrogen target. The nuclei collide with the target, and recoiled protons with a significant momentum are radiated from the target. Accurate proton tracking allow the reconstruction of the collision vertex. The MINOS project used a cylindrical Micromegas-based TPC around the liquid helium target. The cylindrical ring has a thickness of 4 cm and a length of 30 cm along the z-axis. It is read out by a pixelated bulk Micromegas on the front face of the cylinder, which results in a drift region of 30 cm. The pixel read-out has a pitch of 1 mm, and a vertex reconstruction resolution of up to 2.6 mm for $^{53}K \rightarrow ^{52}Ar$ reactions. It reaches, together with a time resolution of <20 ns, a spatial resolution of 1 mm along the drift field [79].

ILC-TPC

Micromegas-based TPCs are planned to be used in future HEP collider experiments. One example is the International Linear Collider (ILC) with a prospected center-of-mass energy of 500 GeV for e^+e^- collisions [80]. Different detector designs are proposed for the ILC, and some of them include the use of a TPC. A TPC for ILC experiments has to deal with certain constraints. These are in the following: track separation of <3 mm; a momentum resolution ten times better than at LEP; low ion backflow in the drift region; a working gas with low hydrogen content to suppress a neutron background; and operation under a magnetic field of ∼4 T [80]. Micromegas are ideal for this use, as they are unaffected by magnetic fields and have a robust design with low ion backflow and high gain and resolution.

Final designs of a cylindrical TPC with a radius of 1.8 m are discussed for a future ILC-TPC. Prototypes are tested on resistive Micromegas, inGrid Micromegas, and GEM based with a diameter of 72 cm and a length of 60 cm. The endcap has a pixelated read-out with a space resolution of ∼30 µm and a material budget of 16.9 % water-equivalent X_0 [81].

4.2.3 Neutron Detection with Micromegas

Charged particle and photons can be directly detected with Micromegas detectors, as they ionise gas atoms in the conversion region. Neutrons can also be detected with a Micromegas,

but an additional neutron/charged particle converter is necessary to create primary electrons in the gas. There are different ways of creating a neutron/charged particle converter. It can be realised by a solid target in front of the detector, or by additions to the operational gas. Different converter materials are necessary depending on the neutron energy, and a combination of materials can be used to widen the neutron energy range. Next to the additional converter, all typical benefits of a Micromegas like the low material budget, the high-rate capability, and the precise tracking and energy resolution are conserved.

n_TOF

The neutron Time Of Flight (n_TOF) facility at CERN first used Micromegas as neutron beam profile monitors. The n_TOF facility was initially designed as a pulsed neutron source with an energy range from 1 eV to 250 MeV [62] and was later upgraded to measure energies ranging from meV to GeV [82]. The demands on the beam monitoring system grew with increasing energy, and different Micromegas detectors were used along time. The first one was a standard Micromegas used for flux measurements providing 1D tracking information. Stacks of single pad microbulk Micromegas were also used to measure the cross-section of fission processes. The first 2D beam profile detector used a CAST-like detector with a bulk Micromegas and segmented anode. Later beam profile monitors use microbulk Micromegas with strip read-out in x- and y-direction [83].

The most recent Micromegas used in n_TOF as flux monitors use BC_4 converter foils with an enrichment of ^{10}B as a neutron converter for the lower energetic neutrons up to 1 MeV. The low energetic neutrons are captured by the Boron and an α-particle is emitted as,

$$n + {}^{10}B \rightarrow \alpha + {}^{7}Li\ . \tag{4.3}$$

The charged α-particle or $^7Li^+$ can afterwards ionise the gas in the conversion region of the Micromegas [84]. Higher energetic neutron can be converted by elastic reactions with hydrogen or helium atoms. These elements are added to the gas mixture, either as pure helium or hydrogen bound in organic molecules like methane (CH_4) or isobuthane (iC_4H_{10}). The organic gases are added in a small percentage <10 % to keep the mixture non-flammable.

nBLM

The principle of neutron detection with a Micromegas has been later used machine protection, which is very different from physics measurements. The future European Spallation Source (ESS) is integrating a Micromegas based neutron beam loss monitor (nBLM) for the lower energy part of its primary beam. The ESS linear accelerator will provide a proton beam of up to 2 GeV with an intensity of 62,5 mA to a Tungsten target. The high-intense beam may create irreparable radiation damage in case of a beam loss. Even smaller fractions of beam loss need to be avoided and monitored to prevent activation of the surrounding machines.

The nBLM detector is designed to be sensitive to fast neutrons produced by a beam loss and insensitive to thermal neutron and photons from the background. Two configurations for the

neutron/charged particle converter are available for the nBLM detector. The first design uses a hydrogen-rich converter (e.g. Polypropylene) in front of the Micromegas. Fast neutrons can create proton recoils by interacting in the medium, while the recoils of thermal neutrons do not have enough energy to escape the target.

The second model encapsulates the Micromegas detector within a 4 cm thick Polyethylene moderator. An additional coating around the moderator absorbs thermal neutrons, and the fast neutrons are slowed down in the hydrogen-rich material and lead to the Micromegas chamber. A boron carbide (B_4C) layer is used as a converter in front of the Micromegas. This detection model has much higher detection efficiency for neutrons but also a time delay due to the moderation process of up to 200 µs. Both nBLM detector models are using a bulk Micromegas, and the detected neutron energy will range between 0.5-10 MeV [85].

4.2.4 UV Detection

Micromegas can be used as UV photon detectors. Similar to the detection of neutrons, a photon/charged particle converter needs to be coupled to a Micromegas. The most common method of converting photons to electrons is the photoelectric effect [42]. Photons with sufficient energy interact with electrons bounded to an atomic orbital or a lattice band. Photons can transfer enough energy to the electrons and remove them from the bound state. Those free electrons are further amplified in the Micromegas with the same mechanism as any other primary electron.

Reflective Photocathode

One way of using the photoelectric effect in a Micromegas are thin layers of solid photocathode material like CsI. The photocathode material is deposited on top of the Micromegas mesh, and UV photons are guided in the detector by a transparent window [86]. Figure 4.4a illustrates this detection mode. The photocathode works in a reflective mode, as photoelectrons are extracted on top of the photocathode. They follow the electric field lines through the mesh holes into the amplification region.

This method has some drawbacks and some benefits. Photoelectrons have to follow an inhomogeneous field until passing through the mesh, and the actual path of each electron may vary. The second drawback is the mesh opacity. Photons passing through the holes of the mesh cannot be detected. A high opaque mesh provides a larger active area of the photocathode but also increases the inhomogeneity of the electric field. The benefits of applying the photocathode on the mesh are the shielding of the delicate photocathode material against ion-backflow and against avalanche UV-photons that create photon feedback on the photocathode. It consequently allows a higher gain of the amplification stage. The photon only needs to penetrate the surface of the photocathode and a thicker layer of the photocathode material with an optimal quantum efficiency (CsI ∼300-400 nm) can be applied. With a reflective photocathode on the mesh, the detector can be operated at a higher gain or higher occupancy.

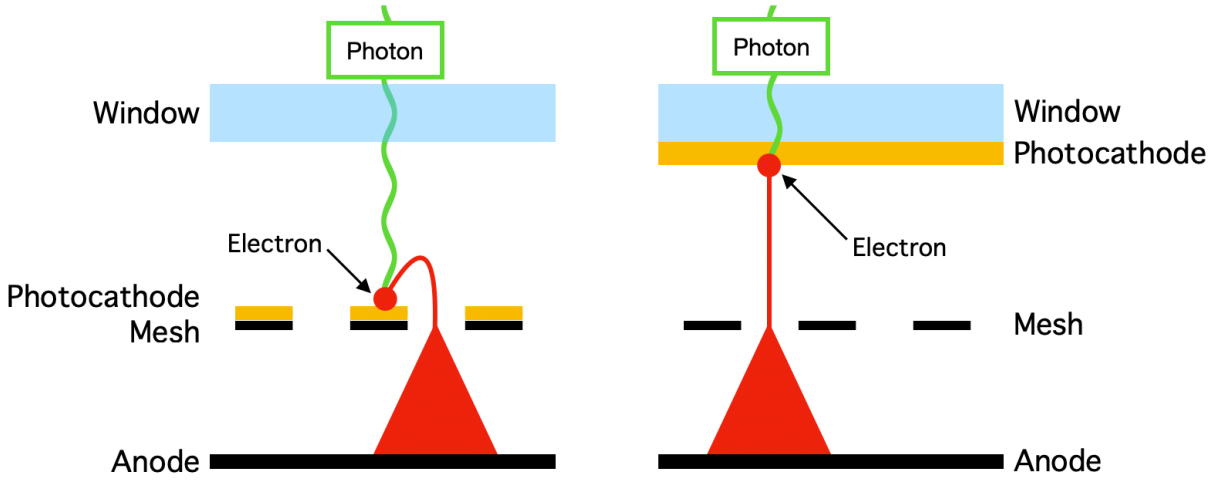

(a) Reflective mode (b) Transmissive mode

Figure 4.4: Sketch of UV-photon detection with Micromegas in a) reflective- and b) transmissive mode.

Transmissive photocathode

The second method of coupling a photocathode to a Micromegas is a direct coating on the transparent window. A sketch of the transmissive detection mode is given in figure 4.4b. This method decouples the photocathode from the mesh, and all different Micromegas mesh technologies can be used. The photocathode can be parallel to the mesh and can generate a homogenous drift field. Primary electrons are generated on the surface of the photocathode directly facing towards the mesh. As the drift length is the same for each photonelectron, the time resolution is better. The PICOSEC-Micromegas concept is based on this transmissive photocathode configuration (see chapter 5.2).

The transmissive photocathode has also some drawbacks compared to the reflective one. Photons have to pass through the whole photocathode layer. The efficiency depends on the opacity of the photocathode layer. Compared to the reflective mode, only thin photocathodes with sufficient transparency work well. A second drawback is the lower robustness against ion-backflow. The photocathode is parallel to the mesh and can be irradiated by ions generated in the amplification region (see section 11.3.1). Moreover, the photocathode can be damaged by detector sparks, and a thin but robust photocathode material is needed for operation at higher particle flux.

TMAE

An alternative method of converting photons to electrons is using an additive to the gas mixture. One common used gas with a quantum efficiency of >50 % is Tetrakis-(dimethylamine)-ethylene (TMAE). It has an ionisation energy of $E_\mathrm{i} = 5.4\,\mathrm{eV}$ and is sensitive to UV photons [87]. The base

gas and quenchers used in a Micromegas with TMAE should have a low UV absorption coefficient to keep high the quantum efficiency, like argon with methane or isobutane [88].

However, the mean free path length for photons in TMAE is in the order of 15-20 mm. A longer conversion region of several millimetres to centimetres is required causing uncertainty of the ionisation position. The usage of TMAE as a photon/charge converter results in a worse time resolution than a transmissive photocathode due to the uncertainty of the ionisation position. On the other hand, a higher detection efficiency can be reached with TMAE compared to solid photocathodes, as more photons can reach the detector.

ForFire

The ForFire detector is one example of Micromegas used as UV detector [89]. It uses the reflective mode with a CsI photocathode coated on top of the mesh. An optical MgF_2 lens is used as a window material resulting in sensitivity for UV photons in the range of $180\,\text{nm} \leq \lambda \leq 260\,\text{nm}$. This wavelength is only emitted by artificial light sources like open fires, as the sunlight in the wavelengths of $<250\,\text{nm}$ is cut by ozon in the upper parts of the atmosphere.

The use of a Micromegas gives additional advantages for a low threshold fire detector. Micromegas can provide a high gain as UV detector, which gives a sufficient signal-to-noise ratio even for the detection of single photoelectrons. Electric sparks or hidden flames can be detected. Micromegas have moreover shown good spatial resolutions as large area particle detectors. The spatial resolution can be used in the ForFire detector to precisely localise the light source. The last benefit of Micromegas is the low-cost production compared to silicon-based detectors, and large amounts of detectors can be built economically.

4.3 Time Resolution of a Micromegas

Micromegas, and MPGDs in general, can not achieve the demanded sub-nanosecond time resolution for vertex separation of MIPs at future HEP experiments. The ionisation process and the initial drift spread of the primary electrons are limiting the time resolution. A particle forms multiple ionisation clusters when passing through the drift region of the detector. The number of clusters and their location are distributed according to the average ionisation length of the particle in the given gaseous medium. The location of the clusters may vary around 100 µm for a MIP affecting the distance of the last cluster to the mesh. The gas type and the electric field are limiting the drift velocity of the electrons. The different location of the last cluster and the limited drift velocity ends up in a time jitter of the electrons when reaching the mesh. This effect is illustrated in figure 4.5. Two particles simultaneously passing through the detector are symbolised by the green lines. The red dots are clusters of primary ionised electrons formed in the drift gap. These clusters are statistically distributed along the drift gap and the distance from the last cluster to the mesh variates. As soon as the electrons enter the amplification stage, an avalanche of ionisations is formed. The time spread of the avalanche propagation can be neglected compared to the time jitter of the single electron drift, as the avalanche length is one order of magnitude shorter

than the drift. A second-order time jitter is additionally added by the diffusion of the electrons in the gas. This effect is not further included in the following calculation, as only the lower limit of the Micromegas time resolution is shown.

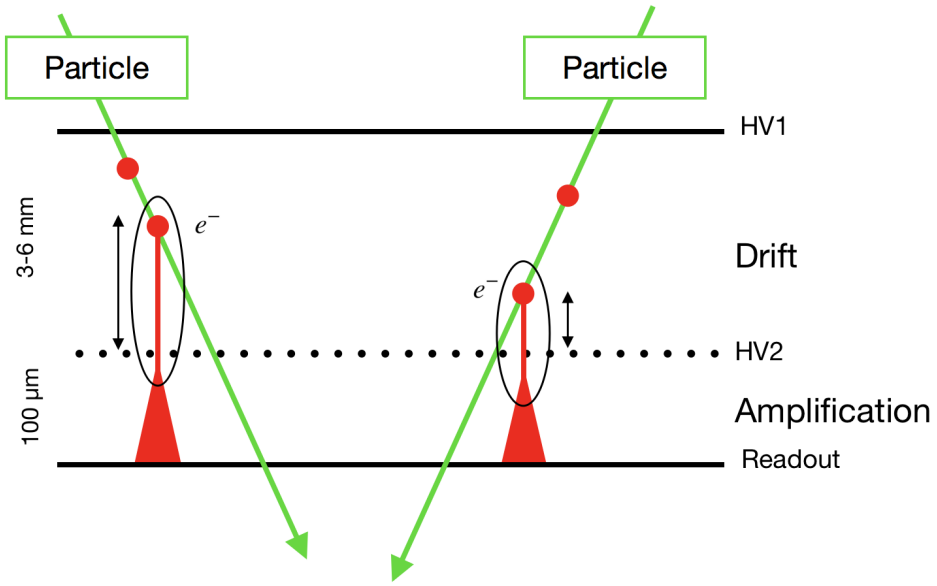

Figure 4.5: The time resolution of the Micromegas detector is limited by the different distances from the last ionisation clusters to the amplification region. Graphic first published in reference [90]

The lower limit of the time resolution of a Micromegas can be calculated in terms of average ionisation length (σ_I) and the drift velocity (v_d) for a given gas mixture and electric field. The average ionisation length (σ_I) is estimated with the linear stopping power [MeV/cm] for relativistic particle ($\beta = 1$) derrived from the Bethe-Bloch equitation (see section 3.1.1) as

$$-\left\langle \frac{\rho \mathrm{d}E}{\mathrm{d}x} \right\rangle = \rho k z^2 \frac{Z}{A} \left(\frac{1}{2} ln \left(\frac{2 m_\mathrm{e} c^2 (\beta\gamma)^2 T_\mathrm{max}}{I^2} \right) \right) , \tag{4.4}$$

where $\langle \frac{\rho \mathrm{d}E}{\mathrm{d}x} \rangle$ is the mean energy loss of a particle per distance in the gas of a density ρ; k is the natural constant as ($4\pi N_\mathrm{A} r_\mathrm{e}^2 m_\mathrm{e} c^2$). T_max is the maximum kinetic energy transfer as

$$T_\mathrm{max} = \frac{2 m_\mathrm{e} c^2 (\beta\gamma)^2}{1 + 2\gamma \frac{m_\mathrm{e}}{m_\mu} + \left(\frac{m_\mathrm{e}}{m_\mu} \right)^2} . \tag{4.5}$$

The average ionisation lenght (σ_I) can be written as

$$\sigma_\mathrm{I} = \frac{w}{\langle \frac{\mathrm{d}E}{\mathrm{d}x} \rangle} , \tag{4.6}$$

where w is the mean energy for electron-ion pair creation.

Table 4.1: Values used to estimate the average ionisation length in neon with muons in the COMPASS tracker.

variable	value	unit
Momentum of a SPS Muon: P_{SPS}	200	GeV/c
Rest mass of a Muon: m_{μ}	105	MeV/c^2
Velocity of the electron over speed of light (v/c): β	1	
Lorentz factor · relativistic velocity: $\beta\gamma$	1905	
Maximum kinetic energy transfer: T_{max}	190	GeV
Electron charge: z	1	
Mean ionisation energy: I	21.6	eV
Atomic number / atomic mass: $\frac{Z}{A}$	$\frac{10}{20}$	
Gas density: ρ	0.839	g/l
Mean energy loss per distance: $\langle\frac{\mathrm{d}E}{\mathrm{d}x}\rangle$	284.4	eV/mm
Mean energy for electron-ion pair creation: w	35.3	eV
Average ionisation length: σ_{I}	124	µm/ion pair

In the following, the lower limit of the time jitter is calculated for a Micromegas used in the COMPASS experiment [66]. These Micromegas are operated with the so-called COMPASS gas mixture composed of 80 % neon with an additional quenching of 10 % ethane and 10 % CF_4 with reduced electron diffusion. It is also used for most PICOSEC-Micromegas measurements due to this property. In the following, a mean ionisation length (σ_{I}) estimation is calculated for pure neon gas, as the added quenching gases are mainly affecting the drift velocity and not the ionisation length. Table 4.1 lists the specific values of the gas for this calculation.

The estimated drift velocity (v_{e}) of the free moving electrons under a given electric field has to be calculated next to the mean ionisation length of the gas (σ_{I}). This velocity consists of the omnidirectional thermal electron diffusion and the accelerated movement of the electrons along the electric field. The thermal diffusion is a statistical process and is correlated to the composition of the gas, its pressure, and temperature. The added gases to the neon are affecting the drift velocity, in particular, CF_4 reduces the electron diffusion. The specific drift velocity for this gas mixture depending on the applied field was previously measured for common operation settings [91]. COMPASS gas reaches a drift velocity of up to $v_{\text{d}} = 84\,\text{mm/µs}$ at an electric field of $E_P = 1\,\text{kV/cm·atm}$, it is operated at 500 V for a drift distance of 5 mm.

The lower limit of the time resolution for a COMPASS Micromegas is calculated with the estimated mean ionisation length and the empirically measured drift velocity. The lower limit for the given COMPASS detector in its best possible conditions is estimated to

$$\sigma_{\text{t}} = \frac{\sigma_{\text{I}}}{v_{\text{d}}} = \frac{124\,\mu\text{m}}{84\,\frac{\mu\text{m}}{\text{ns}}} > 1.47\,\text{ns}\,, \tag{4.7}$$

where σ_{t} is the minimal time jitter, σ_{I} is the average ionisation lenght and v_{d} is the drift velocity.

For other detector setups, this value can change, but the time resolution for standard Micromegas detectors is limited in the range of some nanoseconds due to the shown effects. The PICOSEC-Micromegas is a detector concept based on Micromegas that minimises the time jitter and reach sub-nanosecond time resolution.

Part II

PICOSEC-Micromegas: Concept Performance

[. . .] je me contente de croire qu'il y a plus de choses possibles qu'on ne pense.

— Voltaire (1694-1778), ***Micromégas*** *(1757)*

"I content myself with believing that many more things are possible than one could think of", Voltaire (1694-1778), ***Micromégas*** *(1757)*

5 The PICOSEC-Micromegas

Contents

5.1 PICOSEC-Micromegas Collaboration

PICOSEC-Micromegas is a collaboration of leading international institutes with decades of experience in MPGD R&D to develop a new detection mode for Micromegas detectors to overcome the nanosecond limitation in time resolution. HEP experiments have an increasing demand on fast-timing detectors in the order of several picoseconds, due to the ever-increasing beam luminosities and energies. Most fast-timing solutions have disadvantages in high-flux environments, while MPGDs like Micromegas are designed for operation in these specific circumstances. The PICOSEC-Micromegas concept was first presented at the 4th International Conference on Micro Pattern Gaseous Detectors in 2015 [4].

This chapter will shortly introduce the different protagonists of the PICOSEC-Micromegas collaboration followed by the presentation of the detection concept highlighting the prototypes characterised and the general waveform analysis.

5.1.1 RD51 Collaboration

RD51 is a CERN based collaboration of institutes aiming for the development of MPGD technologies. The 2008 founded collaboration covers all kind of MPGD structures [50], as described in section 3.3.1. RD51 is not only stimulating and developing new detector technologies but also supporting the industrialisation of the production processes and MPGD applications in

physics experiments. RD51 developes and provides whole detection chains from detectors up to the front-end electronics.

Four large working groups and several independent researchers are part of the PICOSEC-Micromegas collaboration. The main groups are the Gaseous Detector Development (GDD) lab at CERN, the Aristotle University of Thessaloniki (AUTh), the University of Science and Technology of China (USTC) and several groups from CEA bundled in the RADIAMM programm presented in section 5.1.2. Each of these groups has different profiles and contribute to the collaboration by providing either testing infrastructures, production facilities, or developing simulation and analysis code. The collaboration work is supplemented by the effort of independent researchers around the world, contributing with experience, advise and their professional network.

The PICOSEC-Micromegas collaboration has steadily grown over time. A deeper collaboration identity was formed after the first results were published, leading to the design of an own collaboration logo shown in figure 5.1. It shows a stylised waveform of one of the first prototypes. The fast-timing characteristics of the detector are highlighted by the red coloured short and steep electron peak of the waveform. The long and flat ion tail is coloured in blue. The collaboration name "PICOSEC Micromegas" is written with a bolt capital P and M under the ion tail and limited to the left side by the electron peak.

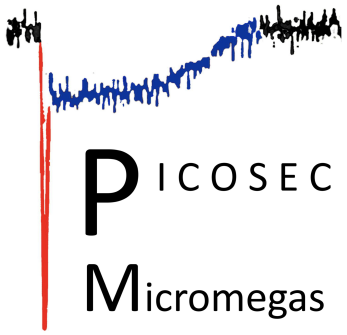

Figure 5.1: Logo of the PICOSEC-Micromegas collaboration.

5.1.2 CEA-PTC RADIAMM

The presented work has been done in the frame of the "RAdiation hard DIAmond-based secondary emitter for development of an ultra-fast timing MicroMegas detector" (RADIAMM), a 3-year project supported by the Cross-Disciplinary Program on Instrumentation and Detection (PTC, "Programmes Transversaux de Compétences") of the CEA ("Commissariat à l'Énergie Atomique"). The RADIAMM project is funding the contribution of CEA institutes to the PICOSEC-Micromegas collaboration with a focus on the development of radiation hard photocathodes and secondary emitter as well as performance characterisation of different prototypes. Three laboratories based at CEA Paris-Saclay have worked together in the realisation of RADIAMM. The origin of the laboratories is very different ranging from fundamental research to industrial-near production chains. In the following, the three laboratories and their contribution to the RADIAMM project will be presented.

The coordinator of the RADIAMM project is the Department of Detectors, Electronics and Informatics for Physics (DEDIP, "Département d'Électronique des Détecteurs et d'Informatique pour la Physique") of the Institute for Research on the Fundamental Laws of the Universe (Irfu, "Institut de recherche sur les lois fondamentales de l'Univers"). It is a department specialised in the development of detectors, electronics and information systems for physics applications. It is embedded in the research institute of the fundamental laws of the universe, mainly involved in particle-, nuclear- and astrophysics. DEDIP contributes to RADIAMM by providing innovative detector concepts, a Micromegas production facility, the design of mechanical and electrical components for the prototypes and a laboratory for detector testings.

The second partner is the Laboratory for Interactions, Dynamics and Lasers (LIDYL, "Laboratoire Interactions, Dynamiques et Lasers") of Saclay's Radiation-Matter Institute (IRA-MIS, "Institut Rayonnement-Matière de Saclay"). It is the laser department of the Institute for studies of material radiation interaction at CEA-Saclay. The main task of this laboratory is to provide a femtosecond UV beam to characterise the PICOSEC-Micromegas prototypes. The beam set-up at LIDYL used for PICOSEC-Micromegas is described in chapter 8.1.

The third group is the Diamond Sensor Laboratory (LCD, "Laboratoire Capteurs Diamant"). It is part of the Laboratory for Industrial Integration of Systems and Technology (LIST, "Laboratoire d'intégration des systèmes et des technologies"), an institute collecting all laboratories at CEA working on the integration of new systems and technologies into industrial applications. LCD provides its know-how in the production of thin diamond and diamond-like structures. These thin layers are investigated in the RADIAMM project as possible robust and efficient photocathodes for PICOSEC-Micromegas detectors in a high-flux environment. The photocathode materials and their characterisation are presented in chapter 13.

5.2 PICOSEC-Micromegas Detector Concept

The main idea of the PICOSEC-Micromegas concept is to suppress the inevitable time jitter of the ionisation in a classical Micromegas, due to different ionisation cluster positions, as shown in section 4.3. Figure 5.2 illustrates the PICOSEC-Micromegas detector concept. A Cherenkov radiator [92] and a photocathode are placed in front of the gaseous volume. The passage of a charged particle through the Cherenkov radiator produces UV photons, which are then absorbed in the photocathode and primary electrons are created on the bottom surface of the photocathode. These electrons are subsequently preamplified and then amplified in the two high-field stages, and induce a signal which is measured between the anode and the mesh.

The crystal material is selected, so that particles move faster than the propagation wave of light in the material. When a particle passes through the crystal, it polarises the atoms and dipoles are formed, radiating electromagnetic waves called Cherenkov light [92]. Those waves can not interfere with each other as the propagation velocity is smaller than the velocity of the particle. The crystal will emit electromagnetic waves in a conical shape in the direction of the passing particle. The opening angle (θ_λ) depends on the refractive index of the radiator material (n_λ) and the relative velocity of the passing particle (β) as

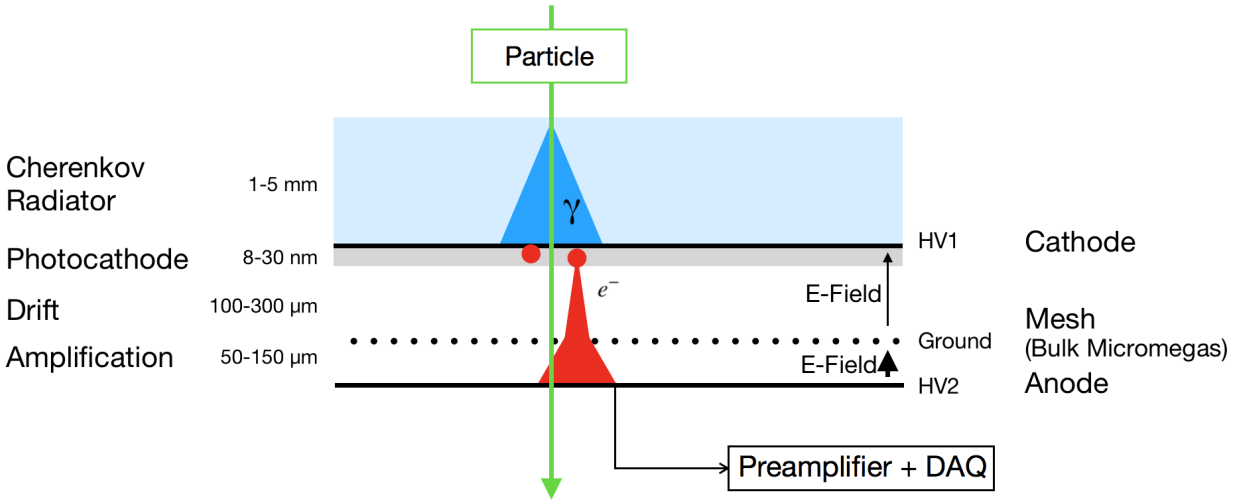

Figure 5.2: The PICOSEC-Micromegas detection concept, described in detail in the text. Schema was first published in reference [5].

$$\cos(\theta_\lambda) = \frac{1}{n_\lambda \beta} \,, \tag{5.1}$$

where λ is the wavelenght of the emitted Cherenkov light.

The photocathode will absorb the Cherenkov light and re-emit electrons. The number of primary photoelectrons ($N_{\text{p.e.}}$) created in the PICOSEC-Micromegas depends on the radiator thickness (L), the transmission efficiency of the radiator material (T_λ), and the quantum efficiency of the photocathode (QE_λ). $N_{\text{p.e.}}$ is calculated as

$$N_{\text{p.e.}} = L \frac{\alpha^2 z^2}{r_e m_e c^2} \int T_\lambda QE_\lambda \sin^2(\theta_\lambda) \mathrm{d}\lambda \,, \tag{5.2}$$

where α=1/137 is the fine-structure constant; z is the charge of the passing particle; r_e and m_e are the radius and mass of an electron and c is the speed of light. The formula can be simplified with β=1 and z=1 for single charged relativistic particle like MIPs,

$$\frac{\alpha^2 z^2}{r_e m_e c^2} = 370 \frac{1}{\text{cm} \cdot \text{eV}} \,, \tag{5.3}$$

and

$$\sin^2\left(\arccos\left(\frac{1}{n_\lambda \beta}\right)\right) = 1 - \frac{1}{n_\lambda \beta} \,. \tag{5.4}$$

Resulting in

$$N_{\text{p.e.}} = 370 \frac{1}{\text{cm} \cdot \text{eV}} \cdot L \int T_\lambda QE_\lambda \left(1 - \frac{1}{n_\lambda \beta}\right) \mathrm{d}\lambda \,, \tag{5.5}$$

for the number of photoelectrons generated by MIPs in a PICOSEC-Micromegas.

Electrons emitted on the photocathode surface experience the same electric field along the same distance to the mesh. The gaseous volume is only needed to amplify the electrons and to induce a readable signal on the anode. A Micromegas-like detector with a grounded mesh between two electric fields with parallel field lines is chosen. A negative voltage is applied to the cathode and a positive voltage to the anode to provide a unidirectional electric field in both regions. With the grounded field, the voltage will only drop until the mesh when a spark occurs. The other region is inversely polarised and stays unaffected by the spark. Additionally, fields can be independently tuned with a grounded mesh and field scans are easily doable.

The drift region is much longer than the amplification region in a classical Micromegas. In the PICOSEC-Micromegas, the drift gap is reduced to the same order as the amplification. The drift gap is operated with an electric field similar to that of the amplification gap. In this field configuration, a first preamplification of the electrons happens in the drift gap, improving the time resolution as it reduces the drift time of the primary electrons. Even though the gaps in the PICOSEC-Micromegas have different purposes than in a classical Micromegas, they will be further referred as drift and amplification gaps.

Different prototypes have been constructed and tested. The design of the gas chamber, as well as the Micromegas detector itself, are designed for different purposes, which will be explained in section 5.3. Various photocathodes, gases and Micromegas technologies have been tested to find the optimal performance for different applications. These tests are presented in part II.

The first prototype generation of this detection concept reached a time resolution of up to 24 ps in tests at a particle beam [5]. It was the first proof-of-concept that demonstrated the ability to reach a time resolution in the order of picoseconds with an MPGD.

5.3 Test Chambers and Prototypes

Different test chambers and prototypes of the PICOSEC-Micromegas concept have been developed. Each prototypes is designed to test and optimise particular detector features. The two universal prototypes, the first and the picolarge chamber, are explained in the following, while the specialised resistive and multipad prototypes are presented in detail in the corresponding measurement chapters. All chambers are modular and can host different detector readout planes, like bulk Micromegas with woven and electroformed meshes, or microbulk detectors. An explanation of the Micromegas detector technologies can be found in section 4.1.

The main differences of the chambers are the size and the accessibility to the photocathode. Small prototypes that can host detectors with 1 cm diameter and larger prototypes, with segmented anodes up to 5 cm diameter total active area are constructed. Modular detectors with easy and fast access to all the components are beneficial for R&D studies, as several components are tested and replaced during measurements.

The prototypes can host a wide variety of photocathodes on two different Cherenkov radiator sizes. The single-channel detectors are equipped with a radiator of 2.5 cm diameter and

the larger multipad hosts 5 cm windows. Different materials are used for the radiator with quartz, MgF_2 and sapphire glass. A variety of thicknesses from 1 mm up to 5 mm (depending on the material) is available. The reflection and absorption of the Cherenkov light in a MCP-PMT radiator has been simulated and compared to measured data (see section 9.2.1 and [9]). Different materials are studied as possible photocathodes (see chapter 13). The materials are evaporated directly onto the radiator or on conductive interlayers. The electric field voltage of the Micromegas is directly applied to the photocathode or conductive interlayer.

The prototypes of the PICOSEC-Micromegas discussed in this manuscript are partly designed and produced at CEA (section 5.3.1 & 5.3.2) and partly by CERN (section 11.1 & 12.2). Table 5.1 gives an overview of the prototype models and its characteristics.

The PICOSEC-Micromegas prototypes are characterised in three different measurement set-ups. The three main set-ups are the ASSET-Chamber at CERN, to measure the quantum efficiency of photocathodes (section 13.2.1); the Laser-Setup at the RADIAMM partner laboratory LIDYL at CEA, to test PICOSEC-Micromegas prototypes with a controlled number of photoelectrons (section 8.1); and the particle beam at the CERN-SPS extraction line, to test the PICOSEC-Micromegas prototypes with MIPs and in high-flux conditions (section 9.1). Additional detailed modelling of the t_0-reference MCP-PMT detector, used during the CERN-SPS beam test, is presented in section 9.2. A small test bench for the PICOSEC-Micromegas prototypes is additionally used at CEA-Saclay next to the described set-ups. This test bench, located in a shared laboratory, is equipped with all necessary modules to power-on a detector and to perform functionality tests and smaller comparative studies.

Table 5.1: Overview of the PICOSEC-Micromegas prototype chambers with the features and the optimisation studies for each one.

	First Chamber	Resistive	Multipad	Picolarge
Window diameter	2.5 cm	2.5 cm	5 cm	2.5 cm or 5 cm
Micromegas technology	Bulk (woven and electroformed meshes)	Bulk	Bulk	Bulk and Microbulk
Anode	1 cm diameter copper	1 cm diameter resistive strip "ATLAS-like" or floating strip resistive	19 Hexagonal pads with 1 cm diameter each	1 cm diameter copper or 7 resistive hexagonal pads
Optimisation goals:				
General characterisation	✓			✓
Mesh types	✓			✓
Photocathodes	✓	✓		✓
High-rate capability		✓		
Durability		✓		
Resistive readout		✓		✓
Scalability			✓	✓
Tracking			✓	✓
Charge sharing			✓	

5.3.1 First Prototype

A technical exploded view drawing of the first prototype chamber of the PICOSEC-Micromegas is shown in figure 5.4. It can support a circular Micromegas with a circular active area and a diameter of 1 cm, as shown in figure 5.3. Micromegas detectors with different technologies (bulk, with woven and electroformed meshes, and microbulk, see section 4.1) have been produced to operate in this chamber. A thin PCB ring with a copper contact is placed on top of the coverlay

around the mesh to provide the drift field voltage to the photocathode and defining the drift distance of 194 µm. The detector hosts circular Cherenkov radiators of 2.5 cm diameter.

The crystal and the Micromegas is held together by a two-piece mechanical structure (figure 5.4b (1) & (4)). The electrical connections for the anode (6a), mesh (6b) and cathode (5) are led out from the mechanical holding on strip conductors. As the first tests were performed with CsI photocathodes, which rapidly deteriorate when exposed to humidity, crystal mounting was designed for a fast manual mounting to limit CsI degradation. A "chamber opening - window changing - chamber closing" cycle can be performed in under five minutes.

The chamber is designed vacuum tight and uses material with minimized outgassing and sealed operation without an exchange of the gas is possible for several days. This operation mode is important for laser tests and other set-ups without permanent gas flow. The detector unit (figure 5.4b) is mounted to the right flange of the gas chamber (figure 5.4a) with a window opening for single-photon calibration. On the opposite side, the anode and mesh of the Micromegas are wired to two high voltage feedthrough connectors. Coaxial cables are used for the internal wiring, leading to a significant reduction of the signal noise. The mesh contact is externally grounded by a long cable with a 50 Ω connector to delay possible reflections of the signals, so that they do not affect the electron peak shape.

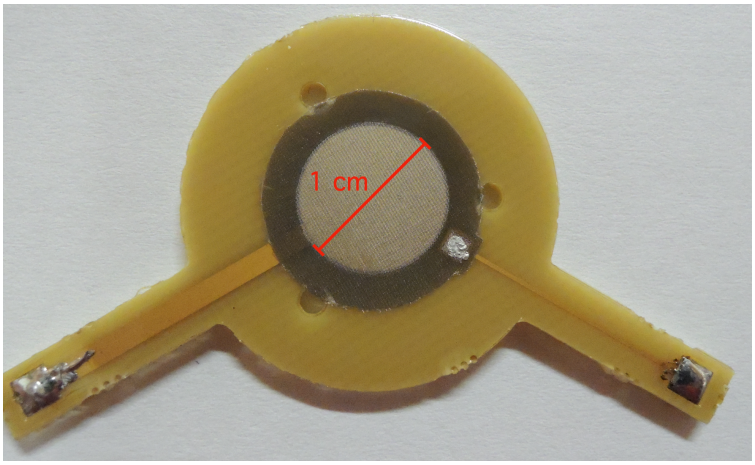

Figure 5.3: Picture of a Micromegas sensor used in the small PICOSEC chamber.

5.3.2 Picolarge

The most recent developed prototype is the "Picolarge" chamber. It was developed from the combined operation experiences of the first prototype and the Multipad. It is the only prototype that can hold both 2.5 cm and 5 cm (1 " and 2 ") Cherenkov radiators. Figure 5.5a shows a CAD model of the Picolarge chamber and figure 5.5b shows a transverse section through the model. The Picolarge chamber consists of a round aluminium vessel similar to the first prototype. The detector is embedded on a PCB larger than the vessel, which is mounted between the back flange and the vessel. A picture of the Micromegas embedded on the PCB is shown in figure 5.5c.

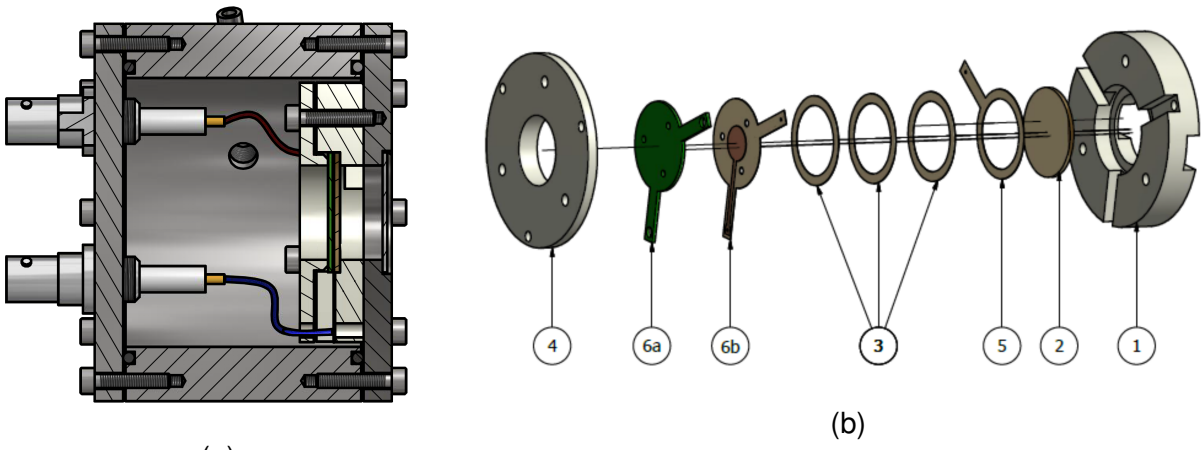

(a) (b)

Figure 5.4: Technical sketches of the first PICOSEC-Micromegas prototype. (a) shows a transverse section of the chamber with the Micromegas mounted on the right. (b) shows an expanded view of the Micromegas and radiator mechanics. The Micromegas (6 a+b) and the Cherenkov radiator (2) are held together by the supporting rings (4 & 1). Four rings (3 & 5) define the drift gap with a thickness of 50 µm each. The last ring (5) has an additional copper ring that gives electrical contact to the cathode.

A mechanic similar to that of other prototypes holds the Cherenkov radiator. The detector with the radiator can be removed from the chamber as one unit which makes the replacement of the radiator with different photocathodes easier and faster. A window is placed on the opposite side of the chamber for single photoelectron and laser measurements.

Figure 5.5d shows a photograph of the assembled chamber with the PCB on the back. Drift and anode voltage are directly wired through the PCB to SMA connectors at the end of the PCB. The mesh is internally connected to ground. Reflections of the electron peak signal return during the ion tail and small dents are visible on the ion tale shape due to the short connection to ground. Figure 6.1 in chapter 6 shows a typical signal of the picolarge prototype with the small dents on the ion tail.

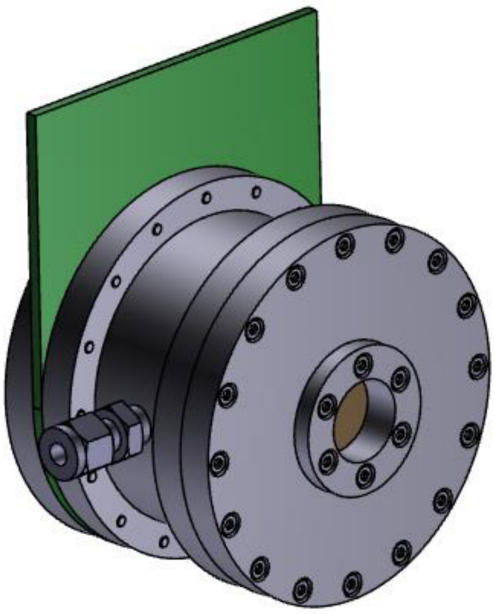

(a) CAD model of the chamber.

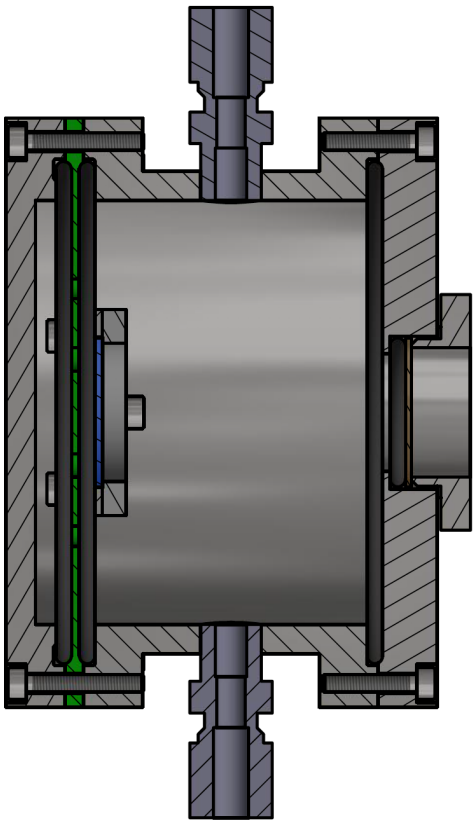

(b) Transverse section of the chamber with the detector on the opposite side of the window.

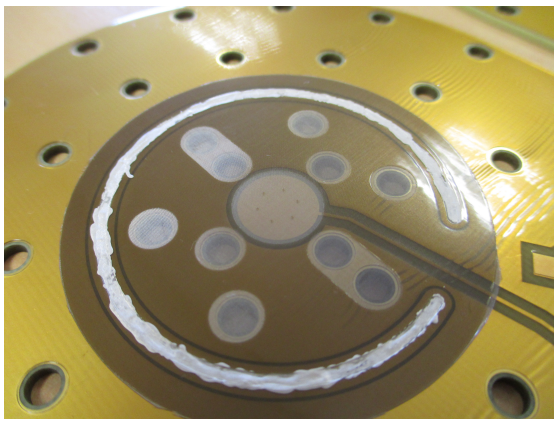

(c) Picture of a single pad Micromegas sensor embedded on the readout PCB.

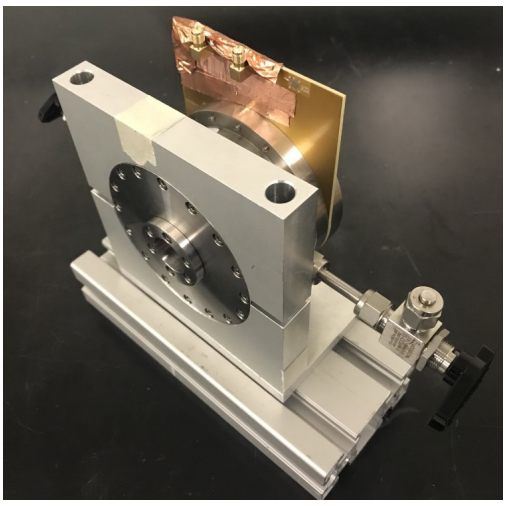

(d) Assembled detector with single pad readout.

Figure 5.5: Technical sketches and pictures of the picolarge chamber.

6 Waveform Characteristics and Analysis

Contents

The PICOSEC-Micromegas detection concept is in an early stage of development, and different studies of the detector behaviour are performed with the prototypes. Only the whole digitised waveforms contain essential information for these studies. This chapter explains the characteristic waveform of the PICOSEC-Micromegas and the waveform analysis techniques. The PICOSEC-Micromegas generates signals created in the amplification gap where electrons and ions drift in opposite directions. Both kinds of particles generate the same signed charge contributing to the detector signal.

The typical shape of a PICOSEC-Micromegas signal is presented in figure 6.1. The signal has a short peak with a rising edge of less than 1 ns[1] rise time induced by the electrons and a broad tail induced by the moving ions. There is also a smaller second peak visible after the electron peak, which origin still needs to be investigated. The shown waveform has been captured from the picolarge prototype operated with COMPASS-gas (see section 5.3.2).

The electrons are several orders of magnitude lighter than the ions, and the mean velocity of the electrons is equal to the dispersion velocity of the amplification avalanche. The electron peak has a width (FWHM) of less than 20 ns. The drift velocity of the ions is thermally distributed due to its heavier weight. The ions form the long tail of more than 150 ns. The signal arrival time (SAT) is determined by the rise time and the amplitude of the electron peak (see section 6.4). Therefore, the waveform analysis of the PICOSEC-Micromegas detector signals and determination of the time resolution only considers the electron peak.

[1] 10%-90% leading edge

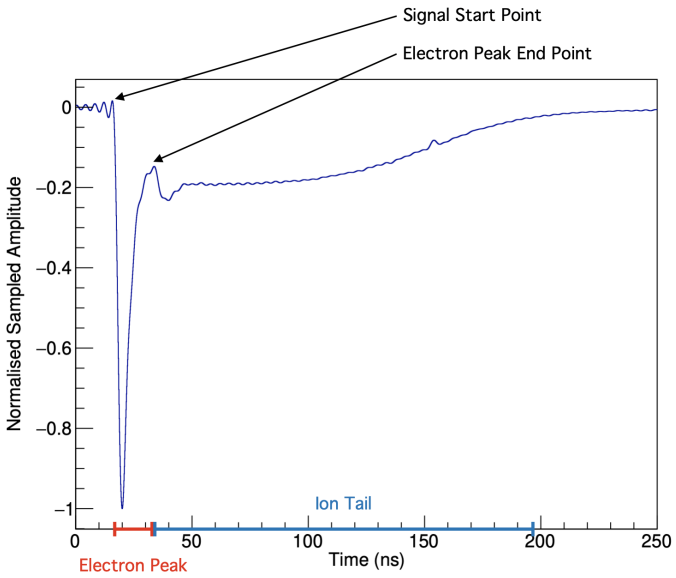

Figure 6.1: Digitized waveform of a PICOSEC-Micromegas signal. The sharp thin electron peak and the long ion tail are distinguishable. The signal overshoot between the electron peak and the ion tail is generated by a reflection of the signal on the grounded mesh (see section 5.3.2).

6.1 Data Aquisition

It is important to preserve as much as possible of the original detector signal shape without modification due to electrical integration and shaping. If not otherwise mentioned, for all measurements presented in this thesis, the full waveform is sampled and analysed off-line. Fast amplifiers with low integration and shaping are needed for the amplification of the signals. The PICOSEC-Micromegas prototype measurements are performed with amplifiers from the CIVIDEC series [93], with a bandwidth from 1 MHz to 2 GHz and a gain of 40 dB, as well as with internally developed amplifiers (see chapter 12.5),

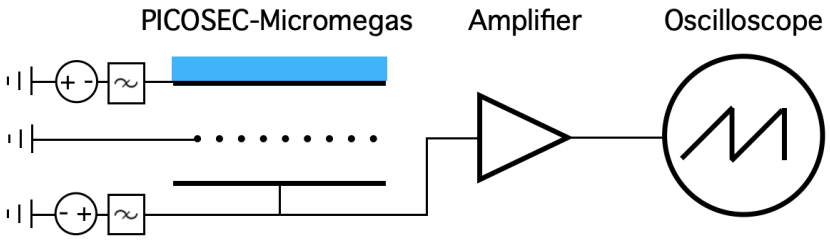

Figure 6.2: Sketch of the operation and DAQ setup for measurements with the PICOSEC-Micromegas prototypes.

The signals of the PICOSEC-Micromegas detector are sampled with oscilloscopes from the LeCroy Waverunner Series [94]. Different oscilloscopes with a sampling rate between 10 GS/s and 80 GS/s, depending on the availability and measurement setup, have been used. Figure 6.2 gives a sketch of the PICOSEC-Micromegas operation setup with amplifier and oscilloscope for the data acquisition. The sampled waveforms, as well as reference and trigger signals (see chapters 8.1 & 9.1), are saved as binary files by the oscilloscope, which are then read by a dedicated software created by the collaboration [95]. Various mathematical algorithms have been applied to the sampled waveforms to extract the demanded information for understanding the detector, which is explained in the following sections.

6.2 Signal Charge

The amplitude and integrated charge of the electron peak are the main ingredients for evaluating the timing performance of a PICOSEC-Micromegas. With these parameters, the gain of the detector and its correlation with the time resolution (see chapter 4 & reference [5]), as well as the impact of different gas mixtures on the signal shape (see section 8.3), can be evaluated. The gain is calculated by the signal charge divided by the amplifier gain and the single electron charge. Moreover, the signal electron peak size is needed for the slewing correction of the time resolution, as explained in section 6.4.3.

The global maximum of the waveform samples is defined as the signal amplitude, and the sum of all samples from the beginning of the signal until the end of the electron peak is defined as the electron peak charge. The beginning of the signal is determined by the last sample of the noise that crosses the baseline before the global maximum of the waveform, and the endpoint of the electron peak is defined by the global minimum in the transition to the ion tail. Both points are indicated in the sample waveform in figure 6.1. The sum of the sample values is converted to pico coulomb with the sampling width and the termination of $50\,\Omega$.

6.2.1 Polya Fit

The signal charge and also the signal amplitude of the PICOSEC-Micromegas forms a distribution as shown in figure 6.3. The Polya function (red line) describes this distribution as

$$P(Q;c;\Theta;\bar{Q}) = \frac{c}{Q}\frac{(\Theta+1)^{\Theta+1}(Q/\bar{Q})^{\Theta}}{\Gamma(\Theta+1)}\exp^{-(\Theta+1)Q/\bar{Q}}\,, \tag{6.1}$$

where Q is the signal charge, c is the amplitude, and $\bar{Q}$ and Θ are the mean and width of the Polya function. In this way, the mean of the Polya function represents the mean signal charge of the PICOSEC-Micromegas. This value is in particularly important to determine the gain of the detector. As the signal charge is given in pico coulomb, the detector gain is calculated by dividing the mean signal charge $\bar{Q}$ of a single photoelectron measurement by the gain of the amplifier and the electron charge (e). The Polya fit of the charge distribution is furthermore used for the slewing correction of the time resolution, as explained in section 6.4.3.

For small signals and small signal-to-noise ratio (S/N), the Polya distribution can be dimmed by the baseline noise. In that case, a superposition of a negative exponential fit describing the noise band and the Polya fit can be done. The overall threshold settings and S/N ratio during the measurements are essential for an accurate Polya fit.

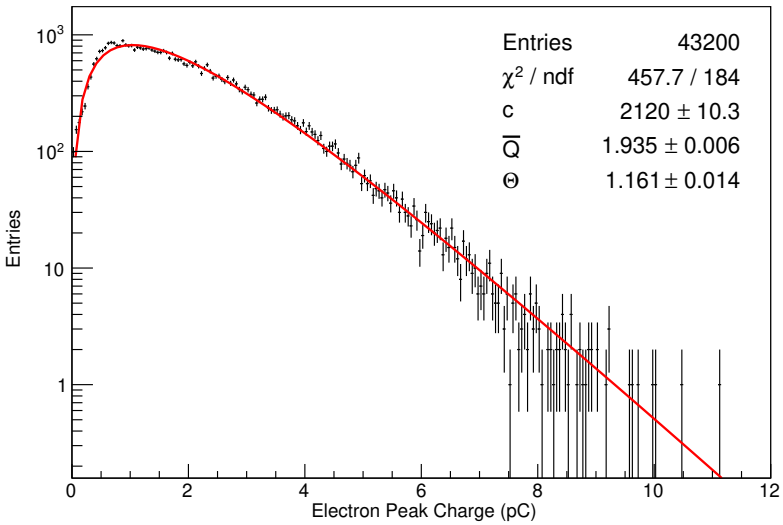

Figure 6.3: The distribution of the signal charge can be described by a Polya function (red line).

6.3 Calculation of the Number of Photoelectrons

An estimation of the number of photoelectrons extracted from the photocathode at a given particle energy or photon intensity is important to compare and classify the obtained time resolution. The number of extracted photoelectrons forms a Poissonian probability density function (PDF) and for low mean number of photoelectrons the time resolution improves approximately linearly with the number of photoelectrons. For larger numbers of photoelectrons the Poissonian distribution tends towards a normal distribution due to the central limit theorem. The time resolution ($\sigma(U_\mathrm{a}, U_\mathrm{d}, N_\mathrm{p.e.})$) can be expressed as

$$\sigma(U_\mathrm{a}, U_\mathrm{d}, N_\mathrm{p.e.}) \approx \frac{\sigma_0(U_\mathrm{a}, U_\mathrm{d})}{\sqrt{N_\mathrm{p.e.}}} \,, \tag{6.2}$$

where $\sigma_0(U_\mathrm{a}, U_\mathrm{d})$ is the time resolution at single photoelectron conditions and $N_\mathrm{p.e.}$ is the mean number of photoelectrons [3]. The measured time resolution depends on the voltage applied to the drift (U_d) and amplification region (U_a) of the detector.

For cases with a low expected number of photoelectrons, the efficiency of the photocathode is estimated by the ratio of the mean signal size of the measurement and the mean signal size with single photoelectron conditions with the same detector settings. The mean of the Polya distribution

determines the mean signal size in both cases. Single photoelectron measurements are performed with a dedicated light source extracting precisely one photoelectron. One way of creating these conditions is in the laser setup, as explained in section 8.1.3.

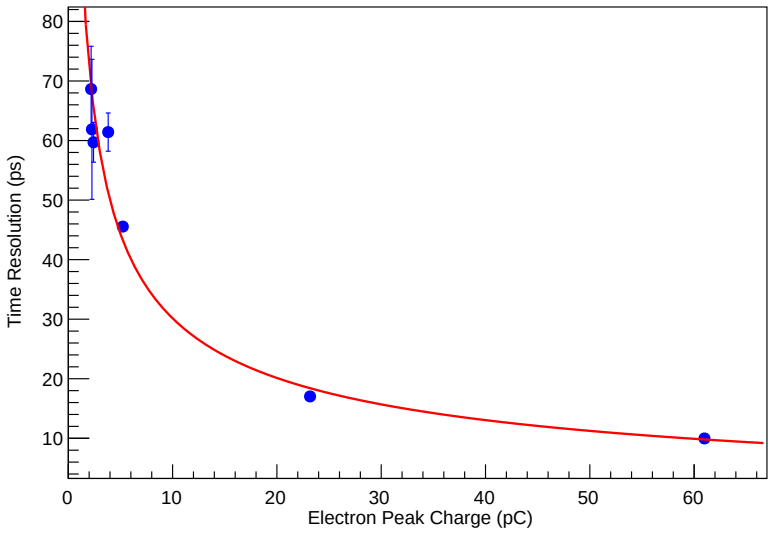

Figure 6.4: Measurement of the time resolution for different light settings and fit of equation 6.3. The detector is operated with $U_\mathrm{a} = 275\,\mathrm{V}$ and $U_\mathrm{d} = 500\,\mathrm{V}$.

For measurements with many photoelectrons, this method shows high discrepancies from the expected number of photoelectrons. An alternative method to calculate the number of photoelectrons is done by performing several measurements with the same detector setting under different numbers of photoelectrons. This method is only possible when the initial number of photoelectrons can be tuned by the set-up. The following measurements are performed in a laser with the light intensity variated with different attenuators. By this way, the Cherenkov light of different energetic particles is simulated. For each of these measurements, the time resolution and the mean signal charge ($\bar{Q}$) is determined and plotted against each other. Afterwards the function

$$\sigma(U_\mathrm{a}, U_\mathrm{d}, \bar{Q}) = A(U_\mathrm{a}, U_\mathrm{d}) \frac{B(U_\mathrm{a}, U_\mathrm{d})}{\sqrt{\bar{Q}}} \,, \tag{6.3}$$

where $A(U_\mathrm{a}, U_\mathrm{d})$ and $B(U_\mathrm{a}, U_\mathrm{d})$ are fit parameters, is fitted against these points. Figure 6.4 gives an example for this curve with the points measured with a PICOSEC-Micromegas operated in a laser beam with different light intensities. The number of photoelectrons is afterwards calculated with equation 6.2 and 6.3 as

$$\sqrt{N_\mathrm{p.e.}} = \frac{\sigma_0}{\frac{B}{\sqrt{\bar{Q}}} A} \,. \tag{6.4}$$

Table 6.1 gives the calculated values for the number of photoelectrons for the example shown in figure 6.4 and figure 6.5 gives an overview of both presented methodes to determine the number of photoelectrons. The column with “estimated” number of photoelectrons gives the number of

Table 6.1

Time Resolution (ps)	Signal Charge (pC)	Attenuation Factor	Estimated $N_{\text{p.e.}}$	Calculated $N_{\text{p.e.}}$
68.64 ± 7.19	2.19 ± 0.04	780	1	0.99
61.88 ± 11.76	2.27 ± 0.05	289	1.04	1.03
59.71 ± 3.34	2.42 ± 0.03	123.9	1.11	1.10
45.55 ± 0.76	5.23 ± 0.03	45.9	2.39	2.52
17.03 ± 0.29	23.18 ± 0.07	8.5	10.59	13.91
9.97 ± 0.12	60.20 ± 0.10	2.7	27.51	48.21

photoelectrons calculated by the fraction of the mean signal charge and the "calculated" number of photoelectrons are the values calculated by fitting the points.

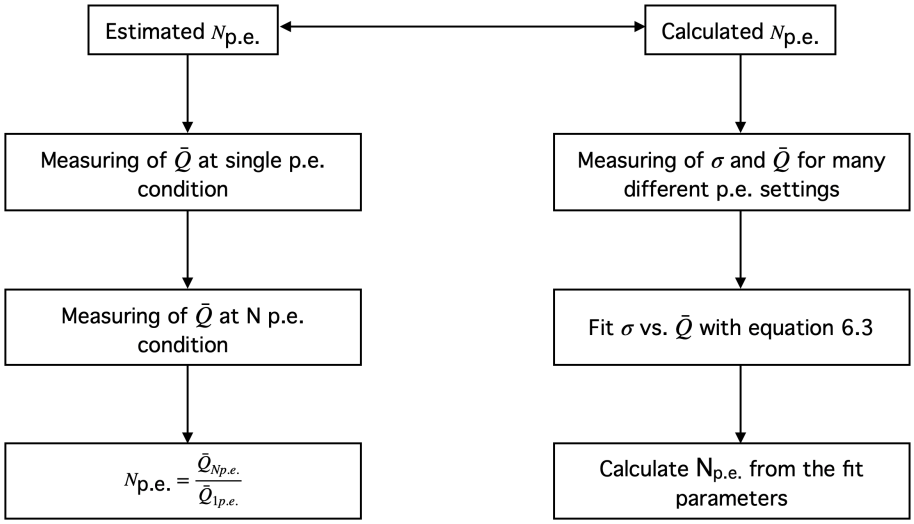

Figure 6.5: Block diagramm of the different procedures to extract $N_{\text{p.e.}}$.

For a smaller number of photoelectrons ($< 3\, N_{\text{p.e.}}$), both methods provide comparable results, but at larger mean signal sizes, the first methods calculate systematically lower number of photoelectrons. Table 6.2 shows a quantitative comparison for the three highest light settings in table 6.1, which are significantly higher than single photoelectron conditions. The first column gives the fraction of attenuation between these settings, which means the factor of change in light intensity. The second and third column gives the factor of change in the number of photoelectrons determined by both methods for each change of light intensity. Especially for larger amounts of light, the calculated numbers of photoelectrons by the fitting method are in a better agreement with the expected ratio of light intensity.

All in all, the determination of the precise number of photoelectrons is challenging. For higher light intensities, the method with fitting several points provides a more reasonable number, but this method is sensitive to the fit quality, and several measurements at different high-intense

Table 6.2

Fraction of attenuation	Fraction estimated $N_{\text{p.e.}}$	Fraction calculated $N_{\text{p.e.}}$
$\frac{45.9}{8.5} = 5.4$	4.4	5.5
$\frac{45.9}{2.7} = 17$	11	19
$\frac{8.5}{2.7} = 3.2$	2.6	3.5

light settings are necessary. For smaller expected number of photoelectrons, the ratio between the mean signal size provides sufficient accurate results.

6.4 Time Resolution

PICOSEC-Micromegas is a detection concept aiming to achieve superb time resolution. In the following, it will be described as the uncertainty of the detector signal arrival time (SAT). A precise determination of the SAT for each waveform in crucial for the calculation of the time resolution.

6.4.1 Signal Arrival Time

A software analysis of the sampled waveforms determines the SAT of each signal, similar to the determination of the signal charge presented in section 6.2. The waveforms are sampled with finite datapoints limited by the digitisers sampling rate of typically 20 GS/s. A direct evaluation of the SAT from the sampled dataset, for example with common constant fraction discrimination (CFD) algorithm, could lead to a non-negligible uncertainty of the SAT due to the digitising error [43]. This systematic error is avoided when the waveform is fitted by a continuous mathematical function, which will be then used to calculate the SAT and the time resolution.

A function describing the rising edge of the PICOSEC-Micromegas waveform is the generalised logistic function as

$$S(t) = \frac{P_0}{\left(1 + P_1 \exp^{-P_2(t-P_3)}\right)^{P_4}} , \tag{6.5}$$

where P_0 is the upper asymptote, P_1 is the scaling factor related to $S(0)$, P_2 is the growth rate, P_3 is the translation in t-dimention, and P_4 defines the asymmetry of the growth rate.

The generalised logistic function in equation 6.5 will be fitted to the rising edge of each sampled waveform, as shown in figure 6.6. The SAT is afterwards numerically calculated to the 20 % constant fraction of the generalised logistic function. The SATs defined by the generalised logistic function fit will be used to evaluate the ΔSAT distribution, whose standard deviation represents the time resolution. The particularities by calculating the standard deviation of the ΔSAT distribution are presented in the following section.

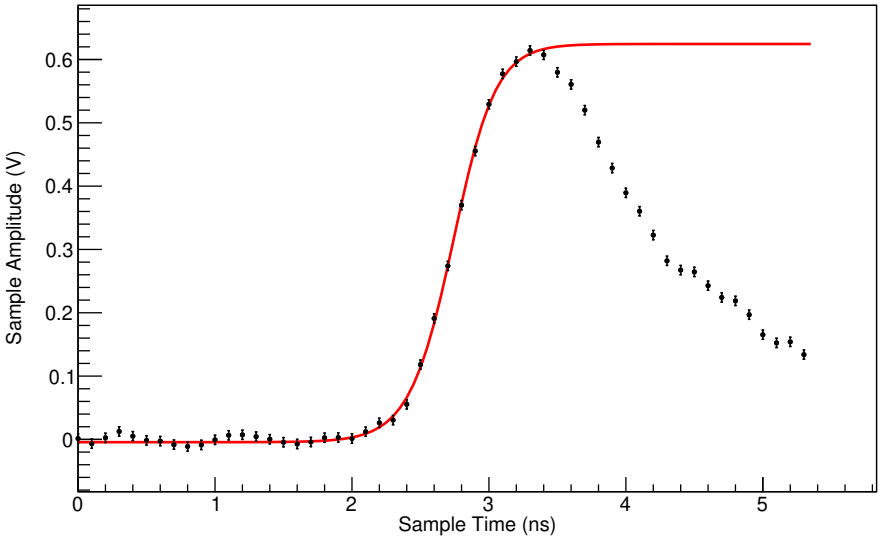

Figure 6.6: A general sigmoid function is fitted to sampled data points of the rising edge of a PICOSEC-Micromegas waveform.

6.4.2 SAT Uncertainty

The uncertainty of the SAT is evaluated by measuring the SAT difference (ΔSAT) of the detector under test (DUT) and a reference detector with known time resolution. A large number of signals will be acquired in one measurement, and the ΔSATs of all signals will form a distribution similar to figure 6.7a, which can be described as a convolution of many Gaussian functions, as further explained in section 6.4.3. The first standard deviation of this resulting distribution describes the time uncertainty of the whole system as

$$\sigma_{\text{tot}} = \sqrt{\sigma_{\text{DUT}}^2 + \sigma_{\text{REF}}^2}\,, \tag{6.6}$$

where σ_{tot} is the standard deviation of the ΔSAT distribution, σ_{DUT} is the time resolution of the DUT and σ_{REF} is the combined time resolution of the reference detector and the acquisition system (oscilloscope and cabling). When the time resolution of the reference system (σ_{REF}) is way smaller than the expected time resolution of the DUT $\sigma_{\text{REF}} << \sigma_{\text{DUT}}$. The time resolution of the DUT can be approximated to $\sigma_{\text{tot}} = \sigma_{\text{DUT}}$.

For each measurement setup, the reference time resolution (σ_{REF}) will be determined, and the measured standard deviation will be corrected if needed. Furthermore, read-out electronics and the constant fraction discrimination (CFD) algorithm contribute to the observed time resolution, which is estimated by recording an identical signal on two oscilloscope channels and determining the variance in the SAT.

The measurement inaccuracy of the DAQ (σ_{DAQ}) is experimentally determined with the use of a time reference detector (MCP-PMT) that is further characterised in section 9.2. An 18 GHz

power divider is used to split the signal of one MCP-PMT into two identical signals, and no impact on the signal quality is observed. The time difference of the SAT of both signals follows a distribution with a width of $\sigma = 3.09 \pm 0.04$ ps. This leads to a combined timing jitter of the read-out electronics and the CFD algorithm of $\sigma_{\mathrm{DAQ}} = 3.09 \pm 0.04$ ps, which yields a time resolution per channel of $\sigma_{\mathrm{DAQ}}/\sqrt{2} = 2.18 \pm 0.03$ ps. The measured instrument response function agrees with the trigger and interpolation jitter of <2.5 ps (RMS) expected for the oscilloscope [94].

6.4.3 Slewing

The width of the ΔSAT distribution defines the time resolution. The ΔSAT has a Gaussian-like shape, but a single Gaussian function fit will in most cases not agree with the distribution as shown in figure 6.7a, because the SAT and the time resolution depends on the signal pulse height. The signal arrives earlier at higher signal sizes. This correlation, known as slewing, has to be considered in the evaluation of the ΔSAT distribution width.

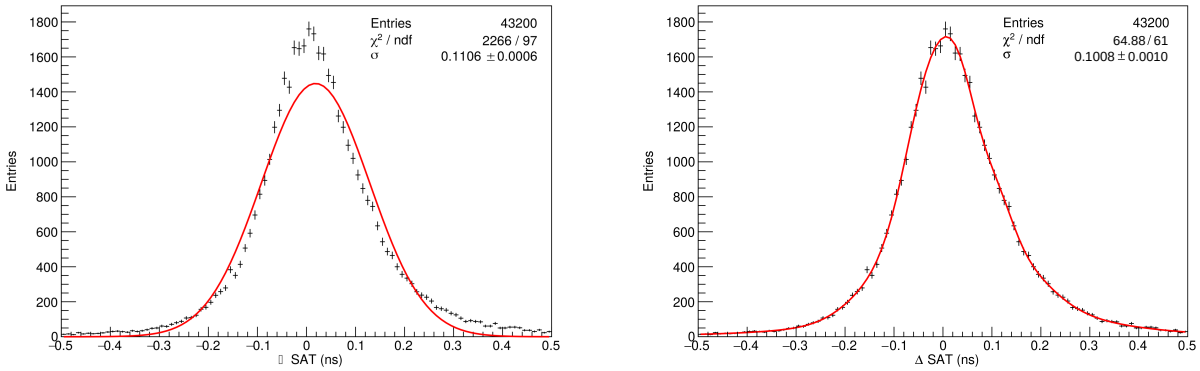

(a) The distribution of the SAT difference can not be described with a single Gaussian fit without considering slewing effects.

(b) A convolution of all Gaussians from the slewing correction shows a good agreement with the distribution of the SAT difference.

Figure 6.7: Comparison of the fit quality without and with slewing correction.

Figure 6.8 shows the slewing curves corresponding to the ΔSAT distribution in figure 6.7a. The time resolution (figure 6.8b) and the mean SAT (figure 6.8a) is calculated separately for different signal charges. The division of the signal charge regions is done with the charge distribution and the fitted Polya function, as explained in section 6.2.1. Each division should contain a sufficient number of entries to deviate the time resolution from the ΔSAT distribution. The slewing curves show an improvement of the time resolution for large signals and an early SAT.

The information gathered by the slewing curves improves the fitting of the ΔSAT distribution. Not only a single Gaussian function (like in figure 6.7a) is fitted to the ΔSAT distribution, but a superposition of the individual Gaussians for the different signal charge divisions (as used in figure 6.8b) is used to describe the ΔSAT distribution. The resulting curve is shown in figure 6.7b. This curve shows an agreement with the measured distribution. The time resolution (σ) is cal-

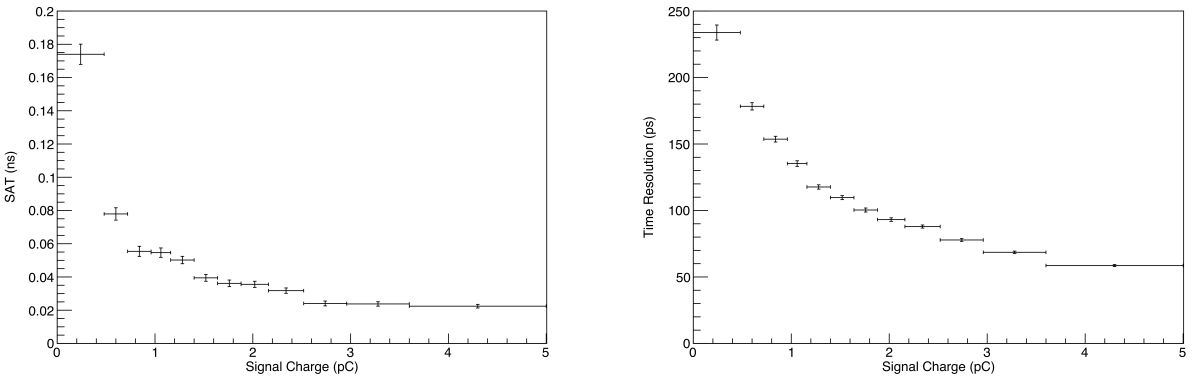

(a) The mean SAT moves with higher signal charges.

(b) The time resolution improves with higher signal charges.

Figure 6.8: Slewing of the SAT and time resolution.

culated out of the sum of the width of the individual Gaussian functions for the different signal charges as

$$\sigma^2 = \sum_{i=1}^{n} a_i \sigma_i^2 + \sum_{i=1}^{n} \sum_{j=i+1}^{n} a_i \times a_j \times \left(\sigma_i^2 + \sigma_j^2 + (\mu_i - \mu_j)^2\right) \ , \tag{6.7}$$

where σ_i, σ_j are the standard deviation and μ_i, μ_j are the mean of the Gaussian functions for each signal charge division (which represents the time resolutions and the mean SATs as shown in the slewing curves in figure 6.8), and a_i, a_j are the probability factors for each signal charge division derived from the Polya distribution.

7 Modelling

Contents

7.1 Definition of the Model Components

The Aristotle University of Thessaloniki (AUTh) group of the PICOSEC-Micromegas collaboration (see section 5.1.1) has developed a mathematical model of the PICOSEC-Micromegas signal propagation [95, 96, 97]. This chapter compares the model to simulated and measured data from the PICOSEC-Micromegas and identifies the components in the amplification process with the main impact on the time resolution. The model uses input parameters from GARFIELD++ simulations [98] of the electron drift and avalanche propagation in the detector for variating electric fields. In this chapter, the different steps of the signal propagation, from the single electron drift and the pre-amplification avalanche up to the transition through the mesh are calculated with the model. The main physical interactions are explained, and a new factor "time-gain per interaction" is introduced to describe the transmission time and time jitter of each step. Finally, the performance of the model calculations is compared to results from GARFIELD++ simulations and measurements with the prototypes.

7.1.1 Photoelectron Drift Time

The first step in the signal creation process is the drift of single photoelectrons before creating a pre-amplification avalanche. The model calculates the probability per unit length for a free-moving electron in the electric field to gain enough energy for a further ionisation of a Noble gas atom. One parameter used in the model to describe the energy transfer from the photoelectron to the gas atoms is the Penning transfer rate (r), which gives the probability of an ionising energy transfer from an excited inert gas atom.

The drift time of the initial photoelectron increases at each interaction with a momentum transfer to the gas, and this mean increase in drift time per interaction is hereafter expressed as the average time-gain factor τ. The average number of inelastic interaction of the photoelectron with sufficient energy transfer but without indirect ionisation ($n(x)$) on a distance Δx is given as

$$n(\Delta x) = (1 - r) \cdot \beta \cdot \Delta x \ , \tag{7.1}$$

where β is the proportional factor of the Townsend coefficienct increase due to the Penning transfer as

$$\alpha(r) = \alpha(0) + r\beta. \tag{7.2}$$

The time interval (Δt) needed for the photoelectron to drift a certain distance (Δx) in the gas, depending on the Penning transfer rate (r), is given as

$$\Delta t = \frac{\Delta x}{V_0} - (1 - r) \cdot \beta \cdot \Delta x \cdot \tau \ , \tag{7.3}$$

where V_0 is the effective photoelectron drift velocity for $r = 1$. The effective drift velocity of the electrons ($V_{\text{eff}}(r)$) under consideration of the time-gain per interaction is hereafter calculated as

$$\frac{1}{V_{\text{eff}}(r)} = \frac{\Delta t}{\Delta x} = \frac{1}{V_0} - (1 - r) \cdot \beta \cdot \tau \ . \tag{7.4}$$

The model shows an inverse proportionality between the Penning transfer rate and the effective drift velocity of the single photoelectron.

7.1.2 Avalanche Propagation Time

The first ionisation of the photoelectron will initiate an avalanche. The time-gain per interaction of the electron generation process in the avalanche is modelled to understand the propagation characteristics of the avalanche. The ionisation of a new atom is a scattering process of the drift electron, and the drift velocity of the parent electron suffers from a time delay due to the elastic back-scattering. The newly ionised electron gets by this way an advantage in drift time (ρ_{i}) compared to the mean electron velocity of a single drift electron (V_{d}) that only undergoes elastic-scattering. The newly ionised and its parent electron are then equally accelerated and go through further scattering processes. As the electrons are indistinguishable in the avalanche after the ioni-

sation, the effective velocity of each avalanche electron (V_{ea}) is determined by one parameter, the mean time advantage of newly created electrons (ρ).

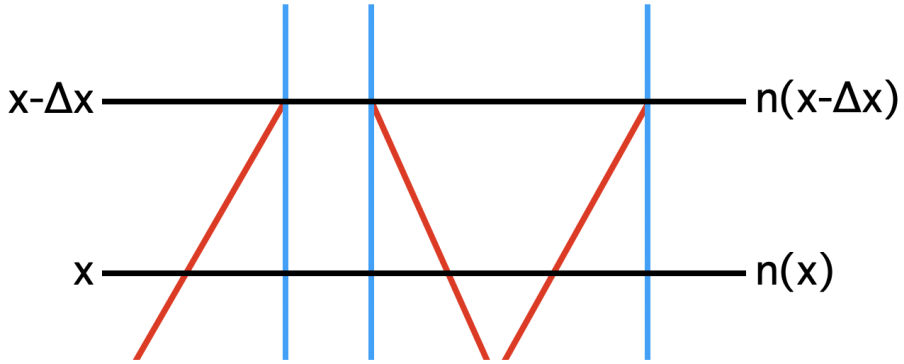

Figure 7.1: A schema of the avalanche propagation for a small extract from the whole avalanche length. In plane $x - \Delta x$ arrive $n(x - \Delta x)$ parent electrons (blue) and after a distance Δx, new electrons (red) are created and $n(x)$ electrons reach the plane x.

A schema of the avalanche propagation for a small extract from the whole avalanche length (Δx) is shown in figure 7.1. The mean transit time of the pre-amplification avalanche reaching a plane x with $n(x)$ electrons from the plane $x - \Delta x$, while ionising Δn new electrons, is expressed as

$$T(x, n(x)) = T(x - \Delta x, n(x - \Delta x)) + \langle \Delta t \rangle - \frac{\Delta n}{n(x)} \rho \,, \tag{7.5}$$

where $\langle \Delta t \rangle$ is the mean drift time of the avalanche for the distancs Δx and

$$T(x - \Delta x, n(x - \Delta x)) = \frac{1}{n(x - \Delta x)} \sum_{k=1}^{n(x-\Delta x)} t_k(x - \Delta x) \tag{7.6}$$

is the mean time all parent avalanche electrons needed to reach plane $x - \Delta x$. This relation uses the mean velocity of k avalanche electrons

$$V_{\text{ea}} = \left\langle \frac{\Delta x}{\Delta t_k} \right\rangle \,, \tag{7.7}$$

and for infinitesimal Δx can be written as

$$\mathrm{d}T(x, n(x)) = \frac{dx}{V_{\text{ea}}} - \frac{dn}{n(x)} \rho \,. \tag{7.8}$$

This relation is integrated for the whole avalanche length L and is written as

$$T(L, N_L) = \frac{L}{V_{\text{ea}}} - \rho \ln(N_L) + C \,, \tag{7.9}$$

where N_L is the number of electrons reaching the mesh after an avalanche length of L and C an integration constant.

7.1.3 Mesh Transition Time

The last step in the modelling of the PICOSEC-Micromegas signal transmission time is the transit of the avalanche electrons through the mesh into the amplification region. This step is simplified with the assumption that the electrons undergo only non-ionising processes while moving through the mesh, which is not true for the real detector. The mesh transparency under given field settings is simulated with the GARFIELD++ simulation, and the number of the electrons entering the amplification stage (M) is for all tested electric field settings reduced by approximately a factor of four compared to the ones reaching the top of the mesh (N). This factor is found to be independent of the avalanche length and the electron multiplicity on the mesh.

The mean arrival time of the electrons after the mesh ($T_{\mathrm{m}}(L,N)$) is calculated as

$$T_{\mathrm{m}}(L,N) = \frac{1}{M}\frac{M}{N}\sum_{k=1}^{N} t_k + \frac{1}{M}\frac{M}{N}\sum_{k=1}^{N}\Delta t_k + T_{\mathrm{p}}(L)\ , \tag{7.10}$$

where t_k is the arrival time on the mesh of the kth pre-amplification avalanche electron; Δt_k is the transit time of the kth electron passing through the mesh; and $T_{\mathrm{p}}(L)$ is the initial photoelectron drift time. $T_{\mathrm{p}}(L)$ depends on the drift length L as

$$T_{\mathrm{p}}(L) = \frac{(D-L)}{V_{\mathrm{eff}}(r)} + d_{\mathrm{off}}\ , \tag{7.11}$$

where D is the distance of the drift region and d_{off} is an offset in the time reflecting the minimum acceleration time needed for the electron to perform an interaction. The electron arrival time after the mesh is hereafter equal to the electron arrival time on the mesh ($T_{\mathrm{tot}}(L,N)$) plus the mean transit time through the mesh as

$$T_{\mathrm{m}}(L,N) = T_{\mathrm{tot}}(L,N) + \langle\Delta t\rangle\ . \tag{7.12}$$

The variance of the time after the mesh is the sum of the variance on the mesh and the variance of the mean transit time. The three components t_k, Δt_k, and $T_{\mathrm{p}}(L)$ are uncorrelated, and each of them is contributing independently to the variance of the electron arrival time after the mesh. Further calculation of the model will show, that the time resolution of the PICOSEC-Micromegas detector is dominated by the time spread of the initial photoelectron drift time. The time resolution is therefore mainly determined by the drift length of the primary electron ($D-L$) and the electron multiplication reaching the mesh from the avalanche pre-amplification (N). Both parameters improve with a higher electric field in the drift gap, reducing the drift path and increasing the pre-amplification gain.

7.2 Mathematic Model

Based on the discussed components of the model, the signal transition time distribution for the two steps, the single electron drift and the avalanche propagation, and the total SAT before and after the mesh are calculated. In a second step, the mean signal transition time and its standard deviation are calculated as a function of the avalanche length and the electron multiplication on the mesh, as both are characteristics of the pre-amplification in the drift region. The avalanche multiplication after the mesh is assumed to give only a constant time delay to the signal, as many electrons start the avalanche nearly simultaneously from the mesh creating a higher statistic and minimising the individual jitter effects of each electron. With this assumption, the standard deviation of the SAT after the mesh is approximately equal to the standard deviation of the SAT on the anode. The calculated model is for all steps compared with the GARFIELD++ simulation results performed by the AUTh group [97]. In the last step, a Monte-Carlo simulation of the expected time resolution for several photoelectrons is performed, and the characteristics of the results are compared with results obtained with the PICOSEC-Micromegas prototype.

The model calculation can be performed for various settings of the electric field and gas mixture with different Penning transfer rates. For the presented calculation, a Penning transfer rate of 50 % with the COMPASS gas and a fixed anode voltage of 450 V is chosen. The calculation is performed for different drift voltages ranging from 325 V up to 425 V and the drift length is set to 182 µm. Several physical parameters are necessary as an input for the calculation. These parameters are extracted from the GARFIELD++ simulation [97], and a table with all input parameters for the different drift voltage settings is given in in the appendix A.2 .

7.2.1 Time Distribution

Up to 100k events for each drift voltage setting are simulated with GARFIELD++. The drift time and length of the primary electron before starting the avalance, the time of all avalanche electrons reaching the mesh with the number of electrons on the mesh, as well as the arrival time and number of electrons after the mesh are extracted for each simulated event. The transition times for each stages are forming a continous probability distribution that is described by an inverse Gaussian function, which is also known as the Wald distribution [99]. The general description of the probablity density function (PDF) is

$$f(x,\mu,\lambda) = \left(\frac{\lambda}{2\pi x^3}\right)^{1/2} \exp\left(\frac{-\lambda(x-\mu)^2}{2\mu^2 x}\right) , \tag{7.13}$$

where μ is the mean value and λ is the shaping parameter. The variance of this function is

$$V[x] = \frac{\mu^3}{\lambda} . \tag{7.14}$$

The variance of the photoelectron drift time depends linearly on the drift lenght as

$$V[T_{\mathrm{p}}(L)] = (D - L) \cdot \sigma_{\mathrm{p}}^2 + \Phi \,, \tag{7.15}$$

and the variance of the avalanche electrons on the avalanche integration lenght (x) as

$$V[T_{\mathrm{ea}}(x)] = \sigma_0^2 + \phi \,, \tag{7.16}$$

where the slopes (σ_{p}^2, σ_0^2) and the constant terms (Φ, ϕ) are extracted by linear fits from the GARFIELD++ simulation results. With the given terms, the PDFs for the single photoelectron drift and the avalanche transmission time are calculated. The total transmission time before the mesh is the sum of both functions.

The variances depend on the drift length and the distribution of the transmission time for any possible drift length is calculated by integrating the inverse Gaussian distribution together with the probability to observe an avalanche of length L in the interval of $[x_1, x_2]$ as

$$F(T) = \int_{x_1}^{x_2} f(T, \mu(L), \lambda(L)) \cdot R(L) \mathrm{d}L \tag{7.17}$$

where

$$R(L) = \frac{a}{\mathrm{e}^{a \cdot x_2} - \mathrm{e}^{a \cdot x_1}} \mathrm{e}^{a \cdot L} \,, \tag{7.18}$$

and a is the Townsend coefficient at a given Penning transfer rate. The calculated time distributions are compared with the results obtained by the GARFIELD++ simulation given in figure 7.2 for a drift voltage of 350 V. The black points are the transmission times extracted from the simulation, and the coloured curves are the corresponding calculated inverse Gaussian distribution integrated over the whole drift region. The model of the photoelectron (red) and avalanche electron (blue) transmission time shows a good agreement with the simulated data. The variance of the additional time delay of the electron transmission through the mesh is slightly overestimated due to the assumption in the model, causing a wider calculated distribution of the transmission time after the mesh (green).

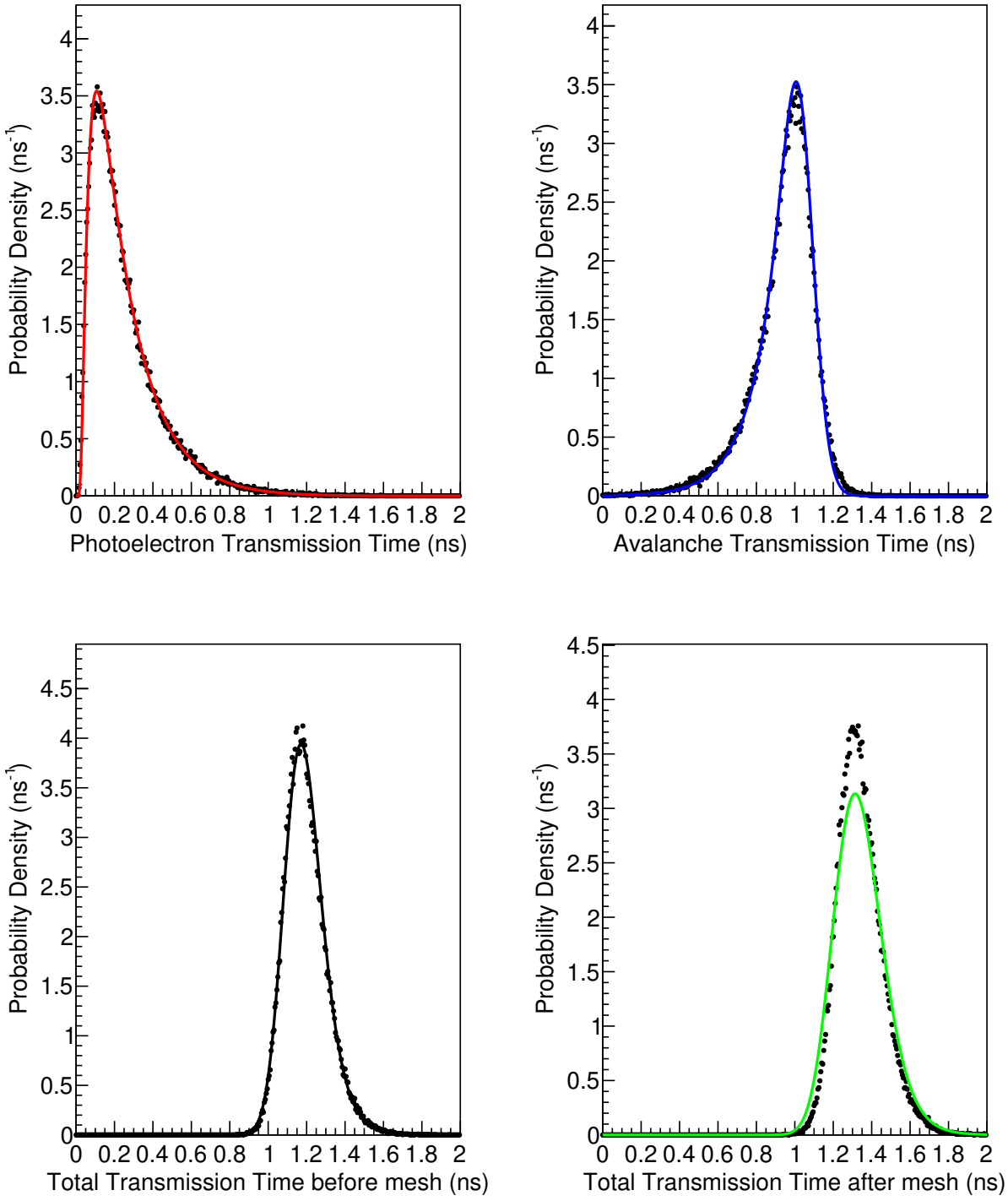

Figure 7.2: Calculated Wald distribution of the model for 350 V drift field compared with points generated by the Garfield++ simulation. The modelled distributions for other drift fields are presented in the appendix A.2

7.2.2 Comparison of Different Drift Fields

The different input parameters for the modelling of each setting are extracted from the GARFIELD++ simulation results, and the values are given in the appendix in table A.2. The mean and standard deviation of the calculated transmission time distributions are compared to the simulation result for each field setting given in table 7.1. The calculated results show, in general, a good agreement with the results from the GARFIELD++ simulation and the model works for different detector settings. The most significant discrepancies between the model and the simulation are observed by the calculated standard deviation of the mean time after the mesh, where the model predicts a systematically higher time jitter after the mesh transparency.

Table 7.1: Comparison of model prediction and GARFIELD++ results of the mean transmission time and the standard deviation for different drift voltages.

Drift Voltage (V)		Photoelectron transmission time		Avalanche transmission time		Time on the mesh		Time after the mesh	
		μ (ns)	σ (ns)	μ (ns)	σ (ns)	μ (ns)	σ (ns)	μ (ns)	σ (ns)
325	GARFIELD++	0.326	0.230	0.952	0.201	1.279	0.128	1.426	0.136
	Model	0.327	0.232	0.948	0.189	1.275	0.128	1.428	0.163
350	GARFIELD++	0.253	0.184	0.943	0.160	1.197	0.110	1.341	0.116
	Model	0.255	0.189	0.942	0.152	1.197	0.110	1.342	0.135
375	GARFIELD++	0.169	0.147	0.951	0.123	1.121	0.089	1.261	0.093
	Model	0.169	0.152	0.954	0.124	1.123	0.090	1.263	0.109
400	GARFIELD++	0.144	0.121	0.917	0.108	1.061	0.079	1.196	0.081
	Model	0.143	0.127	0.919	0.102	1.062	0.079	1.197	0.094
425	GARFIELD++	0.139	0.105	0.873	0.091	1.011	0.072	1.142	0.073
	Model	0.138	0.109	0.871	0.087	1.010	0.072	1.140	0.085

The standard deviation of the inverse Gaussian distribution used to model the total transmission time of the electron after the mesh is expected to be equal to the time resolution of the detector, as only a constant delay is added to the SAT by the amplification avalanche. The modelled standard deviation for the different drift voltages is compared to results obtained with the PICOSEC-Micromegas in a laser beam under single photoelectron conditions (chapter 8). Figure 7.3 gives the modelled field scan for an amplification voltage of 450 V and the black curve gives the results measured in the laser for the same amplification voltage. The modelled curve shows a good agreement with the measured results when all approximations in the model and the measurement uncertainties are taken into account. This result demonstrates the good performance of the model in reproducing the timing properties of the PICOSEC-Micromegas with mathematical calculation.

Up to now, each time distribution is calculated by integrating over all possible avalanche lengths. The effect of the drift length on the time distribution is studied by dividing the whole drift gap into smaller parts and reducing the integration length to these parts. Figure 7.4 gives the

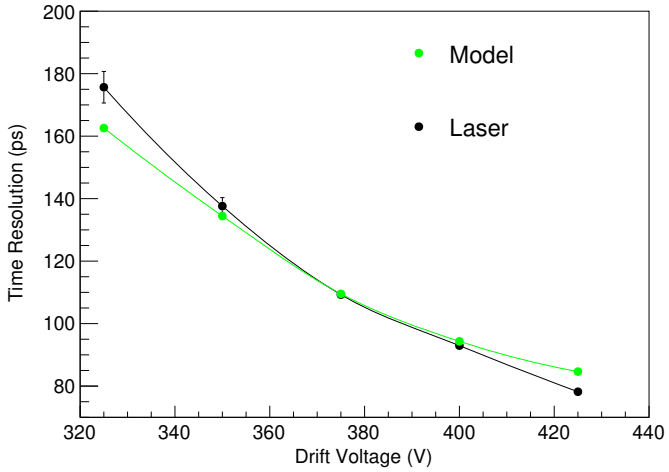

Figure 7.3: Comparison of the modelled time resolution after the mesh with the time resolution measured in a Laser for the same field settings. The results from the field scan for the separate stages of the signal are given in the appendix A.3.

result of the mean transmission time after the mesh and its standard deviation for all drift fields distributed in integration lengths according to the x-axis error bars of each point. The same curve for the photoelectron and avalanche transmission time and the total arrival time before the mesh are presented in the appendix A.4.

A larger avalanche with higher gain is formed at higher drift voltages and the same drift length and shorter transmission time and time resolution at the same integration length are calculated. The relation between the modelled electron multiplicity and thus the avalanche size on the signal time is further discussed in section 7.2.4. The points at large integration length are only considering points with long avalanches and therefore large signals. The mean transmission time reduces at larger signals, which is in agreement with the observed slewing at larger signal sizes in measurements (see section 6.4.3). Also, the standard deviation of the transmission time improves with longer avalanche length and thus shorter photoelectron drift. The effect of the photoelectron drift length on the time resolution is discussed in the following section.

7.2.3 Avalanche Length

The mean transmission time of the avalanche on the mesh as a function of the avalanche length is calculated by averaging the avalanche transition time at a given avalanche length and number of electrons reaching the mesh in equation 7.9 over all possible number of avalanche electrons on the mesh. The number of electrons on the mesh is expressed by the conditional PDF of the number of electrons on the mesh N_L at a given avalanche length L, which is approximated by the Gamma distribution ($P(N, q, \Theta)$). The mean arrival time of the avalanche for an avalanche length

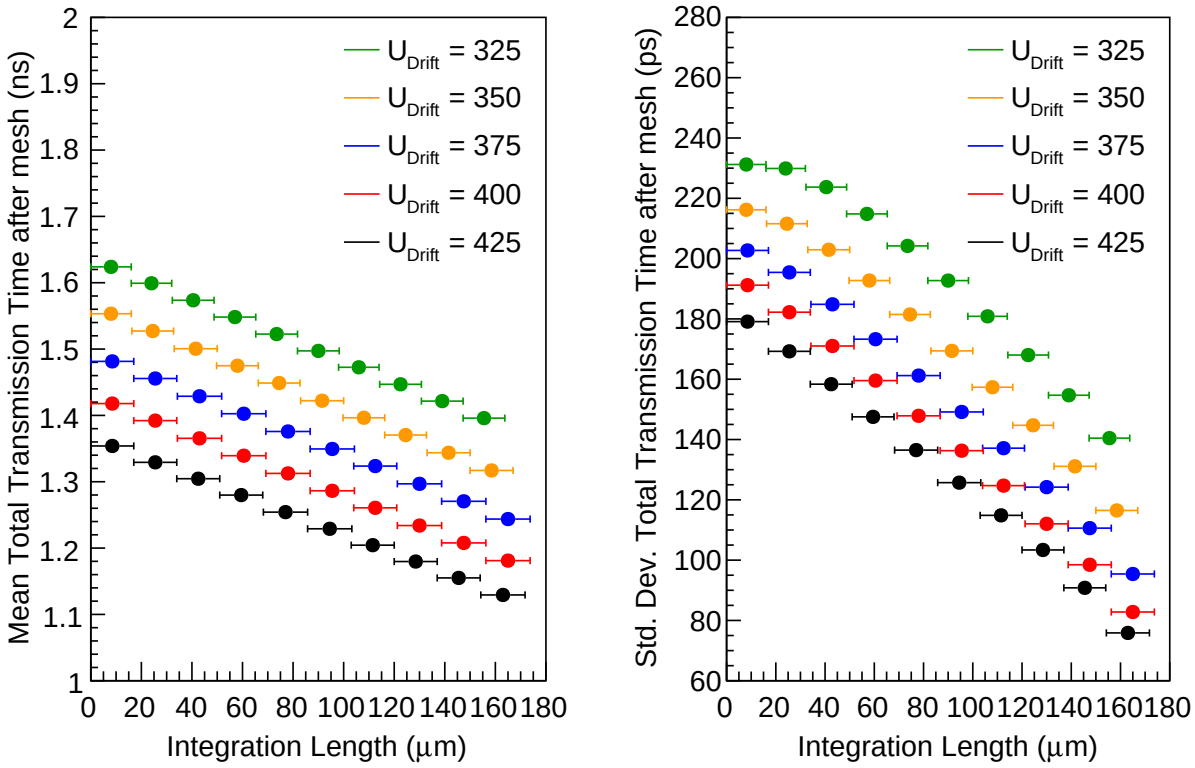

Figure 7.4: Total time after the mesh modelled with different integration length for different drift fields.

L is hereafter calculated as

$$\langle T(L)\rangle = \int_0^L T(L, N_L) \cdot P(N, q = 2\mathrm{e}^{a_{\mathrm{eff}}L}, \Theta)\mathrm{d}N_L \ . \tag{7.19}$$

Replacing $T(L, N_L)$ by equation 7.9 and the Gamma function, the mean avalanche time is written as

$$\langle T(L)\rangle = L\left(\frac{1}{V_{\mathrm{ea}}} - \rho \cdot a_{\mathrm{eff}}\right) + (-\rho\ln(2) + C + \rho\ln(\Theta + 1) - \rho\phi(\Theta + 1)) \ , \tag{7.20}$$

where $\phi(x)$ is the Digamma function. The mean transmission time is dominated for long drift lengths by the linear relation

$$\langle T(L)\rangle \approx L\left(\frac{1}{V_{\mathrm{ea}}} - \rho \cdot a_{\mathrm{eff}}\right) \ , \tag{7.21}$$

where the avalanche drift velocity is the proportionality factor. The model predicts a faster drift velocity of the whole avalanche compared to the avalanche electrons, as ρ and a_{eff} are by definition positive-valued.

The dependences of the mean arrival time and the time spread with the avalanche length are shown in the left plot of figure 7.5 for a drift voltage of 350 V and a fixed drift gap of 182 µm. The results for the other drift fields are given in the appendix A.4. The modelling of the avalanche transmission time (black line) is in a good agreement with the simulation (blue points) for long avalanche lengths. The transmission time of the avalanche rises, and the transmission time of the photoelectron (red points) decreases for longer drift length and the sum of both, the total transmission time (black points) decreases. It also shows that the avalanche drifts faster than the initial photoelectron.

Furthermore, the model shows that the average velocity of each electron in the avalanche is higher than the single electron drift velocity but smaller than the avalanche velocity as a whole. Electrons in the avalanche are losing drift velocity by the recoil from each interaction, while the newly ionised electrons are directly accelerated along the electric field. Moreover, the reduced drift velocity through the Penning effect is not affecting the propagation velocity of the avalanche as a whole in the same way as it affects single electrons.

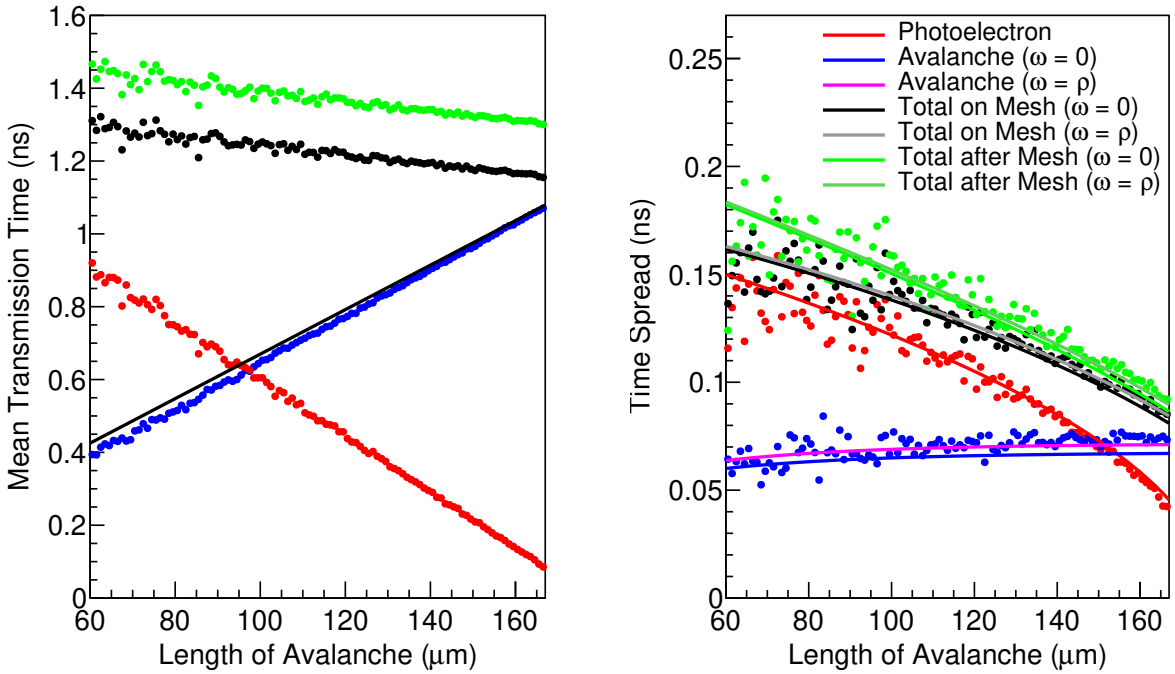

Figure 7.5: Modelled signal time vs avalanche length for 350 V drift field compared with points generated by Garfield++. The modelled distributions for other drift fields are presented in section A.5

The variance of the avalanche transmission time is calculated with the help of the mean avalanche electron velocity in equations 7.7 and the time variance of the avalanche electrons fitted from the GARFIELD++ simulation in 7.16 including the jitter of all newly created electrons in the avalanche propagation distance Δx and the time correlation between the created electrons and their parent electron moving in the same avalanche. It is assumed that $n(x)$ is following the Gamma

distribution as for the mean transit time per avalanche length in equation 7.20 and the differential term of the avalanche transmission time variance is calculated as

$$\frac{\mathrm{d}V[T(x)]}{\mathrm{d}x} = \frac{(\Theta+1)}{2\Theta}\mathrm{e}^{-a_{\mathrm{eff}}x}(\sigma_0^2 + \omega^2 a_{\mathrm{eff}}) \,, \tag{7.22}$$

where ω^2 is the variance of the time gain per newly created avalanche electron. The mean time gain of the ionisation process (ρ) is extracted from the GARFIELD++ simulation and given as an input parameter to the model. The variance of this time gain (ω^2) can not be fitted with a mathematical function from the simulation results. In the following, two assumptions are made. The first one is to assume that the time gain is a constant value and $\omega = 0$. The second assumption is that the distribution of the time gain is a broad function with an RMS equal to 100 % of its mean and therefore $\omega = \rho$. The true value of ω lies in between both assumptions.

The variance of the avalanche transmission time is calculated from the differential form by integrating over the whole avalanche length L as

$$V[T(L)] = \frac{(\Theta+1)}{2\Theta}\frac{1-\mathrm{e}^{-a_{\mathrm{eff}}L}}{a_{\mathrm{eff}}}(\sigma_0^2 + \omega^2 a_{\mathrm{eff}}) \,. \tag{7.23}$$

The variance of the single photoelectron drift time is given by the fit of the GARFIELD++ results in equation 7.15 and the total variance is calculated by the sum of both variances as

$$V[T_{\mathrm{tot}}(L)] = V[T_{\mathrm{p}}(L)] + V[T(L)] \,. \tag{7.24}$$

The modelled time spread in the right plot of figure 7.5 shows a good agreement with the GARFIELD++ simulation when considering the standard deviation of the time gain (ω) equals to the mean time advantage factor (ρ) (blue points and magenta line). The longitudinal diffusion is found to be nearly constant for the avalanche electrons at high avalanche length (blue points in the right plot in figure 7.5), while the time spread of the single electron transmission time (red points) reduces with longer avalanches. The smaller time spread of the photoelectron at longer avalanche length leads to the main improvement of the total time resolution of the signal.

7.2.4 Electron Multiplication

An alternative description of the transmission time and the time resolution is done by evaluating the relation to the number of electrons arriving on the mesh and thus the pre-amplification gain, instead of the pre-amplification avalanche length. GARFIELD++ simulations show that the mesh has a nearly constant electron transparency of ∼25 % in the given drift field range and at a constant amplification field the anode signal is mainly determined by the pre-amplification gain. Taking this into account, the following model of the time spread as a function of the electron multiplicity describes the relation of the PICOSEC-Micromegas time resolution to the measured signal size. The adaptation of the model is done by the conditional PDF for the case that an avalanche reaching the mesh with N electrons have an avalanche length in the region of $[L, L + dL]$

as

$$G(L|N) = \frac{p(N|L)R(L)}{p(N)} \,, \tag{7.25}$$

where $p(N|L)$ is the conditional PDF that the avalanche with N electrons reaches the mesh after the length L, $R(L)$ is the probability to observe an avalanche with length L given in equation 7.18 and $p(N)$ is the normalisation term

$$p(N) = \int_{x_1}^{x_2} p(N|L)R(L)\mathrm{d}L \,. \tag{7.26}$$

The conditional PDF ($p(N|L)$) is approximately described by the Gamma distribution ($P(N, q, \Theta)$) giving the conditional PDF for N electrons at length L as

$$G(L|N) = \frac{P(N, q = 2\mathrm{e}^{a_{\mathrm{eff}}L}, \Theta)R(L)}{\int_{x_1}^{x_2} P(N, q = 2\mathrm{e}^{a_{\mathrm{eff}}L}, \Theta)R(L)\mathrm{d}L} \,. \tag{7.27}$$

The average transmission time for a pre-amplification avalanche of N electrons on the mesh is calculated with the conditional PDF and the avalanche transition time for a given avalanche length and number of electrons on the mesh in equation 7.9 as

$$\langle T(N)\rangle = \int_{x_1}^{x_2} T(N, L)G(L|N)\mathrm{d}L = \frac{\langle L(N)\rangle}{V_{\mathrm{ea}}} - \rho\ln(N) + C \,, \tag{7.28}$$

where

$$\langle L(N)\rangle = \int_{x_1}^{x_2} L(N, L)G(L|N)\mathrm{d}L \tag{7.29}$$

is the average avalanche lenght for all result with N electrons on the mesh. The mean transition time of the single photoelectron drift before multiplication is analoguely calculated with the photoelectron drift time in equation 7.11 to

$$\langle T_{\mathrm{p}}(N)\rangle = \frac{D - \langle L(N)\rangle}{V_{\mathrm{p}}} + d_{\mathrm{off}} \,. \tag{7.30}$$

The average total transmission time is the sum of both times as

$$\langle T_{\mathrm{tot}}(N)\rangle = \langle T(N)\rangle + \langle T_{\mathrm{p}}(N)\rangle = \langle L(N)\rangle \left(\frac{1}{V_{\mathrm{ea}}} - \frac{1}{V_{\mathrm{p}}}\right) - \rho\ln(N) + \frac{D}{V_{\mathrm{p}}} + C + d_{\mathrm{off}} \,. \tag{7.31}$$

The constant time delay of the passage through the mesh is additionally added for the calculation of the average time after the mesh.

The mean variance of the avalanche transmission time depending on the electron multiplicity is calculated with the difference between the transmission time variance on plane x and $x - \Delta x$. The transmission time variance on each plane is calculated with the transmission times given in equations 7.5 and 7.6, averaged over $n(x)$ under the condition that $n(x) = N_L$ for $x = L$ given by

the PDF $P(n(x)|n(L) = N_L)$ as

$$\langle V(x)\rangle_{n(L)=N_L} = \int_0^\infty V[T(x, n(x))] \cdot P(n(x)|n(L) = N_L)\,\mathrm{d}n(x)\,, \tag{7.32}$$

and

$$\langle V(x-\Delta x)\rangle_{n(L)=N_L} = \int_0^\infty V[T(x-\Delta x, n(x-\Delta x))] \cdot P(n(x-\Delta x)|n(L) = N_L)\,\mathrm{d}n(x-\Delta x)\,. \tag{7.33}$$

The difference of both variances is calculated for the whole avalanche length with $x = L$ and $x - \Delta x = 0$ as

$$\langle V(L)\rangle_{n(L)=N_L} - \langle V(0)\rangle_{n(L)=N_L} = \sigma_0^2 \cdot \Delta x \sum_{i-1}^{L/\Delta x} \left\langle \frac{1}{n(L - i\cdot\Delta x} \right\rangle_{n(L)=N_L} - \omega^2 \left(\left\langle \frac{1}{n(L} \right\rangle_{n(L)=N_L} - \left\langle \frac{1}{n(0} \right\rangle_{n(L)=N_L} \right)\,. \tag{7.34}$$

At the limit of Δx going to zero, some terms are simplified as

$$\langle V(0)\rangle_{n(L)=N_L} = 0;\ \left\langle \frac{1}{n(0)} \right\rangle_{n(L)=N_L} = \frac{1}{2};\ \left\langle \frac{1}{n(L)} \right\rangle_{n(L)=N_L} = \frac{1}{N_L}\,. \tag{7.35}$$

By inserting these terms, the mean variance of the avalanche transmission time for an avalanche length L and an electron multiplicity of N_L is

$$\langle V(L)\rangle_{n(L)=N_L} = \sigma_0^2 \cdot \int_0^L \left\langle \frac{1}{n(x)} \right\rangle_{n(L)=N_L} \mathrm{d}x - \omega^2 \left(\frac{1}{N_L} - \frac{1}{2} \right)\,. \tag{7.36}$$

To express this relation only on N_L, the mean variance for an avalanche length L is integrated over all possible avalanche lengths weighted by the likelihood function $G(L|N)$ that an avalanche with length L and multiplicity N is created. The mean variance of the avalanche transmission time for an electron multiplicity N is hereafter calculated as

$$V[T(N)] = \int_{x_1}^{x_2} \langle V(L)\rangle_{n(L)=N_L} \cdot G(L|N)\mathrm{d}L + \int_{x_1}^{x_2} T(N,L)^2 \cdot G(L|N)\mathrm{d}L - \left[\int_{x_1}^{x_2} T(N,L) \cdot G(L|N) \right]^2 \mathrm{d}L\,. \tag{7.37}$$

The mean variance for the single photoelectron drift time is similarly calculated with the variance of the photoelectron drift time at a given avalanche length in equation 7.15 and the mean

photoelectron drift time for N electrons reaching the mesh in equation 7.30 as

$$V[T_\mathrm{p}(N)] = \int_{x_1}^{x_2} V[T_\mathrm{p}(L)]G(L|N)\,\mathrm{d}L + \int_{x_1}^{x_2} T_\mathrm{p}(L)^2 \cdot G(L|N)\,\mathrm{d}L - \left[\int_{x_1}^{x_2} T_\mathrm{p}(L) \cdot G(L|N)\right]^2 \mathrm{d}L\,. \quad (7.38)$$

The total variance of the electron time on the mesh is calculated by the addition of both variances as

$$V[T_\mathrm{tot}(N)] = \int_{x_1}^{x_2} \left[V[T_\mathrm{p}(L)] + \langle V(L)\rangle_{n(L)=N_L}\right] G(L|N)\,\mathrm{d}L + \int_{x_1}^{x_2} [T_\mathrm{p}(L) + T(N,L)]^2 \cdot G(L|N)\,\mathrm{d}L - \left[\int_{x_1}^{x_2} [T_\mathrm{p}(L) + T(N,L)] \cdot G(L|N)\right]^2 \mathrm{d}L\,, \quad (7.39)$$

and the total variance after the mesh is calculated with the added transit time through the mesh, given in equation 7.10.

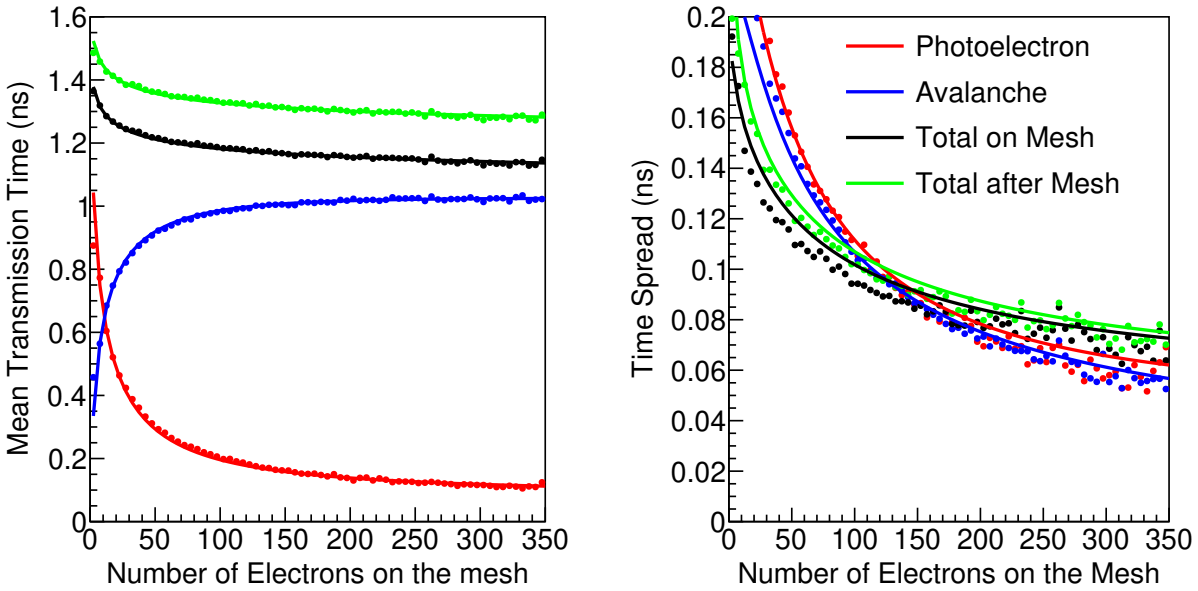

Figure 7.6: Dependence of the mean transmission time and time spread with the number of electrons on the mesh for 350 V drift field compared with points generated by Garfield++. The modelled distributions for other drift fields are presented in section A.6

The dependences of the mean transmission time and the time spread on the pre-amplification gain are given in figure 7.6 for a drift voltage of 350 V. The results for the other drift fields are given in the appendix in section A.6. The solid lines are the calculated model, and the points are the corresponding results from the GARFIELD++ simulation. In general, the results are in a good agreement with the simulation points, and the modelled time spread is slightly higher compared

to the simulated one due to the approximation with the PDF. The mean total transmission time and the time spread reduces at a higher multiplication. This result is expected, as the avalanche electrons drift faster than the single photoelectron and the time resolution improves at larger pre-amplification gains. Moreover, the results of the model are in agreement with the measurements of the PICOSEC-Micromegas, where larger signal sizes provide better time resolution.

The time resolution for the different number of electrons on the mesh is compared for the different drift voltages in figure 7.7. The smaller drift fields provide a better time resolution than the larger ones at the same electron multiplication on the mesh. Anyhow, the time resolution integrated over all number of electrons on the mesh is better for larger drift field. The probability of having more electrons in the avalanche is higher for larger drift fields and the best time resolution at low drift fields is reached in the simulation at rare cases when the avalanche length is nearly equal to the whole drift region.

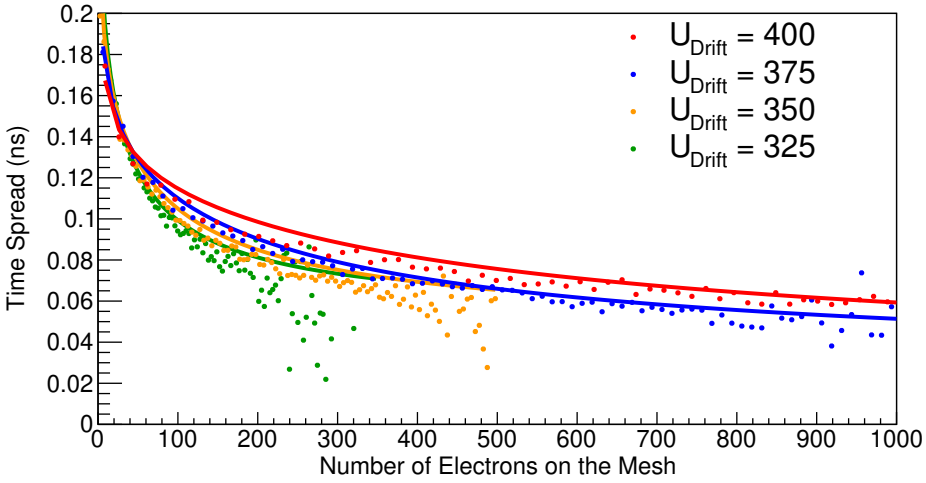

Figure 7.7: Comparison of the time spread with the number of electrons on the mesh for all modelled and simulated drift field settings.

7.2.5 Several Photoelectrons

The previous discussed mathematical model is extended by a toy Monte-Carlo simulation to reproduce the detector time resolution for several photoelectrons. The principle of a toy Monte-Carlo simulation is the creation of statistical distributions by performing the same mathematical operation several times with randomly generated input variables. A block diagram of the toy Monte-Carlo procedure used to simulate the time resolution for the PICOSEC-Micromegas for N mean photoelectrons is given in figure 7.8. The simulation calculates for 10.000 individual events, with (n) parallel photoelectrons each, the mean SAT of the electrons after the mesh. The standard deviation of all SAT distributions superposed describes the time resolution of the signal. This simulation is performed for fixed numbers of mean photoelectrons (N), and for each generated event a precise number of photoelectrons (n) is selected by a random number weighted with

a Poissonian distribution and an expected rate of occurrence of N ($P_{\lambda=N}$). For each of the photoelectrons, a random SAT (t_n) and time jitter (Δt_n) is selected. The SAT is selected by a random number weighted with the inverse Gaussian distribution of the electron transmission time after the mesh, as described in section 7.2.1. The additional time jitter (Δt_n) takes into account that photoelectrons are not instantaneously emitted from the photocathode due to the propagation of the Cherenkov light. The emission time of the photoelectrons is estimated to be Gaussian distributed with a standard deviation of 5 ps, which is approximated from the geometrical propagation time differences of the Cherenkov photons through the crystal. After calculating n SATs and time jitters for one event, the mean SAT of this event is calculated as

$$t = \frac{\sum_i^n t_n - \Delta t_n}{n} \,. \tag{7.40}$$

This procedure is repeated for ∼10.000 events, for which the SAT distribution has sufficient statistics. The standard deviation of this distribution is the simulated time resolution of the PICOSEC-Micromegas at a given mean number of photoelectrons (N) and for the drift field settings according to the modelled distribution of the transmission time after the mesh.

The toy Monte-Carlo simulation is performed for all field settings included in the mathematical model and for 1 to 40 photoelectrons. The simulated time resolution for the different mean number of photoelectrons and the modelled drift fields is presented in figure 7.9. The time resolution improves with the number of photoelectrons. For a high number of photoelectrons, the simulated time resolution shows a good agreement with the expected relation of the time resolution with the number of photoelectrons as

$$\sigma \approx \frac{\sigma_{TTS}}{\sqrt{N_{\text{p.e.}}}} \,. \tag{7.41}$$

The electron transit time spread (σ_{TTS}) is the time resolution calculated by the model in section 7.2.1 and not the single photoelectron time resolution calculated by the Monte-Carlo simulation. The Poisson distributed photoelectrons with $\lambda = 1$ have a probability of ∼42 % that more than one photoelectron is produced in one signal generating event and thus the simulated single photoelectron resolution is better than the time resolution of exactly one photoelectron, which explains the disagreement of the simulation with the curve for low number of photoelectrons. A PICOSEC-Micromegas measurement with the same field settings and many photoelectrons is not available, as the detector gain would exceed the spark limit. A resistive PICOSEC-Micromegas and operation with different gas mixtures or lower field settings in needed to operate the detector at such numbers of photoelectrons.

7.3 Summary

The calculation of the mathematical model provides a good agreement with the simulation results and the measurement data from the prototypes, while it needs fewer resources than a full GARFIELD++ simulation of the electron propagation in the pre-amplification stage

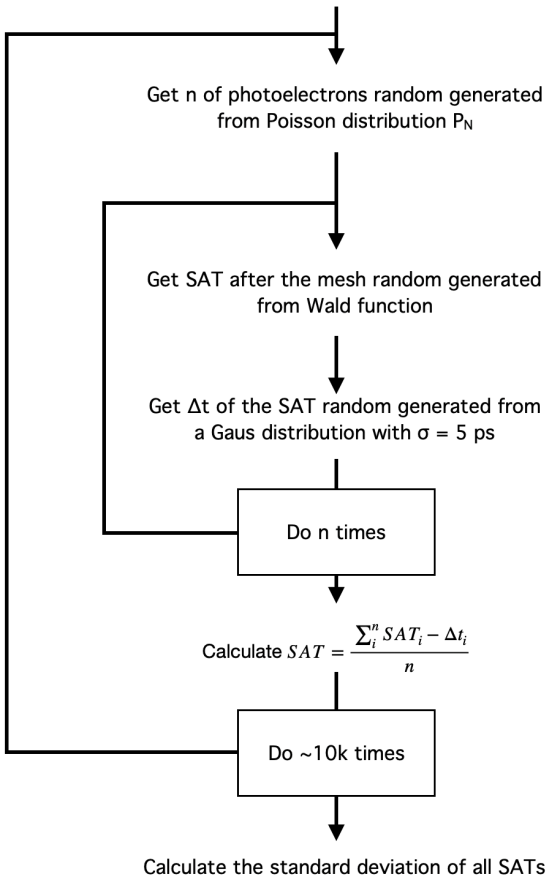

Figure 7.8: Block diagram of the toy Monte-Carlo method to simulate the time resolution for Poissonian distributed N number of photoelectrons.

of a PICOSEC-Micromegas. Moreover, the model helps to understand the physical processes defining the time resolution in the signal propagation of the PICOSEC-Micromegas. The time resolution of the PICOSEC-Micromegas is defined by the length of the single photoelectron drift before starting the pre-amplification avalanche. The avalanche has a faster mean drift velocity than the single photoelectron and the variance of the transmission time stays constant along the avalanche length, while the variance of the photoelectron transmission time improves for short drift lengths. The impact of the drift region length on the time resolution is further studied with a PICOSEC-Micromegas prototype in the laser beam, and the results are presented in section 8.2.

The second observation is the correlation between the avalanche size and the time resolution. A stronger avalanche multiplication creates more electrons on the mesh and through the mesh and the amplification after the mesh gives the transition a constant contribution to the transmission time. In the model, the signal size is defined by the pre-amplification avalanche multiplication in the drift region, as the further amplification field is kept constant. In future studies, the model needs to be extended to describe the signal for different amplification voltages. The model shows that a higher number of electrons on the mesh and therefore, a higher pre-amplification improves the

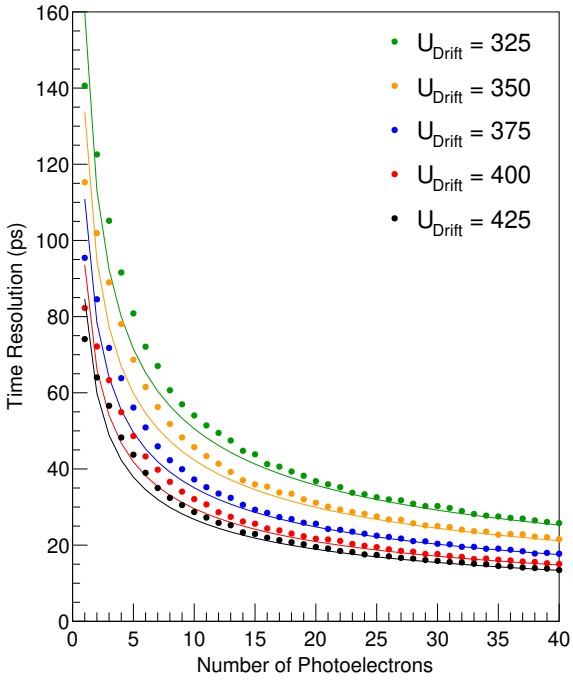

Figure 7.9: Monte-Carlo modelling of the time resolution after the mesh for several photoelectrons and all modelled drift fields. The lines are the calculated single photoelectron time resolution scaled with $\sqrt{N_{\text{p.e.}}}$, and the points are the Monte-Carlo modelled time resolution for each mean number of photoelectrons.

time resolution. The same observation is made at measurements with the PICOSEC-Micromegas, where higher drift fields with stronger pre-amplification at constant amplification provides better time resolution.

The toy Monte-Carlo shows an extension of the model for multiple photoelectrons. The operation of the PICOSEC-Micromegas in settings providing several photoelectrons improves the time resolution. In some applications, like detecting MIPs, many photoelectrons will be created in the detector, and the toy Monte-Carlo is an excellent way to generate results similar to real operation settings of the detector. The missing parts of the model to describe the whole detector are the description of the amplification avalanche after the mesh and the contribution of the read-out and electronics to the time jitter. The integration of the amplification in the model is needed to perform the calculation for different amplification field settings than the given 450 V. The best measured time resolution of the PICOSEC-Micromegas in stable condition with 150 GeV muons is reached at an amplification voltage setting of 275 V (see section 10). The mathematical model needs to be adjusted, and new input parameters need to be calculated with dedicated GARFIELD++ simulations to describe the detector in these settings.

8 Characterisation in a Laser Beam

Contents

One method to study the performance of the PICOSEC-Micromegas prototypes is the use of a UV laser light that creates single photoelectrons in the photocathode, and any Cherenkov light propagation effect inside the window can be neglected. These measurements allow the independent study of the impact of different detector parameters like the gas mixture and the drift field on the PICOSEC-Micromegas timing performance. This chapter will first describe the laser set-up used for characterisation measurements. Afterwards, the prototypes and its configuration are presented. The results of drift field scans and gas mixture studies complete the chapter and are compared to modelisation results.

8.1 Laser Setup

PICOSEC-Micromegas prototypes have been characterised in several measurement campaigns at the LYDIL laser laboratory of CEA-IRAMIS. A sketch of the laser set-up is shown in figure 8.1. A mode-locked Ti:Sapphire laser source (MIRA 900 [100]), pumped

by a continuous wavelength solid-state laser at 532 nm (VERDI V10 [101]), has been used to generate 120 fs pulses. Construction-wise, a Ti:Sapphire laser has typically different oscillation modes in a bandwidth of 300 nm around its peak wavelength of 800 nm. Controlled interference of the oscillation modes produces a short light pulse in the order of femtoseconds. This technique, known as a mode-lock laser, controls the interference by the phase between the oscillation modes. The laser pulses from the source have a wavelength maximum at 800 nm with a peak power of 2.2 W and a repetition rate of 76 MHz.

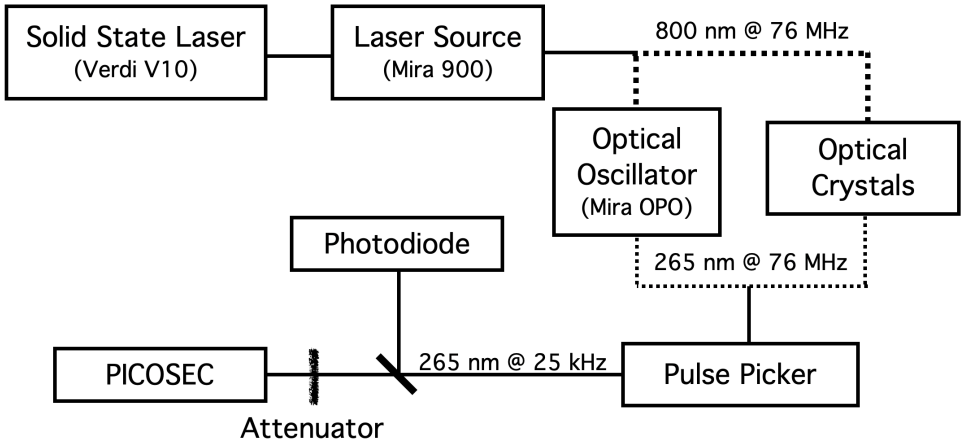

Figure 8.1: Sketch of the laser set-up.

The wavelength needs to be adjusted subsequently to 265 nm. High intense light can be transformed to a shorter wavelength by nonlinear optical processes. The most common process is called a second-harmonic generation (SHG), and materials with specific optical properties, like barium-borate (BBO), are needed. The laser transfers energy to a crystal, and the exited crystal emitts nonlinearly polarised light. This method is known as laser pumping [102]. The polarised light from the crystal oscillates at a doubled frequency of the pumped light.

Two methods are available to adjust the wavelength in the used laser set-up, depending on the laser stability and needed wavelength. The first one is an adjustable optical parametric oscillator (MIRA-OPO [103]) pumped by the original Ti:Sapphire laser. It consists of a ring cavity for visible light and an SHG inside of the cavity. This oscillator provides a tuneable <200 fs pulse with a peak power of 0.6 W at 580 nm and a range between 530 nm and 660 nm. The wavelength is further reduced with a 5 mm frequency-doubling crystal to 265 nm. The second method is directly mixing the 800 nm pulse from the Ti:Sapphire laser with an array of nonlinear optical crystals to the demanded wavelength. A more stable pulse without the possibility of wavelength fine-tuning is created.

The repetition rate of 76 MHz has to be lowered before mixing the wavelength with the crystals, because it is higher than the ion collection time in PICOSEC-Micromegas photocathode. This repetition rate level could produce a charge accumulation, causing damages in the detector. An adjustable pulse picker (Model 9200 [104]) tunes the repetition rate between 4.76 MHz and

25 kHz. It uses an acousto-optic modulator, consisting of an optical crystal and a piezoelectric driven vibrating traducer. The transducer is coupled to the crystal and can generate acoustic waves. The acoustic wave compresses and expands locally the crystal lattice, which affects its refractive index. The laser pulse gets diffracted in different directions depending on the local refractive index of the crystal lattice. Only the chosen amount of pulse gets diffracted towards the opening of the pulse picker. An acousto-optic modulator is necessary for a laser with a higher repetition rate, as it reacts faster than a mechanical or electrical switch. The laser pulses exiting the pulse picker lose 40 % intensity and have an energy per pulse between 40 pJ/pulse and 18 pJ/pulse at 265 nm.

The light beam is split at the laser output, one part is sent to a photodiode (DET10 A/M [14]) and the second one to the PICOSEC-Micromegas. The signal from this diode triggers the data acquisition system, and its signal is used as time reference. An estimation of the photodiode time resolution is given in section 8.1.2.

One crucial point in these measurements is the control of light intensity on the photocathode, which is then converted into a mean number of photoelectrons. For this purpose, a combination of mechanical meshes of different transparency situated before the detector work like light intensity attenuators. The calibration of these attenuators is described in section 8.1.3.

Aluminium of 10 nm is chosen as photocathode material because its work function (4.25 ± 0.05 eV [105]) is lower than the laser photon energy ($E_{(\lambda)} = 4.68$ eV), which allows a sufficient quantum efficiency for the given setup. Moreover, a metallic photocathode is easier to handle and store than CsI, and it is more robust against the high laser intensities needed to produce many photoelectrons for the measurements.

8.1.1 Background Correction

During some measurements, a periodic noise has been observed. Such noise is created by the different high frequency devices connected to the same power network. The background has been measured to include it in the analysis, in order to improve the signal to noise ratio and by this the signal quality. A good signal to noise ratio is especially difficult to reach with single photoelectron measurements as the amplitude signal is very low. Background measurements have been performed after each modification in the system for this correction, where the detector has been powered on, and the full acquisition system was running while the light of the laser beam was blocked. Several thousand signals of the noise have been recorded for each background measurement and the mean signal noise has been calculated for them, after having removed the baseline offset. This periodic noise is then substracted from all recorded PICOSEC-Micromegas signals. Figure 8.2a shows the mean noise of 2k signals from one of these background runs. If there were no periodic noise, this figure would show a flat line. Instead, a periodic wave can be spotted.

The difference of the noise RMS before and after the background correction is calculated for each waveform. The improvement of the noise with the correction is statistically distributed and figure 8.2b shows the difference in RMS for a set of 10,000 waveforms. The mean of the distribution is located at $+14.2 \pm 0.1$ µV, which means that the noise RMS improves in the mean

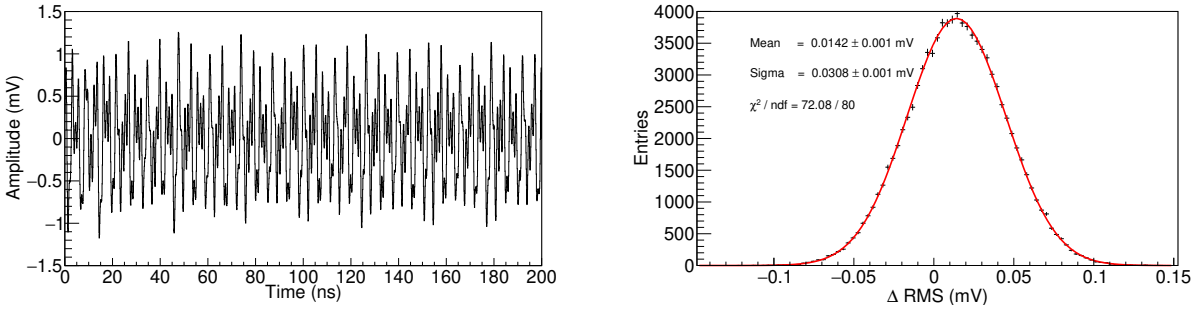

(a) The mean background noise of 2k signals shows a periodic behavior

(b) The noise RMS shows a mean improvement of $14.2 \pm 0.1\,\mu V$ after the background correction.

Figure 8.2: The periodic background noise in a) is substracted from the signal and the RMS difference of the signal noise before and after correction is given in b).

of $14.2 \pm 0.1\,\mu V$ after the correction. This is only a small improvement of the noise RMS as especially the standard deviation of this distribution is larger than the mean.

8.1.2 Photodiode Performance

The exact time resolution of the t_0-reference photodiode (Thorlabs DET10A/M) has not been determined for the presented laser studies of the PICOSEC-Micromegas. Only an upper limit of the photodiode performance has been calculated from the best combined time resolution of both detectors. Indeed, the operation settings of the photodiode have not been changed during the whole laser studies; hence it should provide the same performance. Meanwhile, the PICOSEC-Micromegas has been operated under very different conditions with different intrinsic time resolutions. For this reason, the best achieved combined time resolution of DUT and t_0-reference is a reasonable limit for the time resolution of the photodiode time resolution.

The following PICOSEC-Micromegas configuration achieved the best measured time resolution in the laser set-up: A bulk Micromegas with a gas mixture consisting of neon (89 %), ethane (2 %) and CF_4 (9 %) and an electric field in the drift of 32 kV/cm and in the amplification of 17 kV/cm. These settings are selected to secure a stable operation within the specifications of the amplifier and acquisition system at the maximum possible amount of light. The highest light intensity from the laser without an attenuator is used for this measurement. A high amount of photoelectrons is crucial for improving the time resolution of photodetectors like the PICOSEC-Micromegas. The effects of different gas mixtures and electric fields on the time resolution and stability of the PICOSEC-Micromegas are discussed in part II.

Figure 8.3 shows a screenshot from the DAQ oscilloscope with 500 overlapped events. The photodiode waveforms are displayed in blue, and the PICOSEC-Micromegas waveforms in red. The PICOSEC-Micromegas waveforms in the described setting show a shape and stable rising edge and a long and flat ion tail. The amplitude of the ion tail is in the order of factor 10 smaller than the amplitude of the electron peak.

The ΔSAT of the PICOSEC-Micromegas and the photodiode follows a Gaussian distribution shown in figure 8.4. The sigma of the Gaussian curve represents the combined time resolution of both, the PICOSEC-Micromegas detectors and the photodiode, as well as the additional jitter added by the DAQ system and CFD algorithm. It is calculated to 6.79 ± 0.04 ps for the presented settings.

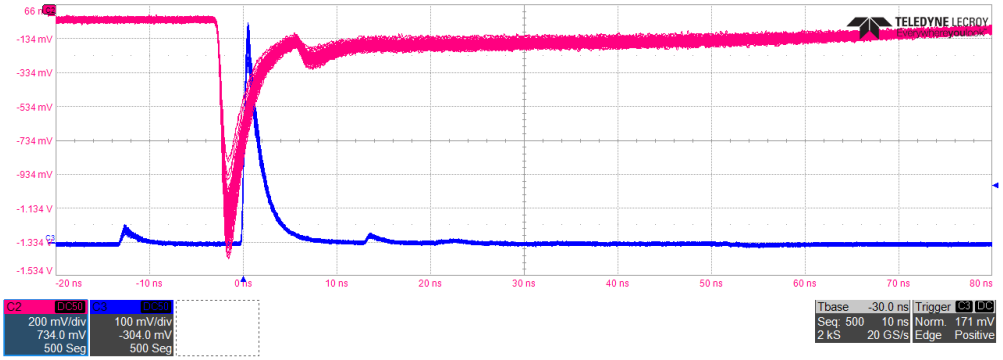

Figure 8.3: Screenshot of the DAQ with 500 overlapping waveforms of the photodiode in blue and 500 waveforms of the PICOSEC-Micromegas with the configuration described in the text.

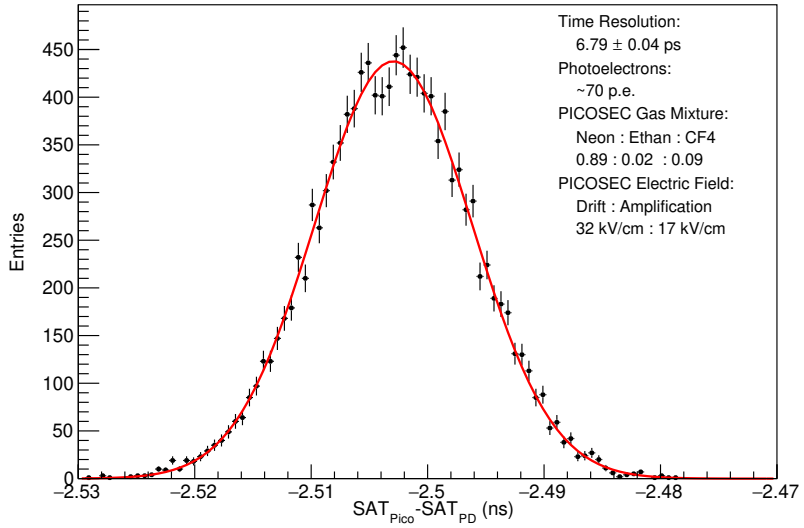

Figure 8.4: Signal Arrival Time difference distribution between the PICOSEC-Micromegas detector and the photodiode with the smallest width (6.79 ± 0.04 ps) in laser measurements.

8.1.3 Attenuator Calibration

The laser creates an intense but small light spot on the photocathode that generates many photoelectrons. If it is not attenuated and the detector is operated at high gain and high laser

repetition rate, the detector could become unstable and a spark may happen, damaging the photocathode or the detector mesh itself.

Furthermore, an attenuation of the light is essential to qualify the exact amount of photoelectrons created in order to compare with muon beam test conditions, where several photoelectrons are created depending on the photocathode material. This is especially important for single photoelectron measurements, in order to evaluate the impact of detector parameters (like the drift and amplification gaps or the gas pressure) on the timing performance.

The attenuation of the laser beam is done mechanically, using thin mesh sheets with different light transparency. Combining several meshes tunes the amount of light. The first step in the calibration process is the determination of single photoelectron measurement conditions in the laser set-up. For this purpose, attenuators are added until the mean amplitude does not further reduce after the addition of one attenuator and only the signal probability (efficiency) gets smaller. When this state is reached, the system is operating in single photoelectron conditions. Two measurements with different sets of attenuators are performed to verify this state. Figure 8.5 shows the comparison of two attenuator configurations in single photoelectron conditions, where figure 8.5b has been measured with an additional factor two attenuator. The Polya fit for both distributions gives the same mean signal charge, while figure 8.5b shows a lower detection efficiency.

The detection efficiency of the PICOSEC-Micromegas compared to the 100 % efficient t_0 reference photodiode gives a second verification of the single photoelectron state. The photoelectron extraction from the photocathode is a discrete process, as the photocathode can only emit a natural number of electrons. The probability for the extraction of a certain number of electrons can be described with a Poisson distribution as

$$P_\lambda(k) = \frac{\lambda^k}{k!}\mathrm{e}^{-\lambda}\,, \tag{8.1}$$

where $\lambda \in \mathbb{R}_{>0}$ is the mean of the Poisson distribution and $k \in \mathbb{N}$ is the number of extracted photoelectrons.

As the detector effiency (ϵ) is the integrated probability that at least one photoelectron is extracted (and detected),

$$\epsilon = \frac{N_{\text{DUT}}}{N_{\text{Trig.}}} = \sum P_\lambda(k>0) = 1 - P_\lambda(0) = 1 - \mathrm{e}^{-\lambda}\,, \tag{8.2}$$

where N_{DUT} is the number of signals from the PICOSEC-Micromegas, and $N_{\text{Trig.}}$ is the number of triggers from the photodiode.

The detector efficiency is 63 % for a mean of one photoelectron ($\lambda = 1$) emitted from the photocathode, but the probability that more than one photoelectron is emitted from the photocathode is still $\sum P_1(k>1) = 26\,\%$ for $\lambda = 1$. A detector efficiency of the order of 10 % is typically reached in single photoelectron conditions, where the probability for more than one photoelectron is $\sum P_1(k>1) < 0.5\,\%$.

After finding one set of attenuators providing the right light amount for single photoelectrons, one attenuator after the other was removed to characterise the detector performance at dif-

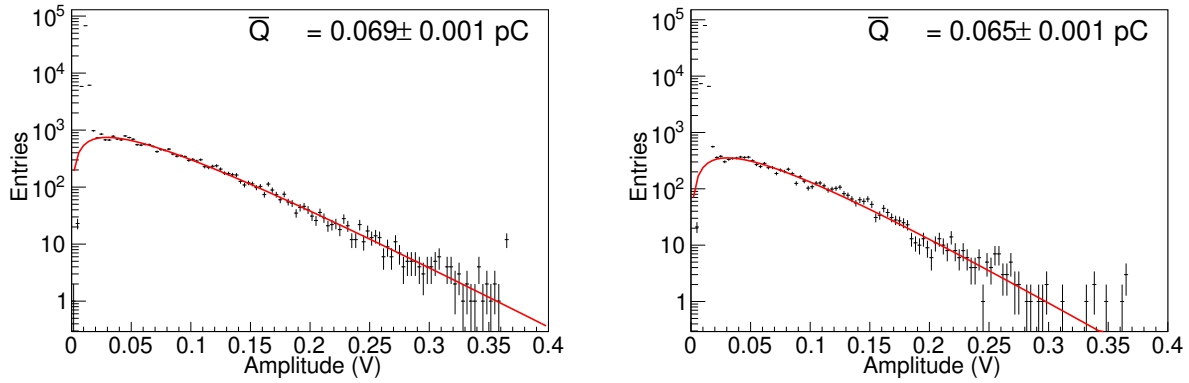

(a) Polya distribution of the signal charge at single photoelectron conditions.

(b) Polya distribution of the signal charge with an additional factor-two attenuator.

Figure 8.5: Comparison of the signal charge distribution for two different attenuator settings to verify single photoelectron conditions.

ferent number of photoelectrons. Figure 8.6 shows the charge distribution for different attenuator settings, where the detector was operated at the same field configuration. A Polya function is fitted to all distributions to estimate the number of photoelectrons for each set of attenuators from the mean signal charge, normalised to the mean charge in single photoelectron conditions.

As the actual number of extracted photoelectrons from the photocathode depends on the drift field setting (see section 13.4), the number of photoelectrons for each attenuator group is defined at the same field settings. A new calibration of the attenuator set-up is also performed after each change of photocathode, as photocathodes have different production quality and therefore efficiency. This step is essential to reach single photoelectron conditions in order to compare timing performances from different measurement campaigns.

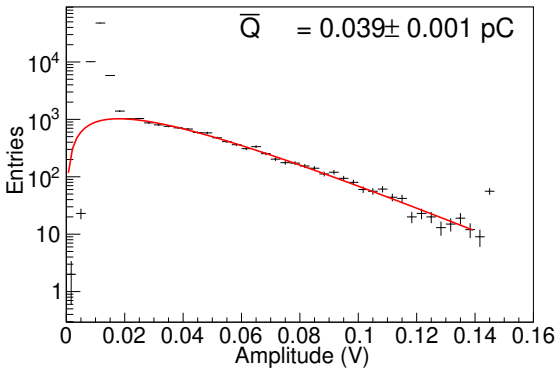

(a) Charge distribution for single photoelectron settings

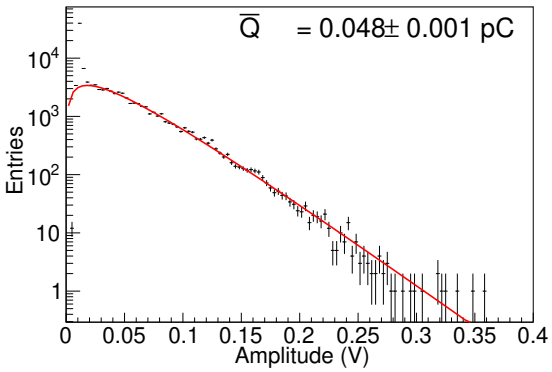

(b) Charge distribution for 1.2 photoelectron settings

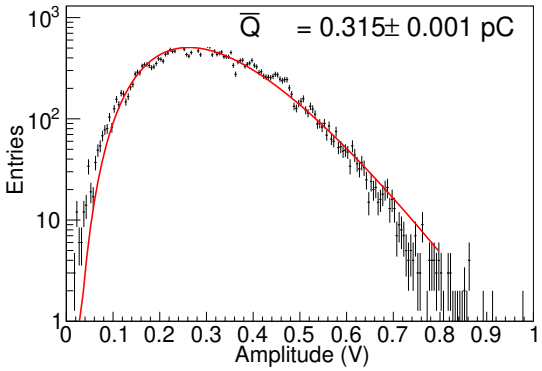

(c) Charge distribution for 8 photoelectron settings

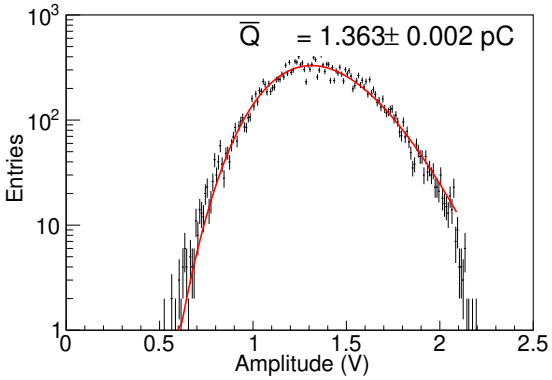

(d) Charge distribution for 35 photoelectron settings

Figure 8.6: The different laser attenuator settings are calibrated with their charge distribution in comparison to the single photoelectron charge distribution at the same detector settings.

8.2 Drift Distance

The time resolution for several electric field settings and drift gap distances is measured in the laser set-up. The presented results are published in reference [106]. For this measurements, the picolarge prototype is used (see section 5.3.2), as it is designed with easy replaceable distance rings between the mesh and the photocathode for a rapid change of the drift distance. The distance of the amplification gap is kept constant at 128 µm, like in beam tests, while the drift gap is varied between 119 µm and 244 µm. The gap is formed by 25 µm-thick Kapton rings. Three different voltage settings have been applied to the fixed amplification gap, chosen from experience of the detector behaviour at previous test measurements. These settings are: 1) 400 V, a setting with the highest possible gain in the amplification region, 2) 350 V, a balanced setting that allows a stable operation, and 3) 275 V, the lowest voltage setting that allows the application of high drift fields. All laser measurements are performed with a gas mixture consisting of neon (80 %) + ethane (10 %) + CF_4 (10 %).

For each drift gap, a scan of drift field is made for the three amplification voltages and for different attenuator settings. The waveform analysis for each measurement is performed by the method explained in chapter 6. The approximated number of photoelectrons for each attenuator setting and photocathode is estimated from the mean of the signal charge distribution for the highest measured field setting each time. The inaccuracy of this methode is described in section 6.3 and 13.4. The measured time resolution for each calculated number of photoelectrons and each drift gap can be found in section B.1. In each case, the highest drift field in stable conditions is first set and it is then reduced two or three times in steps of 1-2 kV/cm. Drift field ranges are different for each amplification and photoelectrons settings. The aluminium photocathode had to be changed several times during the measurements due to its degeneration after sparks. Not every photocathode had the same efficiency and not all photoelectron settings could be measured for the different drift gap settings.

The measured time resolution for all fixed fields and gaps with variating generated number of photoelectrons is given in the appendix in figure B.1. The measurement shows an improved time resolution with increased electric fields for all settings. The same behaviour had been seen in the modelling and all previous PICOSEC-Micromegas measurements. It can be explained with the shorter drift length before amplification, the higher gain and better signal-to-noise ratio of the detector. The number of initial photoelectrons is also affecting the time resolution. The time resolution (σ) depends on the number of photoelectrons ($N_{p.e.}$) by

$$\sigma \approx \frac{1}{\sqrt{N_{p.e.}}} \,. \tag{8.3}$$

With many photoelectrons, the time resolution improves even at lower detector gain.

Figure 8.7 shows all time resolution measurements as a function of the drift fields for different photoelectron settings. The same measurement separated for each drift distance can be found in section B.2. The highest possible electric field of up to 44 kV/cm can be applied for the shortest drift gap without reaching instability. At approximately 20 ps, the time resolution starts to saturate at high fields and the given number of photoelectrons. Operation with fewer attenuators and more

number of photoelectrons would improve the time resolution, but the detector at such high gains is not any more stable. Only with a reduction of the total electric field and higher photoelectrons a better time resolution can be achieved. A time resolution of 17.48 ± 0.25 ps is measured for 35 photoelectrons with the larger drift gap of 244 µm, an anode voltage of 275 V and a drift field of only 24.6 kV/cm.

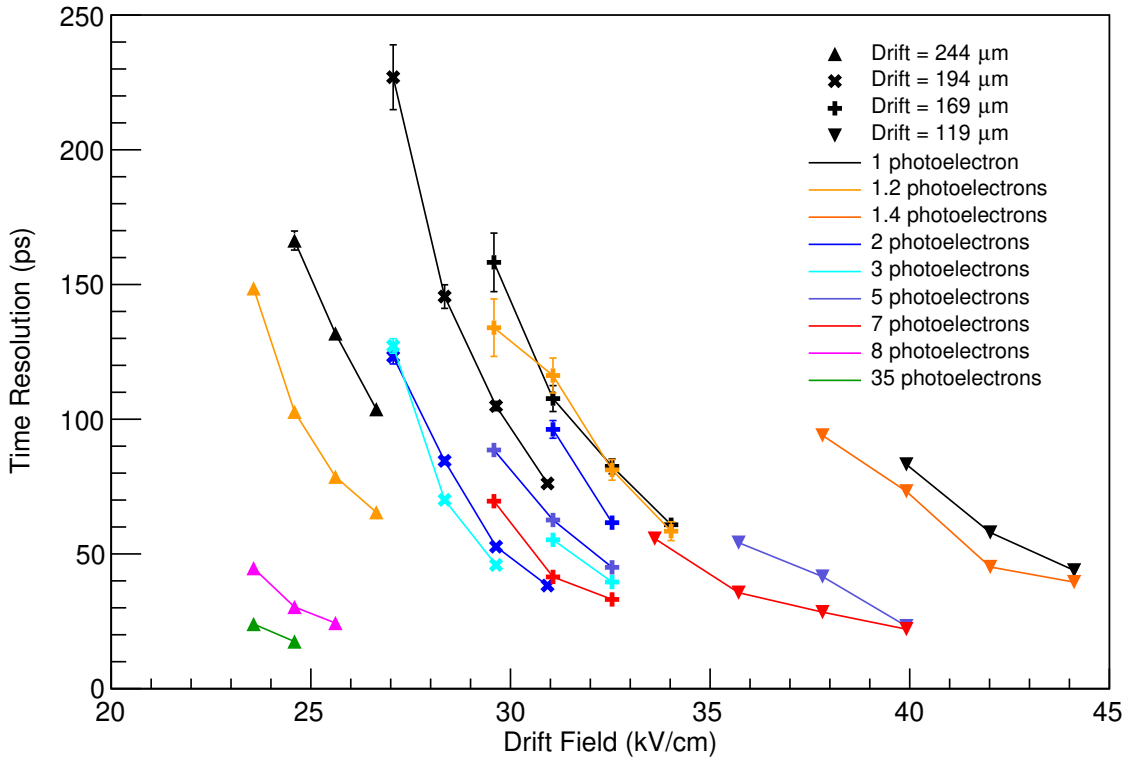

Figure 8.7: Time resolution as a function of the drift field for the approximated number of photoelectrons and drift distances. The amplification gap is 128 µm and the applied voltage is 275 V.

8.2.1 Time Resolution with Single Photoelectrons

The impact of the drift gap and of the drift field on the time resolution is studied more in detail under single photoelectron conditions to remove the timing contribution of multiple photoelectrons. The time resolution for different drift fields and drift gap distances is shown in figure 8.8. The best time resolution of 44 ± 1 ps for a single photoelectron is measured for the smallest drift gap of 119 µm and the highest stable field setting of 44 kV/cm. In these conditions, the electric field of the pre-amplification in the drift gap is higher than in the amplification gap with 21 kV/cm.

At fixed drift and amplification fields, the best time resolution is measured for the largest drift gaps. This happens because the drift distance of the single electron before initialising a pre-amplification avalanche is constant at the same drift field settings. So, a longer avalanche is formed at larger drift gaps resulting in a higher detector gain and thus in an improved time resolution. However, a higher voltage is needed to apply the same drift field at larger drift gaps.

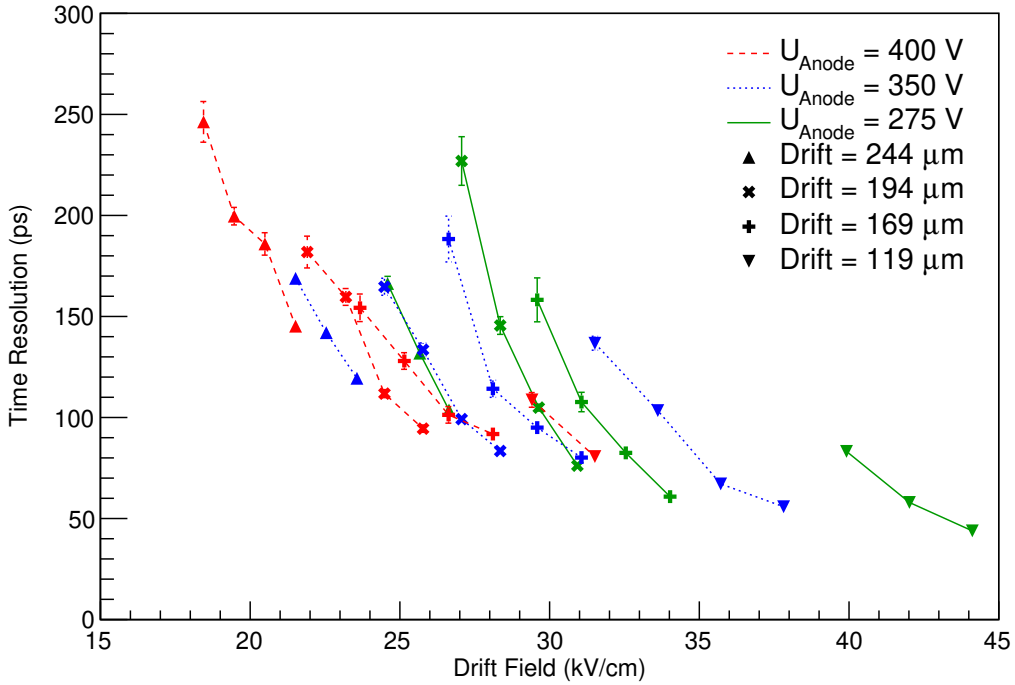

Figure 8.8: Time resolution as a function of the drift field for different drift gaps under single photoelectron condition. The amplification gap is 128 µm deep.

The best time resolution is achieved with the smallest drift gap, as higher fields are applied far from the Roether limit. The drift gap cannot be too narrow; otherwise, it would not provide enough gain before reaching the electrical breakdown [107]. In general, a detector with a higher electric field has a higher gain and provides a better time resolution. The PICOSEC-Micromegas is a two-stage detector and the amplification field needs to be lowered for a higher drift field to operate in stable conditions. Figure 8.9 shows the same measurement as in figure 8.8, with the time resolution shown as a function of the overall gain of the detector. The same measurement separated for each drift distance and for many photoelectrons can be found in section B.3. Field settings with a smaller drift region show a better time resolution than those with larger drift regions and at a similar gain.

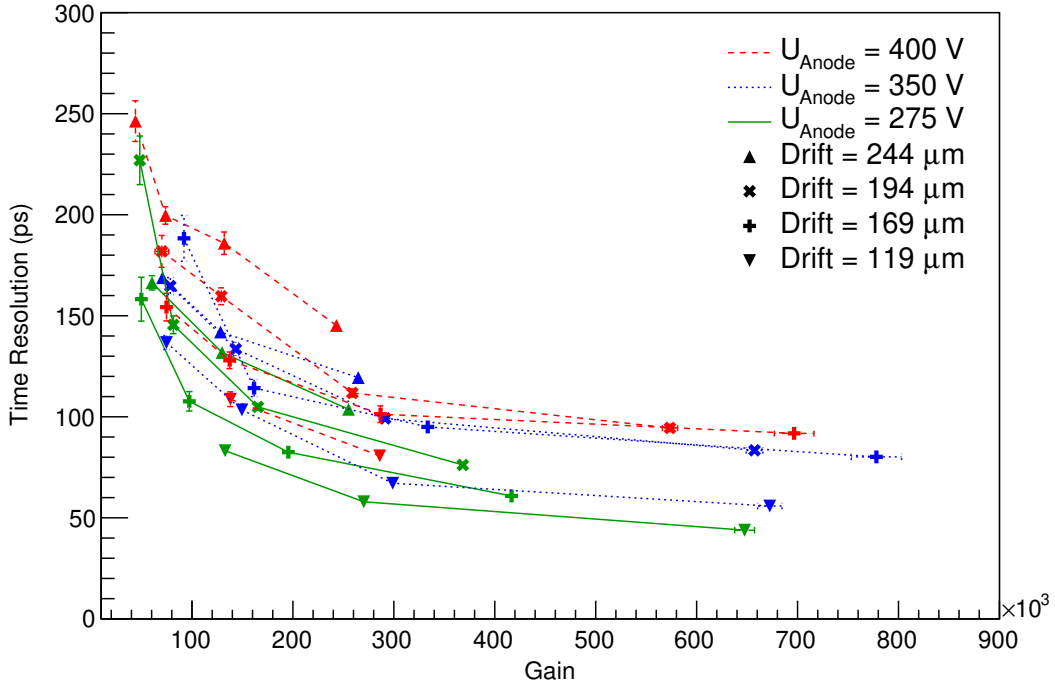

Figure 8.9: Time resolution as a function of the gain for different gap region thicknesses and anode bias voltages under single photoelectron conditions, for an amplification gap of 128 µm.

8.2.2 Summary

Large electric fields have to be applied to the first stage (drift field) of the detector in order to improve the time resolution at a constant gain, as the drift of the primary electrons is shorter at a higher field before starting an avalanche. A larger electric field in the drifts leads consequently to a smaller field in the second amplification stage to maintain a stable operation. Simulations have shown that the propagation velocity of the avalanche is faster than the drift velocity of an individual electron (see chapter 7). This leads to a better time resolution at higher drift fields, even if the total gain remains constant. A smaller drift gap can help to apply higher electric fields. The measurements in figure 8.9 show that time resolutions smaller than 50 ps are possible with the PICOSEC-Micromegas for a single photoelectron.

8.3 Gas Types

The PICOSEC-Micromegas is tested with different gas mixtures to find an optimal gas mixture with high drift velocity and high gain. Neon gas is used with different percentages of ethane and the performance is compared to the “COMPASS” gas as a reference. For this measurement, the picolarge detector with a drift region of 119 µm is used, as it provides the best

results of the different tested drift gaps. A commonly used base gas for ionisation detectors is argon, but neon is the most promising base gas for fast-timing MPGDs, like PICOSEC-Micromegas. Neon is lighter than argon, and it provides a better energy resolution for low energetic particles. Moreover, a higher absolute gain is reached in a neon-mixture compared to argon-mixtures at the same electric field [58, 108].

Simulations have shown (see chapter 7), that short drift times and thus high electric fields are necessary to improve the time resolutions with Micromegas detectors. High electric fields provoke discharges, and the detector operation is unstable. The PICOSEC-Micromegas prototypes are commonly operated with a neon-based mixture called "COMPASS" gas consisting of CF_4 (10 %) and ethane (10 %) added as quenching gases. It is the same mixture as used in the Micromegas of the COMPASS experiment described in section 4.2.1. Micromegas with this neon based mixture are stable at higher electric fields than with argon mixtures. The addition of ethane as a quencher results in a faster gas. The added ethane reduces the time-over-threshold (ToT) of the signal, reaching a ToT of 70 ns in the COMPASS detector. Moreover, the "COMPASS" gas mixture provides superior drift velocities of the electron avalanches due to the added CF_4 as shown in figure 8.10 [91, 68].

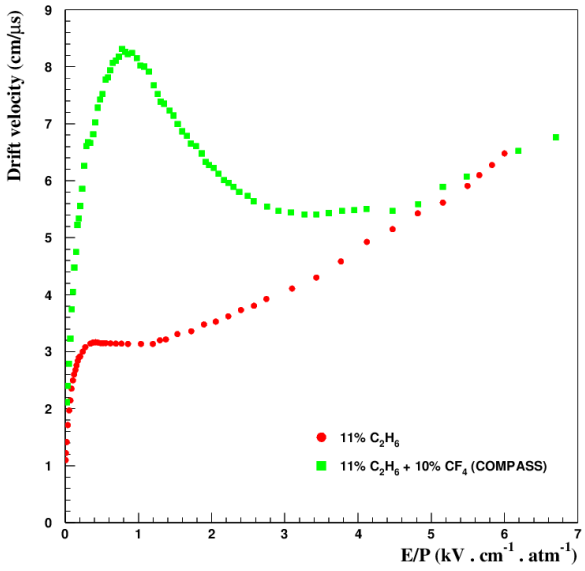

Figure 8.10: Measured drift velocity of COMPASS gas with added CF_4 compared to neon-ethane. Figure extracted from reference [91]

8.3.1 Waveforms of Neon-Ethane(-CF_4) Mixtures

Measurements of neon based gas mixtures with different percentages of ethane ranging from 5 to 20 % have been performed, each with different electric field settings due to the different gain from the percentage of neon. The mean waveform for field settings providing large signals for each of these gas mixtures are presented in figure 8.11a-8.11d. These measurements are per-

formed with one attenuator setting giving a small light reduction and extracting several tens of photoelectrons in the photocathode to generate large signals. The actual number of photoelectrons of each measurement fluctuates heavily (14-55 $N_{\text{p.e.}}/\mu$) as different photocathodes with different efficiencies are used for the measurements, which makes the given values for the time resolution in-compatible for all gas mixtures and the waveforms are only shown for a qualitative description of the impact of the ethane percentage on the signal waveform.

A higher percentage of ethane increases the total detector gain, and larger signals are generated even at lower amplification fields, which is expected and desirable for fast-timing signals. Additionally, it can be observed that the electron peak of the signal widens with a higher percentage of neon. This observation is crucial for the suitability of the gas for the PICOSEC-Micromegas. In a first approximation, the time resolution improves with a better S/N ratio and thus a higher detector gain (see section 2.1). The time resolution is also determined by the consistency of the SAT. At a high percentage of neon,the electron peaks widens, and the rising edge is less steep. Consequently, the time resolution is worse, even if the detector is operated at a high gain.

Figure 8.11e and 8.11f show the waveforms for mixtures with added CF_4, where figure 8.11e is the mean waveform with COMPASS-gas and figure 8.11f with reduced ethane and a composition of neon (89 %) - ethane (2 %) - CF_4 (9 %). CF_4 reduced the drift time of the electrons in the gas and shorter electron peaks are observed for the gas mixture with the added CF_4 compared to the same percentage of neon without CF_4. The comparison of the two mixtures with added CF_4 also shows a signal risetime increase with more neon and less ethane. In general, a CF_4 rich gas mixture is expected to reach the best time resolution, which will be quantified in the further step.

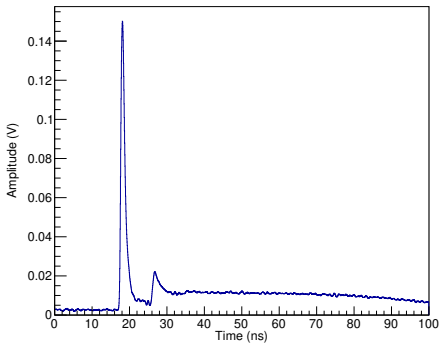

(a) Neon (80 %) - Ethane (20 %); $U_{\text{drift}} = 470\,\text{V}$; $U_{\text{anode}} = 270\,\text{V}$; $\sigma = 27.11 \pm 0.25\,\text{ps}$

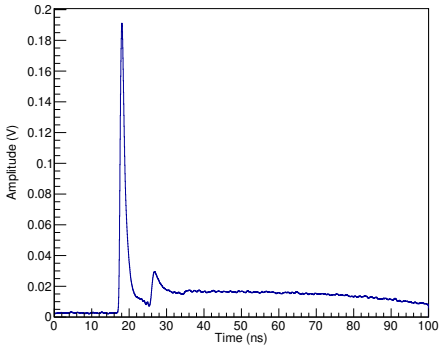

(b) Neon (85 %) - Ethane (15 %); $U_{\text{drift}} = 445\,\text{V}$; $U_{\text{anode}} = 255\,\text{V}$; $\sigma = 26.06 \pm 0.41\,\text{ps}$

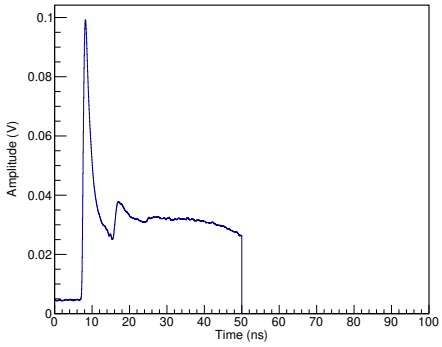

(c) Neon (90 %) - Ethane (10 %); $U_{\text{drift}} = 340\,\text{V}$; $U_{\text{anode}} = 340\,\text{V}$; $\sigma = 41.59 \pm 0.57\,\text{ps}$; shorter aquisition window setting

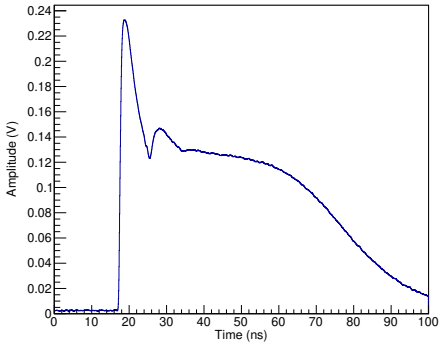

(d) Neon (95 %) - Ethane (5 %); $U_{\text{drift}} = 340\,\text{V}$; $U_{\text{anode}} = 265\,\text{V}$; $\sigma = 22.70 \pm 0.41\,\text{ps}$

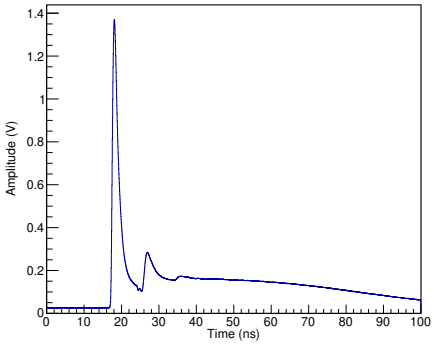

(e) Neon (80 %) - Ethane (10 %) - CF_4 (10 %); $U_{\text{drift}} = 500\,\text{V}$; $U_{\text{anode}} = 275\,\text{V}$;
$\sigma = 10.66 \pm 0.13\,\text{ps}$

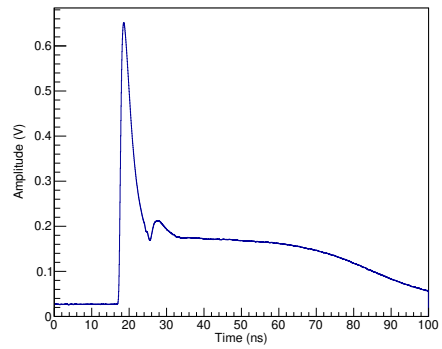

(f) Neon (89 %) - Ethane (2 %) - CF_4 (9 %); $U_{\text{drift}} = 445\,\text{V}$; $U_{\text{anode}} = 255\,\text{V}$;
$\sigma = 15.13 \pm 0.33\,\text{ps}$

Figure 8.11: Mean waveform at different mixtures of neon - ethane - CF_4. The same light attenuator (Attenuator No. 4) is used for each measurement providing a high amount of photoelectrons. Each gas mixture is operated at electric field settings that provide the best time resolution.

8.3.2 Neon-CF_4 Mixture

An operation of the detector with only neon and CF_4 to enhance the steepness of the rising edge further is not possible. Ethane, as a quenching gas, is crucial for the signal propagation to have a clear separation between the electron peak and ion tail. Figure 8.12 shows similar to figure 8.11 the mean waveform from a PICOSEC-Micromegas operated with a gas mixture of neon (90 %) - CF_4 (10 %). While it provides a very steep rising edge, the total signal shape is spoiled from the missing quenching gas. Without the strong quenching effect of ethane, photons created in the avalanche are not absorbed and continuously ionise the detector, leading to an increased ion tail and a reduced total gain of the detector. A waveform analysis to extract the SAT is more difficult without a clear separation between the electron peak and the ion tail and gas mixtures without quencher are not further investigated for the PICOSEC-Micromegas.

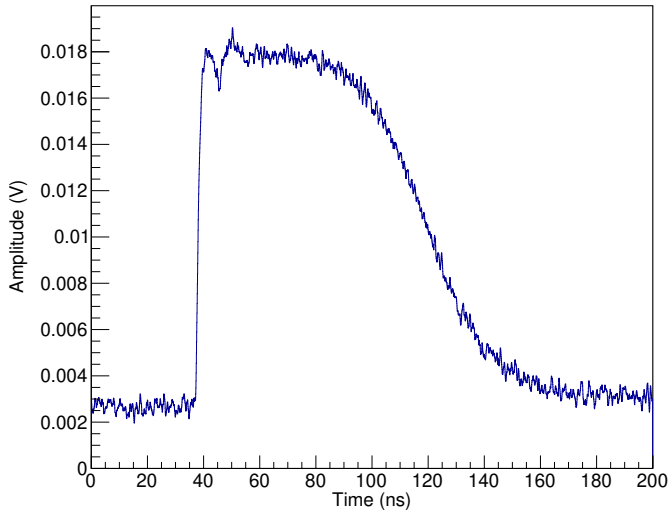

Figure 8.12: Mean waveform of a PICOSEC-Micromegas operated with a gas mixture of neon (90 %) - CF_4 (10 %) under the same laser conditions as the mixtures in figure 8.11.

8.3.3 Time Resolution

The time resolution is measured and compared at single photoelectron conditions for neon-ethane and neon-ethane-CF_4 gas mixtures. A different percentage of quenchers provides a different gain at the same operating voltage, and thus voltage settings have to be adjusted to get the optimal time resolution. For each gas mixture a set of measurements is performed with varying ratios between amplification and drift field while the total amplification of the detector is kept constant. The exact voltage settings for each mixture are displayed in figure 8.13. The best achieved time resolution for each gas mixture and its corresponding field settings are presented in table 8.1. The previously used COMPASS gas provides the best time resolution with 43.9 ± 1.0 ps, while all other gas mixtures show time resolutions worse than 100 ps. The better time resolution of COMPASS gas is also coherent with a significantly higher signal amplitude and charge of the electron peak, which is reached at higher electric fields without reaching instabilities.

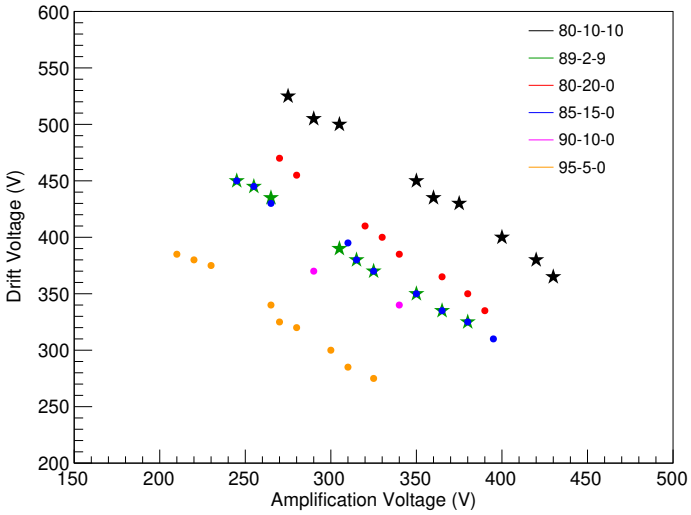

Figure 8.13: The highest possible voltage for each gas type at a high light intensity is determined. The drift region is 119 µm and the amplification region is 128 µm deep. The gas mixture is given in the legened with the percentages of neon-ethane-CF_4. Each gas is measured with different ratios between the drift and the amplification field.

The relation between time resolution and field settings is further investigated. Figure 8.14 gives several plots of the time resolution for each gas considering the different field settings and the signal amplitude for single photoelectron settings. The same plots for other attenuator settings providing many photoelectrons are given in appendix C. In the modelling (chapter 7) and the measurements of the drift distance (section 8.2) the time resolution improves with a higher drift field, and it is expected to see the same behaviour in figure 8.14a. Anyhow, this effect is only barely noticeable for the single photoelectron measurements of the gas mixtures. For the black points belonging to the COMPASS gas, the points tend to have an expected rising slope towards higher drift fields. For the other measurements, the calculated time resolution for single photoelectron conditions has large error bars as the signal amplitude of these signals is very low and close to the

Table 8.1: Time resolution of the different gas mixtures at the best field configuration and single photoelectron conditions.

Gas mixture (%) (Neon-Ethane-CF_4)	U_{drift} (V)	U_{anode} (V)	e-peak charge (pC)	Amplitude (mV)	Time resolution (ps)
80-10-10	525	275	8.58 ± 0.13	166.3 ± 0.20	43.89 ± 1.00
89-2-9	445	255	1.69 ± 0.01	31.56 ± 0.44	112.15 ± 4.03
80-20-0	470	270	0.54 ± 0.01	21.61 ± 0.18	129.21 ± 6.03
85-15-0	395	310	0.74 ± 0.01	22.83 ± 0.21	113.48 ± 4.66
90-10-0	340	340	0.82 ± 0.01	20.72 ± 0.09	150.23 ± 3.17
95-5-0	375	230	1.13 ± 0.01	22.98 ± 0.16	181.09 ± 8.91

noise. The calculation of the SAT has higher systematic errors as it varies a lot with the analysis parameters. The signals are larger for measurements with other attenuator settings and more light, and the calculation of the time resolution is more precise. For each gas, at properly sized signals, an improvement of the time resolution with increased drift field is measured and the importance of the pre-amplification for the best time resolution is verified.

The lower signal amplitude of the different gas mixtures compared to the COMPASS mixture due to the lower electric fields is the main reason for the inferior time resolution. Figure 8.14b shows the relation of the time resolution to the signal amplitude for all gases and the COMPASS gas is the only gas with amplitudes between 50 mV and 100 mV. All the other gases are not reaching amplitudes above 30 mV. The observation of the time resolution improvement with higher signal amplitude is valid for each gas individual and for all gases combined. All measured points from the different gas mixtures follow the same tendency. Next to the COMPASS gas, the best time resolution with the highest signals is shown by the gas mixtures neon (89 %) - ethane (2 %) - CF_4 (9 %) and neon (85 %) - ethane (15 %). Similar to the COMPASS gas, the gas mixture with added CF_4 allows higher fields than for the gas with comparable neon percentage and thus a higher signal size. The gas without CF_4 and 85 % neon has the best equilibrium between gain from the neon and the possibility of a high electric field due to the quencher. With more neon, the field has to be reduced, and with less neon, the gain from the higher electric field is not sufficient.

The last comparison for the gas mixtures is the relation of the signal size and the field ratio, shown in figure 8.14c. Similar to figure 8.14a, the signal of all the gas mixtures except the COMPASS gas have a small S/N ratio, and the determination of the mean signal size is difficult. The COMPASS gas shows a significant improvement of the signal amplitude with a higher drift field and thus with stronger pre-amplification. This measurement is therefore coherent with the both previous shown plots in figure 8.14a and 8.14a. The same observation is also made for the other gases at settings with more light and higher S/N ratio as given in appendix C.

Table 8.2: Best measured time resolution of the different gas mixtures at attenuator setting No. 4 with the calculated mean number of photoelectrons.

Gas mixture (%) (Neon-Ethane-CF_4)	U_{drift} (V)	U_{anode} (V)	$\langle N_{\text{p.e.}} \rangle$	Time resolution (ps)
80-10-10	525	275	14	15.19 ± 0.28
89-2-9	445	255	55	15.13 ± 0.33
80-20-0	470	270	33	27.11 ± 0.25
85-15-0	445	255	22	26.06 ± 0.41
90-10-0	340	340	15	41.59 ± 0.57
95-5-0	340	265	47	22.70 ± 0.41

8.3.4 Time Resolution for several photoelectrons

The gas mixtures are also investigated with different attenuator settings, providing several photoelectrons. The photocathode was exchanged several times during the measurements due to damages after sparks. Even though each time a 10 nm aluminium photocathode was used, the effective quantum efficiency varies and the same amount of light is generating different numbers of photoelectrons in the detector. The time resolutions measured at the same attenuator setting for different gas mixtures are only comparable with the determination of the number of photoelectrons for each setting.

Table 8.2 gives the best measured time resolution for each gas mixture and the attenuator No. 4. This attenuator reduces the laser light of a factor $\sim$10, ensuring a stable operation at high electric fields and providing enough light to generate more photoelectrons than a 150 GeV muon generates in the best performing photocathode. The number of photoelectrons for each measurement mentioned in table 8.2 are calculated by the method presented in section 6.3. The best resolution is archived with the mixture containing neon (89 %) - ethane (2 %) - CF_4 (9 %) with 15.13 ± 0.33 ps. The COMPASS gas mixture provides the same time resolution with 15.19 ± 0.28 ps, but at nearly 4 times fewer photoelectrons. With the same number of photoelectrons (55) the COMPASS gas mixture would even reach less than 8 ps time resolution, which shows the superiority of COMPASS gas for fast timing detectors again.

The time resolution of each gas mixture is measured to less than 50 ps at more than 15 photoelectrons and for measurements above 20 photoelectrons, each gas mixture reaches less than 30 ps. Sufficient time resolutions for some applications can be reached with all measured gas mixtures. The reduction of ethane in the gas mixture reduces the flammability of the gas and thus allows the use of PICOSEC-Micromegas in a wide range of applications. Moreover, with a higher percentage of neon, a lower field is needed to reach comparable time resolution, and lower voltages allow different detector and read-out constructions with fewer spark protection.

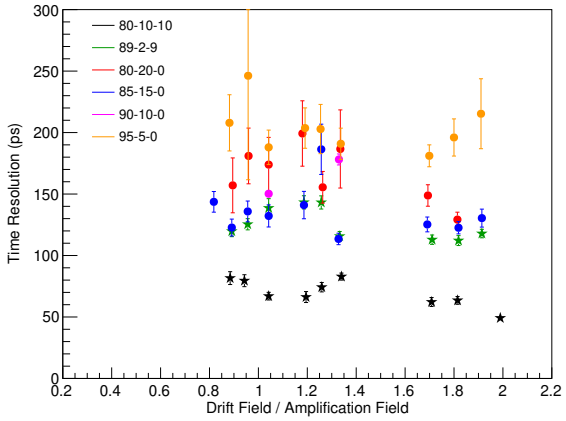

(a) Time resolution versus ratio between the drift and amplification field.

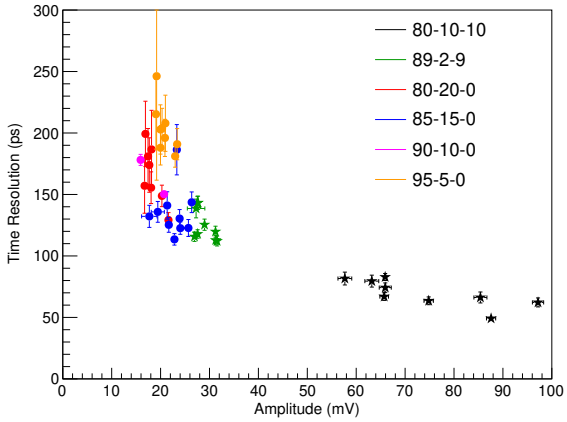

(b) Time resolution versus signal amplitude.

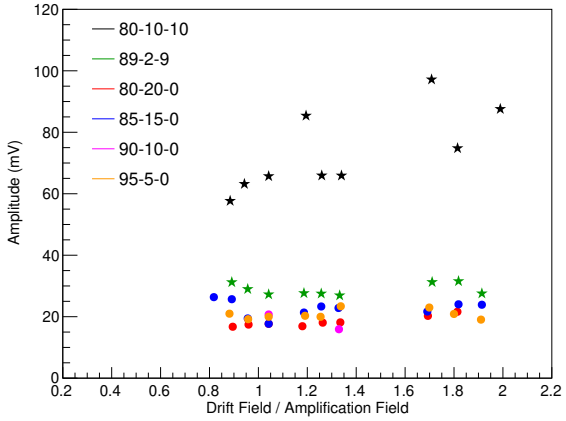

(c) Signal amplitude versus ratio between the drift and amplification field.

Figure 8.14: Time resolution for the different gas mixtures (neon-ethane-CF_4) under single photoelectron conditions.

8.3.5 Gas Pressure

Additional to the studies of the gas mixtures in the laser, the impact of the gas pressure on the detector gain is studied in the laboratory with an UV lamp. The gain (G) of a detector with a parallel electric field in an amplification region with thickness (d) depends on the Townsend coefficient (α) of the gas as

$$G = \mathrm{e}^{\alpha d} \,. \tag{8.4}$$

The Townsend coefficient describes the mean free path of the electrons between ionisations and can be expressed as

$$\alpha = pA\mathrm{e}^{-Bp/E} \,, \tag{8.5}$$

where p is the gas pressure; E is the electric field; and A, B are two specific parameters depending on the gas [107]. Studies have shown that each gas mixture and amplification field has an optimal gas pressure that provides the highest gain [109].

The gain of the PICOSEC-Micromegas is calculated from the mean of the signal charge distribution ($\bar{Q}$) for single photoelectron signals provided by an UV light source and corrected by the gain of the amplificator (g) as

$$G = \frac{\bar{Q}}{\mathrm{e}}/g \,, \tag{8.6}$$

where e is the electron charge. For each measurement, vacuum is pumped into the detector chamber, and the chamber is filled up to different pressures with the COMPASS-gas mixture. The measurement is performed with two different field settings. The first is with an anode voltage of 500 V and a drift voltage of 100 V, given in figure 8.15a. This setting is close to the normal operation of a Micromegas without any pre-amplification. The second setting is with 275 V in the anode and 450 V in the drift, given in figure 8.15b. This setting has high pre-amplification, and it is the field setting that provides the optimal time resolution. For both field settings, the gain improves with lower pressure, as the mean free path of the electrons increases. At the lowest measured pressure for each setting, the gain is too high, and the detector starts to spark. The measurement with a pre-amplification (figure 8.15b) reaches this point already at 725 mBar with a gain >$8{\cdot}10^6$. The other set has a lower electric field, and thus a stable operation at even lower pressure was possible. Under 600 mBar the gain reaches a plateau, which marks the optimal pressure for the given gas mixture and amplification distance.

All in all, the PICOSEC-Micromegas shows the same behaviour of the gain for different gas pressures as other Micromegas [109]. A reduction of the gas pressure improves the detector gain and consequently the time resolution, but with the optimal field settings, the gain is too high, and the gain plateau at lower pressures is not reached. To benefit from the higher gain at lower pressures, the electric field needs to be reduced with maintaining the field ratio between pre-amplification and amplification to preserve optimal timing property.

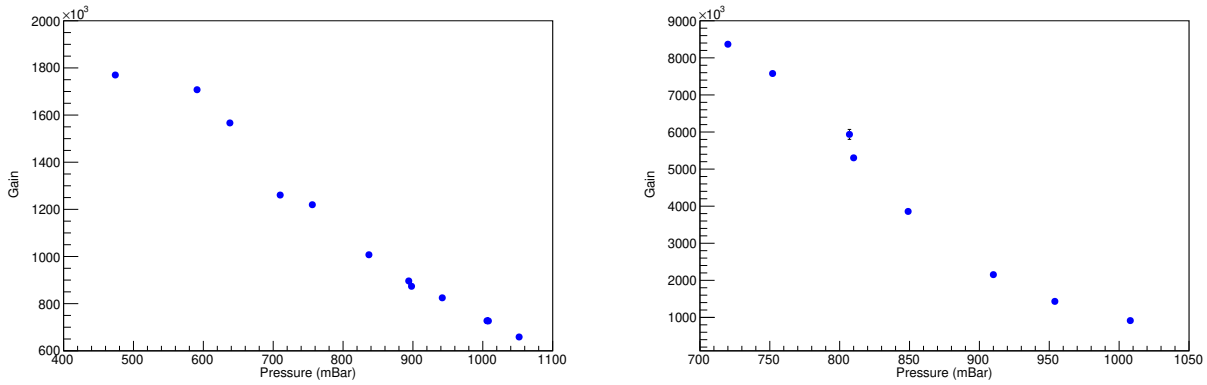

(a) Anode voltage 500 V; Drift voltage 100 V; $U_a/U_d = 5$

(b) Anode voltage 275 V; Drift voltage 450 V; $U_a/U_d = 0.6$

Figure 8.15: Gain at different gas pressures with COMPASS gas for two field settings.

8.3.6 Summary

The gas mixture used in the first proof-of-concept studies of the PICOSEC-Micromegas [5] provides the best detector performance. The gas mixture neon (80 %) - ethane (10 %) - CF_4 (10 %) was chosen for its fast signals providing short ToT in the COMPASS experiment [68]. These are the same properties that are needed for a small jitter of the SAT, as needed in the PICOSEC-Micromegas. The study of different fractions of neon and ethane shows that the signal amplitude is more important for the time resolution than the total gain of the gas. A lower percentage of ethane increases the detector gain, but the electron peak of the signal widens more than the amplitude rises. The wider peaks of the neon-ethane mixtures only allows lower fields for the pre-amplification to avoid sparks when too many electrons are created in the detector. The lower drift field increases again the drift path before pre-amplification, which increases the time jitter.

All gas mixtures reach time resolutions under 100 ps for several photoelectrons. Gases with a low percentage of ethane need lower electric fields for optimal performance, compared to mixtures with a high percentage, and a reduction of ethane reduces the flammability of the gas. Gas mixtures with neon-ethane and with neon-ethane-CF_4 are suitable for the operation in a PICOSEC-Micromegas, while mixtures of neon-CF_4 are missing a quenching gas for a stable electron peak. The gas mixture can be optimised for future applications depending on the required time resolution and other constraints that are linked specific applications, like flammability or availability of the compounds. Operation of the detector at a lower pressure than atmospheric pressure increases further the detector gain, but only slight decreases of the pressure are possible without the need to reduce the electric field to avoid sparks. More studies at different gas pressures are needed to determine the impact of lower gas pressures on the time resolution.

Part III

Developments Towards a Particle Detector for High-rate Environments

πάντων γὰρ ὅσα πλείω μέρη ἔχει
καὶ μὴ ἔστιν οἷον σωρὸς τὸ πᾶν·

— Ἀριστοτέλης (384-322 B.C.), τὰ μετὰ τὰ φυσικά ***VIII 1045a. 8–10***

"pánton gár ósa pleío méri échei kaí mí éstin oíon sorós tó pán", Aristotélis (384-322 B.C.), ***tá metá tá fysiká VIII 1045a. 8–10***

"The totality is not, as it were, a mere heap, but the whole is something besides the parts", Aristotle (384-322 B.C.), ***Metaphysics VIII 1045a. 8–10***

9 Characterisation in a Particle Beam

Contents

This chapter introduces the set-up used for the particle beam measurements at the north area of the SPS beamline at CERN. This area contains several extraction lines for temporary and (semi-)permanent installations. The set-up containing a beam telescope with triggering and tracking units and MCP-PMTs as t_0-reference detectors is described. Additionally, an extensive study of the MCP-PMT time resolution and suitability as a reference detector is presented.

Particle beam measurements are used to study the timing performance with MIPs generating a Cherenkov cone. This chapter presents characterisation measurements with the same prototypes used for the Laser characterisation. The time resolution for different electric fields and different Micromegas technologies is studied. The particle beam was also used to study resistive and segmented readouts, crucial developments for applications in high-rate environments, which will be presented in chapter 11 and chapter 12, respectively. Moreover, measurements in a MIP

beam are the most reliable way to determine the quantum efficiency of photocathodes under working conditions similiar to future applications. The results for photocathodes studied in the beam are presented in section 13.1.

9.1 Beam Setup

The CERN accelerator complex consists of several linear and circular particle accelerators. All of these accelerators can accelerate particles in different energy ranges, and the particles are handled from one accelerator to another by transfer lines. The biggest circular accelerator in this complex is the LHC whose 27 km circumference is currently the largest circular particle collider on Earth. Proton-proton collisions are possible with a centre of mass energy of up to 13 TeV.

The PICOSEC-Micromegas beam tests are performed at the H4A extraction line of the SPS circular accelerator, which is the second-largest accelerator after the LHC. Protons are accelerated up to a momentum of 450 GeV/c. Not all protons in the SPS are dedicated to the LHC. Some are transferred to different extraction lines placed around the accelerator. A moveable beryllium target is placed in front of the H4 extraction line. The accelerated protons scatter at this target, and different secondary particles like muons and pions are generated. Several moveable ledges of the target are controllable by the SPS control room, and specific secondary particles and energies can be produced by moving the ledges and additional collimators [110]. For the PICOSEC-Micromegas measurements, only muons and pions in a momentum range of 150 - 180 GeV/c are used.

The PICOSEC-Micromegas beam telescope was placed in the PPE134 cavern of the H4 beamline. It is located in the experimentation hall EHN1 on the Prévessin site of CERN with the H2 and H8 beamlines, the Gamma Irradiation Facility (GIF++), and the neutrino detector test facility (CENF). The H2 and H4 beamlines as well as the GIF++ facility share the same beam target [111].

The beamtime used for the PICOSEC-Micromegas measurements is declared as RD51 common beamtime. This means that several groups of the RD51 collaboration can participate in this beam test, and each one installs its telescope and set-up in the cavern at the same time. Figure 9.1 shows a photograph of the H4A cavern during one beam test, where the red circle marks the PICOSEC-Micromegas beam telescope. The H4A cavern has additionally the 1.5 T magnet Goliath available, also shown in figure 9.1.

Most RD51 common beam tests are executed in the H4A experimentation area as RD51 is maintaining a semi-permanent installation at the PPE134 cavern. It is equipped with a connection panel to gas bottles outside the cavern with five gas lines each upstream and downstream of Goliath. Furthermore, the cavern provides patch panels with coaxial, high-voltage and ethernet connections to the control room. Set-up parameters like the operating voltage of the detectors or the trigger logic can be remotely changed during beam operation. The specific trigger logic used for the PICOSEC-Micromegas beam telescope is discussed in section 9.1.2.

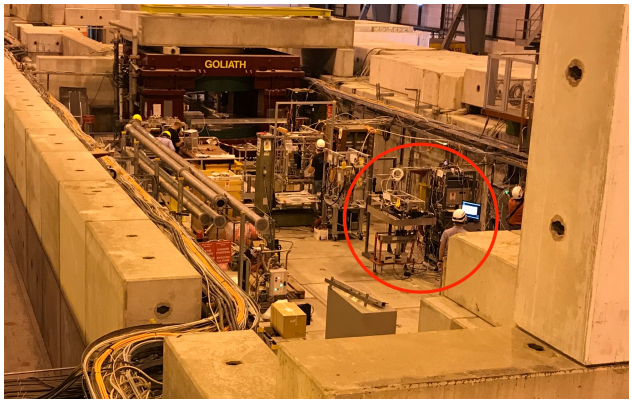

Figure 9.1: Picture of the set-up during one RD51 common test beam in the H4A cavern. The red circled set-up is the beam telescope used for the PICOSEC-Micromegas measurements. Picture first published in [90].

9.1.1 Beam Telescope

A beam telescope is used for the measurements in the particle beam, which consists of several mounting places for the PICOSEC-Micromegas, a trigger system to start the data acquisition (see section 9.1.2), a GEM tracker to reconstruct the particle trajectories (see section 9.1.3), and two MCP-PMTs as a time reference detector (see section 9.2). The PICOSEC-Micromegas waveforms are digitised and off-line paired to the corresponding particle trajectory reconstructed from the tracker signals. The common trigger is used to link the tracker data and the PICOSEC-Micromegas data. The MCP-PMT signals are treated in the data acquisition and off-line analysis analogue to the PICOSEC-Micromegas signals. The determination of the SAT and time resolution is explained in section 6.4.

Figure 9.2 shows a sketch of the detector spots in the telescope and its relative position in the beam direction. The telescope consists of a rigid metal frame with three GEMs and several trigger detectors (see section 9.1.2) mechanically mounted to it. Inside the frame, there are four fixed spots to install PICOSEC-Micromegas prototypes. PICO2 & PICO3 can host chambers of the first prototype series (see section 5.3.1) and PICO4 can host the resistive prototype. The MCP-PMTs are mounted in front of the telescope frame and the larger multipad prototype on a dedicated spot in front of the telescope.

Figure 9.2 gives the z-position for all detectors mounted inside the telescope frame, which were constant over all measurement periods. The remaining detectors were placed outside the telescope, and the distance was individually measured for each beam campaign. The z-positions of the tracking GEMs are necessary for the reconstruction of the particle trajectories (see section 9.1.3) and the z-position of the detector plane of the detector under tests (DUTs) is necessary for the interpolation of these trajectories. The z-position is manually measured on the set-up.

A photograph of the fully functional beam telescope set-up is given in figure 9.3. The different components are labelled with a coloured box. The beam goes from right to left. The maximum of four different PICOSEC-Micromegas prototypes are placed in the telescope on their

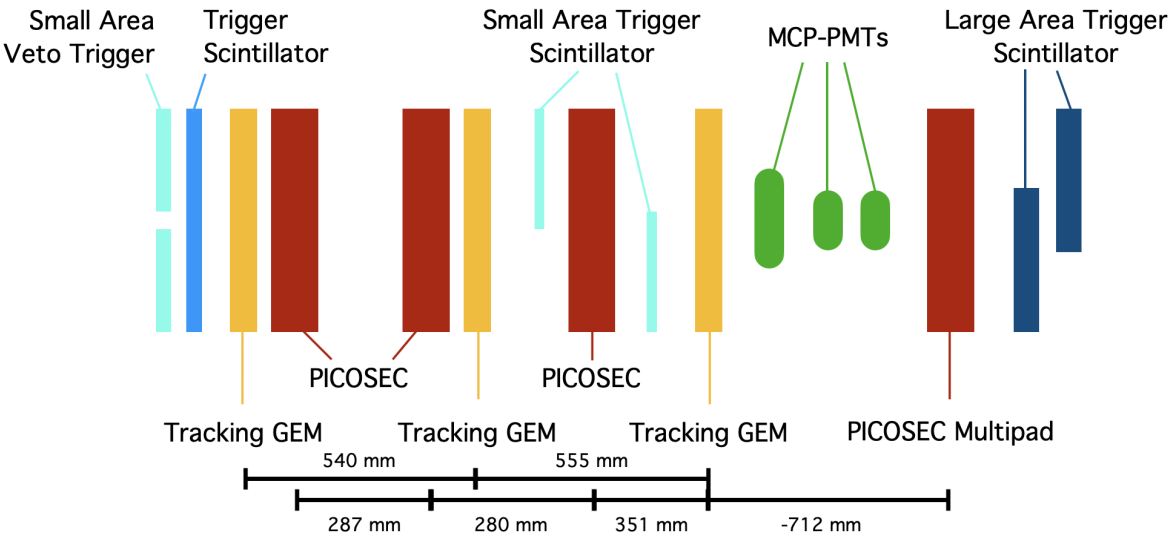

Figure 9.2: Sketch of the detector positions in the beam telescope (not to scale). The first PICOSEC-Micromegas position (PICO1) and the MCP-PMTs are not mechanically bound to the telescope and the position in z-direction variates.

respective positions (red boxes). Additionally, a hyper-fast silicone (HFS) detector from the RD50 working group is hosted in the telescope [112].

9.1.2 Trigger

One important component of the beam telescope for the DAQ is the trigger set-up. It consists of several differently shaped scintillators along the beam axis. Each of the scintillators is read out by a PMT, and the generated signals are further processed by analogue coincidence units (see section 9.1.2). A NIM signal is sent to the scalable read-out system (SRS) [113] unit (see section 9.1.3) that triggers the data acquisition, only when a beam particle passes through a certain combination of scintillators. Each combination of scintillators defines a different acceptance region for beam particle.

The PICOSEC-Micromegas beam set-up has a total of six different trigger scintillators, and these scintillators are forming two different acceptance regions. Figure 9.4 gives a schematic overview of the scintillators and its positions in the beam telescope relative to the GEM plane. Scintillator S3 (red) is a 10 cm square, placed behind the last GEM of the tracker, and it is the reference for all coincidence combinations. Scintillator S1 & S2 are small fingers with a thickness of 5 mm. A 5 mm square acceptance area can be formed with them. Additionally, S4 is a 10 cm square with a 5 mm diameter hole in the middle. This scintillator is included in anti-coincidence with the coincidence of S1, S2 and S3 scintillators to define a 5 mm diameter region referred to as “small area trigger”. The scintillator S4 also rejects any particle shower produced by particles

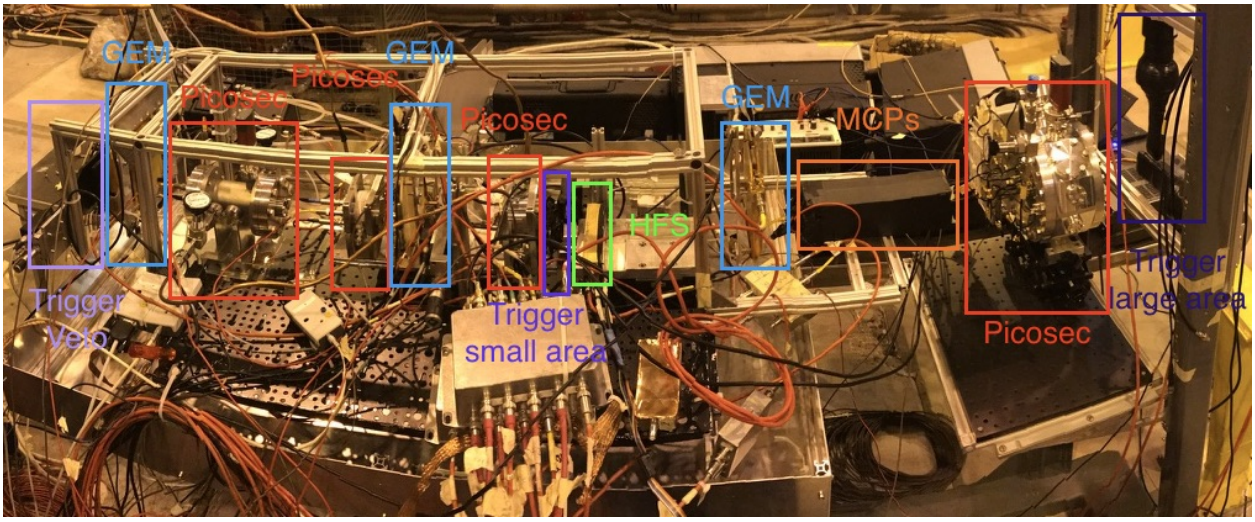

Figure 9.3: This photograph shows the beam set-up during the campaign in August 2017. The marked detectors of this set-up are explained in their corresponding section.

hitting telescope materials. The centre of each PICOSEC-Micromegas detector is aligned with a precision of less than a millimetre to this trigger area so that the waveform analysis does not need any tracking information to estimate its timing performance.

The second trigger set-up consists of the coincidence of S3, S5 & S6. S5 & S6 are two scintillator wedges with a width of 5 cm. An acceptance region of up to 5 cm x 5 cm can be formed with these. This second combination is referred to “large area trigger”. As it is larger than the active area of small PICOSEC-Micromegas prototypes, the track information of the particle is needed to analyse the data. This set-up is primarily needed to understand the radial behaviour of the detector and for the multipad studies (see chapter 12.3).

Trigger Logic

Analogue electronic modules are interconnecting the scintillation detector signals. The process from the detector signals to a single NIM signal is described in the following section. The logic used for the trigger chain is particular, as it allows remote changes in the configuration of scintillator coincidences. A symbolic diagram of the trigger logic is given in figure 9.5.

The light generated in each scintillator by a passing particle is detected by a small PMTs. The PMT signal is amplified and passed to a discriminator unit. The threshold is set slightly above the noise level, and a standardised NIM pulse is generated each time a PMT detects a particle. S4 is set in anti-coincidence to the other detectors. The negated output from the discriminator is used for signals from this detector. It will give out a constant signal and fall back to ground level when a particle hits the scintillator area. Additional detectors can be added to the trigger logic additional to the six described scintillators (S1, ..., S6). Those other possible detectors are labelled with Aux1, Aux2, ... in figure 9.5. One possibility is to add a DUT temporarily to the trigger logic to determine its position relative to the beam telescope.

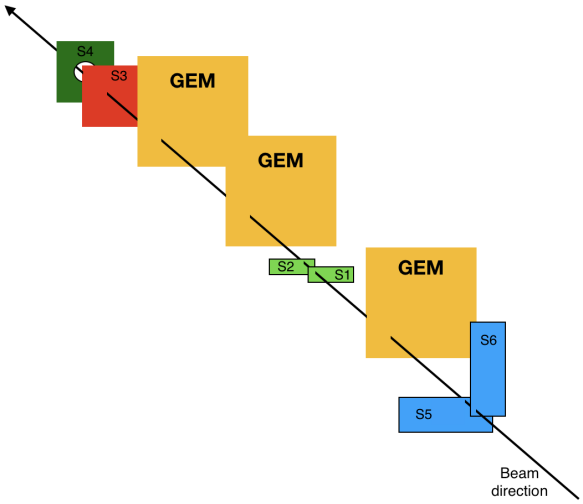

Figure 9.4: Sketch of the trigger scintillators in perspective to the beamline and the GEM. The green scintillators in coincidence with the red one form the small area trigger, and the blue ones with the red scintillator define the large area trigger.

Each of the NIM signals goes to a logical fan-in/fan-out module, which is used to remotely select the different trigger settings. A logical fan-in/fan-out module has two inputs and one output. It acts as a logic OR. If one of both input signals is logic true (negative voltage for a NIM signal), it will give out a logic true signal. The discriminator output takes one input of each module, and long cables take the other from the experimentation area to the control room. In the control room, these signals can either set to ground or to a constant NIM signal. The fan-in/fan-out module will propagate the discriminated scintillator signal if the corresponding line in the control room is set to ground. If the line is set to a constant NIM signal, the fan-in/fan-out will always propagate the constant signal without considering the discriminated detector signal.

The output of the fan-in/fan-out modules is given to the coincidence units linked in a cascade, as one unit has only four inputs. A coincidence unit works like a logic AND. It will give out a NIM signal (logic true) if all inputs are providing a NIM signal. Detectors are set inactive from the control room with a constant NIM signal provided to the fan-in/fan-out, and thus they will not interfere with the AND logic.

This trigger logic is modular and can be extended for more detectors. The output of the last coincidence unit is given to the trigger input of the SRS system, which controls the DAQ and the tracking system and is explained in section 9.1.3.

9.1.3 Triple-GEM tracker

The tracker is after the trigger scintillators the next main component of the beam telescope. The particles trajectory can be reconstructed with the data from the tracker. The reconstruction of each trajectory is important to study the performance of different regions of the DUT. For example, the radial dependence of the time resolution along the active area (see section 9.2) or the perfor-

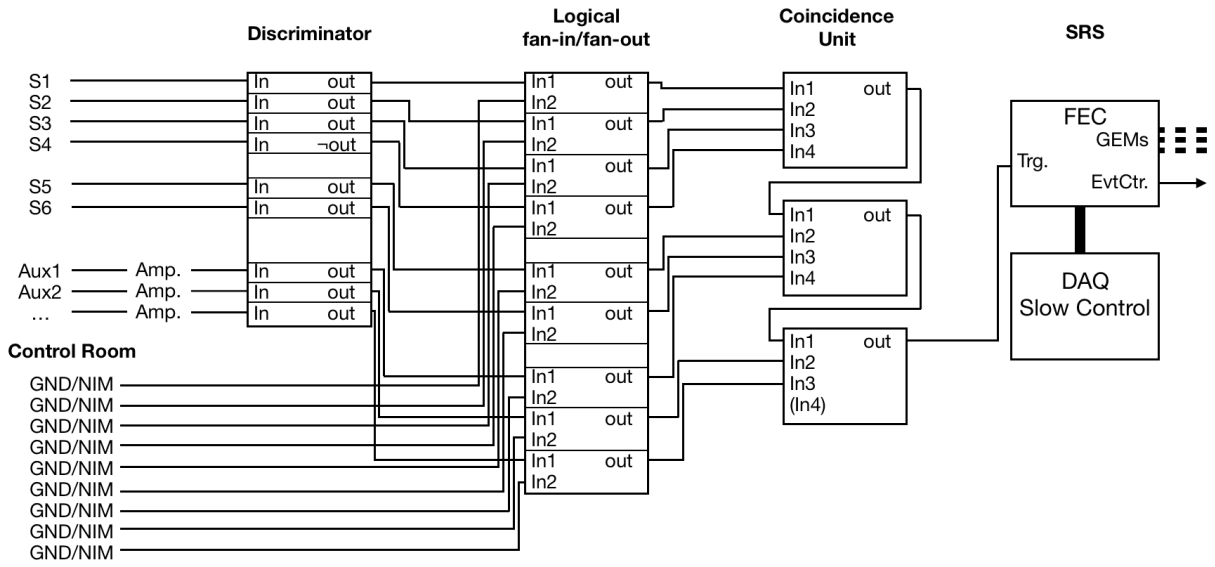

Figure 9.5: Block diagram of the electronic modules used to provide a NIM signal to trigger the DAQ. First published in [90].

mance of a segmented anode (see chapter 12.3) can only be measured with access to the particle trajectory information. The tracker consists of three triple-GEM detector plates with a 10 cm x 10 cm active area. Triple-GEM detectors are a development of the gas electron multiplier (GEM) detectors described in section 3.3.1.

One HV line powers the detector, and a voltage divider distributes the voltage to each amplification stage. Not the same electric field is applied to the three stages of a triple-GEM detector. Previous studies have shown a reduced discharge probability at constant gain with an asymmetric electric field between the amplification stages [114]. Different resistors are chosen for each stage so that the first GEM has a higher field, and the field in the next ones is successively lowered. A sketch with the actual values of the resistors and the gap distances in the triple-GEM used in the beam telescope is given in figure 9.6.

Each triple-GEM detector used in the beam telescope is operated with an argon (90 %) - CO_2 (10 %) gas mixture and has two readout planes with a strip segmentation in x- and y-direction. The pitch of the strips is 400 µm and each layer consists of 256 strips. The detector plane reaches a spatial resolution of 50 µm. Each of these planes is treated as an independent detector in the data acquisition and hit reconstruction, leading to a total of six detectors in the tracking system. The strips are read out by APV25 chips [115] and the SRS described in the following section.

Scalable Readout System (SRS)

The signals from the tracking GEMs are acquired with the SRS [113], that is commonly used in the RD51 community. Figure 9.6 shematically shows the SRS system.

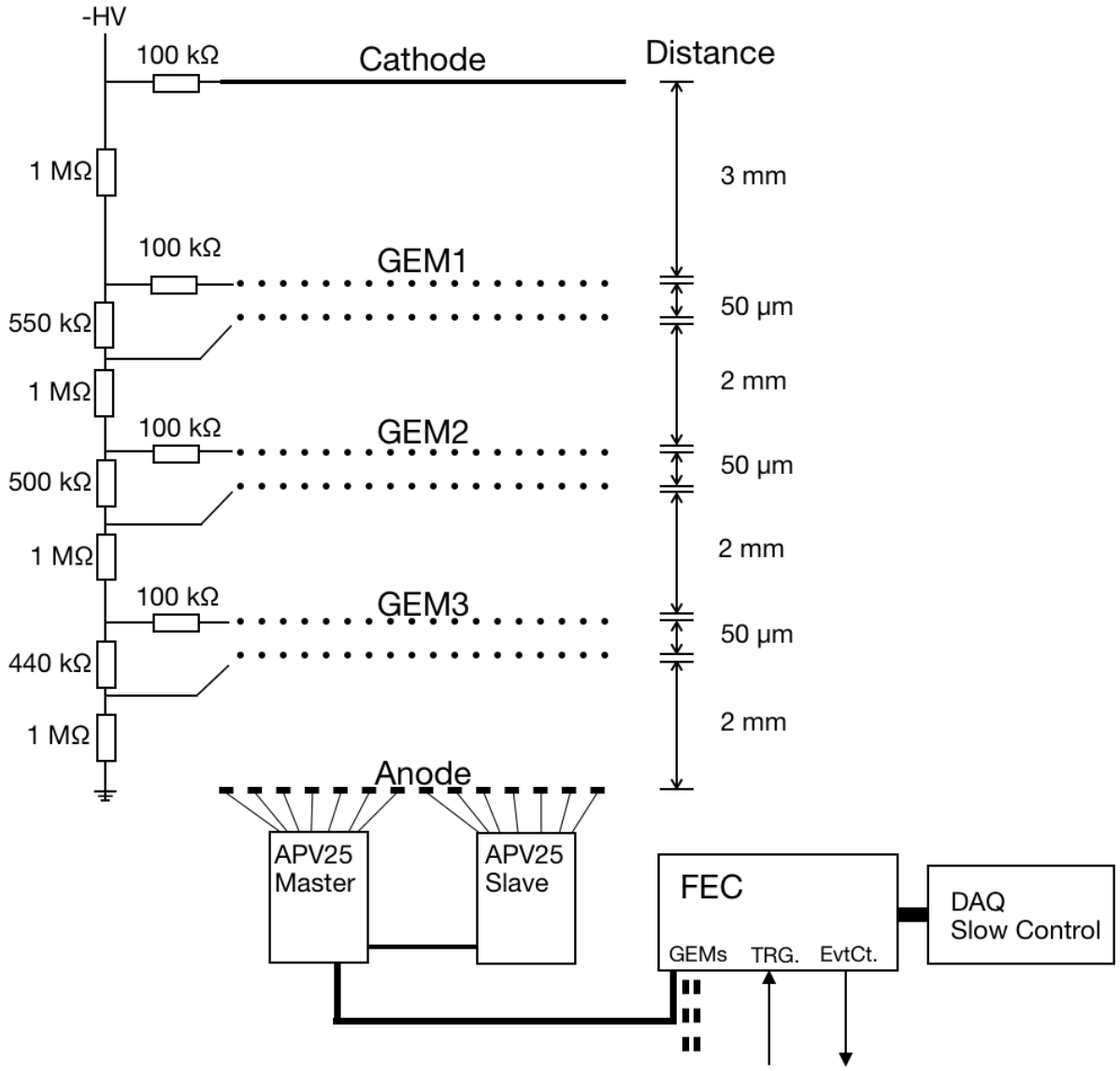

Figure 9.6: Scheme of a triple-GEM detector with a voltage divider and segmented strip read-out, as it is used in the beam telescope. First published in [90].

The SRS system provides a whole readout chain beginning from the front-end electronic. The strips of the GEMs are read out with APV25 chips. These are 128 channel ASIC chips designed to read strip detectors [113]. Two chips in a master-slave configuration are needed to read out a whole detector plane. Each chip includes a pre-amplifier, shaper and signal sample for each channel. The sample rate is equal to the bunch frequency of the LHC (40 MHz) [116]. For this reason, these chips are used in several experiments at CERN [117, 118].

The output signals from all APV25 master-slave pairs are collected at front end cards (FECs). The data bandwidth at higher trigger rate can be a limiting factor in this step even though HDMI cables are used for the data transfer. A high-band Ethernet link connects the FEC that collects the signals from the three triple-GEMs (six readout planes) to a DAQ computer located in the control room. The trigger signal explained in section 9.1.2 triggers the readout of the APV25s and the uplink. The FEC additionally provides a binary encoded event counter signal that is synchronised with the trigger and is digitised together with PICOSEC-Micromegas waveforms in a dedicated channel of the oscilloscope.

The FEC is controlled from the DAQ computer. Different trigger settings and rates, as well as acquisition windows, can be selected to reduce the event data size and to allow higher trigger rates at a constant data bandwidth. Moreover, an internal random trigger can be selected to perform pedestal correction runs. Furthermore, the DATE software developed by the ALICE collaboration is used to acquire the APV25 waveforms [119]. The waveform sample values are stored as `.raw` file and the tracks are calculated off-line as shown in the following.

Tracking Software and Reconstruction

A software written by Jonathan Bortfeld [120] is used to calculate the particle trajectories from the GEM signals. This software evaluates the x and y-coordinates on each detector plane from the raw signals read out by the SRS system. The z-position for each detector plane is predefined and fixed by the beam telescope. The z values are given in the set-up sketch in figure 9.2. For each detector plane, a three-dimensional vector is calculated that represents the crossing of the particle through the GEMs.

The calculated vectors are recorded in a ROOT TTree object and written to an output file, which also provides the SRS trigger number to match the waveforms acquired for the DUTs with the oscilloscope to the corresponding trajectory. Moreover, the file provides quality information of the linear fit and clusters as well as a global timestamp for each SRS trigger.

The first step in calculating the particle tracks is the reconstruction of the particle passage on each GEM plane. The signal from each strip plane is digitised, and a threshold is applied to identify activated strips. Consecutive activated strips in one tracker plane are bound together to clusters. The reconstruction is done for each strip plane individually. This leads to six individual detection planes of the three GEM telescope. The particle trajectories are calculated out of these reconstructed positions. The exact inclination point is calculated out of the mean of the activated strips. This method allows position accuracies of $1/\sqrt{12}$ of the actual strip pitch.

The charge of some strips can be incorrectly measured. These strips will not surpass the threshold even though a sufficient charge was induced. Those strips would not contribute to the cluster, and the mean position would be miscalculated. The reconstruction software allows inactivated strips inside a cluster if the contiguous strip to both sides is activated. One parameter is defining the number of neighbouring strips without a signal allowed inside a cluster. This number needs to be chosen low to avoid the reconstruction of fake clusters. This value is set to one in the used beam telescope. The particles in the beam can create particle showers when hitting surrounding material. Several products from a shower can hit a detector simultaneously creating multiple clusters. Those clusters are reconstructed separately, and an assignment to different particle trajectories is done at the track reconstruction.

The trajectories of the particles passing through the beam telescope are reconstructed from the calculated intersection points of each GEM readout plane. For the reconstruction, a straight flight path is assumed as no additional strong magnetic field is present, and the particle momentum is sufficiently high. Therefore, a linear function describes the trajectory.

The position on each plane is calculated with an uncertainty from the cluster reconstruction. A Kalman filter [121] is used to calculate a linear fit with consideration of the uncertainties of each point. The fit is performed in several iterations, and each iteration adds an additional point from the next detector layer. Two steps are performed in each iteration. First, an estimation of the path is done without considering the new point. In the second step, the new detection plane is added to the calculation. Finally, the difference between both fits is evaluated. A new linear approximation is afterwards calculated with consideration of the new information and its uncertainties.

The final linear fit is calculated after having iterated this approximation for each strip plane. A three-dimensional vector is calculated with origin in the first detector plane ($z = 0$). The particle impact at any DUT spot along the z-axis can be extrapolated from this vector.

An alignment of the GEM detectors with respect to each other and the trigger detectors is done to achieve a higher track accuracy. The mechanical alignment of the detectors is limited to the scale of a millimetre to several hundred micrometres. An additional software alignment of the detection planes is performed, which measures the offset and inclination of each detector plane and corrects the tracks. The fit residual for each iteration is calculated, and residual values variating from zero manifest a misalignment of one detector plane. The correction is manually done by changing offset parameters until the mean residual is zero. The mechanical support of the detectors is fragile, and movements of some micrometres can affect the reconstruction accuracy. A realignment is regularly performed after some measurements and especially after interventions at the set-up.

9.2 MCP-PMTs as a Time Reference

A reliable t_0 time reference detector is needed to measure the time resolution of the PICOSEC-Micromegas prototypes. MCP-PMTs by Hamamatsu (model r3809u-50 [122]) and Photek (model 240 PMT [123]) are used as a t_0 time reference detector for the PICOSEC-Micromegas measurements in the particle beam tests. These MCP-PMTs provide short signals with a

rise time[1] of 160 ps. Signals of this kind are well suited as a time reference for fast-timing detector studies. The calculation of the time resolution out of the PICOSEC-Micormegas signal and the t_0 time reference detector signal is explained in section 6.4.

The measured time resolution during the test beam is the combined time resolution of the reference detector and the DUT. The reference detector needs a time resolution significantly better than the expected time resolution of the DUT to minimise its impact on the measured time resolution. With this aim, the time resolution and its uniformity over the active area have been studied for the Hamamatsu MCP-PMTs. The results of this study have been published in [124, 9].

The MCP-PMT consists of a radiator, where particles generate Cherenkov light, a photocathode, where the light is absorbed and converted to electrons, and an MCP, where electrons are amplified. The operating principle of MCP-PMTs is presented in section 2.2. This specific MCP-PMT has a 3.2 mm thick synthetic silica window coupled to a 11 mm diameter photocathode. Other dimensions and materials are unknown. The propagation of Cherenkov light, including reflections and absorptions, has been analytically modelled simulated by a toy Monte-Carlo, to explain the observed radial dependence of the mean signal charge on time resolution. In the following, the different models will be explained, and the measured data will be compared to the results of the simulation.

9.2.1 Modeling of Cherenkov Light Propagation in the Radiator

When a particle passes through the MCP-PMT far from the photocathode centre, only part of the light reaches the photocathode as the Cherenkov cone is not fully projected onto it. Figure 9.7 shows a sketch of the Cherenkov cones on the photocathode with the assumed dimensions of the detector. A part of the light will be reflected or absorbed due to optical effects on the window surfaces. Part of these reflected light can later reach the photocathode and still contribute to the detector signal. An analytic geometric and a Monte-Carlo model have been developed to predict this amount of light and its effect in the time resolution.

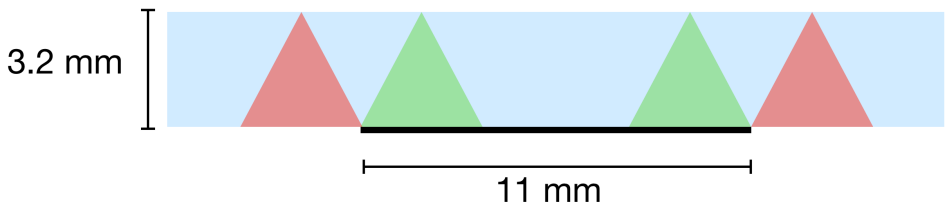

Figure 9.7: Schematic Cherenkov light cone propagation in the radiator, as assumed in the present model. The radiator has a thickness of 3.2 mm, and the photocathode a diameter of 11 mm. The green-coloured cones are fully projected onto the photocathode, while the projections of the red coloured cones are entirely outside of the photocathode area.

[1] 10 % to 90 % amplitude

Analytic Geometric Modeling

A geometric calculation of the overlapping areas of the photocathode and Cherenkov cone for particle impact points at different radii has been done, with and without considering reflections at the radiator and at the photocathode.

Figure 9.8 shows the overlap between the photocathode, the Cherenkov cone and the region where first-order reflected light from the Cherenkov cone would reach the photocathode plane. In this example, the perpendicularly incident particle is hitting the edge of the photocathode area (solid black line). The blue area shows the projected Cherenkov light on the photocathode, and the red area the light from the first-order reflection reaching the photocathode, which is the light that will have survived one reflection on the photocathode, and one on the opposite side of the crystal, before reaching again the photocathode. The part of light lost at each reflection is modelled by a weighting factor ($w < 1$).

The amount of light reaching the photocathode decreases with increasing particle impact radius with respect to the photocathode centre, due to the decreasing geometrical overlap. With this geometric model the relative amount of photons reaching the photocathode depending on the radius ($P_{\text{rel}}(r)$) is calculated by

$$P_{\text{rel}}(r) = \frac{A_{\text{blue}}(r) + w \cdot A_{\text{red}}(r)}{A_{\text{blue}}(0) + w \cdot A_{\text{red}}(0)} \,, \tag{9.1}$$

where $A_{blue}(r)$ and $A_{red}(r)$ are respectively the blue area (direct light) and red area (reflected light) and they depend on the radius to the photocathode centre. This function is scaled to the mean signal charge and w is a free parameter in the fit to the data.

Monte-Carlo Simulation of the Light Propagation

The former analytical geometrical calculation describes the radial behaviour of the signal amplitude well for small and large radii but is lacking precision for medium radii. Therefore, a simulation of the light propagation and conversion to charge in the fused silica radiator crystal has been carried out to model the radial amplitude behaviour. For this simulation, the photons are created as two-dimensional points on the window surfaces as objects in a C++ program. A random generator with a probability threshold decides, for each point, if the photon is reflected on the surface or not. If it is reflected, the new position on the opposite side of the window with respect to the Cherenkov angle is calculated. In the initial step, $25{\cdot}10^6$ photons have been randomly distributed over the radiator surface that carries the photocathode. Photons in the photocathode region can be either reflected or, if not reflected, they can be converted to charge or absorbed and thus lost. Outside the photocathode region, photons are lost after not being reflected. The same holds for photons on the opposite side of the radiator, i.e. at the air-radiator interface.

The results of this simulation give the x- and y-coordinates of the point where each photon is generated and where it leaves the crystal, either by transmission or absorption on the crystal surface. Another indicator is given for each photon if it has generated a charge in the photocath-

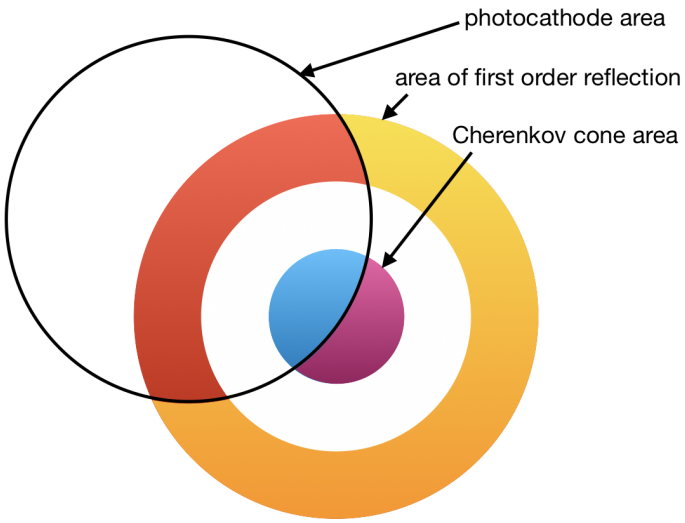

Figure 9.8: Sketch of the geometrical overlap between Cherenkov cone (blue and violet shaded areas) and first-order reflected light (red and yellow shaded areas) with the photocathode area (solid black line).

ode, which means that the photon has not been reflected or absorbed and ends on the area of the photocathode.

The simulation is controlled by the three probabilities for reflection at the photocathode, absorption at the photocathode if not reflected, and reflection at the air-radiator interface. These parameters have been determined from a χ^2 minimisation between simulation results and data.

Monte Carlo Modeling of the Radial Dependence of Time Resolution

The simulation of light propagation has been used as one possible model to quantitatively describe the radial dependence of the time resolution σ_t on the produced charge. It is based on the relation

$$\sigma_t^2 \propto \frac{\sigma_{\text{SPTR}}^2}{N_{\text{p.e.}}} , \tag{9.2}$$

where σ_{SPTR} is the single photoelectron time resolution of the detector and $N_{\text{p.e.}}$ is the number of photoelectrons generated at the photocathode. This relation is valid for MCP-PMTs, albeit without considering the spatial dependence [11]. We generalise this relation in the simulation by introducing, spatially resolved, absorption and reflection at the air-radiator interface and the photocathode.

As the exact quantum efficiency of the photocathode is unknown, we do not extract the number of produced photoelectrons from the simulation. Instead, the ratio between the number of generated photons (N) and those reaching the photocathode (N_x) after x reflections has been

used. The number of photoelectrons is linearly correlated to the amount of light reaching the photocathode. Therefore, it is valid to substitute this parameter and rescale Eq. (9.2) to show the correlation between the time resolution and the amount of light reaching the photocathode.

A distinction between photons reaching the photocathode directly (N_0) and those reaching the photocathode after exactly one reflection N_1 is made. The variance of the timing of one MCP-PMT is calculated by

$$\sigma^2_{\text{MCP1}} = \left(\frac{N_0}{N}\right)^2 \frac{A}{N_0} + \left(\frac{N_1}{N}\right)^2 \frac{B}{N_1} \,, \tag{9.3}$$

where N is the number of simulated photons reaching the photocathode, N_0 and N_1 are the number of photons reaching the photocathode after 0 or 1 reflections, respectively; A is a scaling factor correlated to σ^2_{SPTR}, $A = \sigma^2_{\text{MCP1}}(r = 0)$ in the center of the MCP-PMT, and B is the corresponding scaling factor for the reflected photons. The reflected photons will increase the signal arrival time jitter and may thus slightly worsen the timing resolution. B is defined as

$$B = \left(\sqrt{A} + \Delta\sigma\right)^2 \,, \tag{9.4}$$

with the additional parameter $\Delta\sigma$, introduced to this model to describe the impact of the reflected photons on the rising edge of the signal and therefore the SAT.

9.2.2 Characterisation with Beam Data

Two MCP-PMTs were operated at a nominal gain of $8{\cdot}10^4$ along with the PICOSEC-Micromegas detectors in muon beams at the CERN SPS secondary beamlines (see section 9.1). Each MCP-PMT was providing a time reference signal to one oscilloscope used for the data acquisition of the PICOSEC-Micromegas. The MCP-PMTs feature an unsegmented anode and thus cannot provide position information for the incident particle. Consequently, the tracking information from the beam telescope is used.

The spatial dependence of the mean signal charge has been evaluated from the charge and tracking information of each signal. The radial dependence of the mean signal charge relative to the centre of each MCP-PMT is shown in figure 9.9 for both MCP-PMTs. The results from the analytical geometric model with and without reflections and from the Monte-Carlo simulation are additionally shown. The signal charge decreases as expected with increasing distance from the MCP-PMT centre due to a decrease of the Cherenkov light reaching the photocathode. Maximum average signal charge is observed for tracks with the full cone contained in the acceptance of the photocathode. This can be observed in the inner 2.5 mm of the distribution, as expected for a Cherenkov cone radius of approximately 3 mm and a photocathode radius of 5.5 mm. Above $r > 2.5$ mm the mean signal charge starts decreasing, as part of the light coming directly from the Cherenkov cone starts falling outside the photocathode (see figure 9.7 in section 9.2.1). At radii above 8.5 mm, a linear decrease can be observed before it goes down to a constant background level. In this outer region, no light is directly projected on the photocathode. Only diffuse reflected light from the outer region of the Cherenkov window reaches the photocathode and generates a signal.

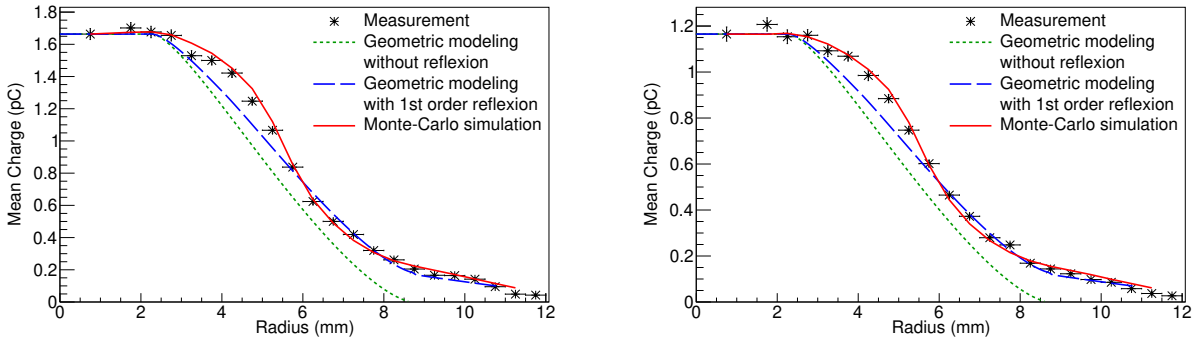

(a) MCP-PMT 1

(b) MCP-PMT 2

Figure 9.9: The radial distribution of the average signal charge for the two MCP-PMTs is shown. Both MCP-PMTs are operated at 2800 V. The green dotted curve shows the expected distribution by geometrical calculation without including reflections, and the blue dashed line shows the geometrical calculation after including first-order reflections. The red line shows the distribution expected from a dedicated simulation that includes the detector characteristics.

The green dotted line in figure 9.9 shows the overlap between the Cherenkov cone and photocathode without considering any reflection, using the geometric modelling and scaled to the mean signal charge at $r = 0$; it shows an agreement with the data for small radii, but it underestimates the signal charge for events at larger radii. For the blue dashed line, first-order reflections, are added to the geometrical calculation, with fitting the weighting factor to $w = 0.08$; the curve shows an agreement with the data in the outer part of the window ($r > 6\,\text{mm}$). In this region, the reflected light dominates the signal.

The red curve shows the result of the Monte-Carlo simulation. From a χ^2 minimisation the reflection probability on the photocathode is determined to be 0.2 ± 0.03, the absorption probability at the photocathode is 0.4 ± 0.05, and the reflection probability at the air-radiator interface is 0.8 ± 0.002. All of these parameters are correlated with each other.

The same model parameters can describe the radial distribution for both MCP-PMTs by scaling the model output to the different mean signal charges in the centre of the photocathode. More refined models with precise knowledge on the MCP-PMT materials and including signal formation processes might yield different results.

Time Resolution

The time difference of the SAT of both MCP-PMTs results in a Gaussian like distribution (figure 9.10), whose standard deviation gives the time resolution of the measurement (σ_{tot}). In the inner area a combined time resolution of $\sigma_{\text{tot}} = 7.2 \pm 0.1$ ps has been measured. This value is the combination of two independent MCP-PMT resolutions (σ_{MCP1}, σ_{MCP2}) and the contribution of the read-out electronics (σ_{DAQ}), calculated in section 6.4. The resulting expression of σ_{tot} is defined

as

$$\sigma_{\text{tot}} = \sqrt{\sigma^2_{\text{MCP1}} + \sigma^2_{\text{MCP2}} + \sigma^2_{\text{DAQ}}}\,. \tag{9.5}$$

Only the combined time resolution of both MCP-PMTs (σ_{MCP}) will be estimated, as the two MCP-PMTs may not have identical performance. Two effects may contribute to different responses of the MCP-PMTs: The first one is a possible misalignment between detectors which has been measured to be 0.38 ± 0.01 mm, given by the 2D-distance between the MCP-PMT centres with the tracking data from the beam telescope. A second possible contribution is a different gain or quantum efficiency of both detectors. In fact, the mean signal amplitude of MCP-PMT 2 is 30 % smaller than that in MCP-PMT 1 and the resulting response of the two MCP-PMTs may also differ. Since the available dataset does not allow for a determination of these effects on the time resolution, the combined time resolution will be estimated as an upper limit for both MCP-PMTs, while the actual timing performance of each MCP-PMT is better. The resulting combined time resolution (σ_{MCP}) is obtained from equation 9.5 as

$$\sigma_{\text{MCP}} = \sqrt{\sigma^2_{\text{MCP1}} + \sigma^2_{\text{MCP2}}} = \sqrt{\sigma^2_{\text{tot}} - \sigma^2_{\text{DAQ}}}\,. \tag{9.6}$$

If the two MCP-PMTs behaved similarly, a time resolution of $\sigma_{\text{MCP}}/\sqrt{2}$ would be expected for each MCP-PMT individually.

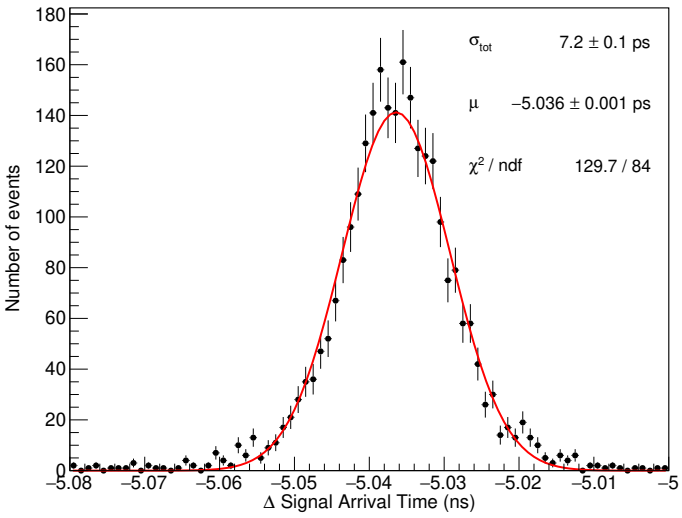

Figure 9.10: The standard deviation of the signal arrival time difference of both MCP-PMTs defines the combined time resolution (σ_{tot}) of the measurement. This distribution considers only particles passing through the inner 11 mm diameter of the first MCP-PMT. In this area a combined time resolution of 7.2 ± 0.1 ps is measured for a Gaussian fit (red line).

Spatial Dependence of the Time Resolution

Different regions of interest (ROI) of the MCP-PMT surface are defined, to calculate the time resolution. Figure 9.11 gives an overview of the different coloured ROIs on the active area of the MCP-PMT. The ROIs are defined by the geometrical overlapping of the Cherenkov cone and the photocathode. Only the size of the cone projected on the window surface is taken, and no further reflections are considered. The cone diameter and the photocathode diameter are chosen as 3 mm and 11 mm, as given by the radial charge distribution (see section 9.2.2). The green ROI ($r < 2.5\,\text{mm}$) in the centre of the MCP-PMT is defined as the area a particle can pass through the detector, and the full Cherenkov cone is projected onto the photocathode. The most prompt light, without reflection, would reach the photocathode and the best time resolution is expected in this region. The second region (blue) is a ring around the centre of the MCP-PMT with the radius of the photocathode ($r_{\text{photo}} = 5.5\,\text{mm}$) and the diameter of the Cherenkov cone ($r_{\text{cone}} = 3\,\text{mm}$) added to both sides. Particles in this region will at least overlap with a fraction of the Cherenkov cone on the photocathode. The outer ROI (red) is the area of the Cherenkov radiator that is so far outside from the photocathode ($r > 8.5\,\text{mm}$), that the light generated needs to reflect at least one time to reach the photocathode. The approach of choosing these ROIs is similar to the geometrical modelling described in section 9.2.1.

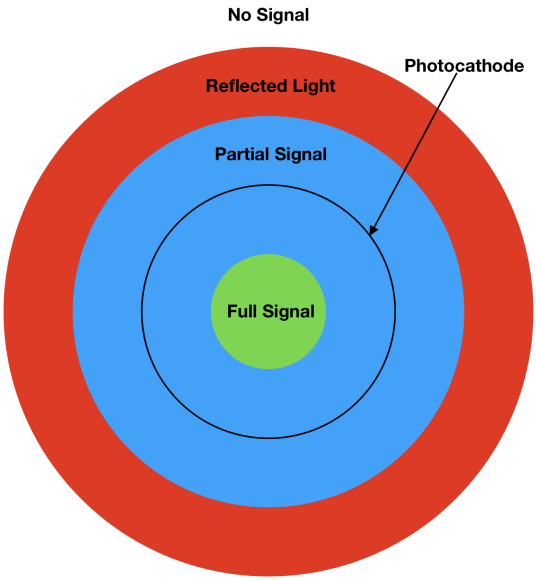

Figure 9.11: The MCP-PMT active area is divided into three ROIs.

The time resolution for particles passing through each area has been calculated. The ΔSAT distribution for each ROI is shown in figure 9.12. Only the σ of the Gaussian fit is given and not the actual time resolution of the detector. The given values contain the time resolution of both MCP-PMTs and the time jitter of the DAQ. Particles in the inner ROI (green) provide the best time resolution with $\sigma_{\text{Full}} = 5.74 \pm 0.20\,\text{ps}$, which is better than the result for all particles passing in the inner 11 mm diameter with $\sigma_{11\,\text{mm}} 7.2 \pm 0.1\,\text{ps}$. The time resolution of the other ROIs degenerates

significantly with $\sigma_{\text{Part}} = 14.68 \pm 0.64\,\text{ps}$ in the blue ROI and $\sigma_{\text{Refl.}} = 27.17 \pm 0.71\,\text{ps}$ in the red ROI.

This result indicates the importance of the prompt Cherenkov light without reflections for the time resolution. A Monte-Carlo guided fit of this model on the impact of the reflected light on the radial time resolution is presented in the next section.

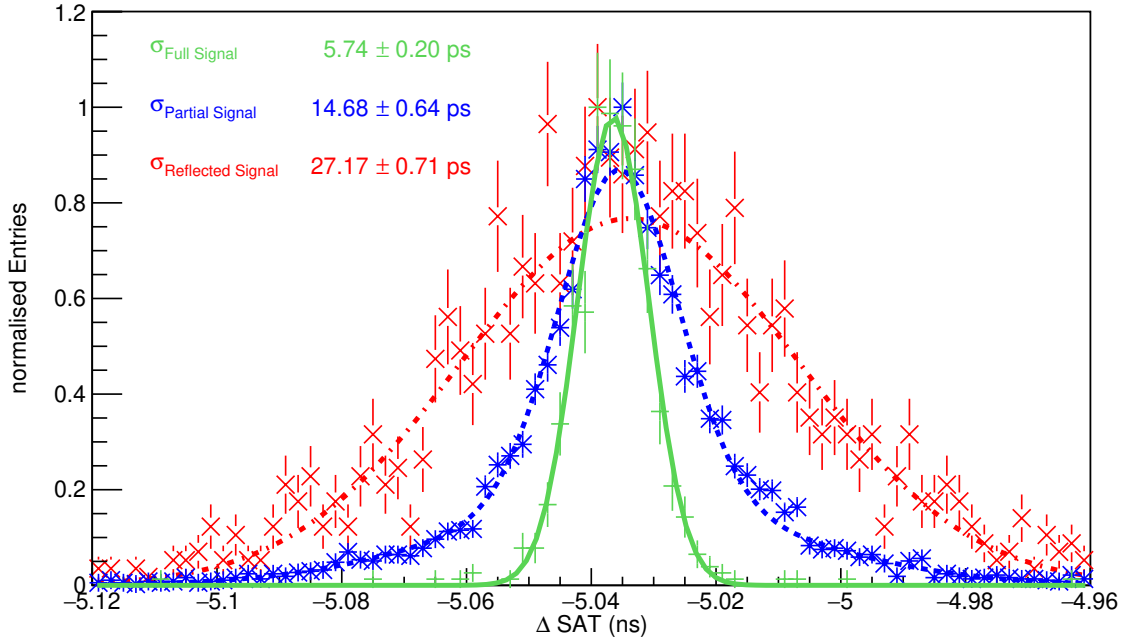

Figure 9.12: The time resolution for particles passing the detector in the three ROIs is calculated independently. The time resolution improves with a higher overlapping of the Cherenkov cone and the photocathode.

Modelling of the Time Resolution

In the following, the time resolution of the MCP-PMTs as a radial function of the particle impact point is discussed and compared with the simulated model. Events are grouped according to their impact radius such that the statistics of events, hitting each ring-like area is equal and the time resolution is then independently calculated for each group. Figure 9.13 shows the combined time resolution σ_{MCP} as a function of the distance with respect to the centre of MCP-PMT 2.

The combined time resolution is better than 10 ps in the inner radius of $r < 4\,\text{mm}$. Beyond that, the time resolution starts gradually degrading up to several tens of picoseconds. This result is consistent with the measured signal mean charge. In the inner radius of 2.5 mm, the full Cherenkov light cone is entirely projected on the photocathode, and the signal pulse amplitude is maximal in this region. As the impinging particles are further away from the centre of the MCP-PMT, the mean signal charge is reduced and the time resolution degrades.

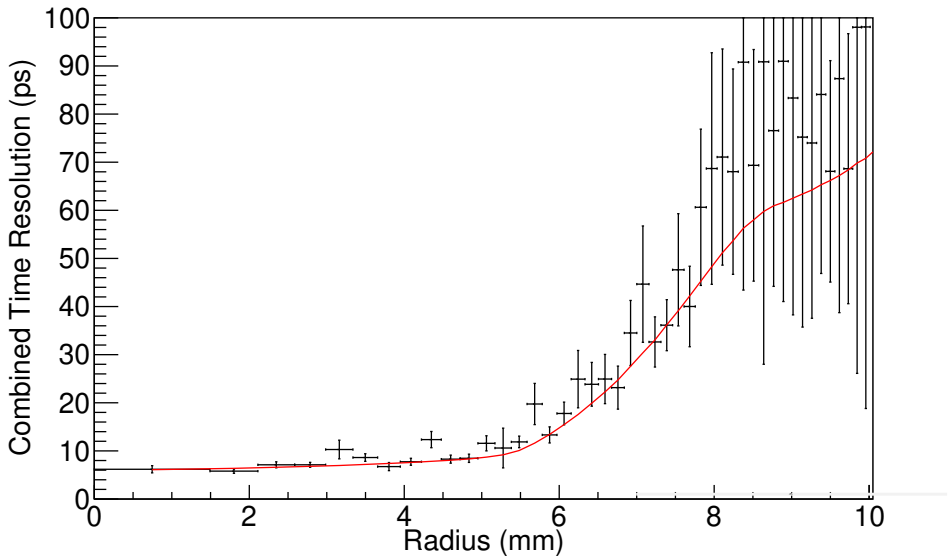

Figure 9.13: Combined time resolution as a function of the track impact point distance from the photocathode centre. The red line shows a possible modelling using results from the Monte-Carlo simulation, as explained in section 9.2.1.

The red curve in figure 9.13 shows the results of the Monte-Carlo simulation (see Eq. (9.3)) described in section 9.2.1. The simulation results reach an optimal agreement to the observed data for $\Delta\sigma = 7.5\,\text{ps}$. The additional spread for the reflected photons of both MCP-PMTs $\Delta\sigma$ must not be confused with the time delay of the reflected photons, which is on the order of $\sim$ 40 to 45 ps. $\Delta\sigma$ depends on the probabilities for reflection and absorption used in the Monte-Carlo model of the charge distribution.

9.2.3 Photek 240 PMT

A Photek 240 PMT was available during some beam measurement campaigns. It has an active area of 40 mm diameter and consists of two microchannel plates in one cylindric volume [123]. This detector was especially helpful for the multi pad studies presented in section 12.3, as it fully covers up to four hexagonal pads within its inner active area.

The upper limit time resolution of the Photek 240 PMT is determined during the beam test with the help of one Hamamatsu r3809u-50. A full study of the radial dependence of the time resolution was not performed, as the availability of the Photek 240 PMT was limited during the beam tests. A similar spatial dependence of the time resolution is expected as for the Hamamatsu MCP-PMT, because its detection mechanism is based in the same way on a Cherenkov window and a photocathode in front of the multichannel plates. Both MCP-PMTs are placed in the beam telescope and centred to each other. The SAT difference for particles hitting both detectors in the inner area (r<5.5 mm) is calculated and presented in figure 9.14, fitted to a Gaussian distribution. The standard deviation of the distribution is fitted with a Gaussian function to $\sigma_{\text{tot}} = 8.0 \pm 0.1\,\text{ps}$.

This is the combined time resolution of the system, which includes the time resolution of the Hamamatsu MCP-PMT in the inner area and the DAQ time resolution ($\sigma_{\text{DAQ}} = 2.18 \pm 0.03$ ps; see section 6.4). σ_{tot} is slightly higher than the combined time resolution of two Hamamatsu MCP-PMTs ($\sigma_{\text{Ham}} = 7.2 \pm 0.1$ ps; see section 9.2.2), but significantly under 10 ps. It is expected, that the contribution of the Photek MCP-PMT is not much different to that of the Hamamatsu MCP-PMT when time resolutions of PICOSEC-Micromegas signals in the order of >20 ps are measured.

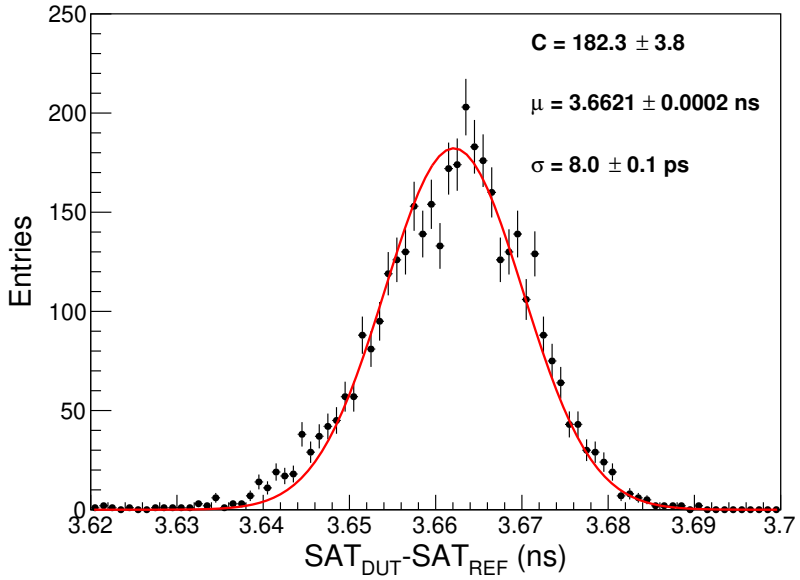

Figure 9.14: The distribution of the SAT difference between the Photek 240 PMT and one Hamamatsu r3809u-50 gives a combined time resolution of $\sigma_{\text{tot}} = 8.0 \pm 0.1$ ps for the central area of both detectors.

10 Time Resolution for MIPs

Contents

PICOSEC-Micromegas detectors with different mesh types are tested in the muon beam to give a proof-of-principle of the detector concept for the detection of MIPs. Most characterisation studies of the PICOSEC-Micromegas are performed with bulk Micromegas and with a woven mesh of 45 µm aperture and 18 µm wire diameter. The transit time of electrons moving through the mesh and the mesh transparency may have an impact on the detector gain and SAT of the detector and thus on the achievable time resolution. The following results present the measured time resolution of PICOSEC-Micromegas prototypes with Micromegas detectors produced in bulk technologie, with a woven and an electroformed mesh structure (thin-mesh), as well as with a microbulk Micromegas. A detailed description of the different Micromegas technologies can be found in section 4.1. All presented results have been obtained with the first PICOSEC-Micromegas prototype (see section 5.3.1) and are operated in the same conditions with the "COMPASS" gas mixture of neon (80 %) - ethane (10 %) - CF_4 (10 %). The data acquisition and waveform analysis performed for these measurements are explained in section 6.

10.1 Woven mesh

The first proof-of-concept measurement was performed with a bulk Micromegas and a woven mesh with a drift region of 200 µm and an amplification region of 128 µm, measured from the centre of the mesh. The best measured time resolution is 24.0 ± 0.3 ps, which is achieved with the woven mesh and voltage settings of $U_{\text{Drift}} = -475$ V and $U_{\text{Anode}} = +275$ V, see figure 10.1. Compared to the laser tests, the quantum efficiency of the photocathodes plays an important role in the measurement of MIPs, as the particles are generating a certain amount of photons in the Cherenkov radiator. The highest measured quantum efficiency is reached with 18 nm CsI photocathodes on a 3.3 nm chromium substrate. With a 3 mm thick Cherenkov radiator and 150 GeV muons this photocathode reaches up to 10.4 ± 0.4 photoelectrons per muon [5]. The number of photoelectrons is determined, similar to the laser measurements, by comparing the charge distribution of the signals from the muons with the distribution from single photoelectron signals

generated by a UV lamp. Figure 10.2 gives the charge distributions measured for the photocathode used for the measurements of the woven mesh.

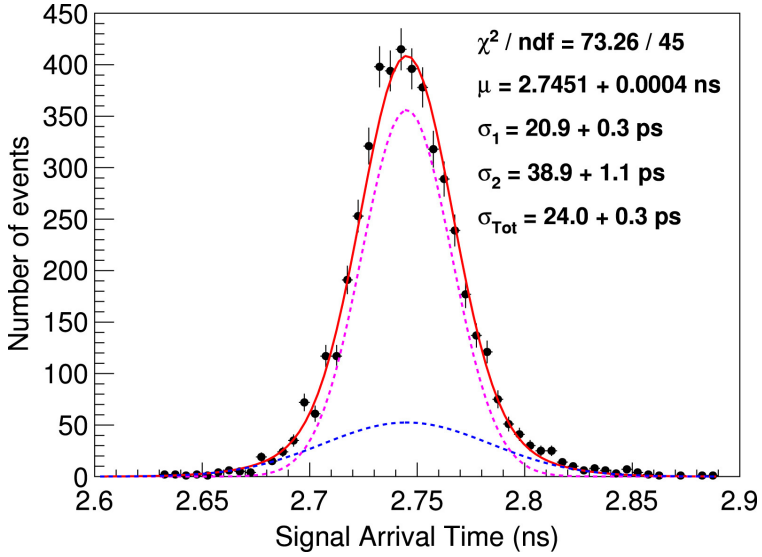

Figure 10.1: Best measured time resolution with a bulk detector with a woven mesh.

The detector is tested in different drift and amplification fields, and for several fixed amplification fields a scan of the drift field starting from the highest stable value is performed, with the results shown in figure 10.3. The best time resolution is achieved in the highest drift field to amplification field ratio and the highest preamplification. The time resolution deteriorates with lower fields, while a reduction of 25 V decreases the detector gain of a factor of $\sim$2. With higher amplification fields and lower drift field, a higher total field can be applied to the detector (see $U_{\text{Anode}} = 375\,\text{V}$ and $U_{\text{Anode}} = 350\,\text{V}$), but the time resolution saturates at higher values. For even lower amplification fields (see $U_{\text{Anode}} = 250\,\text{V}$) the detector starts to spark earlier in the field scan and the same gain and time resolution as with the other anode settings is not reached.

10.2 Thin-mesh

The first PICOSEC-Micromegas prototype chamber (see section 5.3.1) can be alternatively equipped with a bulk Micromegas manufactured with an electroformed "thin-mesh" instead of a woven inox steel mesh. A mesh with uniform thickness, instead of the alternating thickness of the overlapping woven wires is used. The presented results are obtained with an electroformed mesh with a pitch of 106.5 µm and a wire thickness of 37 µm leading to optical transparency of 43 %.

The amplification and drift region distances are fixed at 128 µm and 200 µm. A field scan with four fixed amplification voltages and variable drift voltages is performed. The highest possible, stable drift voltage is selected for each fixed amplification voltage setting (215 V; 250 V; 275 V; 300 V) and measurements are performed for these settings and for up to three consecutive settings

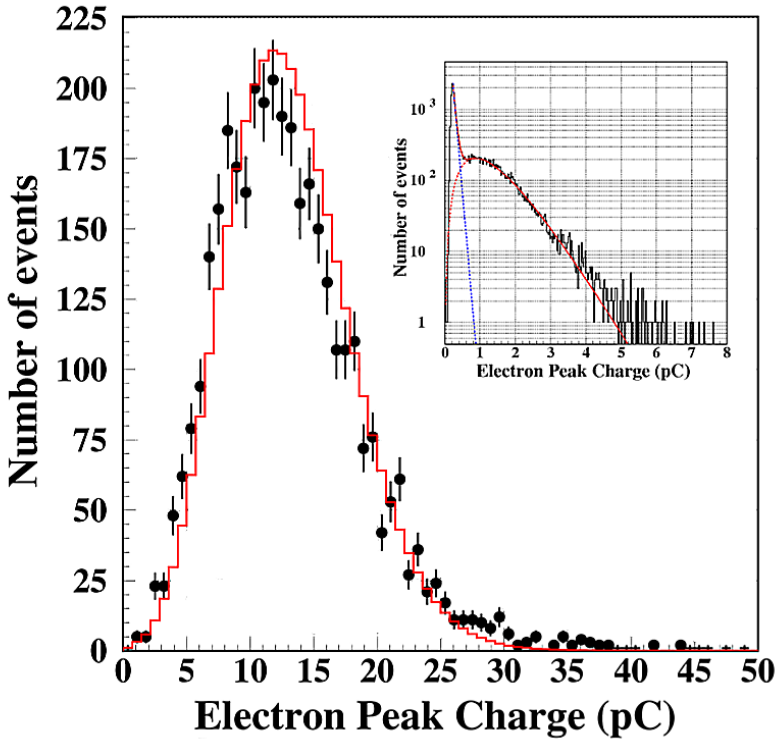

Figure 10.2: The efficiency of the photocathode used for the woven mesh measurements (∼10 $N_{\text{p.e.}}/\mu$) is determinded by the ratio of the mean signal size from muons and the mean single photoelectrons signal size generated by an UV lamp (inset).

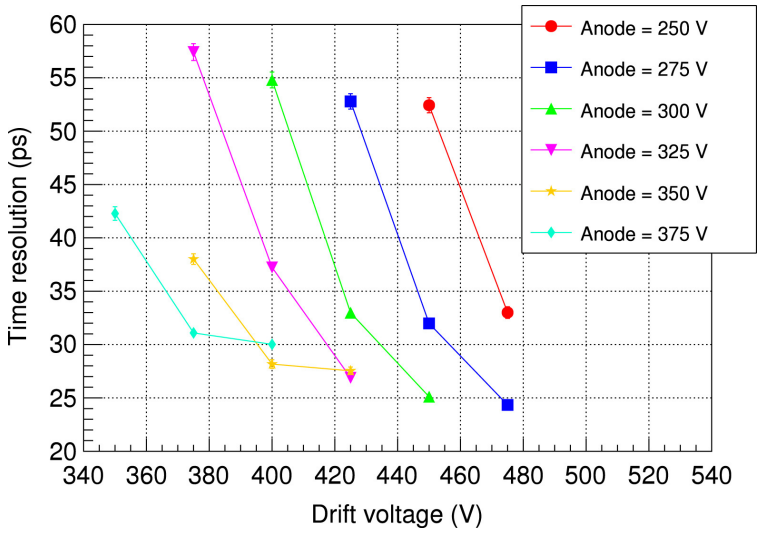

Figure 10.3: Time resolution for different electric fields measured with a woven bulk mesh.

at a reduced drift voltage in steps of 25 V. The result of the time resolution for this field scan is presented in figure 10.4. The quantum efficiency of the CsI photocathodes variates during production

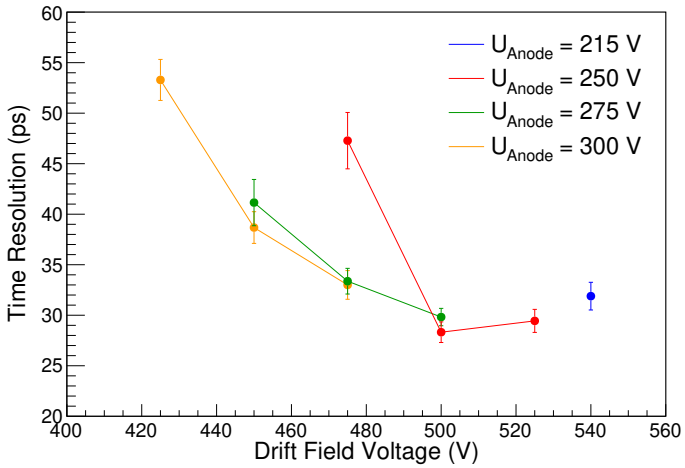

Figure 10.4: Time resolution obtained with a thin-mesh bulk Micromegas for different electric fields in a muon beam with a 6.9 ± 1.7 p.e. photocathode.

and the 18 nm thick CsI photocathode used for this scan provides only 6.9 ± 1.7 photoelectrons in the muon beam. The thin-mesh Micromegas shows the same time resolution behaviour as the woven mesh Micromegas. A better time resolution can be achieved with a higher total gain or higher preamplification field for similar detector gains. The best time resolution achieved in this measurement is 28.0 ± 1.0 ps at $U_{Anode} = 250$ V and $U_{Drift} = 500$ V. Similar to the woven mesh, a further increment of the drift voltage does not improve the time resolution, as the spark limit is reached.

A measurement with a $\sim$10 photoelectron photocathode is not available and a direct comparison with the best possible measured time resolution in a muon beam of 24 ps [5] is not possible. As mentioned before in section 6.3, the relation between the time resolution (σ_N) and the number of photoelectrons $N_{p.e.}$ is following an inverse square-root proportionality as

$$\sigma_N = \frac{\sigma_1}{\sqrt{N_{p.e.}}}, \tag{10.1}$$

with σ_1 the single photoelectron time resolution. Under this consideration, the possible time resolution of the thin-mesh with the same performant photocathode is slightly better than the time resolution with a woven mesh with $\sim 22.8 \pm 0.8$ ps. Anyhow, both values are compatible if we include the systematic errors introduced by the detector stability and gas quality.

10.3 Microbulk

A second alternative Micromegas technology tested in a prototype is the microbulk Micromegas. The capacitance of a microbulk is higher due to its different production technique with a shorter amplification region (50 µm) and the space filled with Kapton (see sec-

tion 4.1). The higher capacitance changes the way the signal gets induced in the read-out. The sharp and separated electron peak of the bulk and classical Micromegas signal gets prolongated and merged with the pronounced ion tail. Figure 10.5 shows a Monte-Carlo modelling of a microbulk Micromegas signal (black) with the individual components (electron peak in blue; ion tail in red) [125]. The simulated signal shows that the rising edge is composed of the rising edge of the electron peak and a contribution from the ion tail. The actual waveform acquired with the microbulk prototype shows the same characteristics as the modelled waveform. Figure 10.6a shows an example waveform of the prototype acquired in the muon beam.

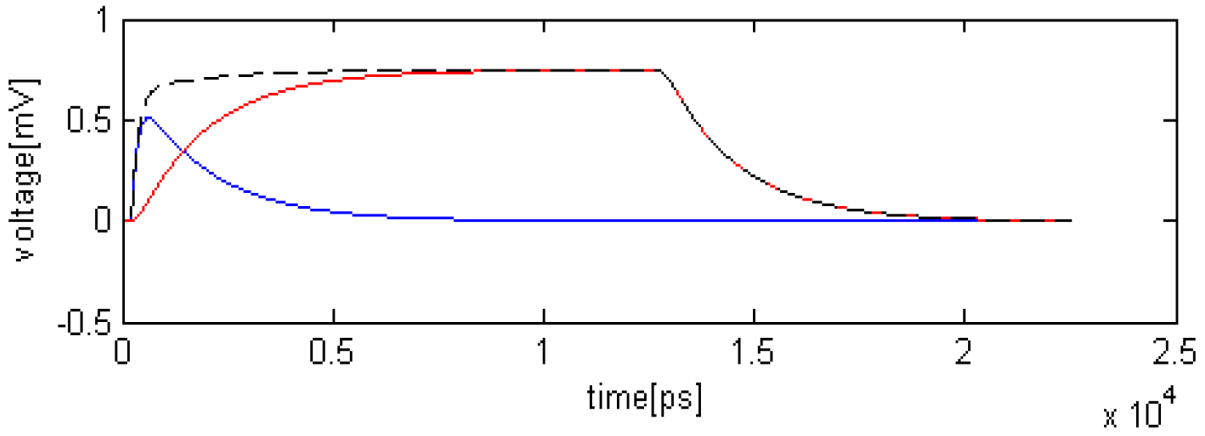

Figure 10.5: Monte-Carlo modelling of a microbulk signal waveform. The blue line represents the electron contribution and the red line the ion contribution to the signal. The black dashed line is the total signal. The model includes the microbulk capacity (35 pF) and the bandwidth limit of the read-out electronics. Figure extracted from reference [125].

This waveform characteristic requires a particular modification of the waveform analysis and the extraction of the SAT. The SAT is calculated by fitting the same logistic function to the rising edge of the electron peak as described in section 6.4, but the definition of the fit start and endpoint is more challenging with the microbulk signals. Figure 10.6b shows a zoom on the rising edge of the example waveform and the fit of the electron peak as a red line. The regular signal waveform analysis would use the global maximum as the fit endpoint, but this procedure does not work well for a microbulk signal. Instead, the saddle point of the waveform function, between the rising edge of the electron peak and the ion tail, is used as fit endpoint.

The saddle point of the rising edge for each waveform is calculated by an algorithm that uses the first and second-order derivative of the waveform. An example of one recorded microbulk waveform, and its derivations are shown in figure 10.7. The maximum of the first derivation (figure 10.7b) gives the inflexion point of the rising edge. The location of the maximum is used then as starting value for the parameter P_3 of the fit function. The second differentiation of the waveform (figure 10.7c) defines the start and endpoint of the fit with the location of the minima and maxima. The amplitude of the waveform at the endpoint and start point position is additionally

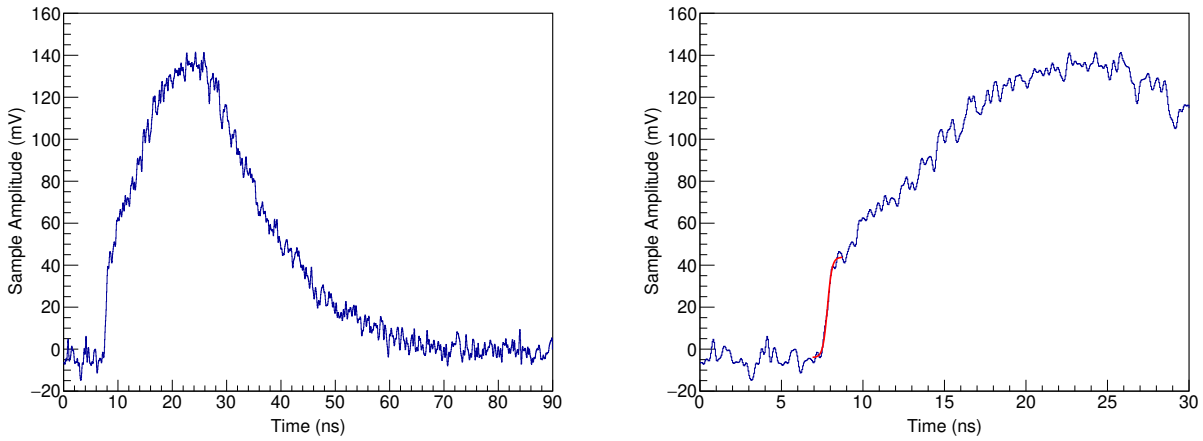

(a) Typical microbulk waveform

(b) Sigmoid fit of the rising edge

Figure 10.6: The PICOSEC-Micromegas with microbulk technology has a higher capacitance and the ion tail dominates. Only the rising edge of the electron peak needs to be fitted with a sigmoid fit to determine the SAT.

used as initial values of the fit parameter P_0 and P_1. A successful fit of the example waveform is shown in figure 10.7a.

The noise and the waveform oversampling have to be also considered at the first differentiation of the waveform. The first derivation of the waveform is smoothed out, and higher frequency contributions to the waveform are cut. In the end, only larger waveform structures, like the saddle point after the electron peak, contributing to the shape of the differentiation.

Figure 10.8 shows the time resolution for different electric fields. As the microbulk amplification region is 50 µm thick (see section 4.1), the amplification voltage is lower to achieve a comparable electric field. The measured time resolution of the microbulk detector is worse than the thin-mesh or woven mesh Micromegas time resolution, even if scaling with the quantum efficiency of the photocathode (7.4 ± 0.1 p.e.). Moreover, the measured time resolution is not saturating at higher electric fields, and the detector was stable with up to 700 V applied to the drift region.

10.4 Summary

Table 10.1 gives an overview of the results for the different mesh technologies. The tested microbulk Micromegas perform worse as a fast-timing detector than the bulk Micromegas alternatives. The main limitation of the microbulk detector is the higher capacity between the mesh and the anode, which deforms the waveform shape and makes necessary an advanced analysis algorithm for the calculation of the SAT. Depending on the future application with demand in the time resolution in the order of some 100 ps, microbulk technology can still be of interest due to its superior energy resolution [61] and its flatness that allows a deposition of CsI on the mesh for reflective operation (see section 4.2.4). Both bulk detectors, with thin-mesh and with

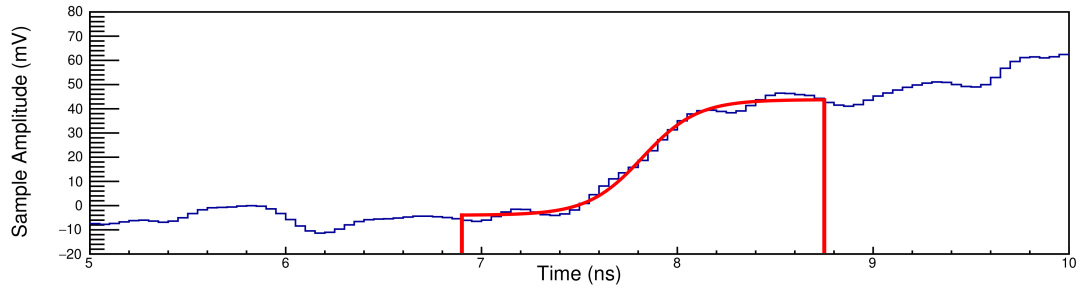

(a) Sigmoid fit of the rising edge

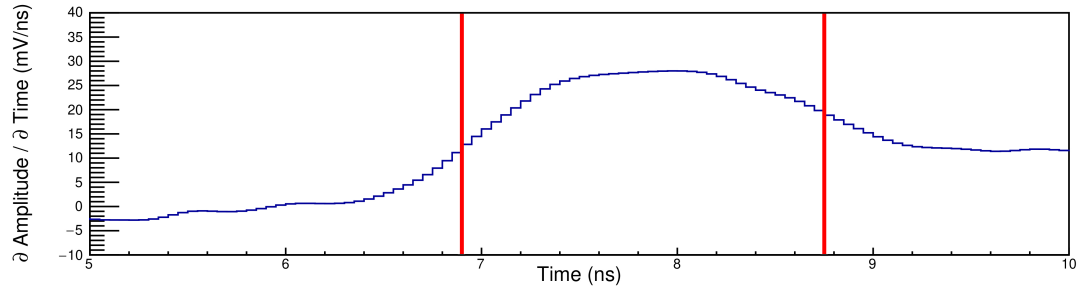

(b) First derivation of the waveform

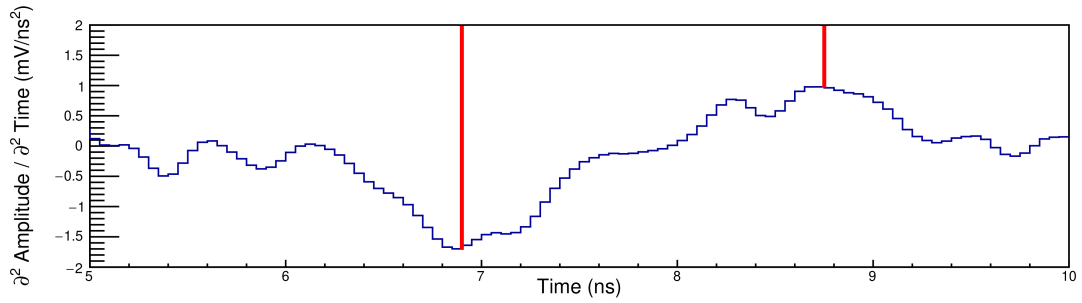

(c) Second derivation of the waveform

Figure 10.7: The start and endpoints of the sigmoid fit are selected according to the minima and maxima of the second derivation. The first derivation is calculated for each point by linear interpolation with the surrounding 50 points.

woven mesh, perform similarly in the beam measurement after correcting the different quantum efficiency of the photocathodes, with a slightly better performance of the thin-mesh. This result is expected, as a thinner mesh without wire crossings should create a more homogenous electric field and thus improving the time resolution. Moreover, the modelling of the detector (see chapter 7) showed the woven mesh contributing a constant delay of 130-150 ps (see table A.2) to the SAT without significantly impacting the time jitter, and thus the actual thickness is not impacting the time resolution

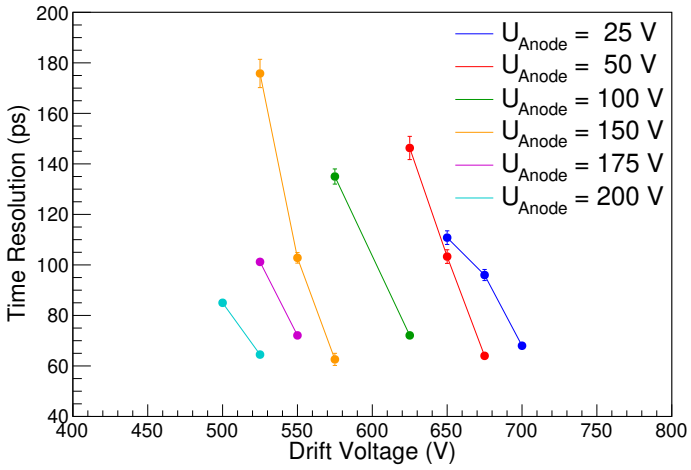

Figure 10.8: Microbulk time resolution for different electric fields in a muon beam with a 7.4 ± 0.1 p.e. photocathode.

Table 10.1: Summary of the measured time resolution for different Micromegas mesh technologies.

	Woven Bulk	Thin-mesh Bulk	Microbulk
Measured time resolution (ps)	24.0 ± 0.3	28.0 ± 1.0	62.6 ± 2.4
Number of photoelectrons	10.4 ± 0.4	6.9 ± 1.7	7.4 ± 0.1
Field settings A / D (V / V)	$+475 \,/\, -275$	$+500 \,/\, -250$	$+575 \,/\, -150$
Time resolution for 10.4 p.e. (ps)	24.0 ± 0.3	22.8 ± 0.8	50.1 ± 2.0

11 Resistive Read-out

Contents

The goal of the PICOSEC-Micromegas project is the development of a fast-timing detector for high-rate environments like the HL-LHC with an expected luminosity of ∼5-10 x 10^{34} $cm^{-2}s^{-1}$ [3]. A resistive detector design is necessary to operate the PICOSEC-Micromegas in such environment with high electric fields, as the spark probability increases with higher detector gain [126]. The spark rate of the detector can be reduced by adding a resistive layer on top of the anode, which reduces the discharge current, and the spark propagation between the mesh and the anode is limited [72].

Resistive PICOSEC-Micromegas prototypes are developed and presented in this chapter. Two different resistive Micromegas technologies have been tested: bulk resistive strip in two configurations with 82 MΩ/□ and 292 kΩ/□, and floating strip anode with a 25 MΩ discrete resistor. A detailed description of the prototypes is given in the following section, while the time resolution for MIPs in muon beam is presented. The chapter is completed with the measurement of the ion-backflow and the degradation of the CsI photocathode. The results from the following chapter have been published in [127]. Furthermore, the outcome of this test leads to the development of the resistive multipad (see section 12.4).

11.1 Resistive Prototype

The resistive prototype chamber was constructed to host the same size detector and radiator as the first prototype. This chamber is conceived for a longtime operation in sealed mode and has a more spacious design in comparison to the first prototype chamber. The inner construction of the mechanics to hold the Micromegas and the crystal are similar to the first

prototype. A more robust flange with a copper o-ring seals the chamber. It improves the vacuum tightness and reduces the outgasing to maintain a good gas quality over longer time periods in sealed operation mode. This chamber is mainly used to study different resistive anodes and is therefore refered to as the resistive PICOSEC-Micromegas.

Figure 11.1 shows the resistive prototype chamber mounted in the beam telescope (see section 9.1). It has an integrated pressure sensor (red box on top) to connect to a pressure monitoring system. The handling and installation of this chamber are delicate in comparison to the first prototype chamber due to its additional weight and its bulkier size.

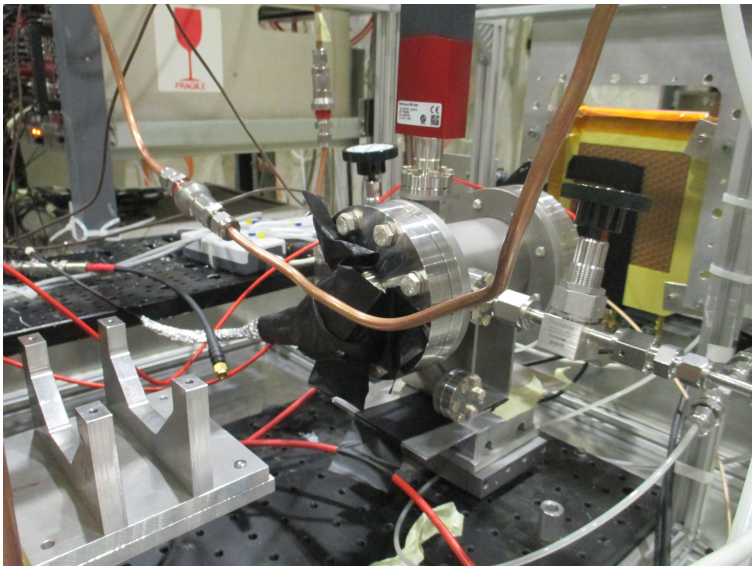

Figure 11.1: Photograph of the resistive prototype chamber mounted in the beam telescope. An UV-LED (black tape) is placed in front of the window to perform a single photoelectron calibration.

The first prototype is based on the Muon ATLAS MicroMegas Activity (MAMMA) R&D project [128]. It consists of a standard bulk Micromegas structure with an 18 µm thick copper anode plane covered by two protection layers: a 64 µm thick layer of an insulator (DuPont Pyralux PC1025) on top of which a resistive layer is deposited. The resistive layer consists of a compound of phenolic resin with an addition of carbon powder. The percentage of added carbon regulates the resistivity and the PICOSEC-Micromegas prototype is tested with two different layers with a resistivity of 292 kΩ/□ and 82 MΩ/□ on a round anode with 1 cm diameter. This resistive layer is grounded at one extremity through an anode section with higher resistivity, equivalent to a discrete resistor of 10-50 MΩ in series. Figure 11.2 illustrates the principle of this read-out.

The second resistive detector technology consists of an amplification region formed by a micro-mesh and a copper anode. This method is also known as the “floating strip” resistive Micromegas [120]. The anode plane is connected to high-voltage via a resistor with a resistivity of more than 20 MΩ. The signals are not read on this copper plane, but on a second plane, so-called read-out plane, situated under the copper anode. Figure 11.3 illustrates this resistive readout concept. Signals induced in the read-out plane are decoupled by a small high-voltage resistant

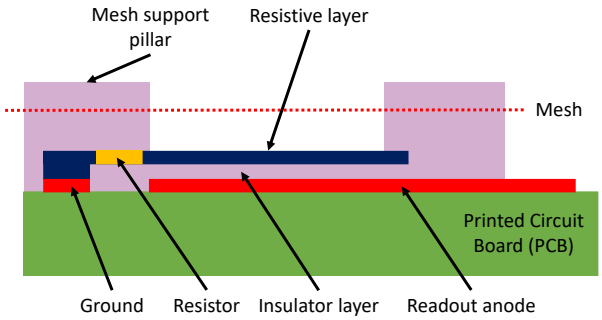

Figure 11.2: Sketch of the resistive Micromegas configuration, described in detail in the text. The scale of some components is exaggerated for clarity. The figure is adapted from reference [72].

capacitor with a value of the same order of magnitude as the anode-readout capacitance. This configuration leads to a loss of signal but enables a robust discharge suppression. One read-out of this type has been tested, with a resistance of 25 MΩ.

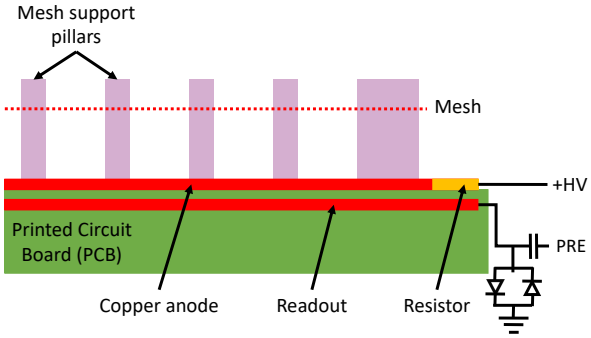

Figure 11.3: Sketch of the floating strip readout, described in detail in the text. The scale of some components is exaggerated for clarity. The figure is adapted from reference [120].

11.2 Time Resolution in Muon Beam

The time resolution of the resistive prototypes is measured in the CERN-SPS muon beam (see section 9.1) with a CsI photocathode to compare its performance with the non-resistive detectors. The best-measured values are summarized in table 11.1. The different technologies did not achieve the same time resolution. The bulk resistive strip anodes could only reach up to 34.8 ± 0.5 ps in the muon beam with the lowest resistivity. The floating strip detector reached 28.8 ± 0.2 ps, a value close to the non-resistive detector within the same conditions (24.0 ± 0.3 ps).

The worse performance in timing cannot be only attributed to the resistive layer as the photocathode performance was also worse for those two cases where the number of photoelectrons was calculated. For the floating strip detector, no estimation of the number of photoelectrons has

been performed. It is expected that the quantum efficiency of the photocathode is in the same order than the one used for the other resistive detectors. All resistive detectors have been measured during the same beam test with photocathodes produced in one bunch.

The correlation of the number of photoelectrons ($N_{p.e.}$) and the time resolution (σ) proportional with $\sigma \approx 1/\sqrt{N_{p.e.}}$. In table 11.1 the measured results corrected to the expected values at a single photoelectron are shown. The resistive strip detectors are still performing worse than the bulk Micromegas, yet the difference is far smaller than a factor ∼2. The resistive strip with lower resistivity (292 kΩ) performs with a single photoelectron time resolution of 97.8 ± 1.7 ps better than the one with higher resistivity (82 MΩ) with a single photoelectron time resolution of 114.1 ± 2.2 ps. The floating strip detector has a comparable performance to the non-resistive detector with an estimated single photoelectron time resolution of ∼80 ps, assuming that the photocathode had a quantum efficiency of ∼8 $N_{p.e.}$.

Table 11.1: The type of Micromegas detector, the mean number of photoelectrons ($N_{p.e.}$), the best time resolution and the optimum operation point (anode and drift voltage) of the PICOSEC detectors tested in beam tests. In all cases, the crystal was composed of a 3 mm-thick MgF_2 and a 5.5 nm-thick chromium layer, and the photocathode was a 18 nm-thick CsI layer. Analysis done with the support of [129].

Readout	Resistivity	$N_{p.e.}$	Time Res. (σ) (ps)	σ_0 (ps)	Anode/Drift (V/V)
Bulk	—	10.4 ± 0.4	24.0 ± 0.3	77.4 ± 1.4	+275/-475
Resistive strip	82 MΩ/□	7.6 ± 0.4	41.4 ± 0.6	114.1 ± 2.2	+300/-525
	292 kΩ/□	7.9 ± 0.2	34.8 ± 0.5	97.8 ± 1.7	+300/-475
Floating strip	25 MΩ	—	28.8 ± 0.2	—	+300/-500

A scan over a wide range of voltage settings is shown in figure 11.4 for the resistive strip with 82 MΩresistivity (left) and the floating strip configuration (right). In both cases, the optimum operating point is found for drift voltages of 475-525 V, with an anode voltage of 300 V. The resistive detectors can be operated with >25 V higher voltage on the anode and the drift without instability. A possible explanation for the higher optimal operation point can be a charging effect of the resistive layer, which is common for resistive Micromegas [72, 130].

11.3 Operation in a Pion Beam

All tested resistive prototypes were operated during several hours in a 150 GeV pion beam. The resistive strip sample of 82 MΩ/□ was operated three hours at an intensity of 4×10^6 pions per spill at an anode and drift voltage configuration of 325 V and 450 V. The intensity is measured with a scintillator configuration of 10 cm by 10 cm and one spill takes approximately 10 s, which leads to a mean pion flux per spill of $\sim 4 \times 10^3$ pions per cm^2 per second. In these conditions, the detector worked at a gain of 30 % lower than in regular operation at muon

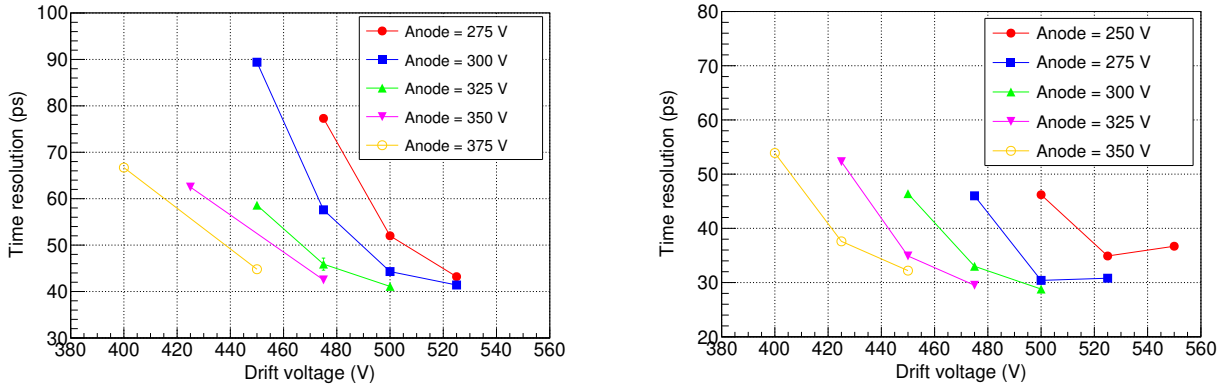

(a) Resistive strip

(b) Floating strip

Figure 11.4: Dependence of the time resolution on the drift and anode voltage for both resistive PICOSEC-Micromegas technologies irradiated by 150 GeV muons. For each curve at a given anode voltage, the maximum drift voltage corresponds to the maximum gain at which the detector can work in stable conditions. Statistical uncertainties are shown. Analysis performed by F. J. Iguaz [129].

beam and suffered an induced current of 92 nA per spill. A time resolution of 71.6 ± 1.1 ps was measured in the pion beam. After the pion beam, the detector gain recovered in some hours of regular operation, showing no degradation in timing performance. The second resistive strip sample (292 kΩ/□) was operated at the same intensity than the previous one at an anode and drift voltage configuration of 450 V and 350 V. The detector gain was by 40 % decreased compared to the muon runs. The detector suffered an induced current of 300 nA per spill with a time resolution of up to 49.3 ± 0.6 ps.

The last sample of floating strip type was tested twelve hours at an intensity of 2.2×10^6 pions per spill ($\sim 2.2 \times 10^3$ pions per cm^2 per second) at different voltage configurations. The detector worked at a gain ten times lower than in regular operation, but the induced current was only 24 nA per spill. In the best case corresponding to an anode and drift voltage configuration of 275 V and 425 V, the time resolution was 128 ± 3 ps, limited by the low detector gain.

11.3.1 Damage of the Photocathode

After longterm irradiation of the 82 MΩ/□ resistive strip prototype with pions, the detector was disassembled, and the CsI photocathode had to be replaced. The old photocathode was removed, and its degeneration was investigated under a microscope. The ion bombardment from the pre-amplification towards the cathode causes damage to the photocathodes. This damage is shown in figure 11.5. Characteristic patterns are visible in the picture. A negative image projection of the mesh and the location of the support pillars can be seen.

Another common degeneration is the small white crack (labelled “spark” in figure 11.5). These small cracks appear when a spark is generated in the detector. A spark is produced when

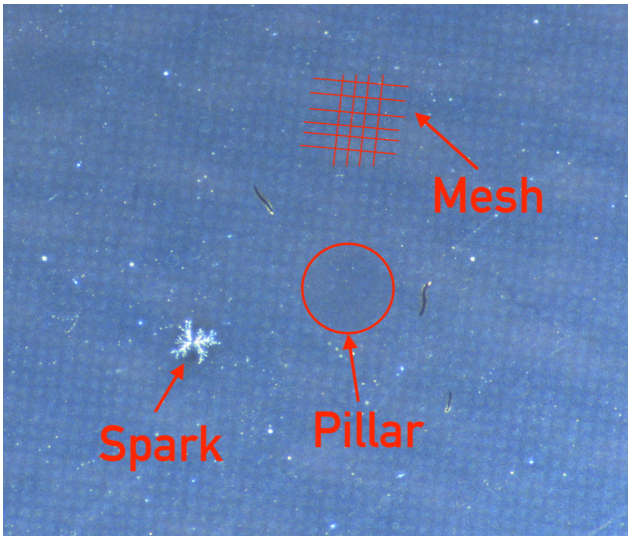

Figure 11.5: Photocathode degenerated by ion bombardement after exposure to a high-intensity pion beam. A few effects of the exposure are shown in the photocathode (see text).

the charge density is too high (Raether limit, gain $> 10^8$). Plenty of free electrons are produced at once, causing a strong current to flow between the cathode and the anode. The spark causes a discharge that is then followed by a voltage drop between the anode and the cathode. A voltage drop implies a gain drop and the detector is not efficient until the field has recovered from the spark. The recovering time depends on the RC value of the detector stage. If too many subsequent sparks appear, the voltage supply fails due to the large current flow, and the detector cannot operate in stable condition. In case of continuous sparks, the photocathode is largely damaged.

11.4 Ion-Backflow

One explanation for the high ion bombardment on the photocathode during high-rate operation is the pre-amplification of the PICOSEC-Micromegas in the drift region and the corresponding larger $E_{\text{Drift}}/E_{\text{Anode}}$ ratio, that leads to distinct differences in the ion-backflow compared to classical Micromegas without pre-amplification. The ion-backflow (IBF) in a classical Micromegas consists of ions, generated in the avalanche multiplication process after the mesh, that travel back through the mesh towards the cathode [131]. In the PICOSEC-Micromegas, additional electron-ion pairs are already produced in the pre-amplification drift gap. Figure 11.6 shows a schematic sketch of the electrons and ions created in the drift and amplification region of the PICOSEC-Micromegas. The amount of IBF depends on the mesh transparency, which is different for electrons and ions, and on the drift field intensity and the ratio between the drift and amplification field. At a low $E_{\text{Drift}}/E_{\text{Anode}}$ ratio, without pre-amplification, the mesh becomes fully transparent for electrons [132].

An estimation of the pre-amplification impact on the ion-flux towards the photocathode is derrived from the electric current read out on the anode and cathode under stable, high-rate

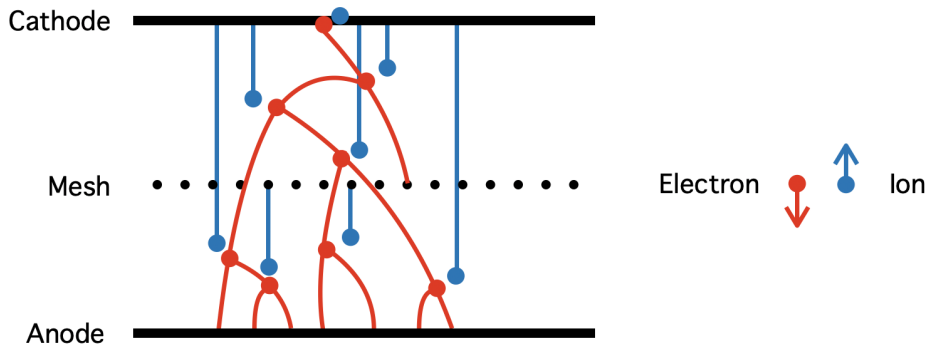

Figure 11.6: Sketch of the electron (red) and ion (blue) movement in a Micromegas with pre-amplification.

operation of the detector. The current on the anode is the sum of all electrons moving towards the anode and the ions moving towards the mesh. It is calculated as

$$I_{\text{anode}} = \tau_{\text{electron}} N_2 N_1 e^- - \tau_{\text{electron}} N_2 N_1 e^+ \Rightarrow I_{\text{anode}} = (-2\tau_{\text{electron}} N_2 N_1) \|e\| \tag{11.1}$$

where N_1 and N_2 are the gain in the drift and amplification region and τ_{electron} is the electron transparency of the mesh. The current on the anode is calculated with the addition, that some ions also travel back from the amplification as

$$I_{\text{cathode}} = -N_1 e^- + N_1 e^+ + \tau_{\text{ion}} \tau_{\text{electron}} N_2 N_1 e^+ \Rightarrow I_{\text{cathode}} = (2N_1 + \tau_{\text{ion}} \tau_{\text{electron}} N_2 N_1) \|e\| \tag{11.2}$$

where τ_{ion} is the ion transparency of the mesh.

11.4.1 Measurements of the IBF in the PICOSEC-Micromegas

A study in the laboratory with the first PICOSEC-Micromegas prototype and a deuterium UV lamp is performed to quantify the effect of IBF created in the amplification and pre-amplification of the PICOSEC-Micromegas. The IBF is measured by the ratio of the current on the anode and the cathode during operation [133]. The current is read from the CAEN N471A power supply unit with a resolution of 1 nA. A scan of drift fields with three fixed amplification fields is performed, and the current is measured with the results are presented in figure 11.7. No current is measured on the cathode at low drift voltage, as nearly all amplification takes place in the amplification region. At high drift voltages, the current in the cathode rises stronger than in the anode and even exceeds the current in the anode. In this stage, the detector is dominated by the pre-amplification. While a stronger drift field in the pre-amplification is beneficial for a better time resolution, it also hugely increases the ion bombardment on the cathode.

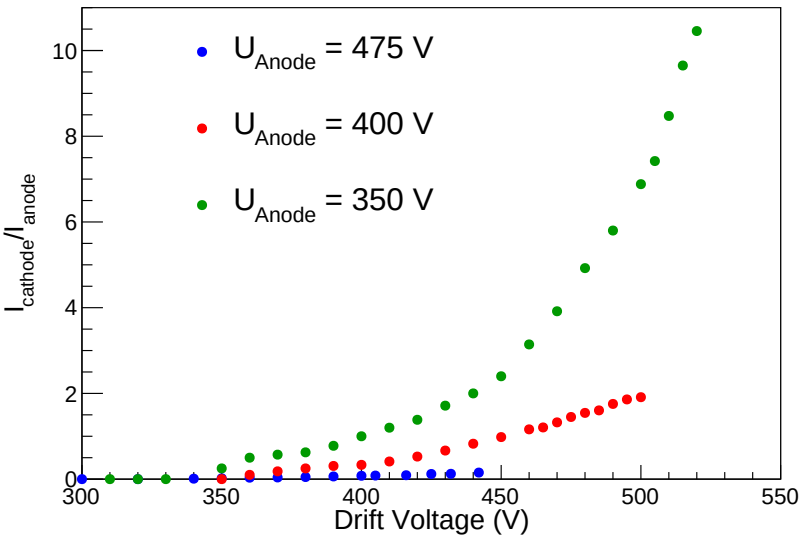

Figure 11.7: Ratio between the current on the cathode and on the anode.

11.4.2 IBF in the Pion Beam

The microscope image of the imprints on the photocathode in figure 11.5 and the laboratory measurements show that the IBF plays a serious role in the deterioration of (resistive) PICOSEC-Micromegas detectors in a high-flux environment, especially as ions are created in the pre-amplification of the drift region and the mesh becomes transparent for the ions created in the amplification region at the given field ratio. During data-taking in the pion beam, the PICOSEC-Micromegas is connected to the CAEN N1471H power supply with 50 pA resolution and the currents given from the power supply to the photocathode and the anode are monitored. The mean current during a pion spill for different field settings is measured and given in table 11.2.

At stable conditions and various field settings, the IBF varies between 20 % and 30 %. When the pre-amplification field is increased to 425 V, the detector operates in unstable conditions. At these fields, several sparks appear, and the current in the voltage supply drops as it is not able to supply enough current to operate the detector. In these unstable conditions, a higher percentage of the current is generated in the pre-amplification (it reaches 63 % in table 11.2), which causes parts of the deterioration that was observed on the CsI photocathode.

The measured IBF and the observed degradation of the photocathode material in a high-flux environment leads to the search for alternative photocathode materials that can provide a sufficient light yield and withstand higher IBF with less deterioration. Possible solutions for more robust and performant photocathodes are presented in chapter 13.

Table 11.2: Anode and cathode voltage settings are shown together with the measurements of the corresponding currents and the IBF in a high flux pion beam. An exceptional IBF of 63 % has been reached in unstable conditions at high electric fields.

U_{anode} (V)	$U_{cathode}$ (V)	I_{anode} (nA)	$I_{cathode}$ (nA)	IBF (%)
+450	-350	98.00	23.40	24
+450	-375	193.85	53.00	28
+450	-325	45.47	10.65	23
+425	-400	193.50	53.10	28
+425	-375	87.30	23.95	27
+425	-350	44.48	10.99	25
+400	-425	178.84	112.39	63[1]
+400	-400	88.55	25.54	28
+400	-375	41.28	11.10	27
+400	-350	20.42	4.44	22

11.5 Summary

Overall the timing properties of the PICOSEC-Micromegas concept are preserved at resistive read-outs. Especially the floating strip read-out with a 25 MΩ discrete resistor reaches 28.8 ± 0.2 ps, a similar time resolution in a muon beam as the non-resistive equivalent. Anyhow, due to the resistivity, a higher voltage needs to be applied to reach the given performance. Stable operation in high-flux ion beam is also possible when the detector gain is reduced with consequentially worse time resolution. The difference in time resolution between operation in pion and muon beam is lower for detectors with higher resistivity. The resistivity of 82 MΩ/□ needs only a gain reduction of 30 % and reaches a time resolution significantly under 100 ps.

The IBF reaching the cathode becomes a severe problem at high rate operation due to the ions produced in the preamplification. The ion bombardment on the photocathode leads to significant damage on fragile material like CsI. The development of robust alternative photocathodes with a high quantum efficiency is essential for the future development of PICOSEC-Micromegas that will be operated for a long time in high flux environments.

[1] unstable conditions

12 Segmented Read-out

Contents

12.1 Challenges of a Multipad detector

Previously, only single pad prototypes have been used to characterise and to optimise the individual components of the PICOSEC-Micromegas detection concept. In the process of developing PICOSEC-Micromegas detectors for future applications, new prototypes with a segmented read-out need to be designed. Robust fast-timing detectors are demanded and find use as pixelated tracking detectors (see chapter 2). The main challenges of increasing the detection area and read-out segmentation are presented in the following section.

Segmentation

A segmentation of the read-out anode can be designed in different ways, like strips, pixels, and pads. A common read-out design for tracking detectors is a strip-segmentation [68, 55]. A 2D position reconstruction is achieved with two strip-segmented read-out layers. Both layers are segmented in strips of equal width and the layers are by 90° rotated to each other. This read-out

allows componentwise the reconstruction of the particle incident point. The x-coordinate and the y-coordinate of the particle related to the detector reference frame are measured by the corresponding plane. This read-out concept is used, for example, by the triple-GEM tracking detectors of the beam telescope presented in section 9.1.3.

A strip-segmented read-out is not suitable to preserve the fast-timing characteristics of the PICOSEC-Micromegas. The signal induced anywhere on the read-out stip has to drift until the connection of the strip to the read-out electronics. This drift time is proportional to the distance between the signal arrival point on the strip and the read-out connector. Even for an ideal conductive material, an electric signal can only propagate with the velocity of the speed of light. The signal propagates on a copper anode with a velocity of $<$0.3 mm/ps, which can cause a considerable SAT delay for strips of some centimetres of lenght and a time resolution in the order of several picoseconds. A radialsymmetric pattern with a central read-out connector reduces the SAT variance for different signal arrival points on the read-out segments, as it has the highest surface to perimeter ratio. The highest possible filling of the active area with a radialsymmetric-like pattern can be achieved with a hexagonal pad segmentation.

The biasing of the electric field through a segmented read-out needs to be different, than compared to a single pad detector. Each segment needs an individual connection to the bias voltage in case of a non-resistive read-out. Moreover the bias voltage can not be provided through the amplifier to ensure that the same potential is on each pad. These constraints have to be taken into account when routing the bias and signal lines through the detector PCB. In case of a resistive detector, the whole resistive anode can be uniformly biased as the segmented electrodes are placed below the anode.

Field Uniformity

One main issue of scaling the active area of a Micromegas detector is the preservation of the drift distance uniformity. The amplification region distance is kept constant by the pillar structure between the mesh and the anode. Production-wise, the first (bulk) Micromegas detectors were produced to an active area of up to some decimeter side-length. The COMPASS Micromegas, one of the first Micromegas detectors used in an experiment, have an active area of 40 x 40 cm^2 for each tile [68]. Modern production facilities are able to increase the active area up to several square metres. The sub-modules of the ATLAS-NSW Micromegas reach areas up to 3 m^2 per sub-module [134, 55]. Producing large-area Micromegas with a uniform amplification region is technically possible.

The PICOSEC-Micromegas is one of the few Micromegas detectors that use the drift region for pre-amplification. The electric field in the drift region reaches the same order of magnitude as the amplification field, if not even stronger. A large-area multipad PICOSEC-Micromegas has the same demands on the drift field uniformity and on the amplification field uniformity. The mechanical design of a large-area PICOSEC-Micromegas needs to take this into account. The design of the first multipad prototype chamber (see section 12.2) has caused a deformation of the read-out PCB. The bent PCB alternates the distance between the mesh and the photocathode locally

and affects the detector performance uniformity (see section 12.3.2). The subsequent designs (section 12.4) are reinforcing the PCB and prevent bendings and deformations of the electric field.

Cherenkov Crystal Size

The PICOSEC-Micromegas requires a Cherenkov radiator to detect massive particles. The thickness of the crystal determines the number of photons radiated due to the Cherenkov effect at a given particle momentum. The photons generated in this process can be partially reflected on the surface between the crystal and the photocathode. Uniform thickness and optical quality of the crystal surface ensure that the number of photoelectrons is constant over the active area of the detector. Well-proven Cherenkov radiator materials, like MgF_2, are artificially grown crystals with a high fracture probability. Producing and processing larger area windows ($> 15\,\text{cm}$ diameter) is a challenging process [135], which reduces the availability and increases the price of larger area crystals. Even larger area coverage with PICOSEC-Micromegas detectors requires a mosaic-like segmentation of the Cherenkov crystals.

Possible inhomogeneities of the crystal and the photocathode have to be corrected when the PICOSEC-Micromegas detector is used in future calorimeter applications. A calibration of the detector is possible with particles providing a narrow energy distribution collimated to a well-defined spot. The signal size differences for these particles need to be mapped along the active area of the detector unit. The signal size measured with a segmented PICOSEC-Micromegas detector needs to be corrected by these signal size differences depending on the inclination point of the particle. This correction needs to be done individually in the commissioning of each produced detector unit.

Read-out Electronics

The last challenge when developing a detector with a pad segmentation is the read-out electronics. The single pad prototypes are read out with a CIVIDEC amplifier [93]. These amplifiers are connected with SMA cables to the detector, and each amplifier has its own dedicated metal box. The multipad prototypes are read-out with CIVIDEC amplifiers at the first test measurements. Each pad needs its own amplifier and its own channel in the oscilloscope. A four-channel oscilloscope can read-out only two pads, as the trigger and event number signal are occupying one input each (see section 9.1). More pads can be measured in parallel by looping the trigger and event number signal over several oscilloscopes.

This way of reading out a segmented detector is impracticable and only doable during R&D. A first step to overcome this problem is the development of optimised amplifiers. First results from the development of specific PICOSEC-Micromegas amplifier are presented in section 12.5. A well-proven amplifier design can later be integrated on the detector PCB or as a small card directly connected to the detector. In a second step, the acquisition of the whole waveforms needs to be changed to a faster and lower data bandwidth-demanding system. Possible solutions are discussed in section 14.1.

12.2 Multipad Prototype

The first PICOSEC-Micromegas prototype with a larger active area and segmented read-out has been developed at CERN. The crystal diameter is doubled to 5 cm (ca. 2 ") and the active area is grown to 3.5 cm diameter. The anode is divided into 19 hexagonal pads with a diameter of 1 cm each. Figure 12.1a shows the CAD sketch of the read-out PCB with the segmented anodes and the mounting mechanism of the Cherenkov radiator. Only the inner seven hexagons are printed in full size. The detector boundary cuts the outer hexagons. Figure 12.2 shows a top view picture of the detector during assembly in the cleanroom. The pad structure with the full pads in the centre and the cut pads on the border are visible.

The PCB with the Micromegas is mounted on one flange of the chamber and sealing the chamber. Over- and under pressure during operation and mechanical stress during assembly have a direct impact on the PCB. As the PCB is sealing the detector, the signal for each pad is routed through the PCB. Figure 12.1b show a CAD drawing of the backside of the PCB. Each pad has an individual SMB connector to read out the signal, while one additional connector biases all pads commonly. The high voltage is routed over a resistor (>20 MΩ) to each pad, to power all pads independently from the read-out. A standard bulk Micromegas with 128 µm amplification gap and 200 µm drift gap distance is used for the multipad prototype. The mesh is directly connected to ground on the PCB.

This chamber is the only chamber without an additional window in the outer gas vessel in front of the detector. A window is essential to calibrate the detector with an external light source or to operate it in the Laser beam. This chamber has alternatively a UV-LED mounted inside of the chamber with the bias voltage fed through the PCB.

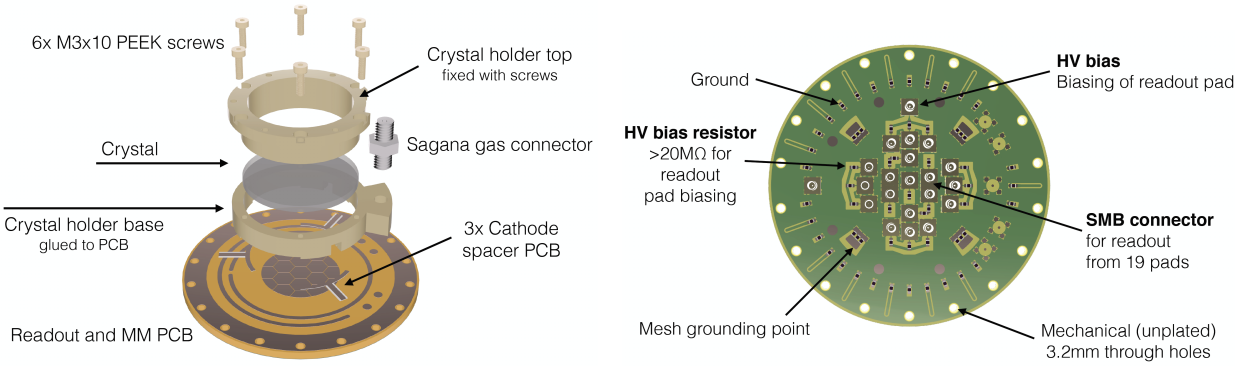

(a) The Cherenkov cristal is held on top of the Micromegas with a mechanic similar to the first prototype.

(b) All pads are read out separately with SMB connectors on the back of the PCB.

Figure 12.1: Technical sketch of the multipad detector [136].

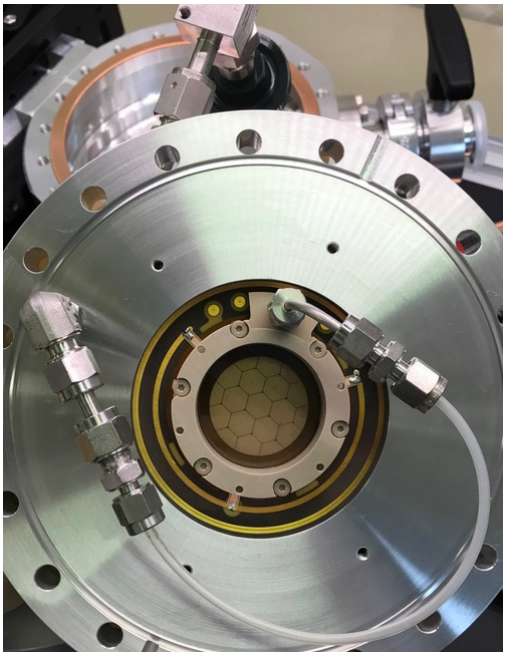

Figure 12.2: Picture of the multipad chamber with the hexagonal readout during assembly in the clean room.

12.3 Beam Characterisation

The multipad prototype (described in section 12.2) is the first PICOSEC-Micromegas prototype with a segmented anode, that has been tested. Measurements have been done in several beam campaigns at the CERN-SPS beam facility. The multipad chamber has its own dedicated mounting spot outside the beam telescope due to it size. The measurement set-up with the beam telescope for measurements at the CERN-SPS beam facility are explained in detaile in chapter 9.1.

The multipad prototype has a segmented anode with 19 pads. Only 14 of these pads could be connected with a SMC connector due to connection problems on the soldering pads. The pads are numbered from top to bottom and from right to left (viewpoint from behind the detector against the direction of the beam). Figure 12.3 shows a map of the pads with its dedicated numbers. Pads with the same distance to the center and the same shape are marked in a similiar colour. The numbering will be kept consistent over the following analysis.

12.3.1 Time performance

In first beam measurements, the multipad detector is treated as a single pad detector. Only the central pad (No. 7 in figure 12.3) is powered and read-out. The time resolution for different drift and amplification fields is measured and compared with the results of the single pad detectors. Figure 12.4 shows the time resolution of a scan over different electric fields. The detector is

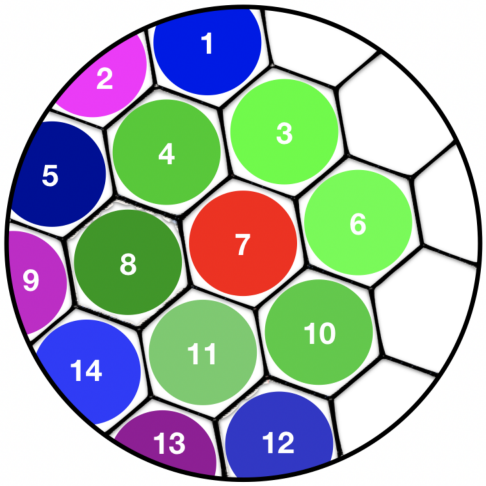

Figure 12.3: Each connected pad has a dedicated number and color. The sketch has the viewpoint from behind the detector (at the side of the connectors) against the direction of the beam. Pads with the same distance to the center are grouped with a similiar colour. The rightermost pads were not connected and therefore not numbered.

operated with a 18 nm CsI photocathode on a 3.3 nm chromium substrate attached to a 3 mm MgF_2 window. The quantum efficiency of the specific photocathode was not determined during the measurement due to connection problems of the reference LED. The multipad detector is produced with a woven mesh in bulk technology, and the distances between the anode, mesh and cathode are the same as for the single pad prototypes.

The field scan shows a similar behaviour of one pad from the multipad prototype compared to the single pad prototypes. The time resolution increases with higher drift fields until a performance maximum is reached. At higher fields the detector starts becoming unstable, and it loses gain due to local discharges. A rapid deterioration of the time resolution can be seen when this limit is reached, like with the red ($U_{\text{Anode}} = 300\,\text{V}$) and green curve ($U_{\text{Anode}} = 325\,\text{V}$) in figure 12.4.

The best time resolution in this field scan is reached at a setting of $U_{\text{Anode}} = 275\,\text{V}$ and $U_{\text{Drift}} = 500\,\text{V}$ with $35.8 \pm 1.0\,\text{ps}$. The same time resolution is reached when the shared signal of neighbouring pads is analysed. This value is in the order of $\sim 10\,\text{ps}$ higher than the time resolution of the single pad detector in comparable settings. A possible explanation for this discrepancy can be quality of the CsI photocathode. The quantum efficiency of the photocathodes variates between the beam tests in the range of up to 4 photoelectrons per muons. No conclusion can be drawn as the photocathode efficiency was not assessed during the measurement. Another explanation for the discrepancy can be inhomogeneities in the detector structure due to the increased active area. A curvature of the read-out PCB has been detected. This curvature modifies the distance of the amplification region and thus the electric field. The consequences of this effect are shown in the next section.

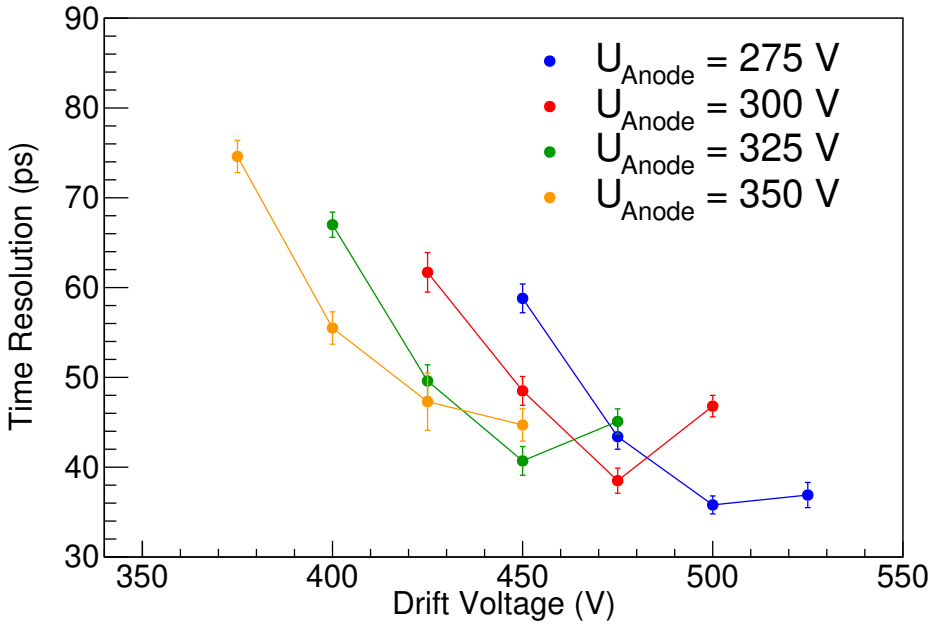

Figure 12.4: The central pad time resolution for different electric fields behaves similiar as the single pad prototype.

12.3.2 Curvature

All pads of the multipad prototype are investigated as a homogenious behaviour of the pads is crucial for future applications. The first aspect, that is measured, is the gain of each pad. Single photoelectrons are generated by a UV-LED inside the chamber. These signals on each of the 14 pads are read out by an ORTEC 142 charge amplifier.

The amplitude distribution for each pad is given in figure 12.5. The colour of the lines corresponds with the colours of each pad in figure 12.6. A clear inhomogenity can be spotted between the pads with different distance to the center. The centermost pad (no. 7) has the smallest mean amplitude and by this way the smallest gain. The gain rises for pads further outside the center. Despide this inhomogenity, all pads in the same distance to the center (same colour tone) are showing the same amplitude distribution and gain. This result shows evidences for a radial inhomogenity of the multipad detector.

The effect and reason for the inhomogenity is further investigated by a detailed examination of selected pads and their time resolution. Only two oscilloscopes were available for the beam measurements and therefore only four pads could be measured in parallel. Only full sized inner pads are selected for a better comparison. The innermost pad (no. 7) and the adjunct pads (no. 4, 8 & 11) are measured. The larger MCP-PMT model “Photek 240 PMT” is used with an active area of 40 cm diameter that covers all four pads (see section 9.2.3).

Table 12.1 shows the measured time resolution of all four pads. The inner pad has a time resolution of $\sim$10 ps better than the adjunct once, even though it has a smaller gain. The gain

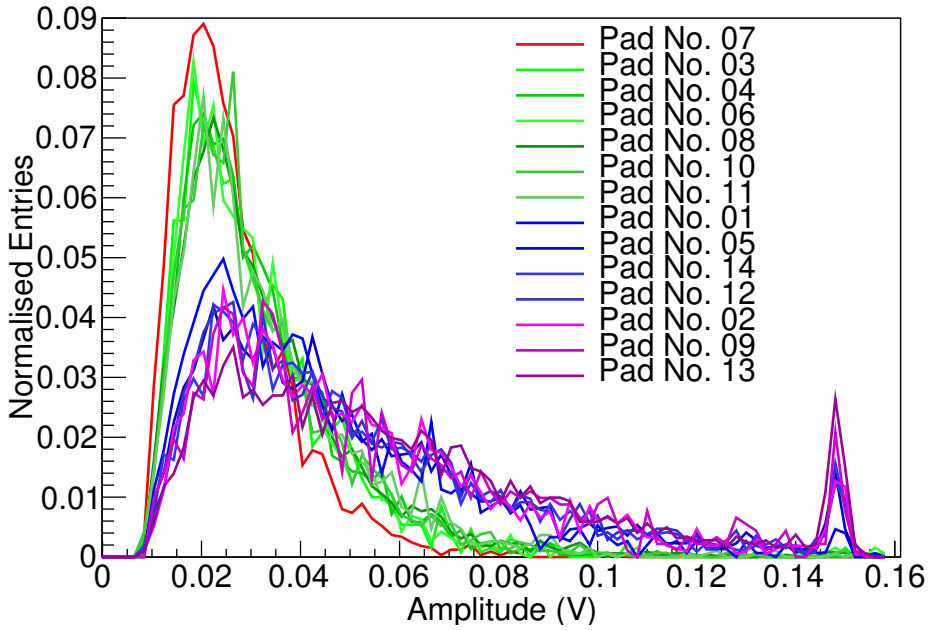

Figure 12.5: The signal amplitude distribution for all pads shows higher mean signals in the outer pads. The peak at the end of the range is caused by clipping in the MCA.

should be correlated with the time resolution, as shown in the behaviour of the field scans and the slewing effect (section 6.4.3).

Table 12.1: Time resolution of the centered (no. 7) pad and three consecutive pads around the center (No. 4, 8 & 11).

Pad Number	Time Resolution (ps)
7	36.94 ± 1.20
4	49.46 ± 1.38
8	45.85 ± 1.44
11	46.87 ± 1.35

The three pads surrounding the center (no. 4, 8 & 11) are studied more in detail. The whole pad surface of each pad is divided in two regions of interest (ROIs). Figure 12.6 shows the separation of the regions. For each pad a region from the center of the pad towards the global center of the detector (green area) and a region towards the outer boundarie (red area) is defined. The performance gradient between these areas for each pad should be maximal, as the inhomogenity seems to be radial symmetric and centered in the global center of the detector (Pad no. 7).

The SAT difference between the signals reaching the dedicated ROIs and the reference MCP-PMT are measured for each ROI. Table 12.2 shows the results for each pad and ROI. The rather high uncertainities of these values are explained by low statistics of $\sim$500 entries each ROI. All three pads are showing a similiar behaviour with the particles passing through the green

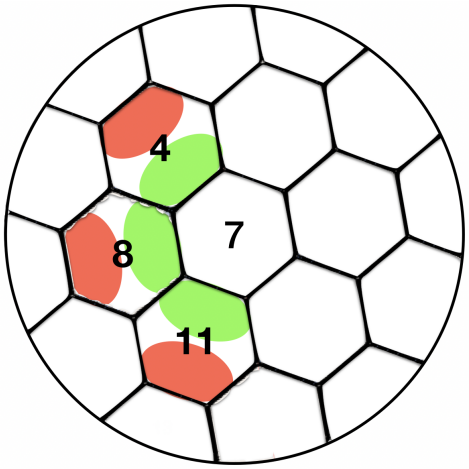

Figure 12.6: Division of the three pads no. 4, 8 & 11 in two ROIs. The green ones are facing towards the global center of the detector and the red ones are facing toward the outside of the detector.

area arriving $\sim$ 20 ps later than signals passing through the red area. An overlapping of both distributions would broaden the overall time resolution of each pad, which explains worsening of 10 ps in the surrounding pads compared to pad no. 7.

Table 12.2: Mean SAT difference on the pads surrounding the centre between the inner and outer ROI.

Pad Number	Colour	SAT (ps)
4	Green	-1858 $\pm$ 4
	Red	-1882 $\pm$ 6
	Δ	24 $\pm$ 7
8	Green	-1818 $\pm$ 7
	Red	-1844 $\pm$ 6
	Δ	26 $\pm$ 9
11	Green	-1798 $\pm$ 8
	Red	-1822 $\pm$ 6
	Δ	24 $\pm$ 10

The only consistent explanation of the unusual behaviour of the gain and the time resolution difference between the pads can be a mechanical inhomogeneity of the detector itself. A lower gain can be the result of lower quantum efficiency in the photocathode or a smaller electric field in either the drift and/or the amplification region. The voltage is uniformly applied to the detector the best time resolution is reached in the central pad. Therefore only differences in the gap distances can cause inhomogeneities in the electric field. A bending of the PCB could be one possible option to cause such a difference in the gaps.

The round PCB is sealing the chamber and it experiences mechanical stress as well as pressure differences between inside and outside of the chamber. Furthermore the soldering of the connectors on the back of the PCB creates thermal stress, which can cause a further extention or shrinking of the PCB material. The radial symetry of the inhomogenity as well as the SAT difference inside of the pads is further supporting the hypothese of a curved PCB. The bending would mainly affect the distance between the flat crystal surface and the mesh. The mesh is in a mechanical compound with the anode and the PCB due to the production methode with the pillars. If the PCB would be curved, the mesh would curve in the same way as the anode.

12.4 Resistive Multipad

A resistive multipad is designed based on the findings of the first multipad and the resistive detector tests. The resistive multipad is produced with PCBs, that are compatible with the picolarge chamber, which is also used for studies of single-pad PICOSEC-Micromegas. The picolarge chamber design used for the single-pad and the resistive multipad prototype is explained in section 5.3.2. The main goal of the design is to adapt for the problems of the first multipad prototype and to introduce a resistive segmented read-out to the PICOSEC-Micromegas project. The picolarge chamber fully hosts the PCB, and the pads are wired through the PCB towards the end. The SMA connectors are soldered at the end of the PCB instead of directly behind the pads like at the first multipad. The idea of this design is to reduce the mechanical and temperature stress on the PCB and consequently reduce the deformation of the PCB and the inhomogeneity of the drift length.

Figure 12.7 shows an image of the PCB for the picolarge chamber. It has seven full-sized pads with the same dimensions as the multipad detector (1 cm diameter). This size is sufficient to study the charge sharing between all combinations of neighbouring pads and diagonal over three pads. Moreover, the design allows using the same 5 cm windows as used in the first multipad. The resistive Micromegas is produced in the same way as the resistive strip Micromegas described in section 11.1. An insulator is placed on top of the read-out pads, and a resistive paste is uniformly applied as an anode on top of the insulator. Prototypes with different mixtures of the resistive paste are produced with a resistivity ranging from 1 MΩ/□ to 10 kΩ/□. A measurement of the detector timing performance is still pending due to delays in the detector production and limited availability of the measurement set-ups.

12.5 Read-out Electronics

An integral part of the multipad development is the development of a new read-out electronics. Up to now, each pad is read out with a single dedicated amplifier. For the future multipad prototypes a new read-out card is developed based on the “ATHR” amplifier circuit designed in DEDIP. It is an amplifier with sufficient bandwidth and no integration to preserve the characteristic signal shape with fast electron peak and long ion tail. A first single-channel

Figure 12.7: Photograph (left) and microscope image (right) of the hexagonal read-out structure. The mesh and the pillars can be clearly distinguished.

prototype of this amplifier, shown in figure 12.8 was tested in the laser beam with the single pad PICOSEC-Micromegas and compared to the CIVIDEC amplifier. The main problem with the CIVIDEC amplifier is its weak protection circuit. Especially at high signal rates and high detector gain, the current released in a spark damaged the amplifier. The ATHR amplifier is specifically designed for the PICOSEC-Micromegas and other MPGDs operated close to the spark limit. With a reinforced input protection circuit, it was operated successfully during many tests with sparking detectors without any damage.

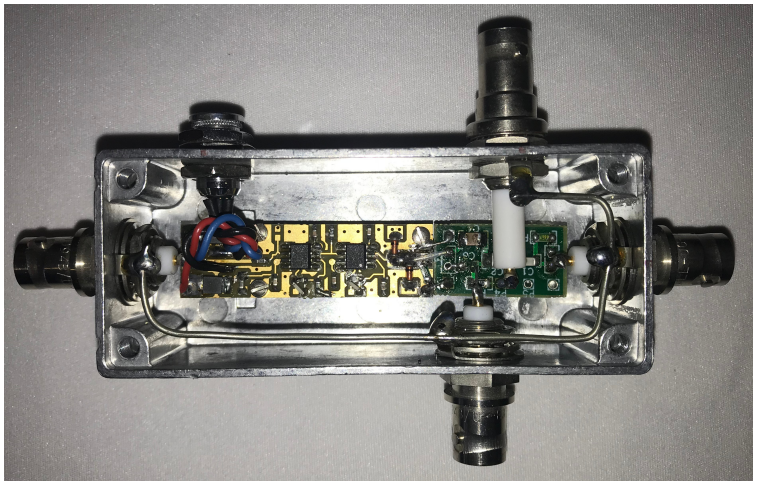

Figure 12.8: Photograph of the single channel ATHR amplifier developed at CEA.

The measured time resolution with both amplifiers is compared in figure 12.9. The detector is operated for this test at field setting with high pre-amplification to obtain an optimal time

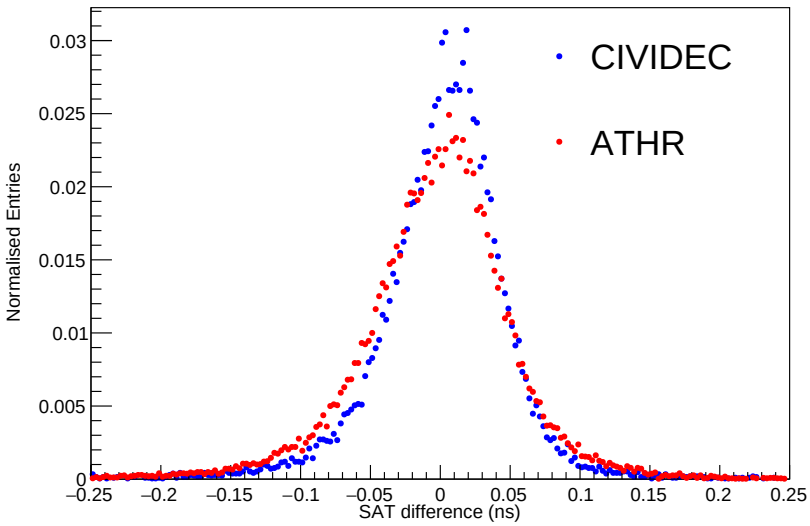

Figure 12.9: Comparison of the time resolution measured in a laser run with many photoelectrons, 275 V in the anode and 600 V in the mesh. The blue point represent the normalised SAT distribution for the CIVIDEC and the red points for the ATHR amplifier.

resolution. The normalised SAT distribution from the ATHR amplifier is slightly wider than measured with the CIVIDEC amplifier. The wider distribution results in a worse time resolution with 46.31 ± 0.25 ps instead of 37.12 ± 0.25 ps. A lower bandwidth at the connection between the PCB and the feed-through connectors of the box causes the weaker performance of the ATHR. A waveform signal comparison between both amplifiers also results in slightly longer signals from the ATHR amplifier due to the integration caused by the lower bandwidth.

Anyhow, the amplifier concept demonstrates its suitability for the fast PICOSEC-Micromegas signals and a time resolution in the same order of magnitude than with the reference CIVIDEC amplifier is achieved with better robustness and protection against sparks. The ATHR amplifier concept will be further used, and small read-out cards based on this amplifier are developed and will be used in a mosaic-like multipad prototype developed at CERN.

12.6 Summary

The adaption of the PICOSEC-Micromegas detection principle for a segmented read-out is a crucial step in the transition from the research of new detection techniques to the development of sub-detectors for physics experiments. Most applications for fast-timing detectors require the preservation of position information from the incident particle, which is only accessible with segmented read-outs. The first tests with the multipad have demonstrated, that the adaption of the PICOSEC-Micromegas principle to larger active areas is possible and time resolutions in the same order of magnitude as with the smaller single-pad PICOSEC-Micromegas are possible. The main concern of the development of larger area PICOSEC-Micromegas detectors

is the drift gap uniformity. The read-out PCB of the first multipad prototype appears to be bent due to the mechanical stress of the PCB mounted to the chamber. The radial bending of the PCB of several tenths of µm causes a progressive delay in the SAT of 20 ps for each additional 1 cm of radius from the centre.

The new designed resistive multipad prototype aims to address the problems of the inhomogeneities of the PCB by embedding the PCB fully inside the chamber and routing the pad connections inside of the PCB. The resistive multipad will combine the development of the resistive PICOSEC-Micromegas with the multipad, and it will be a significant step towards a gaseous tracking detector with picosecond time resolution, suitable for high particle flux environments. Next to the detector itself, the development of dedicated electronic amplifiers for the PICOSEC-Micromegas advances well. The in-house developed ATHR amplifier has sufficient bandwidth to preserve the critical signal information, like the electron peak with the steep rising edge. In the next iterations, this bandwidth will be further improved to fit the needs of the PICOSEC-Micromegas. Moreover, they provide better spark protection compared to commercial solutions, and not a single spark was able to damage the amplifier during tests with the PICOSEC-Micromegas. The integration of the ATHR amplifier will be a central component in the development of future PICOSEC-Micromegas multipad prototypes.

13 Photocathodes

Contents

Measurements of PICOSEC-Micromegas with a resistive read-out have shown a high ion bombardment on the photocathode at measurements in a high-rate pion beam (see section 11.3.1). CsI photocathodes have shown a photoefficiencies in particle beam tests of up to $\sim$10 N_{pe}/µ, but were damaged by the ion backflow under high particle fluxes. The low $E_{\text{Drift}}/E_{\text{Anode}}$ ratio and the pre-amplification of the signal in the drift region generates a higher amount of ions between the mesh and the cathode, compared to standard Micromegas. The low robustness against ion radiation and the general hygroscopic character makes CsI to an unfavourable photocathode material for many applications. However, the general time resolution of the detector improves with the number of photoelectrons and thus the quantum efficiency of the photocathode. The last step in the development of the PICOSEC-Micromegas concept towards a robust detector for high-rate environments is the development of robust and efficient photocathode materials.

The main performance criterium of the photocathodes is the quantum efficiency, which is translated into the number of photoelectrons extracted per muon under beam condition (N_{pe}/µ). This unit is chosen to have a comparison to the measurements of the PICOSEC-Micromegas with a CsI photocathode ($\sim$10 N_{pe}/µ) in the CERN-SPS beam reaching a time resolution of 24.0 ± 0.3 ps. This result is reached with a detector providing a single photoelectron time resolution of $\sim$76 ps

[5]. An improvement of the drift gap reduces the single photoelectron time resolution to 44 ± 1 ps (see section 8.2 and reference [106]). With the improved detector, photoefficiencies of 3-4 N_{pe}/μ are sufficient to reach a comparable time resolution of $\sim$24 ps.

This chapter describes the investigation of different photocathode materials and their suitability for PICOSEC-Micromegas. Metallic photocathode and diamond-like carbon (DLC) based photocathodes with different thickness are tested. Moreover, CsI with a protection layer and nanodiamond coatings are tried. The most promising materials reaching the demanded quantum efficiency are 2.5 nm thin DLC and highly boron-doped DLC (B_4C). Depending on the availability, some photocathodes are tested "in-vivo" during beam tests in the PICOSEC-Micromegas detector (see section 13.1). The number of extracted photoelectrons per muon is calculated with the mean signal charge and UV-LED reference measurements, as explained in section 6.3. Other photocathodes are tested independently of the detector in a monochromator, the ASSET-Chamber at CERN (see section 13.2). Next to the photocathode material, the effect of the high drift field on the extraction efficiency is studied. At intense light, the extraction efficiency of metallic photocathodes increases further with rising electric fields of the order of several 10 kV/cm.

13.1 Characterisation in a Particle Beam

The most reliable characterisation of photocathodes is done in a particle beam. These measurements are the closest to future applications of the detector with light provided from Cherenkov radiation of MIPs. It is moreover the only measurement of photocathodes that can also provide the time resolution. The presented photocathode studies are done during the beam test campaigns in 2017 and 2018 with the set-up as described in chapter 9.1. Afterwards, studies of photocathodes are only performed in the monochromator set-up explained in section 13.2.

13.1.1 Metallic Photocathode

Metallic photocathodes are a simple replacement of CsI. Pure chromium and aluminium are easy to handle without rapid degeneration in humidity and sufficient robustness against ion-backflow. Evaporation of thin layers of a metallic substance is a standard procedure done in industry and many laboratories. Metallic layers are conductive, and the drift voltage is directly applied to the photocathode. Moreover, the common metals used as a photocathode, like chromium or aluminium, have an excellent adhesivity to the window material. Out of these reasons, thin metallic layers, mostly chromium, are used between other photocathode materials and the Cherenkov window to ensure the conductivity and improve the adhesivity of the compound. The common CsI photocathodes are, for example, produced with a 3 - 5 nm thick chromium interlayer.

The measured quantum efficiency of pure photocathodes with a thicker metallic layer are presented in table 13.1, with samples of chromium and aluminium. The table gives additionally the time resolution measured in the best possible field settings. The chromium sample shows an inferior performance with a quantum efficiency of statistically less than a photoelectron per muon and a corresponding time resolution. On the other hand, the aluminium probes provide around

two photoelectrons per muon and accordingly increased time resolution. Especially a probe with a thicker window and thus more Cherenkov photons could achieve 2.2 N_{pe}/µ and a time resolution of <60 ps. Metallic photocathodes are providing inferior quantum efficiency compared to CsI. Aluminium photocathodes can provide sufficient photoelectrons at enough light for some applications, with the main benefit of the robustness and easy production.

Table 13.1: Performance of chromium and aluminium photocathodes compared to CsI.

Photocathode	N_{pe}/µ	Best time resolution (ps)	Optimal Voltage $U_{Ampl.}$ (V) / U_{Drfit} (V)
18 nm CsI (+ 5.5 nm Cr)	10.40 ± 0.40	24.0 ± 0.3	+275/-475
20 nm Cr	0.66 ± 0.13	189.4 ± 5.3	+425/-425
6 nm Al	1.69 ± 0.01	71.4 ± 1.8	+275/-525
10 nm Al[1]	2.20 ± 0.05	57.6 ± 0.6	+275/-600

13.1.2 Protected CsI

CsI photocathodes with an additional protective layer coated on top of the photocathode are another trial. For such a protective layer, two materials are chosen. The first one is a several atomic layer thick coating of LiF, and the second one is a coating of MgF_2. The results for both photocathodes are given in table 13.2. The LiF coating is strongly affecting the quantum efficiency of the CsI with a detection efficiency lower than 40 %. The MgF_2 is only slightly affecting the quantum efficiency with a mean of still 3.55 N_{pe}/µ. Further studies of the protective effects of these coatings against ion-backflow in a high rate pion beam are still pending.

Table 13.2: Performance of 18 nm CsI photocathodes with a thin protective layer of LiF and MgF_2.

	LiF	MgF_2
N_{pe}/µ	<1	3.55 ± 0.08
Detection efficiency (%)	38	90
Time resolution (ps)	87.7 ± 3.7	45.6 ± 1.5
Optimal Voltage $U_{Ampl.}$ (V) / U_{Drfit} (V)	+250/-625	+250/-550

13.1.3 Diamond-like Carbon

Diamond belongs to the wide-band semiconductors with a bandgap of 5.5 eV and it shows under certain circumstances, e.g. on unreconstructed natural diamond(111) surface, a nega-

[1] 5 mm MgF2 window

tive electron affinity with the vacuum energy level lower than the conductive band [137, 138]. This property allows the use of diamond as a photocathode material for UV light. Diamond membranes, applied to a substrate by chemical vapour deposition (CVD) process, have been investigated as UV photocathodes in reflective and transmissive mode with a photocurrent measured for several micron thick diamond layers in both cases [139]. The quantum efficiency of the reflective photocathode increases with the thickness until the specific electron diffusion length is significantly exceeded. On the other hand, the quantum efficiency of the transmissive photocathode is reduced due to the light absorption in the substrate and the diamond membrane.

Diamond-like carbon (DLC) is a material based on amorphous carbon. Carbon atoms are organised in crystalline and disordered structures composed of mixing of three orbital hybridisations sp^1, sp^2 and sp^3. DLC composite of a significant amount of sp^3 bounds reaching similar properties as monocrystalline carbon. Films of DLC are produced in many ways and find application in industry and research applications due to its hardness, elastic modulus and chemical inertness [140]. DLC photocathodes for the PICOSEC-Micromegas are produced in a magnetron sputtering procedure. Carbon molecules are sputtered from a carbon cathode with a radio frequency electron beam, forming a plasma with surrounding argon. The electrons in the plasma are directed with a magnetic field into a long spiral path towards the substrate, which increases the ionisation of the plasma and thus the deposition rate [141]. A 3 inches target is used, allowing a maximal substrate size of 9 x 9 cm.

DLC photocathodes with different thickness ranging from 2.5 to 10 nm are produced by the PICOSEC-Micromegas collaboration laboratory from USTC and tested in the particle beam. A higher thickness reduces the optical transparency but increases the robustness of the material. Overall, the DLC photocathodes are extremely durable against mechanical damage. Even the thinnest probes of 2.5 nm did not show any measurable performance loss after sending from China to Switzerland by mail only protected by a paper envelope. The measured photo- and detection efficiency of the different tested probes is given in table 13.3 with the thinnest probe providing the best performance with a mean of 3.7 N_{pe}/μ and the higher opacity of the thicker probes reduce the performance. A thinner layer may further improve the performance, but the production of even thinner homogenous layers was not successful. The best performing photocathode of 2.5 nm is further investigated, and a field scan of the time resolution and efficiency is performed with the results presented in figure 13.1. Even higher electric fields need to be applied to the DLC probe compared to the CsI photocathodes with up to 575 V in the drift region and 250 V in the amplification region to operate the detector close to its limit, reaching a time resolution of less than 40 ps.

13.1.4 Diamond nanoseeding

The last type of photocathode tested in a particle beam is nanoseeded diamonds. This is a process where 5 nm thick diamonds are uniformly deposited on a substrate by chemical vaporisation [142] and fixed with a H_2 or O_2 plasma beam that also removes remaining C-C Sp2 structures [143]. The main idea behind this type of photocathode is to benefit from the good quantum efficiency of the diamond [139] with the additional advantage of the larger surface due to the

Table 13.3: Number of photoelectrons and detection efficiency for different thickness of DLC.

Thickness (nm)	N_{pe}/μ	Detection efficiency (%)
2.5	3.7	97
5	3.4	94
7.5	2.2	70
10	1.7	68

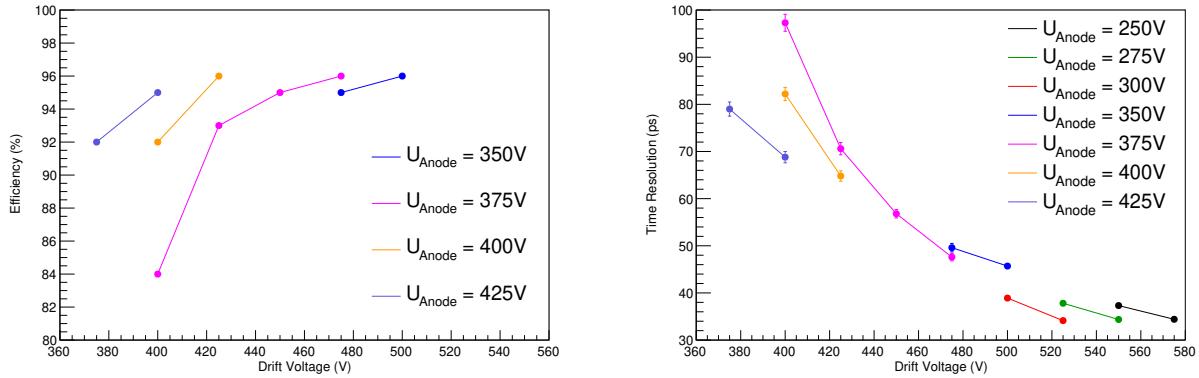

(a) Extraction efficiency

(b) Time resolution

Figure 13.1: Performance of a 2.5 nm thick DLC photocathode with different electric fields.

nanoseeded diamonds. On the other hand, the diamonds are not forming one conductive layer, and the nanoseeding process can not be performed on MgF_2 but needs an additional chromium substrate layer. The tested sample provides an efficiency of 1.85 ± 0.13 N_{pe}/μ and according to that efficiency, the time resolution is measured in figure 13.2 for different electric fields. With these first results, the diamond nano seeding might be an alternative robust photocathode when the quantum efficiency even improves with future development.

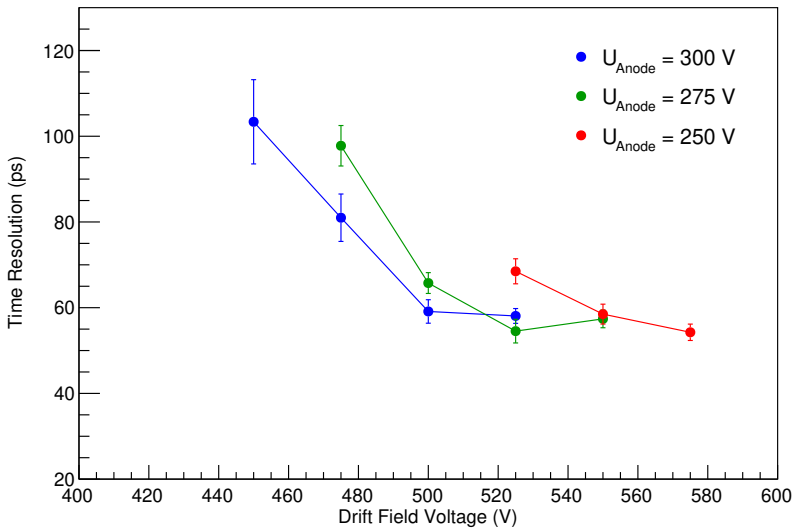

Figure 13.2: Performance of 5 nm nanoseeding on a chromium substrate. The photocathode provides 1.85 ± 0.13 photoelectrons per muon.

13.2 Characterisation in a Monochromator

Photocathodes can be also characterised in a monochromator. In this measurement, the quantum efficiency and transparency of the photocathodes are measured for different wavelength without the PICOSEC-Micromegas detector. The results help to compare different materials and thicknesses, but they are not precisely reproducing the performance of the photocathodes with Cherenkov light radiated through a particle. Without a beam, these measurements are only possible with cosmic muons, and those measurements need to be performed over several days to acquire enough events on the small active area of the detector. The ASSET-setup is used for characterisations of photocathodes in a monochromator with the possibility to perform several measurements in one day, and with larger availability.

13.2.1 ASSET-Chamber

The ASSET-chamber of the GDD lab located at CERN is used to characterise photocathodes of 2.5 cm diameter. This set-up is designed and operated by F. M. Brunbauer and M. Lisowska and is available to RD51 collaborators for measurements. The ASSET-Chamber has two different configurations for quantum efficiency measurements of a photocathode. The quantum efficiency and transparency can be measured either in reflective or in a transmissive mode. Ageing studies of the photocathodes with additional ion irradiation of the samples between reflective measurements are possible.

The ASSET-Chamber uses vacuum UV light emitted from a deuterium lamp (Model 632 Deuterium Lamp, McPherson [144]) to characterise the photocathode samples. A measured spec-

trum of the Deuterium lamp is shown in figure 13.3. Deuterium emits a spectrum with two peaks at 120 nm and 160 nm. The lamp is operated in a monochromator with different filters to select small wavelength bandwidth. The main part for the ASSET-Chamber is around 160 nm as the light emitted around 120 nm is cut off by the MgF_2 windows used to separate the volumes of the chambers. The measurement has to be performed in a vacuum as the oxygen in the air absorbs light with a wavelength shorter 200 nm. Each part of the set-up is placed in vacuum-tight vessels, and the system is pumped continuously with a turbopump. Pressure in the order of nanobar is maintained.

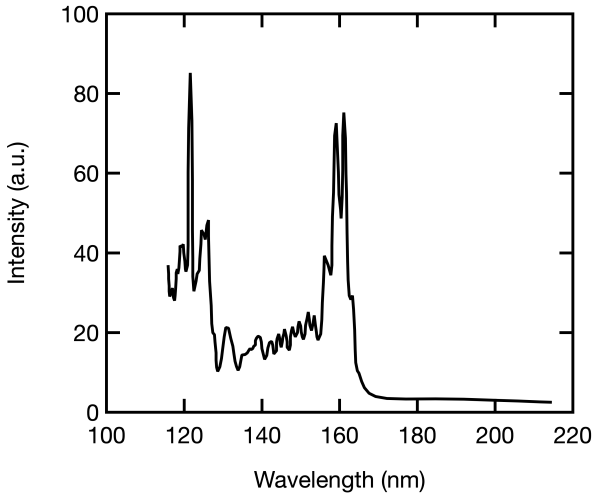

Figure 13.3: The spectrum of the Deuterium lamp has a peak at 120 nm and 160 nm. The 120 nm peak is cut-off during measurements by the MgF_2 windows used to separate the vessels. Spectrum measured by reference [145].

Figure 13.4 shows a photograph of the ASSET-Chamber placed in the laboratory. The blue container in the back contains the Deuterium lamp. The light is directed from the lamp to the lower central piece. This chamber contains a light splitter. Half of the light is directed in the lower front chamber. This chamber hosts a PMT and the mechanics for the transmissive measurement. The other part of the light is reflected in 90° in the top middle chamber. This chamber also hosts a PMT and the mechanics for reflective measurements of the photocathode. The left upper part can be used to store and exchange samples with the attached glovebox. The right part is used for the ion irradiation. This volume is decoupled and filled with an argon-$C0_2$ gas mixture for the ionisation process (see section 13.2.1). Samples can be moved remote controlled with an actuator between the irradiation chamber and the reflective measurement chamber.

Transmissive Measurements

Photons have to pass through the crystal substrate and the photocathode material for transmissive photoemission. This emission method is used in the PICOSEC-Micromegas. UV-light goes through the photocathode and emitting electrons on the opposite surface. The quantum efficiency and the transparency of Cherenkov radiator photocathode combinations can be measured

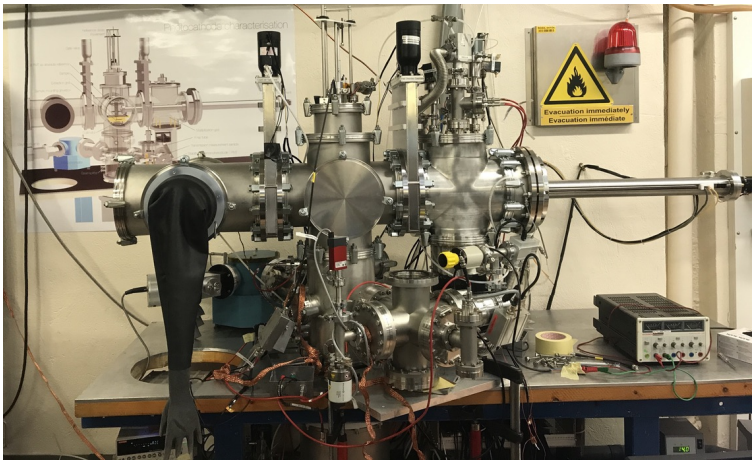

Figure 13.4: Photograph of the ASSER-Chamber installed in the laboratory. The upper middle part is used for reflective measurements. It is connected to the upper right part hosting a X-ray tube for ion irradiation. Transmissive measurements can be performed in the lower central part of the set-up.

with the ASSET-Chamber. Figure 13.5 shows a sketch of the measurement set-up for transmissive measurements. The split light goes to both PMTs of the ASSET-Chamber (see description of figure 13.4). The upper PMT in the empty chamber for reflective measurements is used as a reference, and the front chamber is used for the measurement.

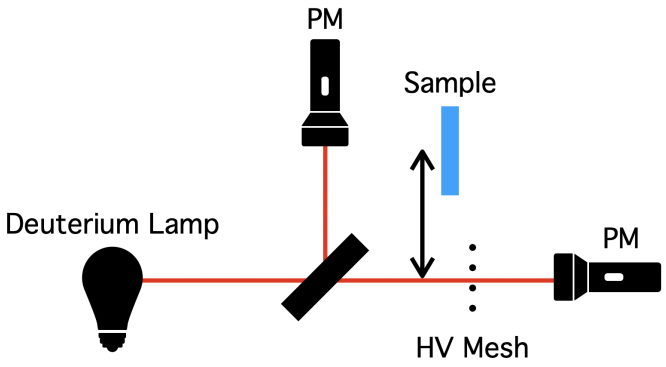

Figure 13.5: Sketch of the ASSET-Chamber set-up for measurements of photocathodes in transmissive mode.

The photocathode sample is placed in a moveable mounting structure, and the sample can be moved outside and inside the light beam without opening the vacuum vessel. A metal wire grid, similar to a MWPC, is placed in the beam in front of the sample. Figure 13.6 shows a photograph of the mechanical mounting with the metal grid in front. Thin cables connect the wire grid to a voltage supply and the photocathode to ground. A low electric field between the photocathode surface and the wire plane extracts the generated photoelectrons and amperemeter measure the flowing current from the photocathode. The measured current from the photocathode and the light

intensity measured with the PMTs is used to calculate the quantum efficiency of the photocathode at a given UV wavelength.

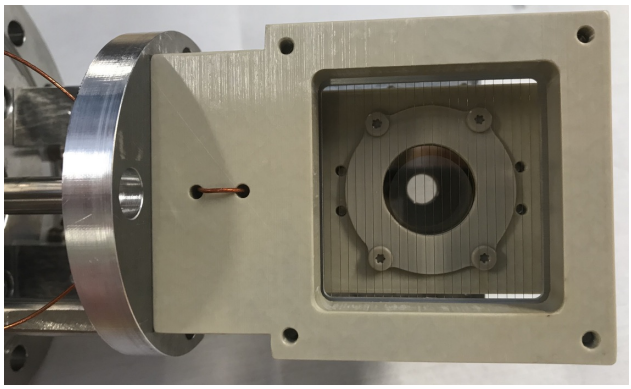

Figure 13.6: Photograph of the mechanical support structure of the photocathode with wire grid in front of the sample.

The measurement of a sample is done in two steps. First, the sample is moved outside the beam, and the whole beam intensity can reach both PMTs. The light intensity is measured with both PMTs for different light wavelengths in 10 nm steps. The number of photons reaching the PMT in each wavelength step ($N_{\text{ph.}}$) is calculated as

$$N_{\text{ph.}} = \frac{I_{\text{PMT}}}{e \cdot cal_{\lambda}} \, , \tag{13.1}$$

with I_{PMT} the current measured at the PMT; e the electron charge; and cal_{λ} a calibration factor for each wavelength, indicated in the datasheet of the PMT.

In the second step, a scan over the same wavelengths is performed with the sample moved into the beam. The current flowing from the sample to the wire grid (I_{sample}) is then measured at this step. After both measurements, the quantum efficiency for each wavelength is calculated as

$$QE_{\lambda} = \frac{N_{\text{e}}}{N_{\text{ph.}}} = \frac{\frac{I_{\text{sample}}}{e}}{\frac{I_{\text{PMT}}}{e \cdot cal_{\lambda}}} = \frac{I_{\text{sample}} \cdot cal_{\lambda}}{I_{\text{PMT}}} \, . \tag{13.2}$$

It is crucial for this method that the same amount of light reaches the sample in both measurement turns. The second PMT is used to correct light fluctuations between both runs, as the fluctuation appears in the same intensity in both PMTs.

A part of the light is passing through the sample in the transmissive mode. Even when the sample is inserted in the beam, a current can be measured in the PMT. The ratio of the PMT current without and with a sample gives the transparency of the sample additionally.

Reflective Measurements

The second measuring mode of the ASSET-Chamber can measure the quantum efficiency of photocathodes in reflective mode. The light is directly emitting electrons on the surface of the photocathode. Even thicker material with higher opacity can be measured in reflective mode, and the measured quantum efficiency is not affected by the transparency of the substrate window.

The ASSET-Chamber uses the top chamber from the splitter for the reflective measurements. Figure 13.7 shows a sketch of the measuring set-up. The previously used PMT for the transmissive measurement is now used as a reference PMT, with the photocathode inserted in dedicated mechanics in front of the upper PMT. Differently to the transmissive measurement, the high-voltage extraction wire mesh is placed before the photocathode, and the photocathode surface is facing towards the light beam. The light can hit the photocathode surface without passing through the crystals substrate and the whole photocathode layer.

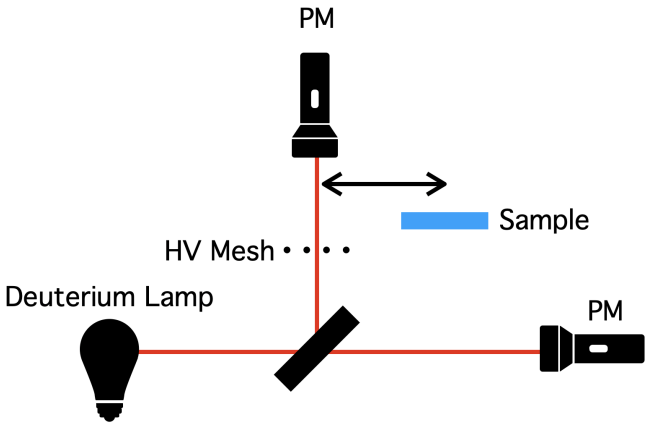

Figure 13.7: Sketch of the ASSET-Chamber set-up for measurements of photocathodes in reflective mode.

The measurement of the quantum efficiency is done in the same way as the transmissive mode measurements. The photocurrent flowing from the photocathode is put in relation to the photocurrent in the PMT without the sample. The second PMT, in the empty transmissive measurement chamber, is used as a reference to correct for fluctuations in the light intensity during the measurement.

The sample measured in the reflective measurement chamber is mounted to a moveable rod that is controlled remotely by an actuator. This rod can move the sample from the measurement chamber to an irradiation chamber. Both chambers and the movement mechanics can be seen in the upper part of figure 13.4. The sample can be automatically moved in the irradiation chamber to be irradiated with ions and afterwards moved back to the measurement chamber. Irradiation and measurement cycles can be programmed, and the degradation of the photocathode after irradiation can be studied.

Irradiation

Samples, measured in reflective mode, can be moved by the actuator in the adjacent chamber. This chamber is used to irradiate the probes with ions to study the ageing and robustness of the photocathode material. The irradiation is done with argon atoms ionised with an X-ray source. The schematic set-up of the irradiation chamber is shown in figure 13.8. The chamber is constantly flushed with a gas mixture of argon (70 %) and CO_2 (30 %), and the volume is sealed to the measuring chamber that is constantly pumped to maintain a proper vacuum.

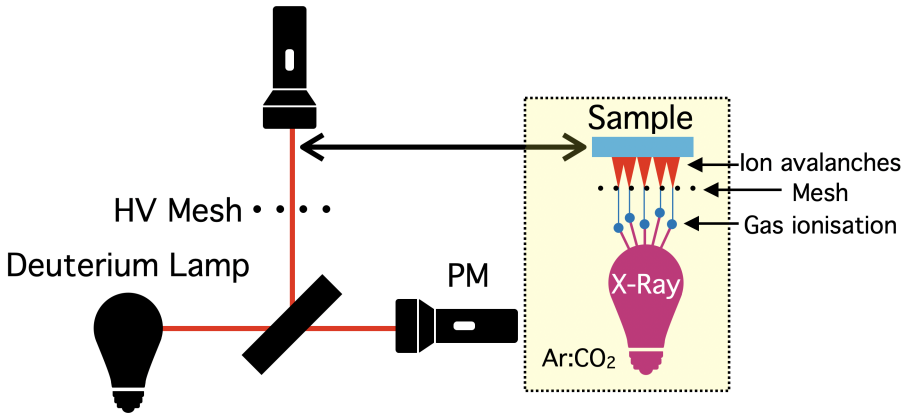

Figure 13.8: Sketch of the ASSET-Chamber set-up for ion irradiation. Ion avalanches are generated from argon ionised with an X-ray tube.

The irradiation set-up consists of an X-ray tube and multiplication wires placed between the tube and the photocathode sample. An electric field is generated between the grounded photocathode and the positively biased multiplication wires. The X-ray photons ionise argon atoms, and free-moving electrons are generated. Those electrons are accelerated towards the multiplication wires. The primary electrons create further electron-ion pairs and multiplication avalanches of ions form in the electric field towards the photocathode. The ion multiplication can be controlled by the field strength between the multiplication wires and the photocathode.

Automatised ageing studies can be performed with the ASSET-Chamber set-up and the connected irradiation and reflective measurement chambers. Several cycles of measurements and irradiations with pre-defined exposure time can be controlled with a LabView [146] interface. Those tests are essential for the study of robust photocathode materials.

13.2.2 Boron Carbide Measurements in the ASSET Chamber

The ASSET chamber is used to do comparative measurements of DLC and boron carbide (B_4C) with CsI to estimate the performance of B_4C photocathodes without an available particle beam. A boron doping of diamond and DLC changes its band gaps and thus reduces its ionisation energy [147, 148]. B_4C has a crystal structure similar to DLC and can be considered as very highly boron-

doped DLC. It is moreover an exceptionally hard material, which makes it an ideal candidate for a robust photocathode. It has after diamond with 0.6 the second hardest abrasive resistance with 0.4 (arbitrary unit) and is used due to its properties in many industrial applications [149]. First monochromator tests with 10 nm B_4C produced by the PICOSEC-Collaboration member group from USTC have shown better results than DLC and samples with different thickness are hereafter produced at CEA and tested in the ASSET set-up. The thin B_4C layers are not conductive enough for a directly biasing of the drift voltage and a small chromium substrate of 3 nm has to be placed between the window and the photocathode, similar to the CsI samples.

A 3 nm DLC sample that provides the best efficiency in the muon bean, and B_4C samples, with different thicknesses ranging from 1.6 to 32 nm, are studied in the ASSET chamber. The quantum efficiency is measured for these samples in transmissive mode between 135 and 170 nm wavelength, and the results are presented in figure 13.10a. The 4 nm thick B_4C sample provides the best quantum efficiency over the whole wavelength spectrum with one order of magnitude higher quantum efficiency than the DLC sample with comparable thickness. With a higher thickness of the B_4C the transmissive quantum efficiency is successively lower. The lower efficiency is explained with lower transparency and thus, fewer photons reaching the surface of the photocathode. The transparency of all samples are measured, and the results are given in figure 13.9. The different B_4C samples show a reduction in transparency with rising thickness. Only the thinnest B_4C sample shows abnormal transparency, which is on the same level as the chromium substrate. The measured quantum efficiency of this sample also behaves differently with a stronger loss in efficiency at wavelengths larger than 150 nm. This sample has probably a production error, as the time calibration for the growth of thin layers is difficult. Only after a certain time and a base layer of B_4C, continuous linear growth of the crystal structure begins.

The quantum efficiency of a reference CsI photocathode is additionally measured in the transmissive mode, and given by the black points in figure 13.10b. The measured quantum efficiency of CsI in the monochromator is one order of magnitude higher than the best-measured efficiency of B_4C and thus two orders of magnitude higher than the DLC. The relative performance of the photocathodes in the monochromator is different from the performance in the muon beam. The different extraction efficiency between DLC and CsI in the muon beam is only a factor 3. A possible explanation for this discrepancy is the secondary emission explained in section 13.3.

The best performance with a carbon-based photocathode is reached with the 4 nm thick B_4C photocathode. A growing of even thinner photocathodes was not successful. The B_4C samples provide a better quantum efficiency, than the DLC probe in the monochromator, but they do not reach the efficiency of the CsI. In the next step, the performance of the B_4C has to be measured in a particle beam to classify the whole potential of B_4C as a photocathode for PICOSEC-Micromegas. Additionally, refractive measurements in the ASSET chamber together with irradiation will be performed to study the robustness and possible performance losses of the DLC and B_4C photocathodes from ion bombardment. The PICOSEC-collaboration partners from USTC are performing parallel studies with DLC and B_4C which are not further discussed in this work [150].

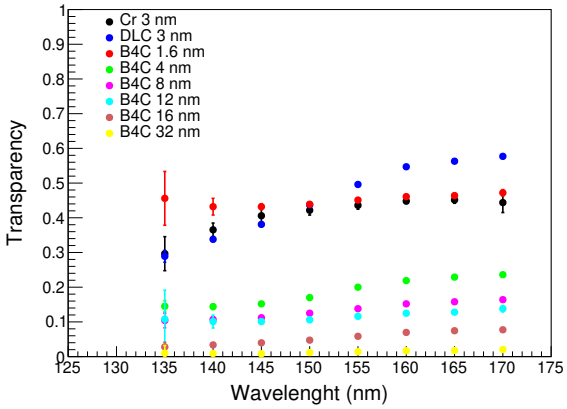

Figure 13.9: The transparency of the B4C samples gives an indication for its thickness. The 1.6 nm sample seems faulty as it has the same thickness as the chromium substrate.

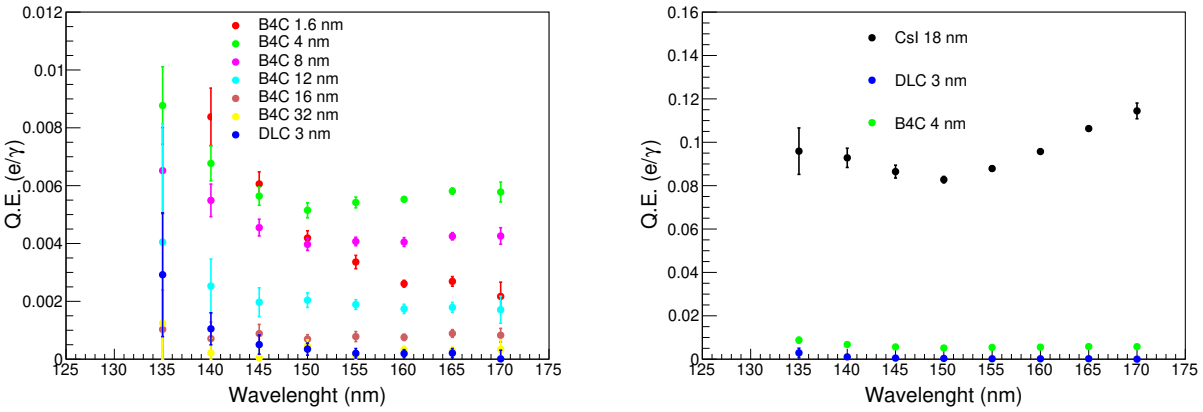

(a) QE for B_4C samples

(b) QE in relation to 18 nm CsI

Figure 13.10: Quantum efficiency measurements of B_4C samples with different thickness for wavelenghts of 135-170 nm. Figure b) shows the efficiency in relation to 18 nm CsI photocathodes on a 3.3 nm chromium substrate.

13.3 Secondary Emission

Another possibility of generating primary electrons is secondary emission. It is a process where electrons are emitted from the material surface by the direct energy transfer from the passing MIPs. The extraction probability depends on the energy loss cross-section of the passing particle and the energy band gaps of the target material. The secondary electrons are only emitted from the target material when they are created near the surface. The escape depth depends on the crystal structure of the target and can range from a few Ångström to several nanometers [151].

Secondary emitters are an alternative solution compared to the Cherenkov converter and the photocathode to generate the primary electrons in the PICOSEC-Micromegas. One potential material for robust secondary emitter is diamond. The Negative Electron Affinity (NEA) of diamond improves the extraction efficiency for secondary emission like for photoemission, and the escape depth and extraction yield depend on the crystal structure [137]. Previous studies have measured the secondary emission yields of CVD and single-crystal samples with different surface orientation for incident electrons in the keV range. All samples are providing the same electron transport properties, and the best extraction yield with higher surface adsorption properties is reached with single-crystals with a C(111) surface [152].

A 5 µm layer of boron-doped nanocrystalline diamond (DNCD) is tested as a secondary emitter in the muon beam. Figure 13.11 shows a photograph of the test sample, grown on a Silicone waver. The secondary emitter did not work correctly, and no signals were collected with this sample. A possible explanation for the malfunction might be the insufficient conductivity of the boron-doped diamond structure. Just like the photocathode, the secondary emitter is also the cathode for the drift field of the PICOSEC-Micromegas. A possible optimisation for the DNCD emitter is a thin conductive substrate, like the chromium substrate of the CsI photocathodes, to apply the electric field to the drift region.

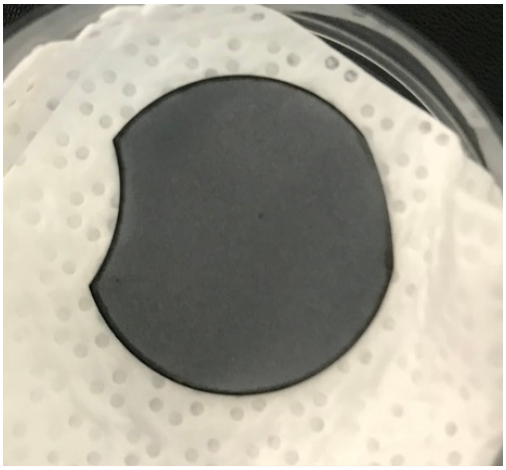

Figure 13.11: DNCD of 5 µm on a Silicone waver was tried as a secondary emitter without success.

Another potential secondary emitter is the nanoseeded diamond, tested in the particle beam in section 13.1.4. The diamond sample provides $\sim$2 photoelectrons per muon. A later measurement in the ASSET monochromator shows no measurable photocurrent. As diamond is likely to be a good secondary emitter, this results could direct to the solution, that the extracted electrons in the muon test are due to secondary emission. Secondary emission and photoelectric emission can also overlap and improve the total extraction efficiency of a material. The 2.5 nm DLC photocathode provides in the muon beam 3.7 photoelectrons per muons and the CsI photocathode provides a factor $\sim$3 more photoelectrons. In the ASSET measurement, the quantum efficiency of the CsI sample is a factor 10 better than the measured quantum efficiency of the DLC. Previous works have shown that DLC is a suitable secondary emitter [153], and one possible explanation for

the discrepancy of both measurements might be a secondary emission yield of DLC for 150 GeV muons.

More studies of secondary emitter for MIPs and of the contribution of secondary emission at photocathodes are necessary to estimate the full potential of secondary emitters for the PICOSEC-Micromegas. The main benefit of (diamond-based) secondary emitters is the robustness against ion-backflow at a high particle flux (see section 11.3.1) and the substitution of the Cherenkov radiator and thus a reduction in material. Further studies require the availability of a controllable MIP source, like a particle beam.

13.4 Electron Extraction at Different Electric Fields

The extraction efficiency of the photocathodes rises with the applied drift field. Previous studies have shown a similar behaviour at MWPCs [154]. At lower electric fields, the increase of the extraction efficiency is explained by the diffusion of the electrons after extraction. Due to elastic collisions with the gas, the extracted electrons are diffused back towards the photocathode and recombine on the surface. At higher electric fields, the directed momentum of the extracted electrons is higher, and they are less affected by diffusion. This effect is more pronounced for monoatomic gases like noble gases and less pronounced for quenching gases, as they tend to perform inelastic collisions with electrons. Another effect at high electric fields causing a better extraction efficiency is a reduction of the electron affinity of the conductive band (E_a). The quantum efficiencyof a photocathode (QE) is assumed to be proportional to the fraction of the photoelectron energy (E_pe) and the electron affinity. An approximation of this relation is given in literature [154] as

$$QE = \frac{1}{2}\left(1 - \sqrt{\frac{E_\mathrm{a}}{E_\mathrm{pe}}}\right)^2 . \tag{13.3}$$

The change of the electron affinity with the electric field (F) is given as

$$\Delta E_\mathrm{a} = \mathrm{e}\sqrt{\alpha \mathrm{e} F} , \tag{13.4}$$

where e is the electron charge and

$$\alpha = (\epsilon_\infty - 1)/(\epsilon_\infty + 1) , \tag{13.5}$$

with ϵ_∞ the specific high-frequent dielectric constand of the photocathode material.

Measurements with a fixed amount of light in the laser and variating drift fields are performed to study the behaviour of the photocathode extraction efficiency with rising drift voltages. The extracted number of photoelectrons is calculated based on the measured charge distribution, as explained in section 6.3. For the COMPASS gas mixture two attenuator settings are selected that provide 2 and 3 photoelectrons at a detector setting of $+275\,\mathrm{V}$ on the anode and $-550\,\mathrm{V}$ on the cathode. The measured number of photoelectrons as a function of the voltage is given in figure 13.12a. The measurements show an increase of the extracted number of photoelectrons with

rising drift voltages and constant amplification voltages, but it also shows an increase of the efficiency with an increasing total gain of the detector. At the same drift voltage, a detector with higher amplification voltage is measured with a higher number of photoelectrons. The same observation is repeated with other gas mixtures as given in figure 13.12b.

An increase of the photocathode extraction efficiency at higher electric fields is in favour of the improvement of the PICOSEC-Micromegas time resolution. The time resolution improves with higher drift field and also with the number of photoelectrons. The synergy of both effects can even be used to improve the PICOSEC-Micromegas time resolution. Further studies are necessary to describe and quantify better the effect of the drift and amplification field on the photocathode extraction efficiency.

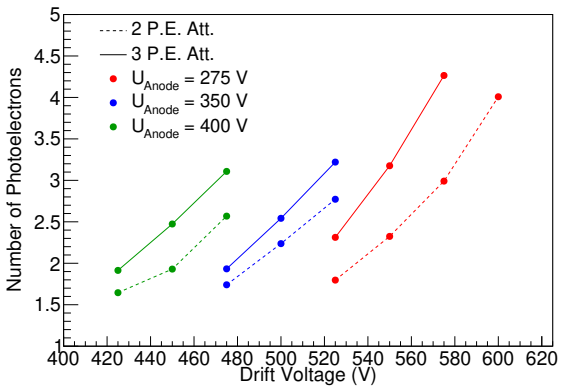

(a) COMPASS gas

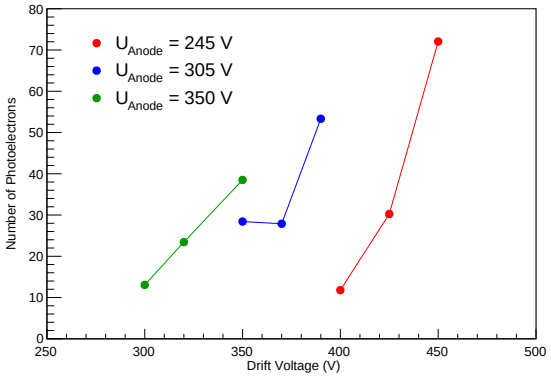

(b) Neon (89 %) - Ethane (2 %) - CF_4 (9 %), Attenuator No. 4.

Figure 13.12: Number of photoelectrons at different drift voltages.

13.5 Summary

The development of a robust photocathode with sufficient quantum efficiency is a crucial point in the development of a robust PICOSEC-Micromegas. The high ion-backflow, due to the $E_{\text{Drift}}/E_{\text{Anode}}$ ratio and the pre-amplification stage of the detector, leads to a high ion bombardment on the photocathodes and to potential damages (see section 11.3.1). This operation mode is necessary to achieve an optimal time resolution. Different photocathode materials are identified, suitable for different applications depending on the needs in quantum efficiency and robustness. CsI is the most efficient material that was tested with 10.4 ± 0.4 photoelectrons per muon. The most promising robust materials are carbon-based photocathodes like DLC, reaching 3.7 N_{pe}/µ, and boron-doped carbon (B_4C) that even surpasses the performance of DLC in the monochromator measurements in the ASSET set-up. Simpler materials, like thin layers of aluminium, are also suitable for photocathodes. The performance is even lower than DLC with only $\sim$2 N_{pe}/µ, but the production of these photocathodes is cheap and easy, and they are suitable for applications with a high amount of light, like the measurements in the laser.

The alternative development of secondary emitter for the PICOSEC-Micromegas needs to be studied more deeply. The first sample with DNCD did not provide any signals, and the further investigation was disrupted due to the limited availability of the beam. Another aspect that needs to be studied in the future is the secondary emission of the photocathode used in the beam. The DLC samples have shown better performance in the muon beam compared to the measurements in the monochromator when compared to the reference performance of the CsI, and the nanoseeded diamond did not provide any photocurrent in the ASSET. The development of a material with high secondary emission yield plays an essential role in the improvement of photocathodes for the detection of MIPs.

For different gases and an aluminium photocathode, a rise in the extracted number of photoelectrons with rising drift fields is observed. Moreover, the extracted number of photoelectrons depends on the total detector gain, and a higher amplification field also improves the extraction efficiency. The synergy between the improvement of the time resolution by increasing the drift field and in the same way extracting more photoelectrons needs to be studied for further improvements of the detector performance.

Epilogue

Alice: "Where should I go?",
The Cheshire Cat: "That depends on where you want to end up."

— Lewis Carroll (1832-1898), ***Alice's Adventures in Wonderland*** *(1865)*

14 Conclusion and Discussion

Contents

This chapter concludes the work and results of the development of the PICOSEC-Micromegas detection technology for fast timing in high-rate environments. Some missing aspects of a detector prototype for R&D development compared to a sub-detector for physics experiments are highlighted in section 14.1 and some possible future applications of the PICOSEC-Micromegas technology are presented in section 14.2.

The work presented in this thesis demonstrates the improvement of Micromegas time resolution of several orders of magnitude with the newly developed PICOSEC-Micromegas concept. The central aspect in the improvement of the time resolution is the localisation of the primary electrons and the reduction of the drift time jitter. This improvement is reached by adding a Cherenkov radiator with photocathode in front of the detector and reducing the distance of the photocathode to the mesh to the order of hundred micrometres provoking a pre-amplification avalanche in the drift region. A first prototype has demonstrated the proof-of-principle by reaching a time resolution as low as 24.0 ± 0.3 ps in a particle beam with 150 GeV muons. This result is reached with a drift field of 23.75 kV/cm and an amplification field of 21.48 kV/cm. In this unusual configuration, where the drift field is comparable to the amplification field, preamplification occurs in the short drift region of 200 µm. This detector was operated with a 18 nm CsI photocathode providing 10.40 ± 0.40 photoelectrons per muon and with the gas mixture used in the COMPASS experiment consisting of 80 % neon, 10 % ethane and 10 % CF_4.

Different studies are performed to investigate the individual steps in the detection and amplification process and to identify possible improvements. A mathematical modelling of the electron movement and multiplication is performed to identify the main processes in the detector that limit the time resolution. The modelling and GARFIELD++ simulation of the detector shows the time jitter of the single photoelectrons before starting the pre-amplification has the most significant impact on the time resolution. The main optimisation of the detector timing performance is achieved by optimising the drift region to reduce the initial drift length of the photoelectron.

A sequential optimisation of the detector is performed with different prototypes during several muons and laser beam tests. An improvement of the time resolution is measured with an increased voltage applied to the drift region. The voltage in the amplification region needs to be adapted to the higher drift field, to prevent the detector from reaching instabilities. An even higher increase of the drift field, with constant voltages, is achieved with reduced drift gaps down to 119 µm. With this configuration, a single photoelectron time resolution of 44 ± 1 ps is reached in the laser with a drift field of 44 kV/cm and an amplification field of 21 kV/cm. This is an improvement of 32 ps compared to the single photoelectron time resolution of the first prototype of 76.0 ± 0.4 ps with 200 µm drift distance, a drift field of 21 kV/cm and an amplification field of 35 kV/cm.

Another aspect that has an impact on the detector performance is the composition of the gas mixture. The best time resolution in all studies is reached with the COMPASS gas mixture used for the first prototype. A lower percentage of ethane increases the detector gain, and a lower voltage is needed to reach the Raether limit of the detector. The added quencher not only reduces the electron diffusion and thus the width of the electron peak, but also allows to apply higher fields to the detector. The added CF_4 is one key component for the increase of the electric fields. The detector can be operated with COMPASS gas up to 44 kV/cm in the drift, while a mixture with the same amount of neon and 20 % of ethane can only be operated with 39 kV/cm. A low electron diffusion and the possibility to apply high electric fields are the main aspects of the gas mixtures to reach good time resolution in the PICOSEC-Micromegas. Additional quenchers, like ethane, are moreover necessary to form precise electron peaks with sharp rising edges to determine the SAT.

The third aspect studied is the mesh technology used in the PICOSEC-Micromegas. Micromegas produced in the bulk technology with woven and electroformed meshes are tested together with microbulk detectors. The timing performance of the woven and electroformed meshes are not significantly different. This result is in agreement with the modelling of the detector, which concludes that the transition time of the electrons through the mesh only results in a constant delay of the SAT minor contribution to the time resolution. The microbulk Micromegas modifies the detector waveform, as it has production-wise a higher capacity in the amplification region. The tested microbulk detectors time resolution is worse than the one of the bulk detectors, but still reaches 50.1 ± 2.0 ps with a photocathode providing 10.40 ± 0.40 photoelectrons in the muon beam together with the other advantages of a microbulk detector, like the energy resolution.

After investigating and optimising each component of the PICOSEC-Micromegas regarding the timing performance, resistive PICOSEC-Micromegas prototypes are tested in muon and high rate pion beams. Resistive strip Micromegas with different resistivities and discrete resistive floating strip Micromegas are tested. The floating strip resistive detector reaches similar time resolution in the muon beam as the non-resistive PICOSEC-Micromegas, and the diffusion of the charge on the resistive strip Micromegas causes a degradation of the time resolution. All prototypes were operated in stable conditions for twelve hours in a pion beam with an average flux per spill of $\sim 2.2 \times 10^3$ pions per cm^2 per second, demonstrating the possibility of adapting the PICOSEC-Micromegas concept for robust detectors in high-rate environments.

The higher particle flux also produces a higher IBF in the detector, which is even more severe due to the electrons generated in the pre-amplification avalanche. The CsI photocathodes,

providing up to 10.40 ± 0.40 photoelectrons per muon, degenerate from the ion bombardment and a part of the PICOSEC-Micromegas development, focuses on the development of more robust photocathode materials with sufficient quantum efficiency. Different alternative photocathodes have been tested in the muon beam and a monochromator. The most promising material is DLC, reaching 3.7 photoelectrons per muon, and B_4C with even better results than the DLC in the ASSET monochromator. Also, pure metallic and nano-seeded diamond photocathodes are robust alternatives with lower quantum efficiency.

The PICOSEC-Micromegas detection concept is additionally adapted to prototypes with larger active areas and segmented anodes. The timing properties of the smaller prototypes are preserved with the multipad prototype with hexagonal segmented read-out. The construction and test of the first multipad prototype reveal the high demand in detector uniformity to preserve the timing performance. The read-out PCB shows slight distortions in the planarity, causing differences in the SAT of several 10 ps. Further demonstrators of (resistive) multipads are in preparation to investigate the full potential of the PICOSEC-Micromegas for future applications.

14.1 Towards Implementation in a HEP Experiment

Prototypes of the PICOSEC-Micromegas detection concept are presented in this work. Those prototypes are suitable to study the detector characteristics and to optimise its properties. However, these detectors are not yet suitable to be used as sub-detectors in physics experiments, and different detector aspects are missing for a useful particle detector. The direction of further developments strongly depends on the aimed applications, but some general aspects are presented in the following.

Most detectors used in physics experiments need to cover a larger area. The development of the multipad PICOSEC-Micromegas demonstrates the ability to use the detection concept for larger segmented read-outs. The design of large area PICOSEC-Micromegas detectors is mainly limited by the size and uniformity of the Cherenkov radiator and the photocathode. It is normal for experiments that the whole area is not covered by one single detector. Many modular sub-units of one detector are built, and these sub-units need to be interlinked with each other. The future development of a segmented PICOSEC-Micromegas needs to focus on high modularity. A mosaic-like PICOSEC-Micromegas would be one solution to cover a large area, where several sub-units are placed next to each other with low dead space as possible to optimise the filling factor of the active area.

Trackers in collider experiments are designed with a reduced mass of the detector and small dimensions. By this way, the interaction cross-section for the traversing particles in dead material is reduced and the sub-detector fits in the designated space between the other detectors and the beam pipe. Different “light-weight” versions of the chamber need to be developed depending on the requirements of the experiment. The development of modular detector planes and the reduction of the bulk material around the chamber are very close topics, and the improvement of both aspects can be linked together.

Another important aspect of the PICOSEC-Micromegas, as many early-stage detector prototypes, is the signal extraction. For the studies of the PICOSEC-Micromegas, the whole waveforms are digitised and later in an off-line analysis, the SAT and signal charge are extracted. This method is needed for the studies of the detector performance, as many pieces of information of the detector response are preserved. It is, on the other hand, very unpracticable for later use of the detector. This method creates a vast amount of data and computing capacities. Moreover, a rapid online process of the data is not possible, as it is needed for the trigger of other sub-detectors. A detector in an experiment is operated only in one setting, which is the optimal setting for the given application, and only the necessary information for the application need to be extracted.

There are electronic cards to extract and digitise different information, like the peak amplitude, the crossing of a threshold or the SAT extracted from a CFD, directly from the electric detector signal. Most available technologies are too slow to extract the correct information from the short PICOSEC-Micromegas signals with a rise time of some hundred picoseconds. Different techniques to extract the SAT with even faster electronic circuits need to be developed. One option is the development of integrated electrical cards that are directly connected to the read-out of the detector and that includes the amplifier and the digitiser, similar to the APV25 chips used in the beam telescope (see section 9.1.3). The amplifier described in section 12.5 is a good starting point for this further development.

After these studies to understand and optimise the detector performance, the next step is to develop a first demonstrator for a possible future application, where the previously raised missing aspects will be addressed. An outlook of possible applications of the PICOSEC-Micromegas is given in the following section.

14.2 Future Applications of Fast-Timing Detectors

The main objective in the study of the PICOSEC-Micromegas is the development of a timing detector meeting the requirements in time resolution and radiation hardness of the HL-LHC upgrade, as given in the introduction. The required time resolution of 20-30 ps with MIPs for a vertex separation in the inner tracker is reached with the presented prototypes and stable operation in the pion beam with up to 2.2×10^6 pions per spill is demonstrated with a resistive read-out. Under consideration of the development of segmented read-outs (see chapter 12) and the development of missing parts for a functional detector sub-system (see section 14.1), the PICOSEC-Micromegas is suitable for future (inner) tracking applications in classical collider experiments at the energy and luminosity range of the HL-LHC and above.

However the decisions for the upgrades of the LHC experiments were made when the PICOSEC-Micromegas project was still in an early stage, and it was not considered as a possible detector for the upgrades. The timing performance and properties of the PICOSEC-Micromegas are suitable for other applications like particle tagging in a calorimeter and time-of-flight particle identification. Examples for this kind of applications are presented in the following sections.

14.2.1 Timing in Electromagnetic Calorimeters

Adding timing properties to electromagnetic calorimeters is a good use-case for the PICOSEC-Micromegas concept, as several photons are formed in the Cherenkov radiator by secondary relativistic electrons in an electromagnetic shower. At these high amounts of light, even the photocathodes with lower quantum efficiency, like aluminium or DLC, will produce enough photoelectrons to obtain a good time resolution. Such photocathodes are also very robust and withstand the ion-backflow at the high particle rate in an electromagnetic shower. The number of photoelectrons produced in a PICOSEC-Micromegas used in an electromagnetic calorimeter is estimated with the equation 5.5 in section 5.2. An electron with a momentum of 5 GeV produces approximately 84 photoelectrons in a MgF_2 window of two radiation lengths thickness ($X_0 = 9.744$ cm [41]) and a B_4C photocathode with the quantum efficiency measured in the ASSET chamber in section 13.2.2. With a PICOSEC-Micromegas that provides a single photoelectron time resolution of ∼44 ps (see section 8.2), the time resolution in the calorimeter could reach down to ∼5 ps.

An electromagnetic calorimeter with good time resolution improves the particle identification capability. One example for this use is the tagging of the production time and flavour of neutrinos in the Enhanced NeUtrino BEams from kaon Tagging (ENUBET) project [155]. This research project aims to develop a neutrino source based on positron tagging from Kaon decays ($K^+ \rightarrow e^+\pi^0\nu_e$). The positrons are expected to be created with a rate of 200 kHz/cm^2 and a separation from background pions with an accuracy better than 3 % is required. This rejection is achieved with a longitudinal segmented electromagnetic calorimeter, based on radiation-hard components and a time resolution in the order of some 10 ps [155]. The PICOSEC-Micromegas detection concept is the ideal candidate for this application.

14.2.2 Time-of-flight Particle Identification

Finally, the PICOSEC-Micromegas can be used for time-of-flight (TOF) particle identification (PID). One application for PID is the background suppression at the future Electron-Ion Collider (EIC) build in Brookhaven, where the majority of the hadrons expected at the EIC will be in a momentum range of 0.5 to 5 GeV [156]. Relativistic particles with different mass at rest need different time to travel a certain distance. The time difference of the TOF can be used for the discrimination between different particles at a certain momentum. The TOF difference (Δt) between two particles with a relativistic momentum of p after a flight distance of L is calculated as

$$\Delta t = \frac{L}{c}\left(\frac{1}{\beta_1} - \frac{1}{\beta_2}\right) , \tag{14.1}$$

where c is the speed of light and β_1, β_2 are the relativistic velocity factor given as

$$\beta = \sqrt{1 + \frac{1}{\gamma^2}} = \sqrt{1 + \frac{m^2c^2}{p^2}} , \tag{14.2}$$

where γ is the Lorentz factor and m is the mass at rest of the particle. For the discrimination of two particles with different mass and the same relativistic momentum, the TOF difference is written as

$$\Delta t = \frac{Lc}{2p^2}\left(m_1^2 - m_2^2\right) \ . \tag{14.3}$$

Several meters are a typical distance between two detectors for TOF PID in physics experiments. As an example, the time difference for different particle pairs up to 20 GeV/c and a flight distance of 4 m is given in figure 14.1. The solid black line marks the best measured time resolution of the PICOSEC-Micromegas in a particle beam (24 ps) and the dotted and dashed lines the 2 and 3 σ value of the time resolution. For accurate discrimination, the time difference should be at least 3σ of the detector time resolution. Particle pairs with a low mass difference are only discriminated with lower momentum. The discrimination of e/π, e/μ and μ/π with PICOSEC-Micromegas detectors at 4 m distance is only possible for less than 2 GeV/c, while the discrimination of these lighter particles with protons is possible up to 9 GeV/c. Current used TOF detectors like the ALICE TOF detector with MRPCs in 4 m distance reaches a 3σ separation between K/π up to 2.5 GeV/c and for K/p up to 4 GeV/c [157]. The PICOSEC-Micromegas achieves a separation up to double the momentum with sufficient robustness for the high secondary particle flux generated at Pb-Pb collisions, like in the ALICE experiment. The expected performance of the PICOSEC-Micromegas would fulfil the requirements of the EIC with a K/π separation of up to 5 GeV/c [156].

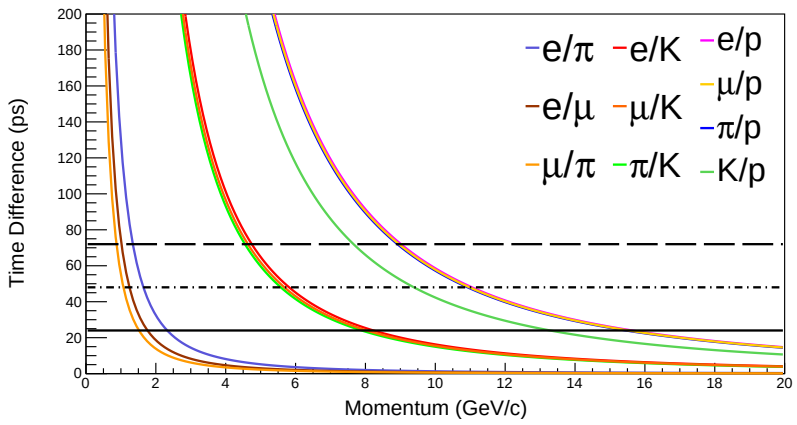

Figure 14.1: Time resolution for TOF particle identification at 4 m detector distance. The black line in the time resolution of the PICOSEC-Micromegas (24 ps), the short dashed line is 2σ of the PICOSEC-Micromegas time resolution and the long dashed line is 3σ.

The distance between the detectors is an easy way to increase the maximal discrimination momentum, and it is an aspect that needs to be decided in an early stage during the planning of a new experiment. Figure 14.2 shows the maximal discrimination momentum at different detector distances for common particle pairs. The solid lines give the detector distance under consideration of 24 ps time resolution and the dashed line gives the distance for 3σ. At reasonable detector distances for modern experiments, like 20 m a discrimination with 3σ of the PICOSEC-Micromegas

time resolution is possible for 2 GeV/c μ/π pairs and up to 20 GeV/c for e/p pairs. The TOF PID is an interesting application for PICOSEC-Micromegas detectors, as it provides a sufficient time resolution and the necessary robustness to be operated at high particle flux.

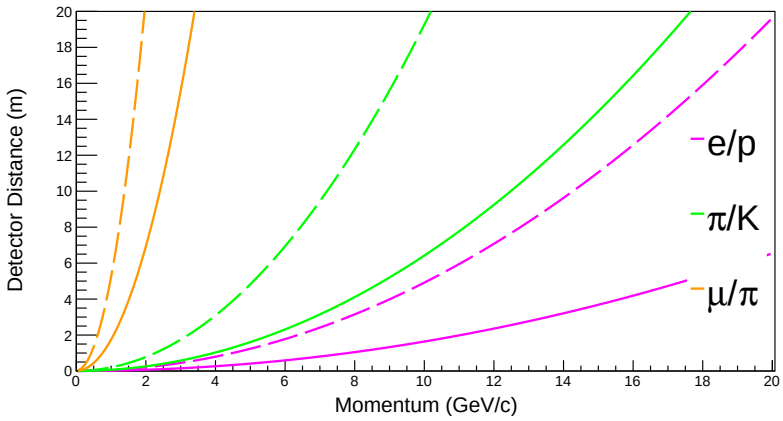

Figure 14.2: Required detector distance for separation of particles at different momentum with 3σ (dashed line) and σ (solid line) time resolution of the PICOSEC-Micromegas.

14.3 Final Remarks

The presented work shows the potential of MPGDs for fast-timing applications. The PICOSEC-Micromegas detection concept reaches well under 100 ps time resolution under various conditions with the potential in robustness and read-out versatility not yet exhausted. With continuous development and first applications, the PICOSEC-Micromegas might be a solution for many future tasks in HEP and beyond. It is a detection concept serving unique requirements in time resolution, detection efficiency and robustness, and it might develop to a strong competitor to other well-proven fast-timing detection concepts like SiPMs and MCP-PMTs. This work provides new insights into the behaviour of fast-timing gaseous detectors and paves the way for further developments and optimisations. The PICOSEC-Detector and its possible future applications are serving as another piece in solving the question “whatever holds, the world together in its inmost folds”.

15 Résumé en Français

Contents

15.1 Contexte Scientifique

Dans le cadre des futures expériences de physique des particules du HL-LHC au CERN, des nouveaux détecteurs de particules sont nécessaires. Pour la mise à niveau du HL-LHC, une résolution temporelle des détecteurs de traces internes de 20-30 ps est nécessaire pour une séparation précise des vertex, tandis que la luminosité devrait augmenter jusqu'a ∼5-10 x 10^{34} $cm^{-2}s^{-1}$ [3]. On rappelle qu'un détecteur de particules est utilisé pour détecter le passage d'une particule et obtenir des informations telles que sa position, son impulsion, ou son temps de passage dans le détecteur. Le détecteur PICOSEC-Micromegas relève ce défi. Cette thése a pour but d'optimiser les différents paramètres de ce détecteur, pour obtenir les meilleures performances possibles.

15.1.1 Micromegas

Le Micromegas (MICRO-MEsh GAseous Structure) est un concept moderne de détecteur gazeux introduit en 1996 [52] par le groupe de I. Giomataris et G. Charpak. Un détecteur Micromegas

consiste en un volume gazeux avec deux champs électriques séparés par une grille conductrice. La figure 15.1 montre une esquisse du principe de fonctionnement du Micromegas. Les particules qui passent à travers le détecteur ionisent le gaz et les électrons libres du gaz créent une amplification par avalanche dans un champ électrique puissant. L'espace de dérive entre la cathode et la grille est la région de conversion où se produit l'ionisation primaire, tandis que l'espace entre la grille et l'anode est la région d'amplification où les électrons sont multipliés et le signal induit. Le volume de détection est au moins un ordre de grandeur plus grand que le volume d'amplification dans la plupart des applications.

Les Micromegas, et les MPGD en général, ne peuvent pas atteindre la résolution temporelle sub-nanoseconde requise pour la séparation des MIP lors des futures expériences HEP. Le processus d'ionisation et la dérive initiale des électrons primaires limitent la résolution temporelle. Une particule forme plusieurs groupes d'ionisation lorsqu'elle traverse la région de dérive du détecteur. Le nombre d'électrons et leur emplacement sont distribués en fonction de la longueur d'ionisation moyenne de la particule dans le milieu gazeux donné. L'emplacement d'ionisations peut varier d'environ 100 µm pour un MIP, ce qui affecte la distance entre le dernier ionisation et la grille. Le type de gaz et le champ électrique limitent la vitesse de dérive des électrons. L'emplacement différent du dernier groupe et la vitesse de dérive limitée se traduisent par une gigue temporelle des électrons lorsqu'ils atteignent la grille. Cet effet est illustré dans la figure 4.5. Deux particules passant simultanément à travers le détecteur sont symbolisées par les lignes vertes. Les points rouges sont des groupes d'électrons primaires ionisés formés dans la fente de dérive. Ces groupes d'ionisation sont statistiquement répartis le long de l'écart de dérive et la distance entre le dernier ionisation et la grille varie. Dès que les électrons entrent dans la phase d'amplification, une avalanche d'ionisations se forme. L'étalement dans le temps de la propagation de l'avalanche peut être négligé par rapport à la gigue temporelle de la dérive d'un seul électron, car la longueur de l'avalanche est inférieure d'un ordre de grandeur à la dérive.

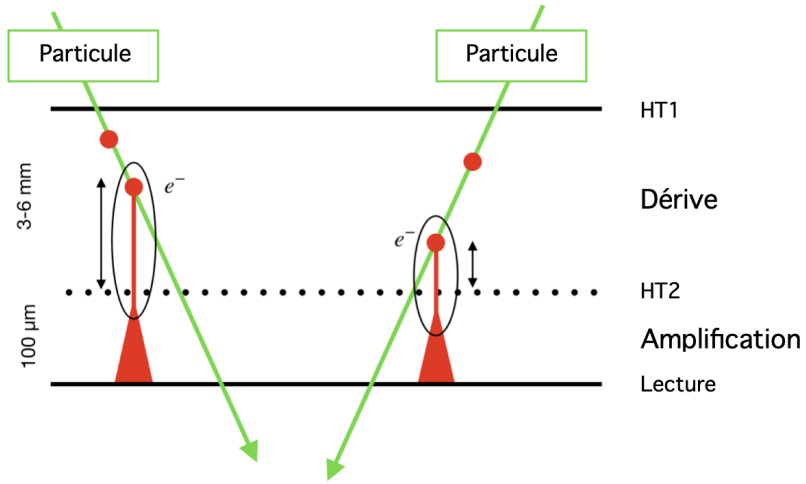

Figure 15.1: La résolution temporelle du détecteur Micromegas est limitée par les différentes distances entre les derniers ionisations et la région d'amplification.

15.2 PICOSEC-Micromegas

L'idée principale du concept PICOSEC-Micromegas est de supprimer l'inévitable gigue temporelle de l'ionisation dans un Micromegas classique, due aux différentes positions des ionisations [5]. La figure 15.2 illustre le concept de détecteur PICOSEC-Micromegas. Un radiateur Tchérenkov [92] et une photocathode sont placés devant le volume gazeux. Le passage d'une particule chargée à travers le radiateur de Tchérenkov produit des photons UV, qui sont ensuite absorbés dans la photocathode et des électrons primaires sont créés sur la surface inférieure de la photocathode. Ces électrons sont ensuite préamplifiés puis amplifiés dans les deux étages de champ élevé, et induisent un signal qui est mesuré entre l'anode et la grille.

Les électrons émis à la surface de la photocathode subissent le même champ électrique sur la même distance que la grille. Le volume gazeux n'est nécessaire que pour amplifier les électrons et induire un signal lisible sur l'anode. On choisit un détecteur de type Micromegas avec une grille mise à la terre entre deux champs électriques dont les lignes de champ sont parallèles. Une tension négative est appliquée à la cathode et une tension positive à l'anode pour fournir un champ électrique unidirectionnel dans les deux régions.

La région de dérive est beaucoup plus longue que la région d'amplification dans un Micromegas classique. Dans le PICOSEC-Micromegas, l'espace de dérive est réduit au même ordre que l'espace d'amplification. L'écart de dérive est exploité avec un champ électrique similaire à celui de l'espace d'amplification. Dans cette configuration de champ, une première préamplification des électrons se produit dans l'espace de dérive, améliorant la résolution temporelle car elle réduit le temps de dérive des électrons primaires. Même si les écarts dans le PICOSEC-Micromegas ont des objectifs différents de ceux d'un Micromegas classique, ils seront appelés espace de dérive et d'amplification.

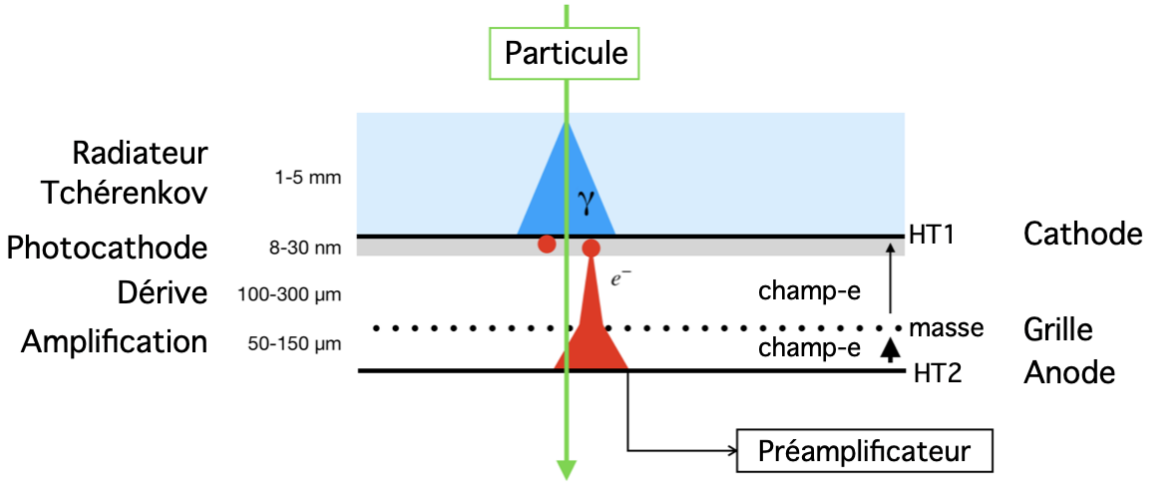

Figure 15.2: Le concept de détection PICOSEC-Micromegas, décrit en détail dans le texte.

15.2.1 Prototypes

Différentes chambres d'essai et prototypes du concept PICOSEC-Micromegas ont été développés. Chaque prototype est conçu pour tester et optimiser des caractéristiques particulières du détecteur. Deux prototypes universels ont été conçus pour les études de caractérisation, tandis que des prototypes spécialisés résistives et multipads ont été mis au point pour étudier la possibilité d'utiliser le PICOSEC-Micromegas pour de futures applications. Toutes les chambres sont modulaires et peuvent accueillir différents plans de lecture des détecteurs, comme les détecteurs bulk Micromegas avec des maillages tissés et électroformés, ou les détecteurs de microbulk.

Les principales différences entre les chambres sont la taille et l'accessibilité à la photocathode. De petits prototypes pouvant accueillir des détecteurs de 1 cm de diamètre et des prototypes plus grands, avec des anodes segmentées jusqu'à 5 cm de diamètre de surface active totale, sont construits. Les détecteurs sont modulaires avec un accès facile et rapide à tous les composants sont avantageux pour les études de R&D, car plusieurs composants sont testés et remplacés pendant les mesures.

15.3 Caractérisation

Les prototypes de PICOSEC-Micromegas se caractérisent par trois configurations de mesure différentes. Les trois principaux dispositifs sont un monochromateur au CERN, pour mesurer l'efficacité quantique (e.q.) des photocathodes; le dispositif laser au CEA, pour tester les prototypes PICOSEC-Micromegas avec un nombre contrôlé de photoélectrons; et le faisceau de particules à la ligne d'extraction CERN-SPS, pour tester les prototypes PICOSEC-Micromegas avec des MIP et dans des conditions de haut flux. D'autres modélisations détaillées du détecteur sont réalisées à l'aide de GARFIELD++ [98] et de simulations numériques de Monte-Carlo.

15.3.1 Modélisation

Une modélisation mathématique du mouvement et de la multiplication des électrons est effectuée pour identifier les principaux processus dans le détecteur formant la résolution temporelle. Une modélisation mathématique et une simulation GARFIELD++ du détecteur sont effectuées [95, 96, 97]. La figure 15.3 montre le temps de transmission et la résolution temporelle du détecteur PICOSEC-Micromegas pour différentes longueurs d'avalanche. Les lignes sont calculées avec le modèle mathématique et les points sont les résultats extraits de la simulation GARFIELD++. La modélisation est en bon accord avec la simulation.

La résolution temporelle du PICOSEC-Micromegas est définie par la longueur de la dérive d'un seul photoélectron avant le démarrage de l'avalanche de pré-amplification. L'avalanche a une vitesse de dérive moyenne plus rapide que celle du photoélectron unique et la variance du temps de transmission reste constante sur la longueur de l'avalanche, tandis que la variance du temps de transmission du photoélectron s'améliore pour les courtes longueurs de dérive. L'impact de

la longueur de la région de dérive sur la résolution temporelle est étudié plus en détail avec un prototype PICOSEC-Micromegas dans le faisceau laser.

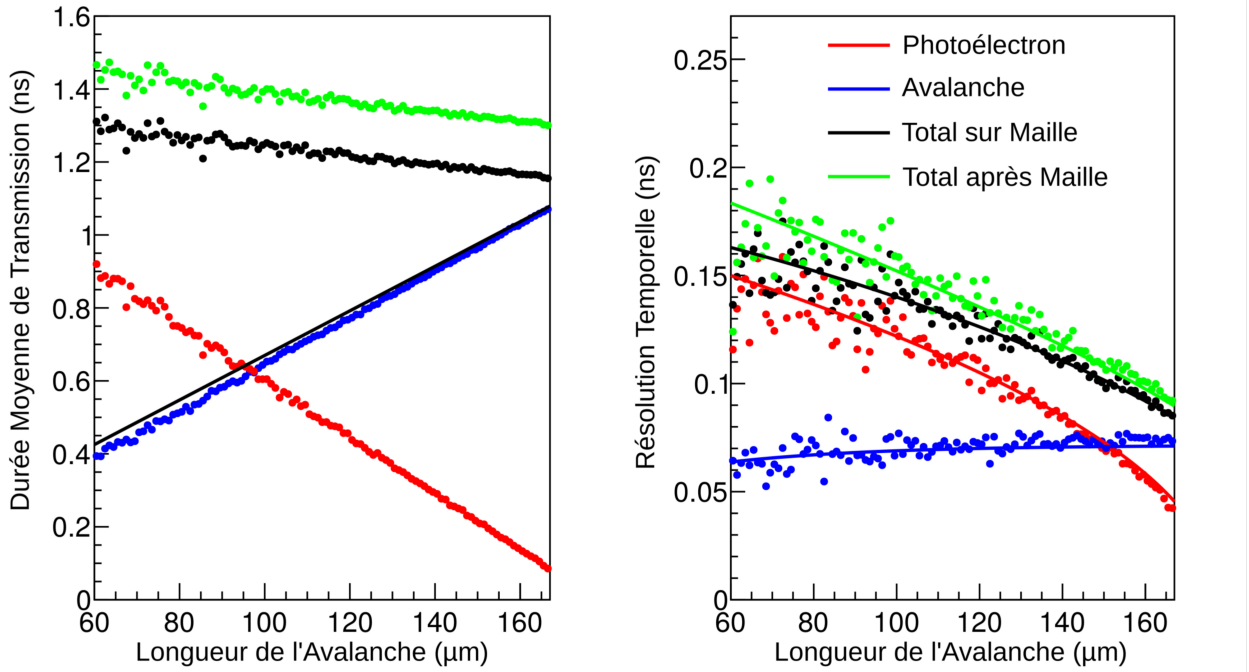

Figure 15.3: Temps de signal modélisé en fonction de la longueur de l'avalanche pour un champ de dérive de 350 V, comparé aux points générés par Garfield++.

15.3.2 Espace de Dérive et Mélange de Gaz

La principale optimisation des performances de synchronisation du détecteur est obtenue en optimisant la région de dérive pour réduire la longueur de dérive initiale du photoélectron. Une optimisation séquentielle du détecteur est réalisée avec différents prototypes au cours de plusieurs tests de muons et de faisceaux laser. Une augmentation de la résolution temporelle est mesurée avec une tension augmentée appliquée à la région de dérive. La tension dans la région d'amplification doit être adaptée au champ de dérive plus élevé, afin d'éviter que le détecteur n'atteigne des instabilités. Une augmentation encore plus grande du champ de dérive, avec des tensions constantes, est obtenue avec des espaces de dérive réduits jusqu'à 119 µm. Avec cette configuration, une résolution temporelle de 44 ± 1 ps est atteinte dans le laser avec un champ de dérive de 44 kV/cm et un champ d'amplification de 21 kV/cm. C'est une amélioration de 32 ps par rapport à la résolution temporelle du premier prototype de $76{,}0 \pm 0{,}4$ ps avec une distance de dérive de 200 µm, un champ de dérive de 21 kV/cm et un champ d'amplification de 35 kV/cm [106].

Une autre façon d'optimiser les performances du détecteur est de varier la composition du mélange de gazeaux. Le tableau 15.1 donne la résolution temporelle de différents mélanges

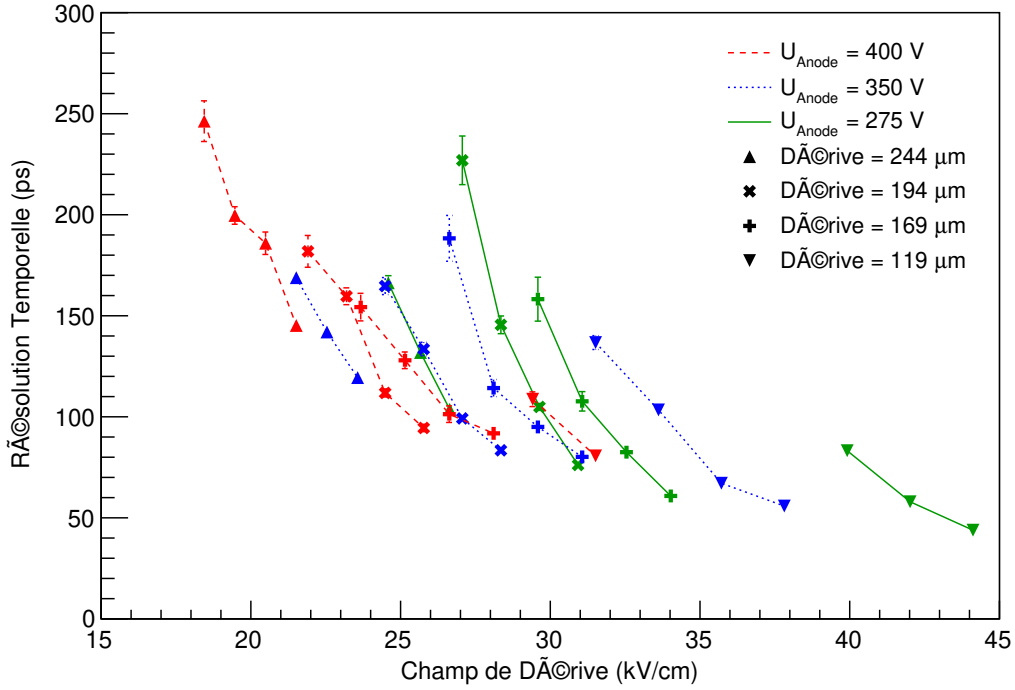

Figure 15.4: Résolution temporelle en fonction du champ de dérive pour différents écarts de dérive sous des conditions de photoélectrons uniques. L'écart d'amplification est de 128 µm de profondeur.

Table 15.1: Résolution temporelle des différents mélanges de gaz dans la meilleure configuration de champ et dans des conditions de photoélectrons uniques.

Mélange de gaz (%) (Neon-Ethane-CF_4)	$U_{\text{dérive}}$ (V)	U_{anode} (V)	Courant de e-pic (pC)	Amplitude (mV)	Résolution temporelle (ps)
80-10-10	525	275	$8{,}58 \pm 0{,}13$	$166{,}3 \pm 0{,}20$	$43{,}89 \pm 1{,}00$
89-2-9	445	255	$1{,}69 \pm 0{,}01$	$31{,}56 \pm 0{,}44$	$112{,}15 \pm 4{,}03$
80-20-0	470	270	$0{,}54 \pm 0{,}01$	$21{,}61 \pm 0{,}18$	$129{,}21 \pm 6{,}03$
85-15-0	395	310	$0{,}74 \pm 0{,}01$	$22{,}83 \pm 0{,}21$	$113{,}48 \pm 4{,}66$
90-10-0	340	340	$0{,}82 \pm 0{,}01$	$20{,}72 \pm 0{,}09$	$150{,}23 \pm 3{,}17$
95-5-0	375	230	$1{,}13 \pm 0{,}01$	$22{,}98 \pm 0{,}16$	$181{,}09 \pm 8{,}91$

de néon-éthane sous condition d'un seul photoélectron. La meilleure résolution temporelle dans toutes les études est obtenue avec le mélange gazeux de COMPASS [66] utilisé pour le premier prototype. Un pourcentage plus élevé de néon augmente le gain du détecteur, et une tension plus faible est nécessaire pour atteindre la limite de Raether du détecteur. L'ajout d'un quencheur réduit non seulement la diffusion des électrons et donc la largeur de leur pic, mais permet également d'appliquer des champs plus élevés au détecteur. L'ajout de CF_4 est un élément clé pour

l'augmentation du champ électrique. Le détecteur peut fonctionner avec le gaz COMPASS jusqu'à 44 kV/cm dans la dérive, alors qu'un mélange avec la même quantité de néon et 20 % d'éthane ne peut fonctionner qu'avec 39 kV/cm. Une faible diffusion des électrons et la possibilité d'appliquer des champs électriques élevés sont les principaux aspects des mélanges de gaz pour atteindre une bonne résolution temporelle dans le PICOSEC-Micromegas. Des quencheurs supplémentaires, comme l'éthane, sont en outre nécessaires pour former des pics d'électrons précis avec des arêtes montantes nettes afin de déterminer le SAT.

15.4 Optimisation

Après avoir étudié et optimisé chaque composant du PICOSEC-Micromegas en ce qui concerne les performances de resolution temporelle, d'autres prototypes sont développés pour optimiser le détecteur. L'objectif principal de cette optimisation est la préparation du concept de détection pour de futures applications. La plupart des détecteurs utilisés dans les expériences de physique doivent couvrir une plus grande surface. Le développement du PICOSEC-Micromegas à multipad démontre la capacité d'utiliser le concept de détection pour des lectures segmentées plus importantes. Un objectif du développement de PICOSEC-Micromegas est la mise au point d'un détecteur de temps répondant aux exigences de résolution temporelle et de dureté de rayonnement de la mise à niveau du HL-LHC, comme indiqué dans l'introduction. À cette fin, des prototypes résistifs de PICOSEC-Micromegas sont testés dans des faisceaux de muons et de pions à haut flux et des photocathodes robustes sont étudiées.

15.4.1 Multipad

L'adaptation du principe de détection PICOSEC-Micromegas pour une lecture segmentée est une étape cruciale dans la transition entre la recherche de nouvelles techniques de détection et le développement de sous-détecteurs pour les expérimentations de physique. La plupart des applications des détecteurs rapide nécessitent la préservation des informations de position de la particule incidente, qui ne sont accessibles qu'avec des lectures segmentées. Un premier prototype de PICOSEC-Micromegas à multipad hexagonales est développé et testé dans un faisceau de muons. Une photographie du prototype pendant l'assemblage, avec lecture hexagonale visible, est présentée dans la figure 15.5. Les premiers tests avec le multipad ont démontré que l'adaptation du principe PICOSEC-Micromegas à des zones actives plus grandes est possible et que des résolutions temporelles du même ordre de grandeur qu'avec le PICOSEC-Micromegas à simple pad sont possibles. La principale préoccupation du développement des détecteurs PICOSEC-Micromegas à grande surface est l'uniformité du champ. Le circuit imprimé de lecture du premier prototype multipad semble être deformé en raison de la contrainte mécanique du circuit imprimé monté sur la chambre. La flexion radiale de la carte de circuit imprimé de plusieurs dixièmes de µm provoque un retard progressif du SAT de 20 ps pour chaque 1 cm de rayon supplémentaire à partir du centre.

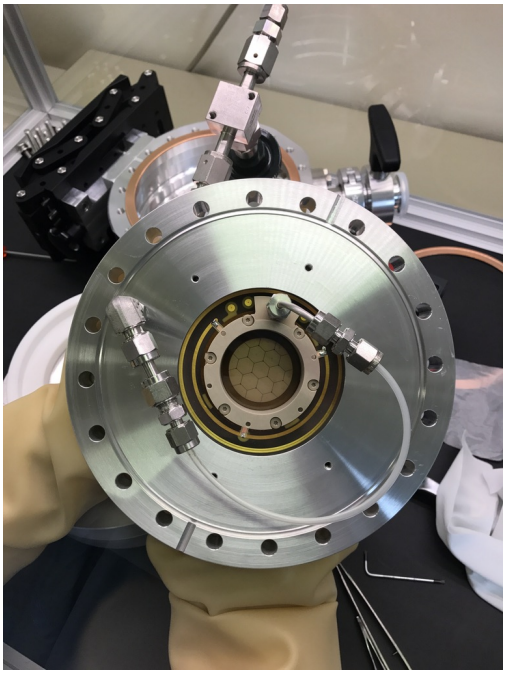

Figure 15.5: Photo de la chambre multipad pendant l'assemblage dans la salle blanche.

15.4.2 Résisitve Micromegas

L'objectif du projet PICOSEC-Micromegas est le développement d'un détecteur rapide pour les environnements à haut flux comme le HL-LHC avec une luminosité attendue de ∼5-10 x 10^{34} $cm^{-2}s^{-1}$ [3]. Une construction de détecteur résistif est nécessaire pour faire fonctionner le PICOSEC-Micromegas dans un tel environnement avec des champs électriques élevés, car la probabilité de claquage du détecteur peut être réduite en ajoutant une couche résistive sur l'anode. La couche résistive réduit le courant de décharge, et la propagation de claquage. Deux technologies résistives différentes de Micromegas ont été testées: bande résistive en deux configurations avec 82 MΩ/□ et 292 kΩ/□, et anode à bande flottante avec une résistance discrète de 25 MΩ. Tous les prototypes résistifs ont fonctionné dans des conditions stables pendant douze heures dans un faisceau de pion avec une intensité de $2,2 \times 10^6$ pions par déversement, démontrant la possibilité d'adapter le concept PICOSEC-Micromegas pour des détecteurs robustes dans des environnements à haut débit [127].

Dans l'ensemble, les propriétés temporelles du concept PICOSEC-Micromegas sont préservées lors des lectures résistives. En particulier, la lecture à bande flottante avec une résistance discrète de 25 MΩ atteint 28,8 ± 0,2 ps, soit une résolution temporelle dans un faisceau de muons similaire à celle de l'équivalent non résistif. De toute façon, en raison de la résistivité, une tension plus élevée doit être appliquée pour atteindre la performance donnée. Un fonctionnement stable dans un faisceau d'ions à haut flux est également possible lorsque le gain du détecteur est réduit, avec une résolution temporelle plus mauvaise. La différence de résolution temporelle entre le fonctionnement dans un faisceau de pion et de muon est plus faible pour les détecteurs à résistivité

plus élevée. La résistivité de 82 MΩ/□ ne nécessite qu'une réduction de gain de 30 % et atteint une résolution temporelle nettement inférieure à 100 ps.

Le reflux d'ions (IBF) atteignant la cathode devient un problème grave à haut débit en raison des ions produits dans la préamplification. Le bombardement d'ions sur la photocathode entraîne des dommages importants sur les matériaux fragiles comme le CsI. La figure 15.6 montre une photocathode CsI après fonctionnement dans un faisceau de pion à haut flux. Une image négative de la grille et des piliers est projetée sur la photocathode en raison de l'IBF et des claquages supplémentaires endommagent la surface. Le développement de photocathodes alternatives robustes à haut rendement quantique est essentiel pour le développement futur de PICOSEC-Micromegas qui sera exploité pendant longtemps dans des environnements à haut flux.

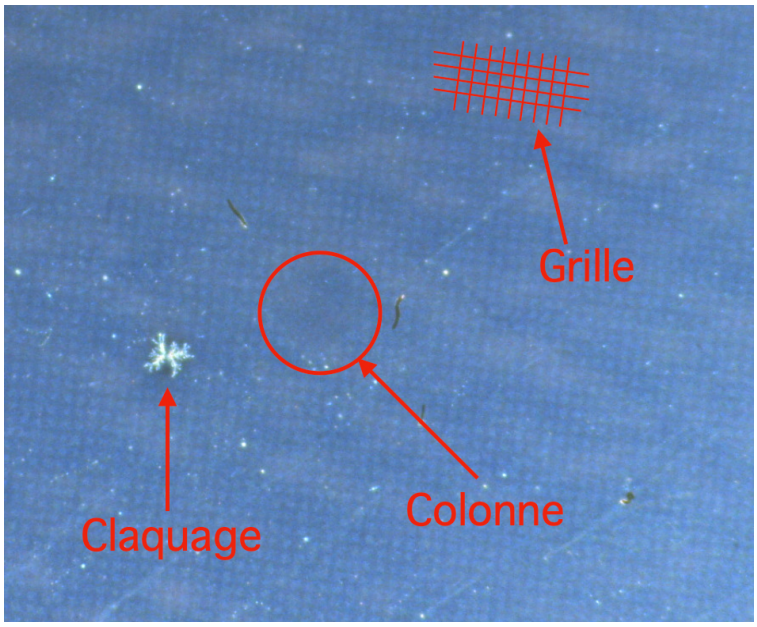

Figure 15.6: Photocathode degradé par bombardement ionique après exposition à un faisceau de pion de haute intensité. La photocathode montre quelques effets de l'exposition (voir le texte).

15.4.3 Photocathode

Le développement d'une photocathode robuste avec une efficacité quantique suffisante est un point crucial dans le développement d'un PICOSEC-Micromegas robuste. Le flux de retour d'ions élevé généré lors de l'étape de préamplification du détecteur, qui est nécessaire pour obtenir une résolution temporelle optimale, entraîne un bombardement d'ions élevé sur les photocathodes et des dommages potentiels (voir section 15.4.2). Différents matériaux de photocathode sont identifiés, adaptés à différentes applications en fonction des besoins en matière d'efficacité quantique et de robustesse. Le CsI est le matériau le plus efficace qui a été testé avec $10,4 \pm 0,4$ de photoélectrons par muon. Les matériaux robustes les plus prometteurs sont les photocathodes à base

de carbone comme le diamond (DLC), qui atteignent 3,7 N_{pe}/µ à une épaisseur de 2,5 nm (voir tableau 15.2).

Table 15.2: Nombre de photoélectrons et efficacité de détection pour différentes épaisseurs de DLC.

Épaisseur (nm)	N_{pe}/µ	Efficacité de détection (%)
2,5	3,7	97
5	3,4	94
7,5	2,2	70
10	1,7	68

Des mesures supplémentaires sont effectuées dans un monochromateur au CERN. Des photocathodes en carbone dopé au bore (B_4C) d'épaisseur différente sont testées dans le monochromateur et comparées à la DLC et à la CsI. B_4C surpasse la performance de la DLC dans les mesures du monochromateur avec les résultats présentés dans la figure 15.7, mais n'atteint pas la même performance que le CsI. Des matériaux plus simples, comme de fines couches d'aluminium, conviennent également aux photocathodes [127]. Les performances sont encore plus faibles que celles du DLC avec seulement $\sim$2 N_{pe}/µ, mais la production de ces photocathodes est bon marché et facile, et elles conviennent à des applications avec une quantité énorme de lumière, comme les mesures dans le laser.

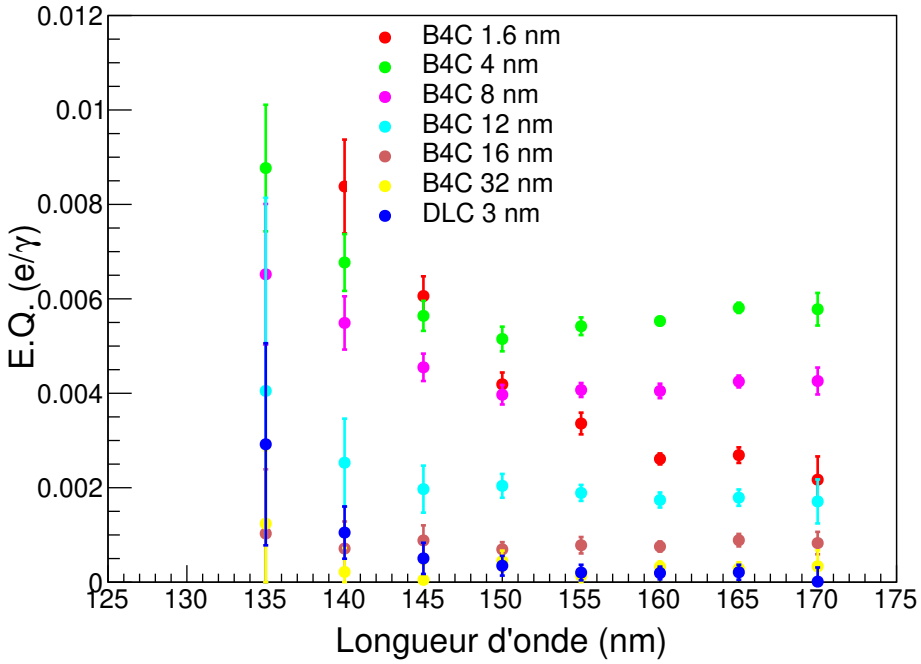

Figure 15.7: E.Q. pour les échantillons B_4Cs.

15.5 Synthèse

Les travaux présentés montrent le potentiel des MPGD pour des applications à haute résolution temporelle. Le concept de détection des PICOSEC-Micromegas atteint une résolution temporelle bien inférieure à 100 ps dans diverses conditions, avec un potentiel de robustesse non encore épuisé. Grâce à son développement continu et à ses premières applications, le PICOSEC-Micromegas pourrait être une solution pour de nombreuses projets futurs dans le domaine de l'HEP et au-delà. Il s'agit d'un concept de détection répondant à des exigences uniques en matière de résolution temporelle, d'efficacité de détection et de robustesse, et il pourrait devenir un concurrent sérieux d'autres concepts de détection rapide bien éprouvés comme les SiPM et les MCP-PMT. Ces travaux apportent de nouvelles connaissances sur la performance des détecteurs gazeux à temps rapide et ouvrent la voie à d'autres développements et optimisations.

Appendix

Numquam ponenda est pluralitas sine necessitate

— William of Occam (1287–1347)

"Plurality must never be posited without necessity", William of Occam (1287–1347)

A Appendix: Modelling

Contents

A.1 Input Parameters

The input parameters given in table A.1 are used for the mathematical modeling. These parameters are extracted from GARFIELD++ simulations and table A.2 gives the extracted values for each parameter and different drift voltages ranging from 325 V to 425 V. The amplification voltage of the simulations is fixed to 450 V.

Table A.1: Input parameters used for the mathematical model of the PICOSEC-Micromegas.

Parameter	Description
a (10^{-2} μm^{-1})	Townsend coefficient
a_{eff} (10^{-2} μm^{-1})	Effective Townsend coefficient under consideration of the Penning ratio
Θ	Shape parameter of the electron multiplicity on the mesh Gamma distribution
V_{ea}^{-1} (10^{-3} ns/µm)	Mean avalanche electron velocity
V_{p}^{-1} (10^{-3} ns/µm)	Mean photoelectron velocity
d_{off} (10^{-2} ns)	Time offset of the photoelectron before first interaction
ρ (10^{-2} ns)	Time gain per interaction
C (10^{-2} ns)	Integration constant
σ_p^2 (10^{-4} ns^2/µm)	Slope of the photoelectron time variance in relation to the drift length
Φ (10^{-4} ns)	Constant term of the photoelectron time variance in relation to the drift length
σ_0^2 (10^{-4} ns^2/µm)	Slope of the avalanche time variance in relation to the avalanche length
tr	Electron transparency of the mesh
Δt_{mesh} (10^{-1} ns)	Mean transition time through the mesh
δ (10^{-2} ns)	Variance of the transition time through the mesh

Table A.2: Values of the input parameters used for the mathematical model of the PICOSEC-Micromegas. The values are extracted from GARFIELD++ simulations performed by the AUTh group [95, 96, 97].

Drift Voltage	325 V	350 V	375 V	400 V	425 V
a (10^{-2} μm^{-1})	3.607 $\pm$ 0.018	4.400 $\pm$ 0.020	5.208 $\pm$ 0.027	6.069 $\pm$ 0.027	6.950 $\pm$ 0.032
a_{eff} (10^{-2} μm^{-1})	2.215$\pm$ 0.001	2.629$\pm$ 0.001	3.055 $\pm$ 0.001	3.484 $\pm$ 0.001	3.912 $\pm$ 0.001
Θ	2.698$\pm$ 0.142	2.906$\pm$ 0.154	3.037 $\pm$ 0.162	3.313 $\pm$ 0.179	3.645 $\pm$ 0.191
V_{ea}^{-1} (10^{-3} ns/μm)	7.311$\pm$ 0.003	6.877$\pm$ 0.003	6.509 $\pm$ 0.002	6.173 $\pm$ 0.002	5.866 $\pm$ 0.004
V_{p}^{-1} (10^{-3} ns/μm)	8.065$\pm$ 0.026	7.678$\pm$ 0.026	7.266 $\pm$ 0.028	6.923 $\pm$ 0.028	6.643 $\pm$ 0.031
d_{off} (10^{-2} ns)	-3.831 $\pm$ 0.084	-3.437 $\pm$ 0.082	-2.883 $\pm$ 0.075	-2.678 $\pm$ 0.068	-2.364 $\pm$ 0.079
ρ (10^{-2} ns)	3.570$\pm$ 0.054	2.919$\pm$ 0.027	2.489 $\pm$ 0.030	2.185 $\pm$ 0.028	1.725 $\pm$ 0.045
C (10^{-2} ns)	7.555$\pm$ 0.218	7.511$\pm$ 0.117	7.668 $\pm$ 0.166	7.778 $\pm$ 0.196	7.001 $\pm$ 0.516
σ_p^2 (10^{-4} $ns^2/\mu m$)	2.137$\pm$ 0.054	1.908$\pm$ 0.046	1.662$\pm$ 0.073	1.554$\pm$ 0.050	1.380$\pm$ 0.063
Φ (10^{-4} ns)	-9.967 $\pm$ 2.417	-7.936 $\pm$ 1.395	-6.40 $\pm$ 1.650	-7.525 $\pm$ 1.343	-5.622 $\pm$ 1.284
σ_0^2 (10^{-4} $ns^2/\mu m$)	2.094 $\pm$ 0.005	1.778$\pm$ 0.003	1.543$\pm$ 0.004	1.341$\pm$ 0.003	1.175$\pm$ 0.004
tr	0.244$\pm$ 0.009	0.248$\pm$ 0.044	0.238$\pm$ 0.011	0.251$\pm$ 0.009	0.247$\pm$ 0.009
Δt_{mesh} (10^{-1} ns)	1.521$\pm$0.005	1.455 $\pm$ 0.005	1.400 $\pm$ 0.004	1.344 $\pm$ 0.003	1.303 $\pm$ 0.004
δ (10^{-2} ns)	7.217 $\pm$ 0.034	6.871 $\pm$ 0.032	6.607 $\pm$ 0.031	6.305 $\pm$ 0.030	5.938 $\pm$ 0.040

A.2 Wald Distributions

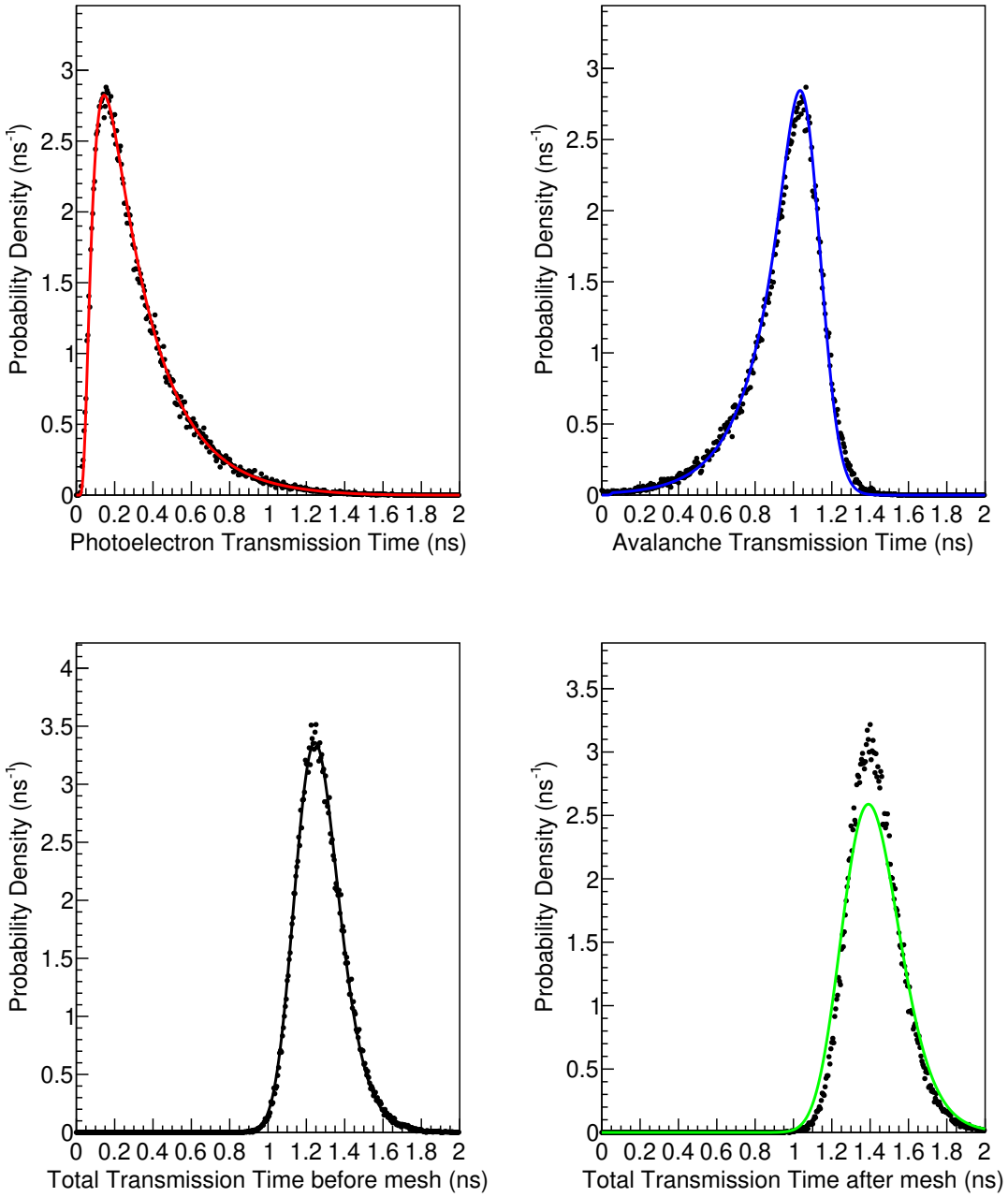

Figure A.1: 325 V drift field.

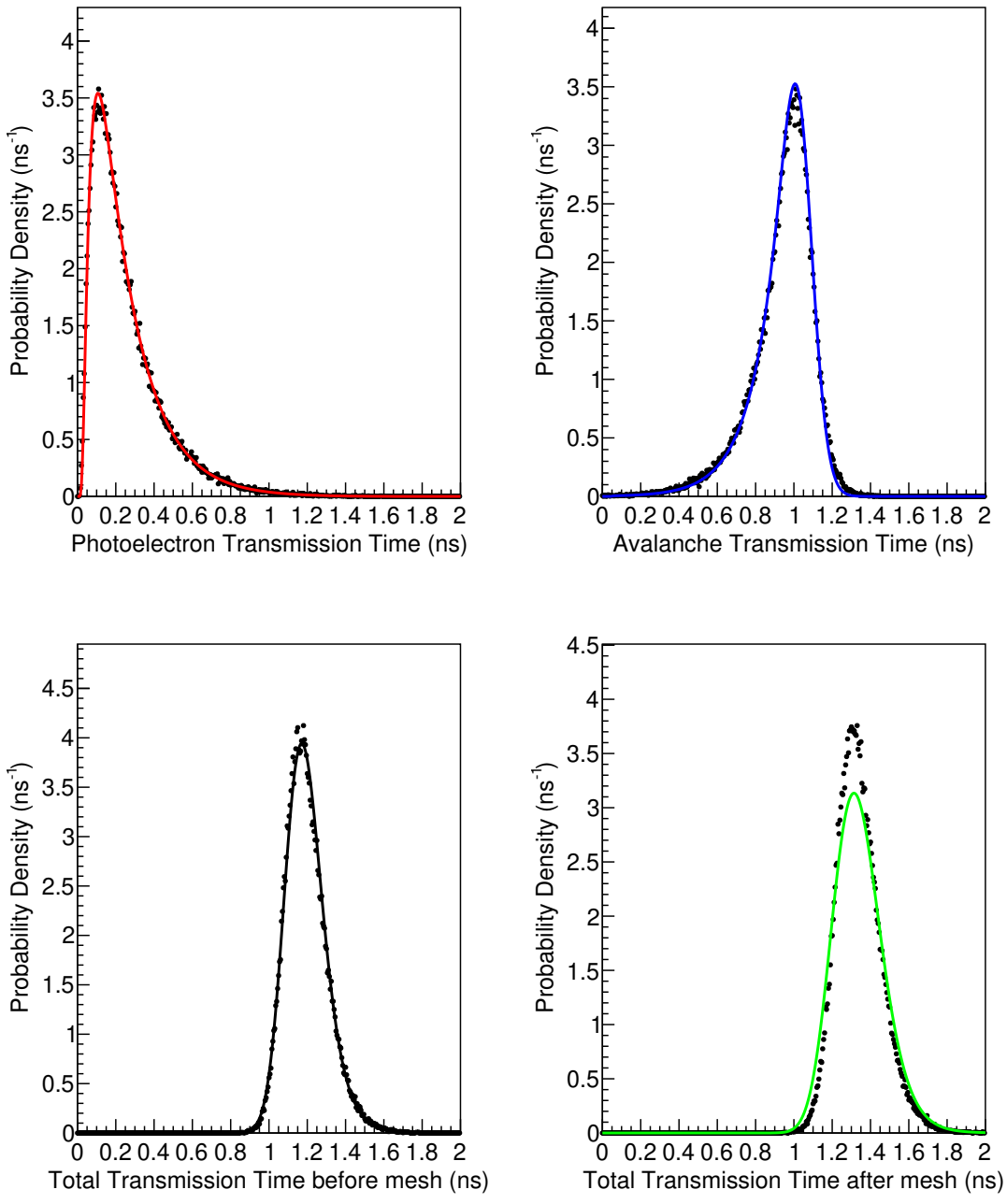

Figure A.2: 350 V drift field.

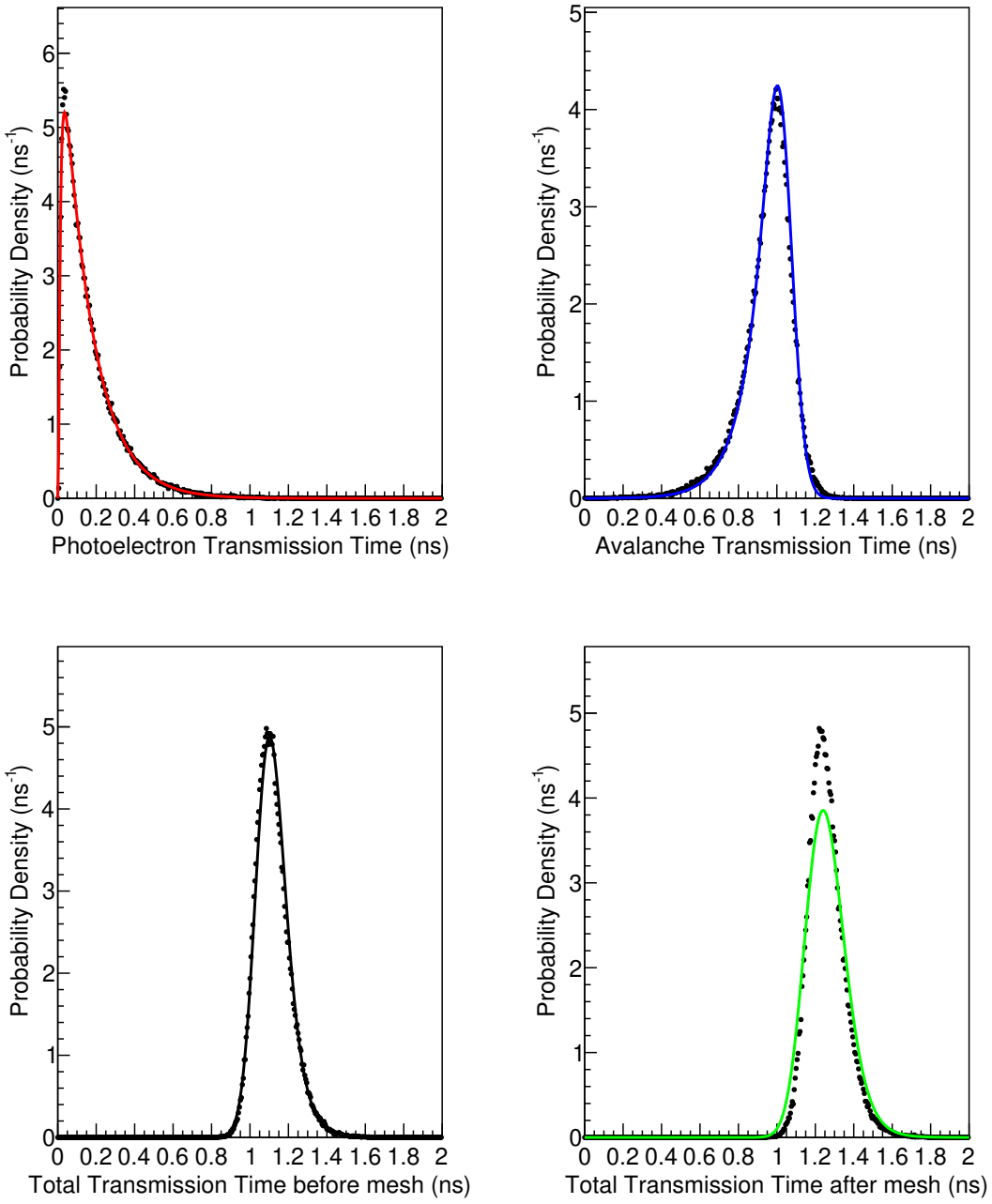

Figure A.3: 375 V drift field.

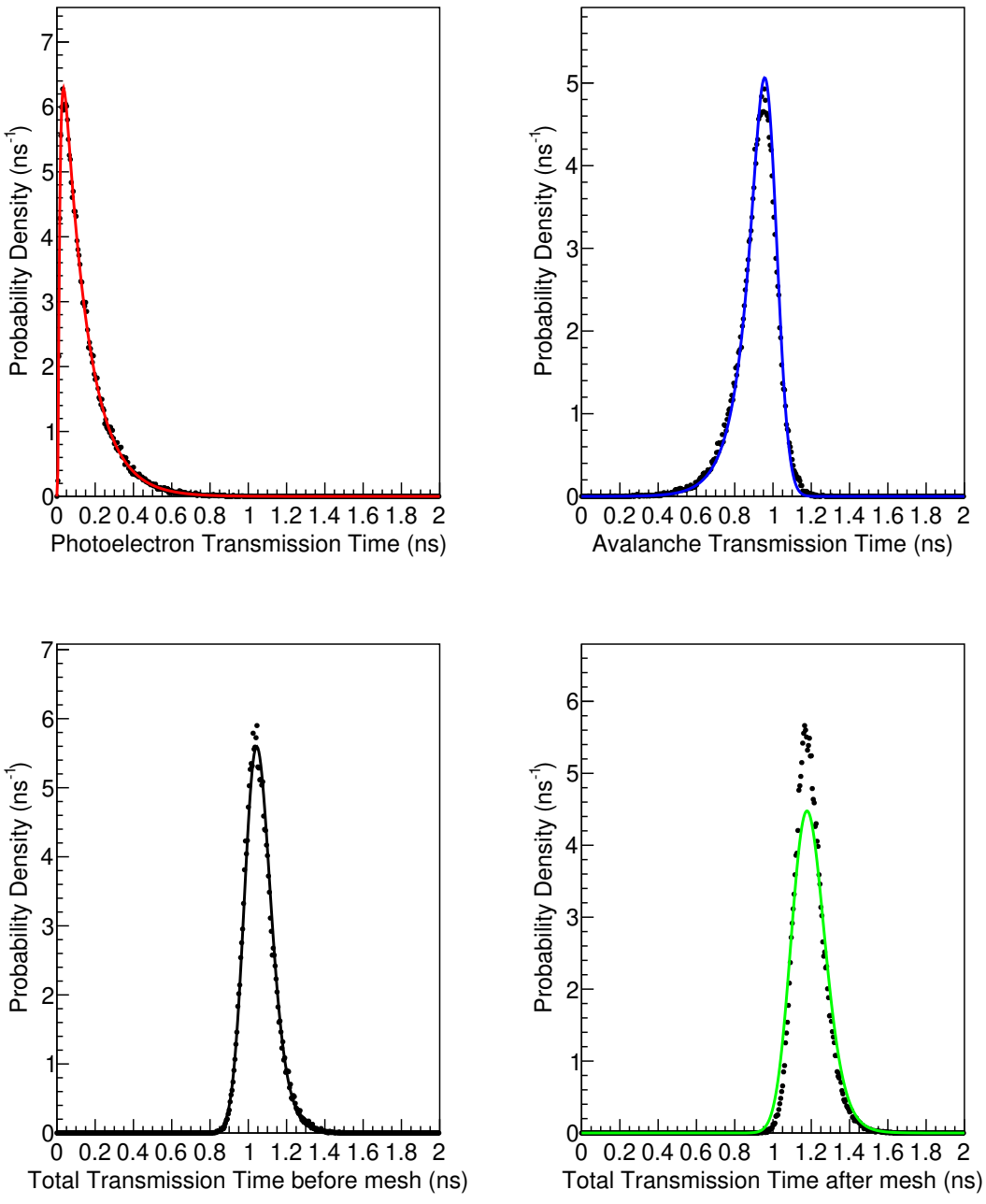

Figure A.4: 400 V drift field.

A.3 Field Scan

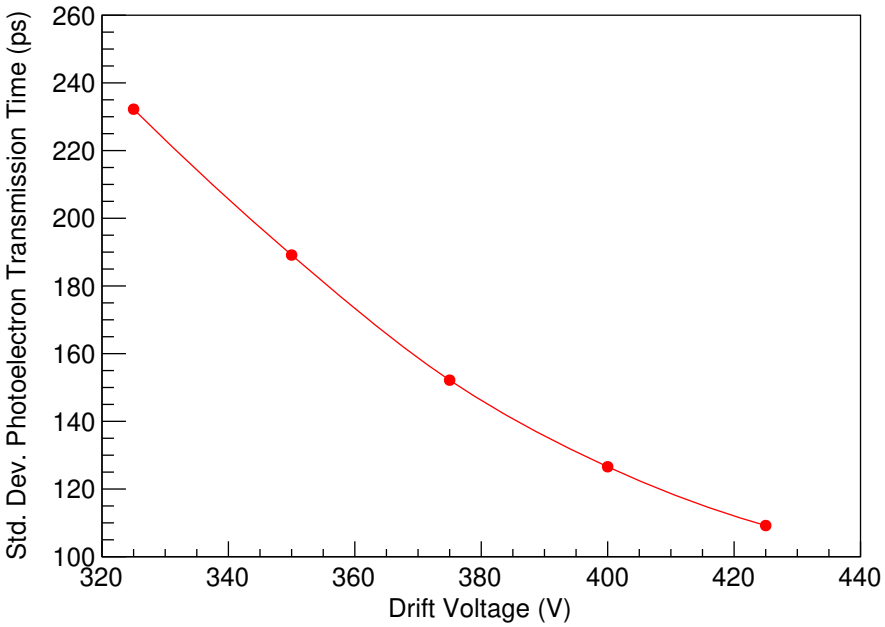

Figure A.5: Photoelectron time

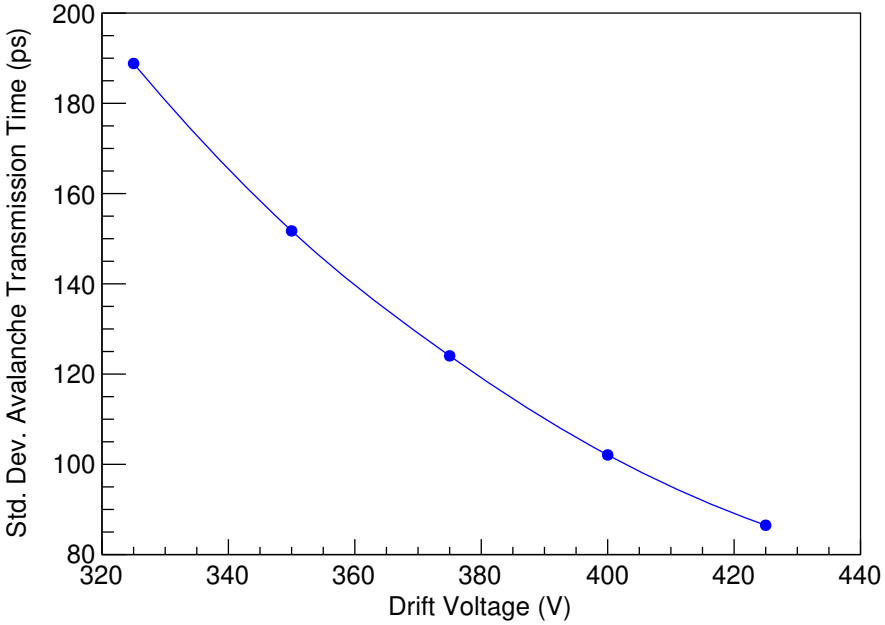

Figure A.6: Avalanche time

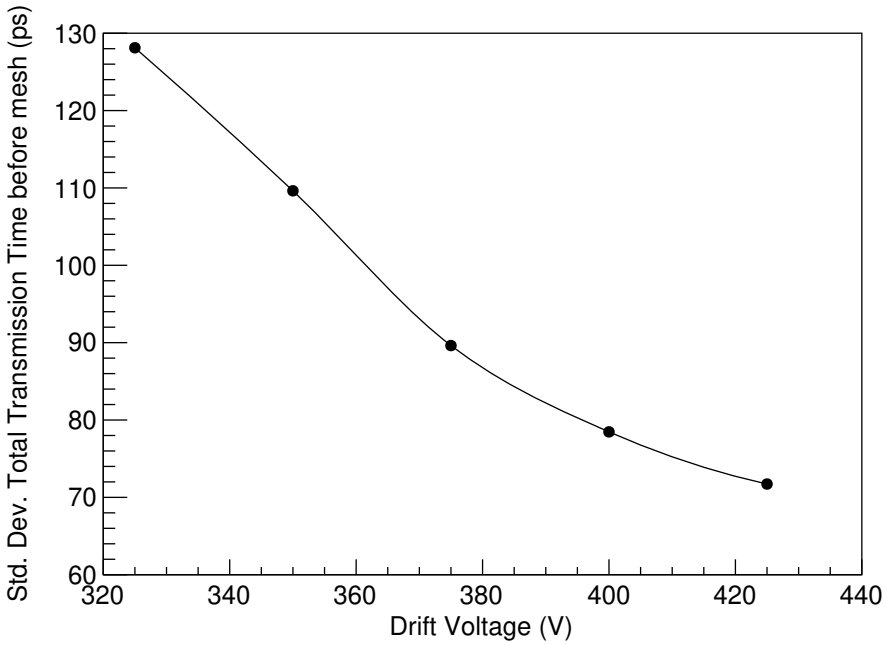

Figure A.7: Total time before the mesh

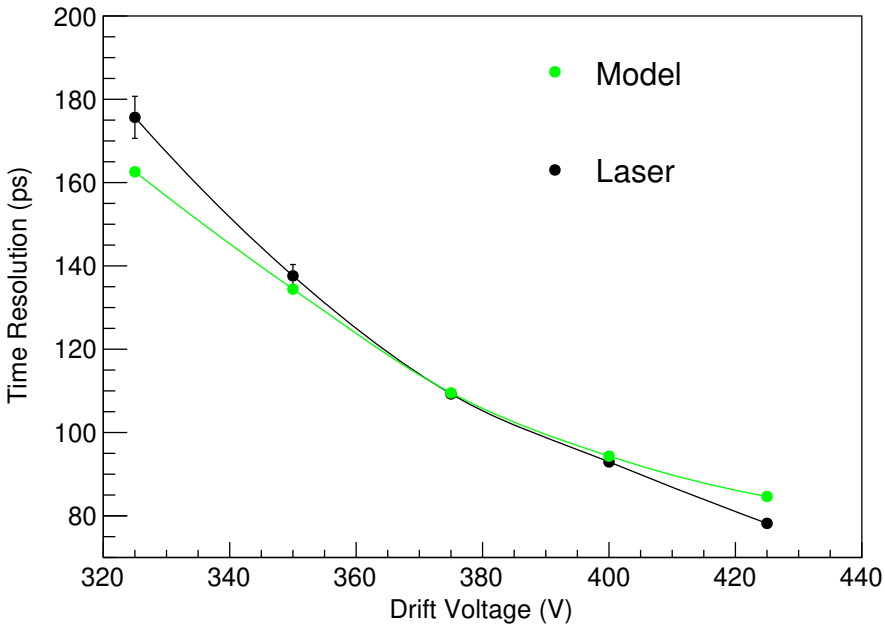

Figure A.8: Total time after the mesh

A.4 Integration Length

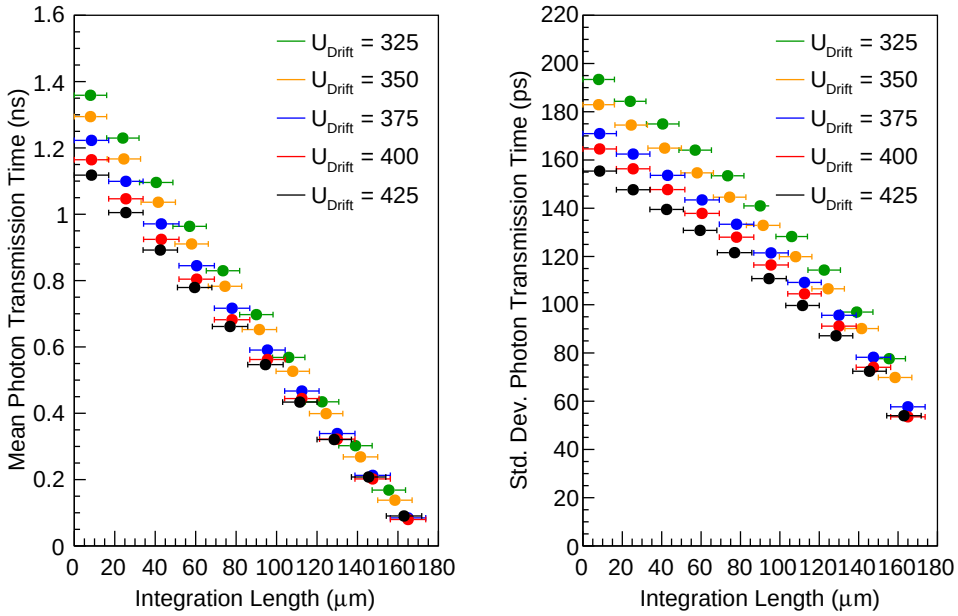

Figure A.9: Photoelectron time

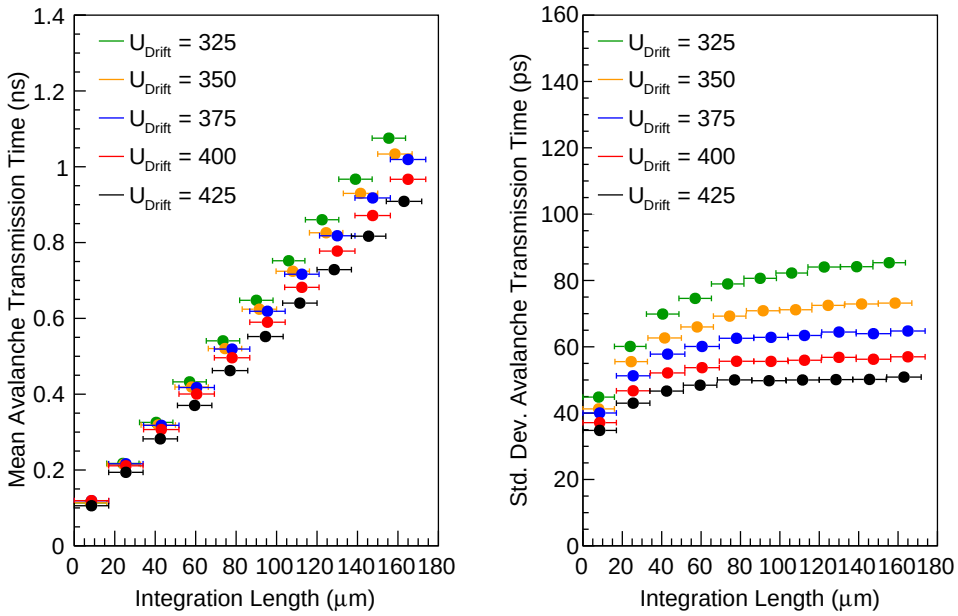

Figure A.10: Avalanche time

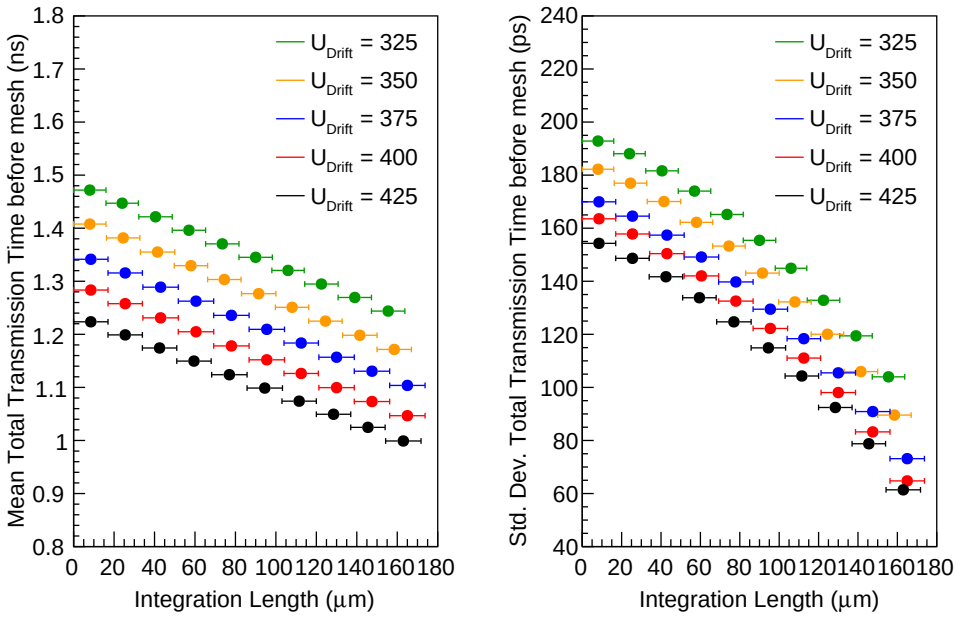

Figure A.11: Total time before the mesh

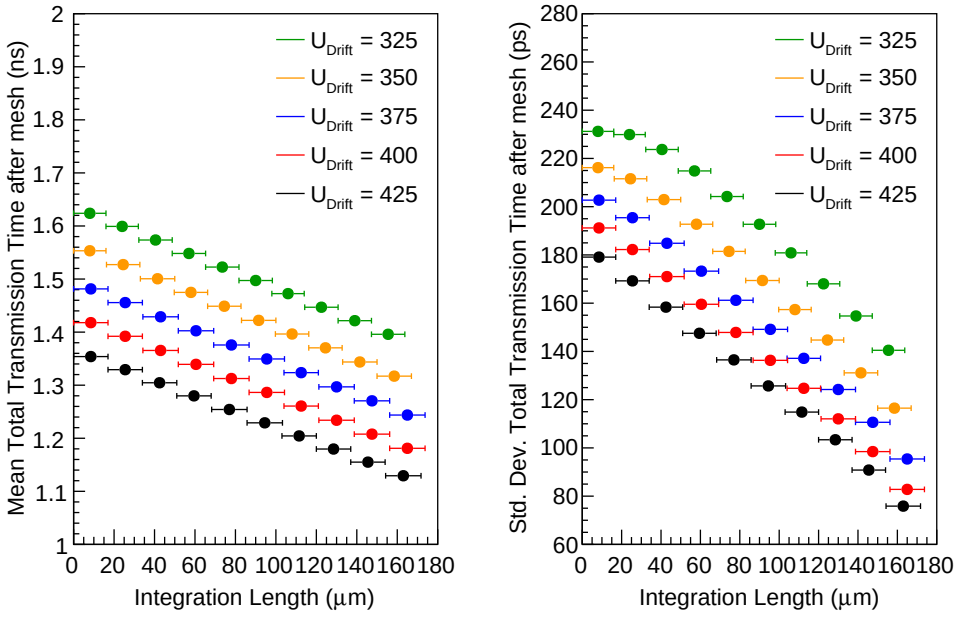

Figure A.12: Total time after the mesh

A.5 Avalanche Length

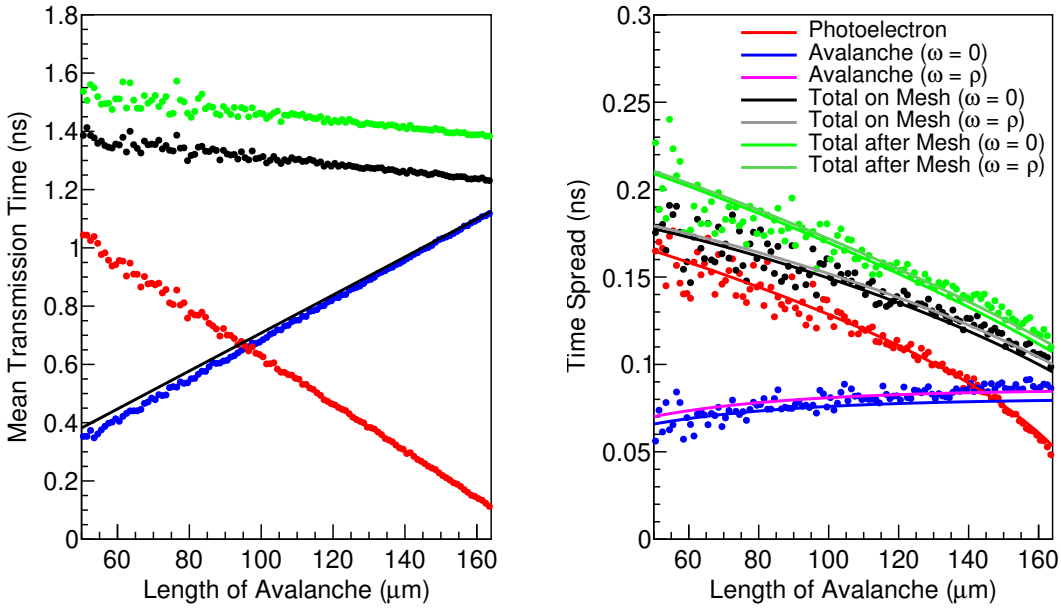

Figure A.13: 325 V drift field.

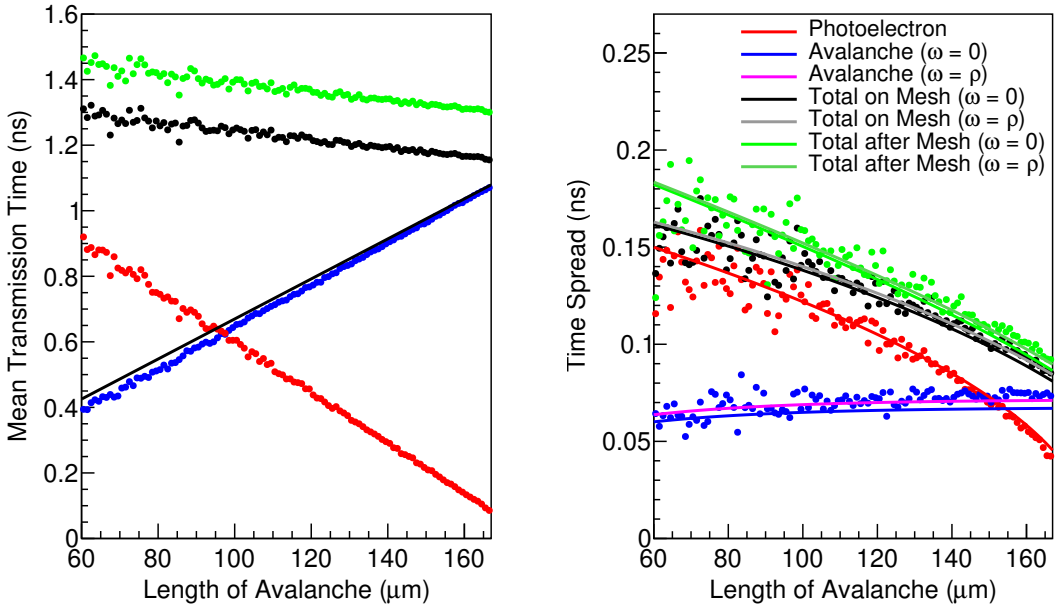

Figure A.14: 350 V drift field.

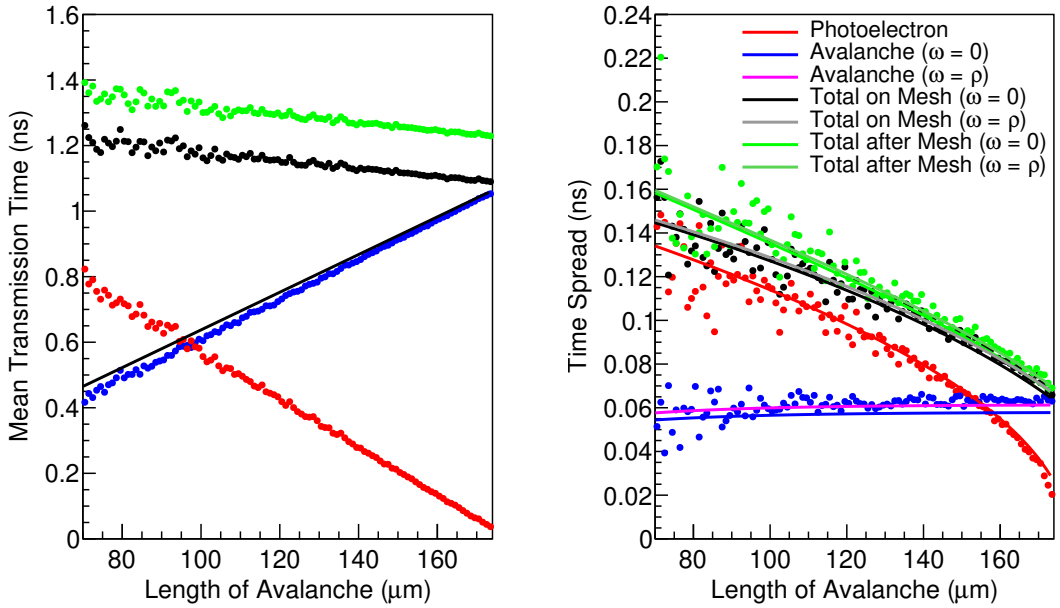

Figure A.15: 375 V drift field.

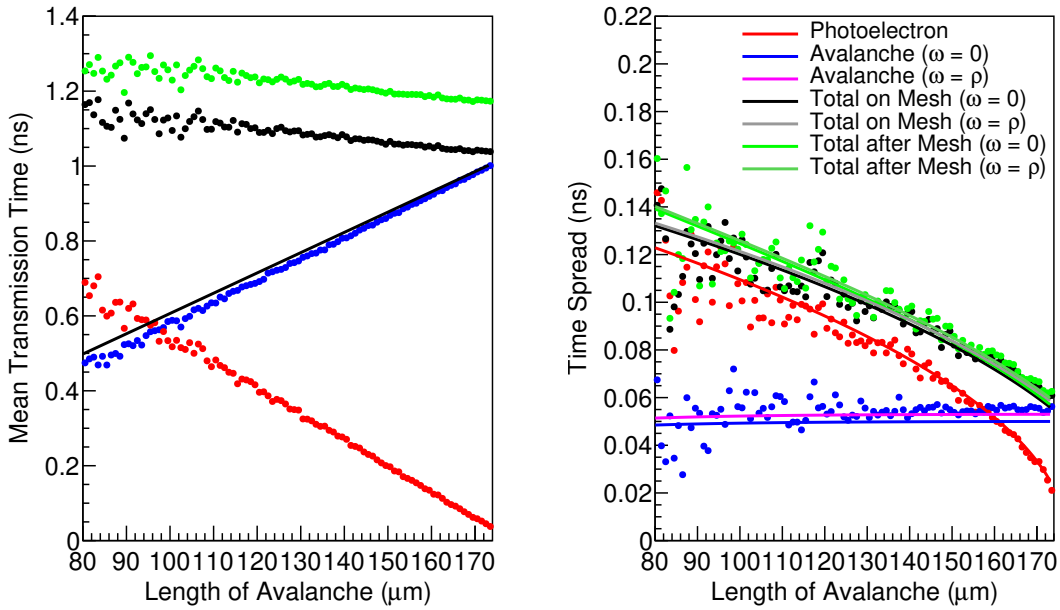

Figure A.16: 400 V drift field.

A.6 Avalanche Multiplication

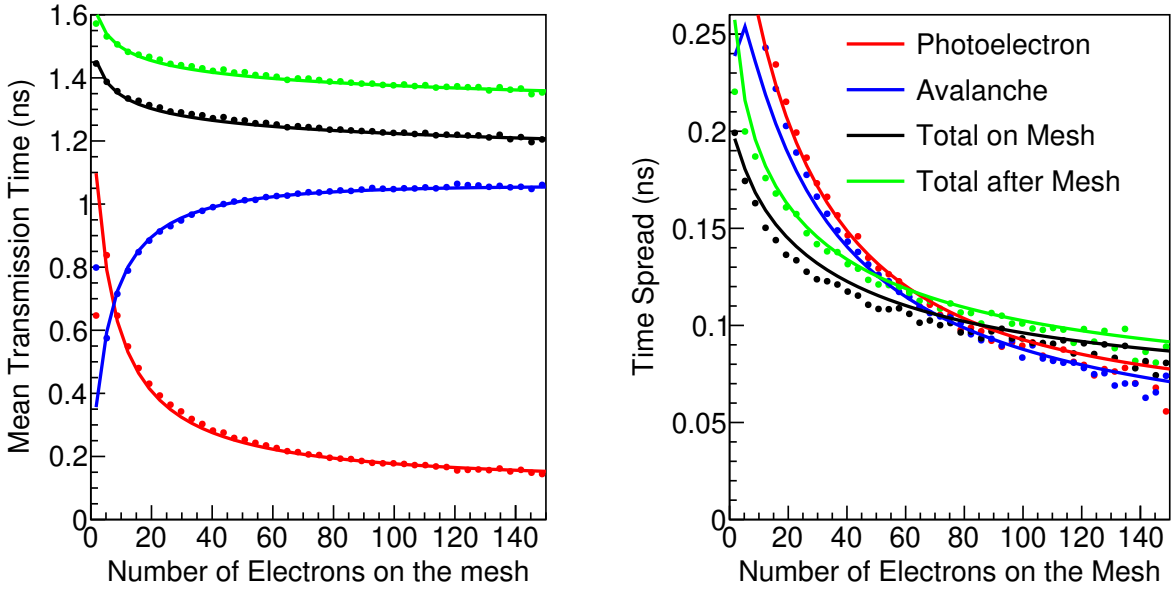

Figure A.17: 325 V drift field.

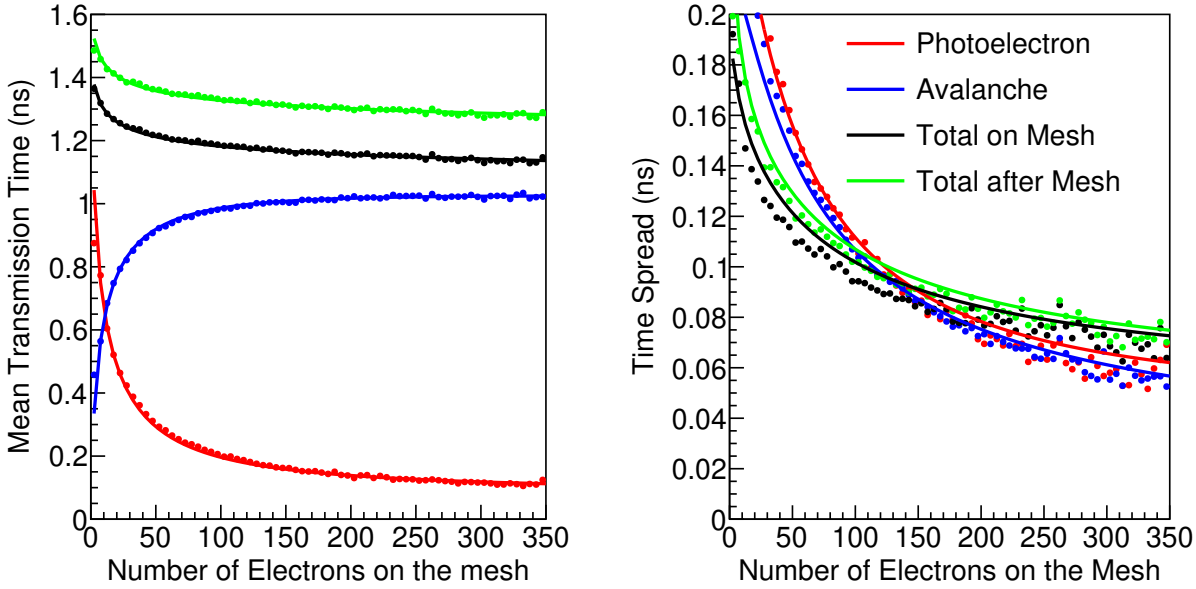

Figure A.18: 350 V drift field.

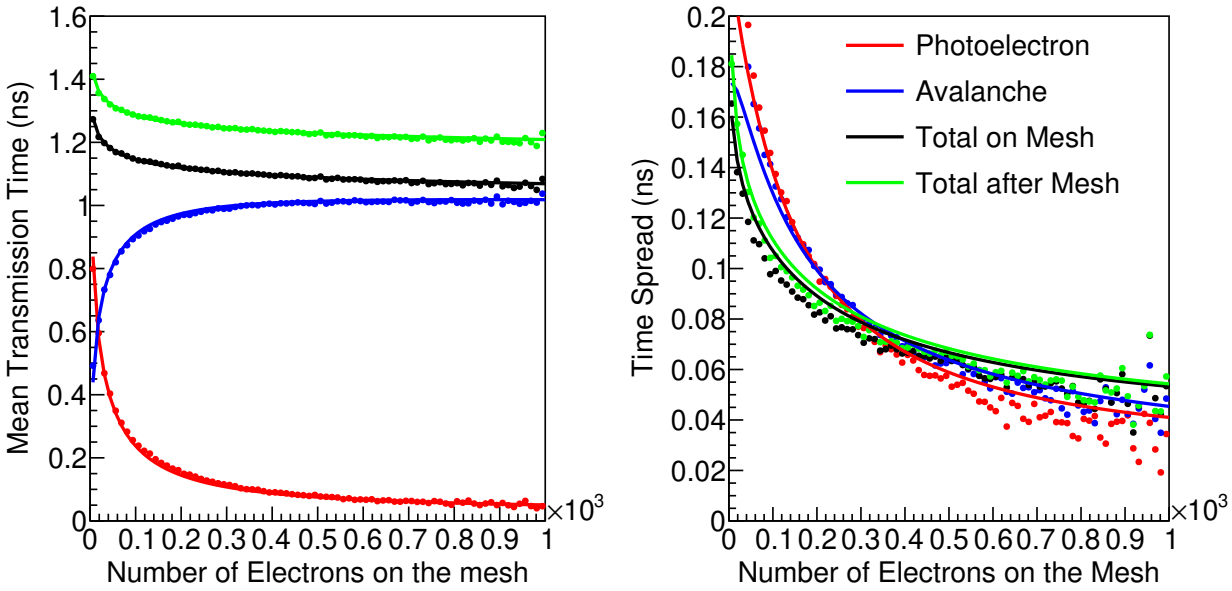

Figure A.19: 375 V drift field.

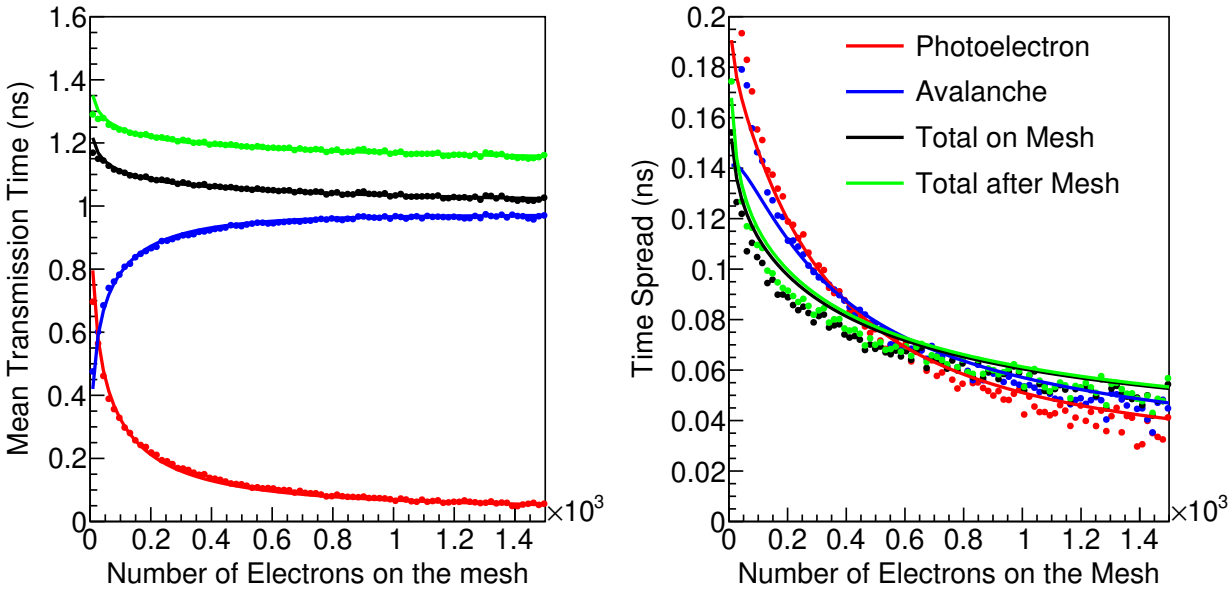

Figure A.20: 400 V drift field.

B Appendix: Drift Distance Measurements

Contents

B.1 Time Resolution vs Number of Photoelectrons

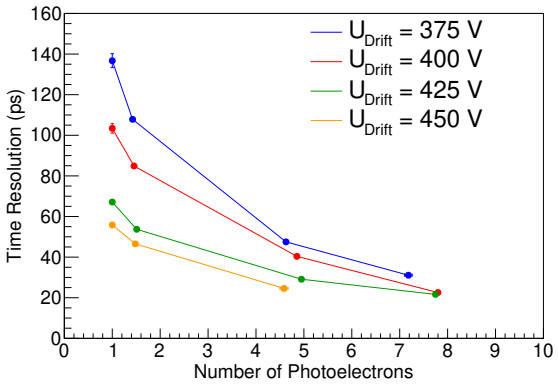

(a) Drift gap 119 µm; Anode voltage 350 V

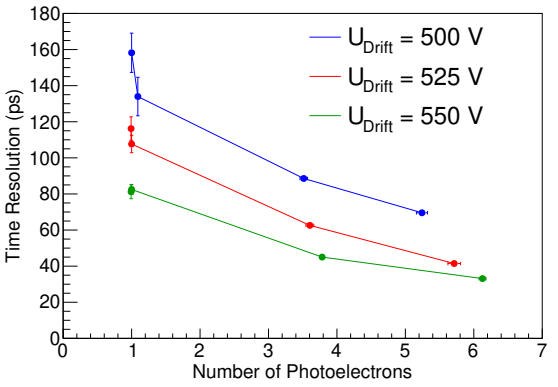

(b) Drift gap 169 µm; Anode voltage 275 V

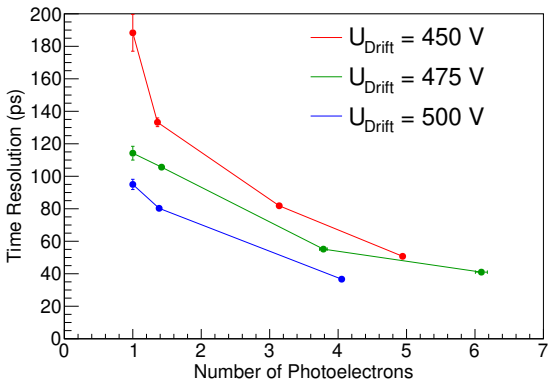

(c) Drift gap 169 µm; Anode voltage 350 V

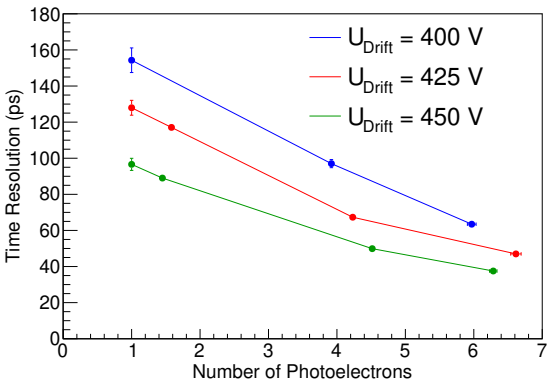

(d) Drift gap 169 µm; Anode voltage 400 V

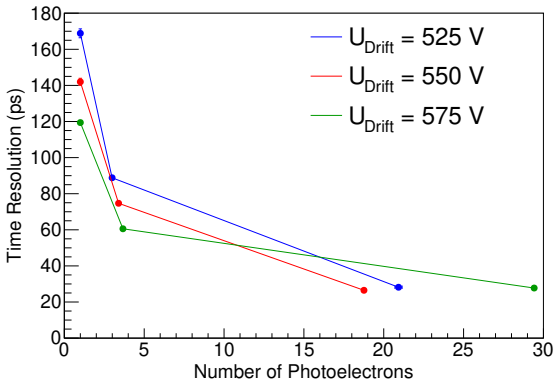

(e) Drift gap 244 µm; Anode voltage 350 V

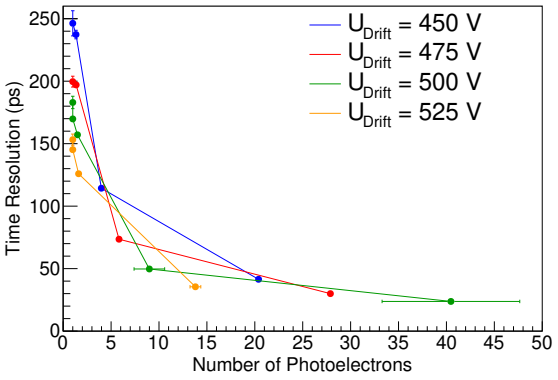

(f) Drift gap 244 µm; Anode voltage 400 V

Figure B.1: Time resolution scan of drift voltage and generated photoelectrons for different drift gaps and fixed amplification voltage.

B.2 Time Resolution vs Drift Field

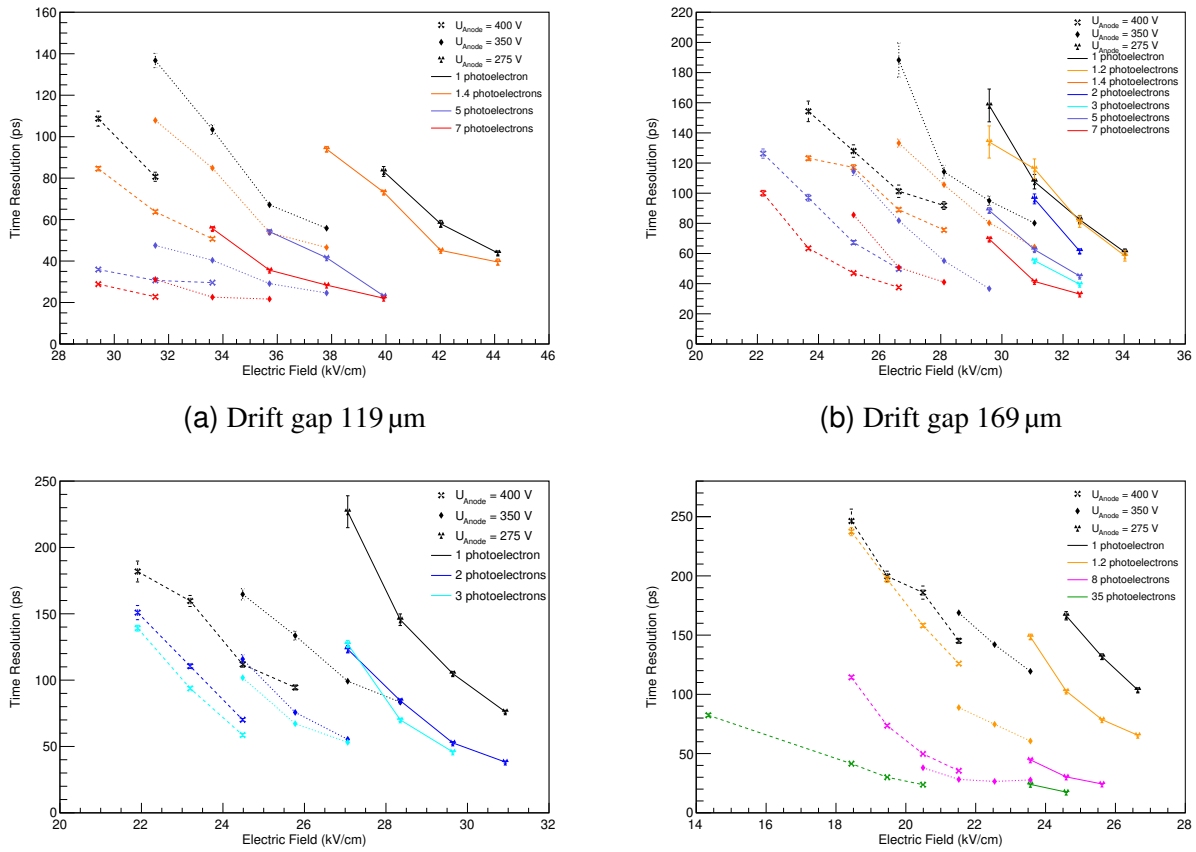

(a) Drift gap 119 µm

(b) Drift gap 169 µm

(c) Drift gap 194 µm

(d) Drift gap 244 µm

Figure B.2: Time resolution scan of drift voltage for all measured Laser intensities.

B.3 Time Resolution vs Gain

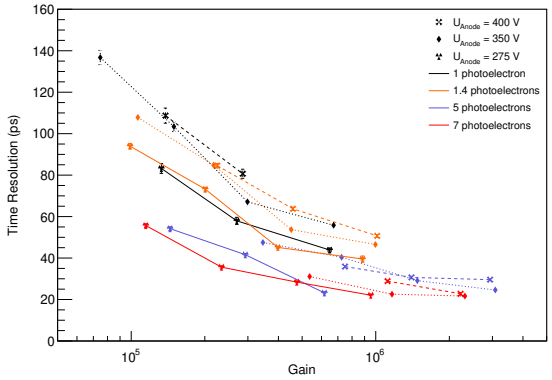

(a) Drift gap 119 µm

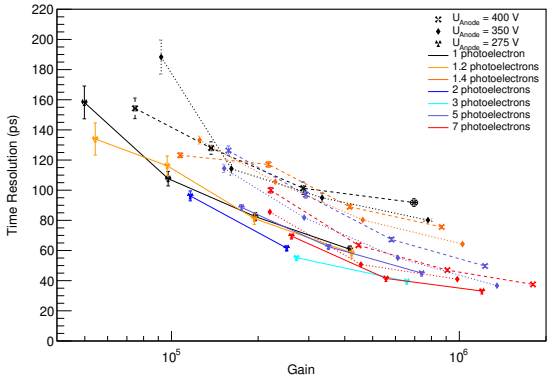

(b) Drift gap 169 µm

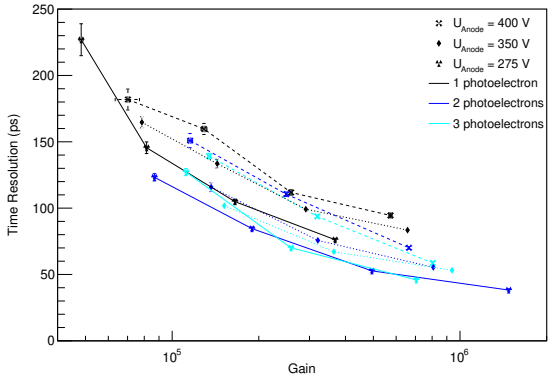

(c) Drift gap 194 µm

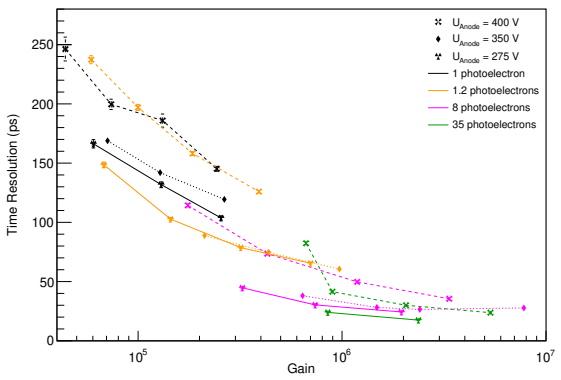

(d) Drift gap 244 µm

Figure B.3: Time resolution versus detector gain for all measured Laser intensities.

C Appendix: Gas Mixture Measurements

Contents

C.1 Time Resolution vs Amplitude

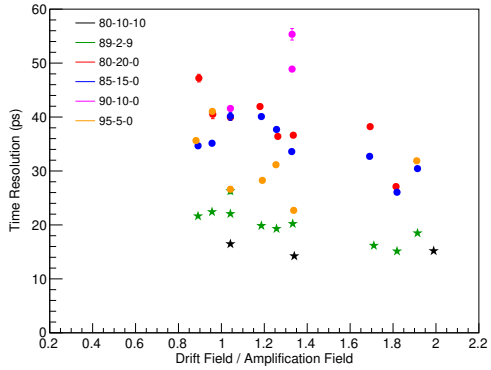

(a) Time resolution versus ratio between the drift and amplification field.

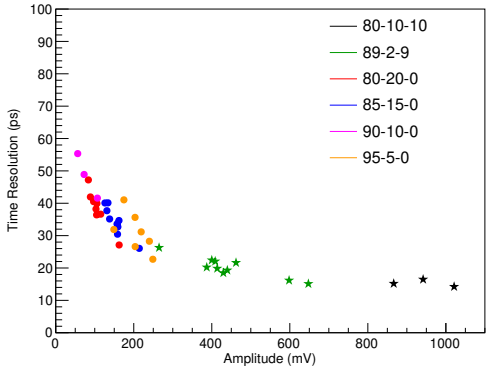

(b) Time resolution versus signal amplitude.

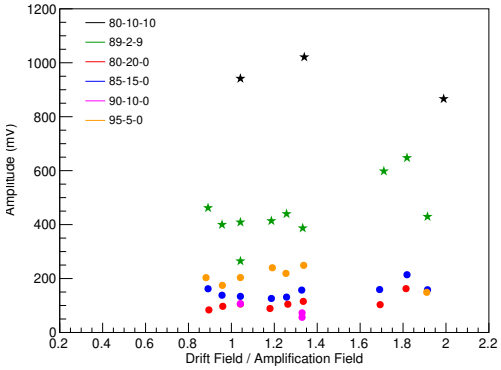

(c) Signal amplitude versus ratio between the drift and amplification field.

Figure C.1: Time resolution for the different gas mixtures and a high light intensity. Only attenuator 4 is placed in front of the Laser beam.

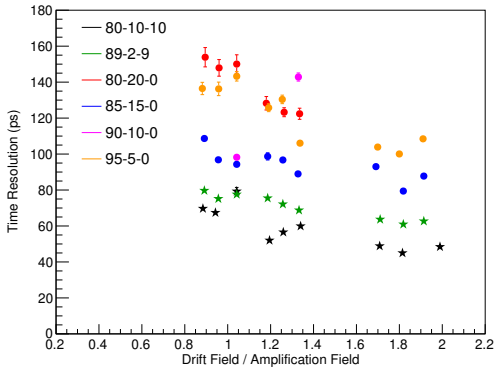

(a) Time resolution versus ratio between the drift and amplification field.

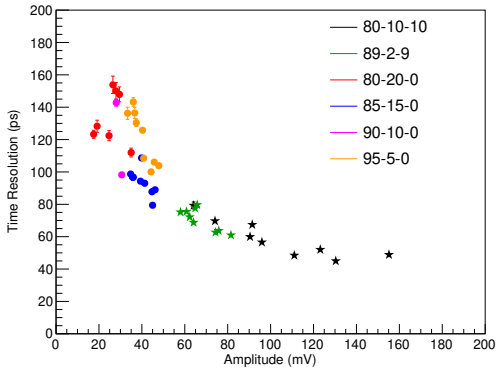

(b) Time resolution versus signal amplitude.

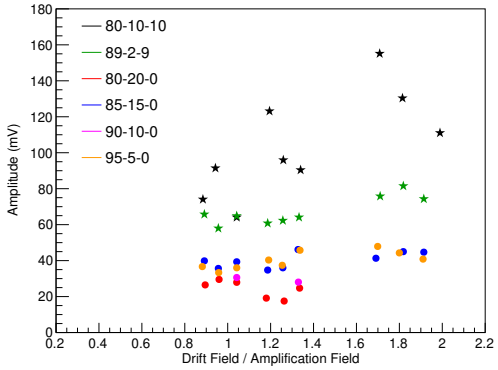

(c) Signal amplitude versus ratio between the drift and amplification field.

Figure C.2: Time resolution for the different gas mixtures and a high light intensity. Attenuator 4 and 8 are placed in front of the Laser beam.

C.2 Field Scan for Different Anode Settings

Table C.1: Each mixture is measured with three anode voltage settings. The settings are selected to provide a similiar gain for all gas mixtures compared to the settings of the "COMPASS" gas (neon (80 %) - ethane (10 %) - CF_4 (10 %)) used in previous measurements.

Gas mixture (%) (Neon-Ethane-CF_4)	U_{high} (V)	U_{medium} (V)	U_{low} (V)
80-10-10	400	350	275
89-2-9	350	305	245
80-20-0	365	320	250
85-15-0	350	310	245
90-10-0	340	290	230
95-5-0	300	265	210

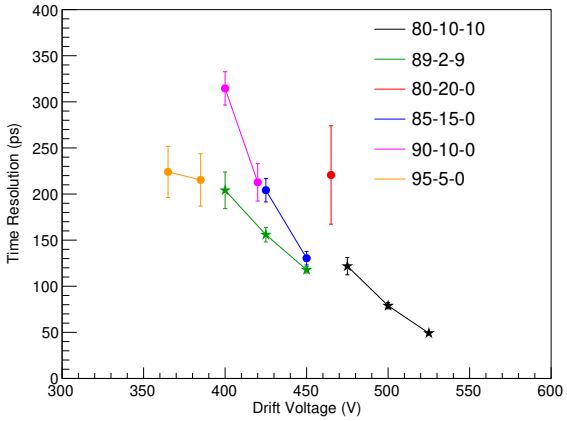

(a) High anode voltage.

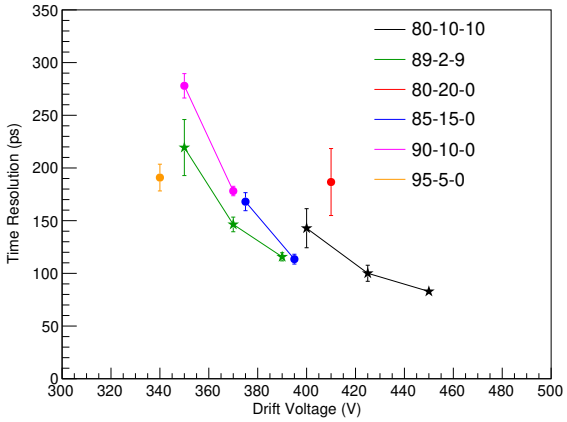

(b) Medium anode voltage.

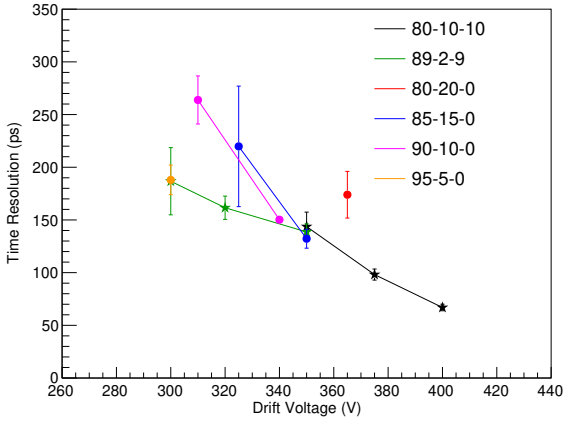

(c) Low anode voltage.

Figure C.3: Time resolution field scan for all gas mixtures with fixed anode voltage at single photoelectron conditions. See table C.1 for the corresponding anode settings of each gas mixture.

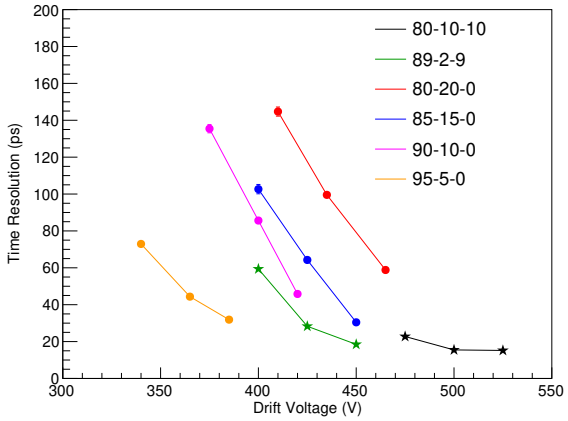

(a) High anode voltage.

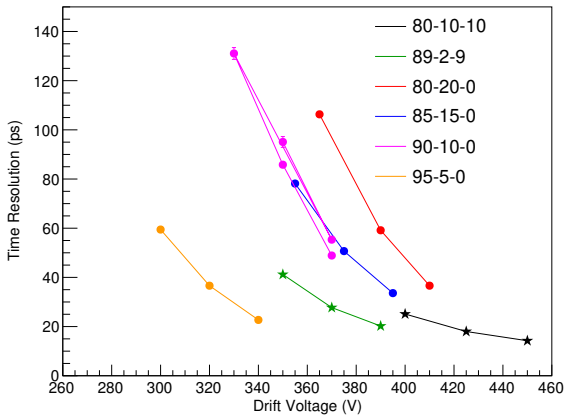

(b) Medium anode voltage.

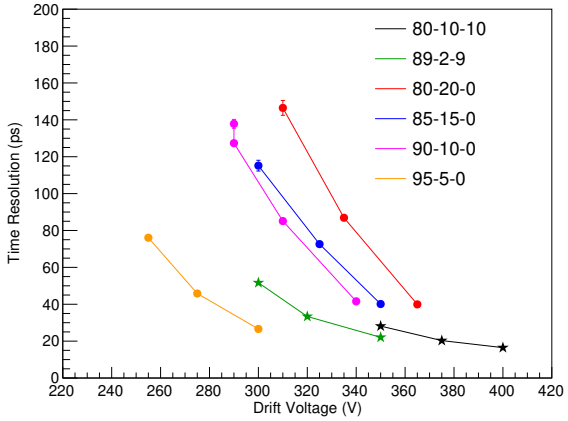

(c) Low anode voltage.

Figure C.4: Time resolution field scan for all gas mixtures with fixed anode voltage. Attenuator 4 is placed in front of the detector providing a high amount of light to the detector. See table C.1 for the corresponding anode settings of each gas mixture.

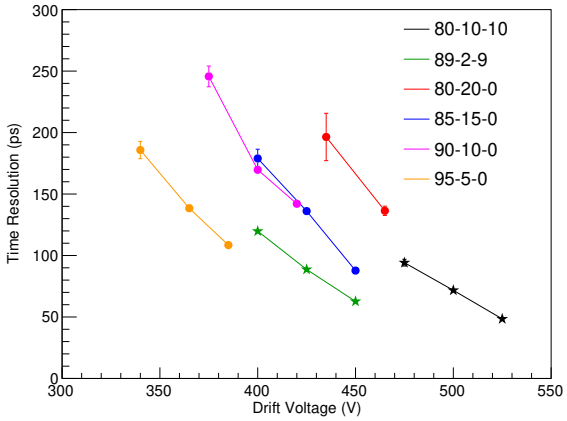

(a) High anode voltage.

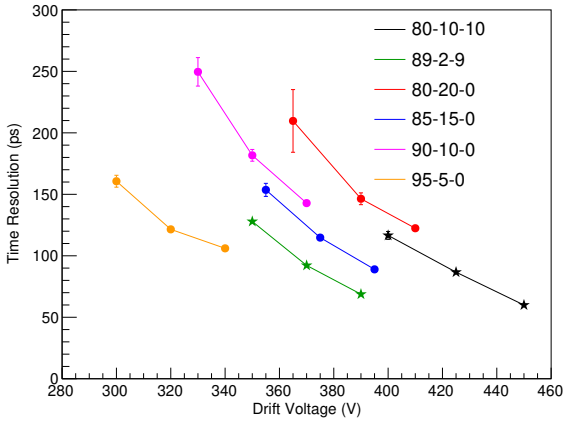

(b) Medium anode voltage.

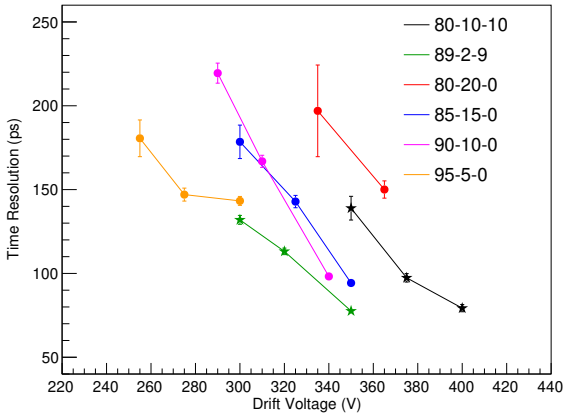

(c) Low anode voltage.

Figure C.5: Time resolution field scan for all gas mixtures with fixed anode voltage. Attenuator 4 and 8 are placed in front of the detector. See table C.1 for the corresponding anode settings of each gas mixture.

Bibliography

[1] *J. W. von Goethe*. Faust. Eine Tragödie. (**1808**).

[2] *R. A. Millikan*. "XXII. A new modification of the cloud method of determining the elementary electrical charge and the most probable value of that charge". *The London, Edinburgh, and Dublin Philosophical Magazine and Journal of Science*, **19** (110); pp. 209–228 (**1910**). doi:10.1080/14786440208636795.

[3] *J. Va'vra*. "PID techniques: Alternatives to RICH methods". *Nucl. Instrum. Meth.*, **A876**; pp. 185–193 (**2017**). doi:10.1016/j.nima.2017.02.075.

[4] *T. Papaevangelou, et al.* "Fast Timing for High-Rate Environments with Micromegas". *EPJ Web Conf.*, **174**; p. 02002 (**2018**). doi:10.1051/epjconf/201817402002.

[5] *J. Bortfeldt, et al.* "PICOSEC: Charged particle timing at sub-25 picosecond precision with a Micromegas based detector". *Nucl. Instrum. Meth.*, **A903**; pp. 317–325 (**2018**). doi:10.1016/j.nima.2018.04.033.

[6] Photomultiplier Tube Handbook. Hamamatsu PHOTONICS K. K. (**2007**).

[7] *K. Inami*. "MCP-PMT production for Belle II TOP detector and further R&D". *Nucl. Instrum. Meth.*, **A936**; pp. 556–557 (**2019**). doi:10.1016/j.nima.2018.09.038.

[8] *F. Benedetti*. "Design of non-invasive profile monitors for the ESS proton beam". Ph.D. thesis, Université Paris-Saclay (**2019**).

[9] *J. Bortfeldt, et al.* "Timing performance of a Micro-Channel-Plate Photomultiplier Tube". *Nucl. Instrum. Meth.*, **A960**; p. 163592 (**2020**). doi:10.1016/j.nima.2020.163592.

[10] *T. Abe, et al.* "Belle II Technical Design Report". *KEK-REPORT-2010-1* (**2010**).

[11] *K. Inami, et al.* "A 5-ps TOF-counter with an MCP-PMT". *Nucl. Instrum. Meth.*, **A560**; pp. 303–308 (**2006**). doi:10.1016/j.nima.2006.01.027.

[12] *S. Kasap, P. Capper, and C. Koughia*. Springer Handbook of Electronic and Photonic Materials. Springer (**2006**).

[13] *M. Turala*. "Silicon tracking detectors: Historical overview". *Nucl. Instrum. Meth.*, **A541**; pp. 1–14 (**2005**). doi:10.1016/j.nima.2005.01.032.

[14] Thorlabs. DET10A/M Data Sheet (**2017**).

[15] *S. Cova, et al.* "Avalanche photodiodes and quenching circuits for single-photon detection". *Appl. Opt.*, **35** (12); pp. 1956–1976 (**1996**). doi:10.1364/AO.35.001956.

[16] *PANDA Collaboration, F. Garcia, and D.-O. Riska*. Technical Design Report for PANDA Electromagnetic Calorimeter (EMC) (**2008**).

[17] *B. Dolgoshein, et al.* "The Advanced Study of Silicon Photomultiplier". *Advanced Technology and Particle Physics*, (pp. 717–728) (**2002**). doi:10.1142/9789812776464_0101.

[18] *A. Ronzhin, et al.* "Tests of timing properties of silicon photomultipliers". *Nucl. Instrum. Meth.*, **A616** (1); pp. 38–44 (**2010**). doi:10.1016/j.nima.2010.02.072.

[19] *M. Nemallapudi, et al.* "Single photon time resolution of state of the art SiPMs". *Journal of Instrumentation*, **11** (10); pp. P10016–P10016 (**2016**). doi:10.1088/1748-0221/11/10/p10016.

[20] *T. Behnke, et al.* "The International Linear Collider - Volume 1: Executive Summary". *Tech. Rep. ILC-REPORT-2013-040*, Geneva (**2013**).

[21] *N. Otte, et al.* "The SiPM — A new Photon Detector for PET". *Nuclear Physics B - Proceedings Supplements*, **150**; pp. 417–420 (**2006**). doi:10.1016/j.nuclphysbps.2004.08.048.

[22] *J. J. van Sluis, et al.* "Performance characteristics of the digital Biograph Vision PET/CT system". *Journal of Nuclear Medicine* (**2019**). doi:10.2967/jnumed.118.215418.

[23] *G. Pellegrini, et al.* "Technology developments and first measurements of Low Gain Avalanche Detectors (LGAD) for high energy physics applications". *Nucl. Instrum. Meth.*, **A765**; pp. 12–16 (**2014**). doi:10.1016/j.nima.2014.06.008.

[24] *G. Kramberger, et al.* "Radiation effects in Low Gain Avalanche Detectors after hadron irradiations". *Journal of Instrumentation*, **10** (07); pp. P07006–P07006 (**2015**). doi:10.1088/1748-0221/10/07/p07006.

[25] *H.-W. Sadrozinski, et al.* "Ultra-fast silicon detectors (UFSD)". *Nucl. Instrum. Meth.*, **A831**; pp. 18–23 (**2016**). doi:10.1016/j.nima.2016.03.093.

[26] *J. Lange, et al.* "Gain and time resolution of 45 μm thin Low Gain Avalanche Detectors before and after irradiation up to a fluence of 10^{15} neq/cm2". *Journal of Instrumentation*, **12** (05); pp. P05003–P05003 (**2017**). doi:10.1088/1748-0221/12/05/p05003.

[27] *C. CMS*. "Technical proposal for a MIP timing detector in the CMS experiment phase 2 upgrade". *Tech. Rep. CERN-LHCC-2017-027. LHCC-P-009*, CERN, Geneva (**2017**).

[28] *C. ATLAS*. "Technical Proposal: A High-Granularity Timing Detector for the ATLAS Phase-II Upgrade". *Tech. Rep. CERN-LHCC-2018-023. LHCC-P-012*, CERN, Geneva (**2018**).

[29] *F. Foulon, et al.* "CVD diamond films for radiation detection". *IEEE Transactions on Nuclear Science*, **41** (4); pp. 927–932 (**1994**). doi:10.1109/23.322833.

[30] *C. Manfredotti*. "CVD diamond detectors for nuclear and dosimetric applications". *Diamond and Related Materials*, **14** (3); pp. 531–540 (**2005**). doi:10.1016/j.diamond.2004.11.037.

[31] *B. Marczewska, et al.* "CVD diamonds as thermoluminescent detectors for medical applications". *Radiation protection dosimetry*, **101** (1-4); pp. 485–488 (**2002**). doi:10.1093/oxfordjournals.rpd.a006033.

[32] *E. Berdermann, et al.* "The use of CVD-diamond for heavy-ion detection". *Diamond and Related Materials*, **10** (9); pp. 1770–1777 (**2001**). doi:10.1016/S0925-9635(01)00443-5.

[33] *M. Pomorski*. "Electronic properties of single crystal CVD diamond and its suitability for particle detection in hadron physics experiments". Ph.D. thesis (**2008**).

[34] *C. TOTEM, et al.* "The TOTEM Experiment at the CERN Large Hadron Collider". *Journal of Instrumentation*, **3** (08); pp. S08007–S08007 (**2008**). doi:10.1088/1748-0221/3/08/s08007.

[35] *G. Antchev, et al.* "Diamond detectors for the TOTEM timing upgrade". *Journal of Instrumentation*, **12** (03); pp. P03007–P03007 (**2017**). doi:10.1088/1748-0221/12/03/p03007.

[36] *R. Santonico and R. Cardarelli*. "Development of Resistive Plate Counters". *Nucl. Instrum. Meth.*, **187**; pp. 377–380 (**1981**). doi:10.1016/0029-554X(81)90363-3.

[37] *E. Cerron Zeballos, et al.* "A New type of resistive plate chamber: The Multigap RPC". *Nucl. Instrum. Meth.*, **A374**; pp. 132–136 (**1996**). doi:10.1016/0168-9002(96)00158-1.

[38] *S. An, et al.* "A 20ps timing device—A Multigap Resistive Plate Chamber with 24 gas gaps". *Nucl. Instrum. Meth.*, **A594** (1); pp. 39–43 (**2008**). doi:10.1016/j.nima.2008.06.013.

[39] *A. N. Akindinov, et al.* "Latest results on the performance of the multigap resistive plate chamber used for the ALICE TOF". *Nucl. Instrum. Meth.*, **A533**; pp. 74–78 (**2004**). doi:10.1016/j.nima.2004.07.004.

[40] *K. Kleinknecht*. Detektoren für Teilchenstrahlung. B.G. Teubner (**1992**). doi:10.1007/978-3-322-94130-5.

[41] *C. Patrignani, et al.* "Particle Data Group - Review of Particle Physics". *Chin. Phys.*, **C40** (10); p. 100001 (**2016**). doi:10.1088/1674-1137/40/10/100001.

[42] *A. Einstein*. "Über einen die Erzeugung und Verwandlung des Lichtes betreffenden heuristischen Gesichtspunkt". *j-ANN-PHYS-1900-4*, **322** (6); pp. 132–148 (**1905**). doi:10.1002/andp.19053220607.

[43] *W. Blum, W. Riegler, and L. Rolandi*. Particle detection with drift chambers; 2nd ed. Springer, Berlin (**2008**). doi:10.1007/978-3-540-76684-1.

[44] *H. Raether*. Electron Avalanches and Breakdown in Gases. Butterworths advanced physics series. Butterworths (**1964**).

[45] *F. M. Penning*. "Über Ionisation durch metastabile Atome". *Die Naturwissenschaften*, **15** (40); pp. 818–818 (**1927**). doi:10.1007/bf01505431.

[46] *A. Bhattacharya*. "Fill gas mixture for glow lamps" (**1973**). US-Patent: US3814971A.

[47] *E. Rutherford and H. Geigerg*. "An Electrical Method of Counting the Number of α-Particles from Radio-Active Substances". *Proceedings of the Royal Society A: Mathematical, Physical and Engineering Sciences*, **81** (546); pp. 141–161 (**1908**). doi:10.1098/rspa.1908.0065.

[48] *G. Charpak, et al.* "The use of multiwire proportional counters to select and localize charged particles". *Nucl. Instrum. Meth.*, **A62**; pp. 262–268 (**1968**). doi:10.1016/0029-554X(68)90371-6.

[49] *A. Oed*. "Position Sensitive Detector with Microstrip Anode for electron Multiplication with Gases". *Nucl. Instrum. Meth. A*, **263**; pp. 351–359 (**1988**). doi:10.1016/0168-9002(88)90970-9.

[50] *M. Titov and L. Ropelewski*. "Micro-pattern gaseous detector technologies and RD51 collaboration". *Modern Physics Letters A*, **28** (13); p. 1340022 (**2013**). doi:10.1142/S0217732313400221.

[51] *F. Sauli*. "GEM: A new concept for electron amplification in gas detectors". *Nucl. Instrum. Meth.*, **A386**; pp. 531–534 (**1997**). doi:10.1016/S0168-9002(96)01172-2.

[52] *Y. Giomataris, et al.* "MICROMEGAS: a high-granularity position-sensitive gaseous detector for high particle-flux environments". *Nucl. Instrum. Meth.*, **A376** (1); pp. 29–35 (**1996**). doi:https://doi.org/10.1016/0168-9002(96)00175-1.

[53] *R. Bouclier, et al.* "The gas electron multiplier (GEM)". *IEEE Transactions on Nuclear Science*, **44** (3); pp. 646–650 (**1997**). doi:10.1109/23.603726.

[54] *Y. Giomataris, et al.* "MICROMEGAS: a high-granularity position-sensitive gaseous detector for high particle-flux environments". *Nucl. Instrum. Meth.*, **A376** (1); pp. 29–35 (**1996**). doi:10.1016/0168-9002(96)00175-1.

[55] *T. Kawamoto, et al.* "New Small Wheel Technical Design Report". *Tech. Rep. CERN-LHCC-2013-006. ATLAS-TDR-020* (**2013**).

[56] *I. Giomataris, et al.* "Micromegas in a bulk". *Nucl. Instrum. Meth.*, **A560** (2); pp. 405–408 (**2006**). doi:10.1016/j.nima.2005.12.222.

[57] *S. Andriamonje, et al.* "Development and performance of Microbulk Micromegas detectors". *JINST*, **5** (02); pp. P02001–P02001 (**2010**). doi:10.1088/1748-0221/5/02/p02001.

[58] *F. J. Iguaz, et al.* "Characterization of microbulk detectors in argon- and neon-based mixtures". *JINST*, **7**; p. P04007 (**2012**). doi:10.1088/1748-0221/7/04/P04007.

[59] *D. Attié, et al.* "Towards smaller gap microbulks". *Journal of Instrumentation*, **9** (04); pp. C04013–C04013 (**2014**). doi:10.1088/1748-0221/9/04/c04013.

[60] *P. Abbon, et al.* "The Micromegas detector of the CAST experiment". *New Journal of Physics*, **9** (6); p. 170 (**2007**). doi:10.1088/1367-2630/9/6/170.

[61] *A. Tomás, et al.* "The new micromegas X-ray detectors in CAST". *X-Ray Spectrometry*, **40** (4); pp. 240–246 (**2011**). doi:10.1002/xrs.1319.

[62] *C. Rubbia, et al.* "A High Resolution Spallation Driven Facility at the CERN-PS to Measure Neutron Cross Sections in the Interval from 1 eV to 250 MeV: a Relative Performance Assessment". *Tech. Rep. CERN-LHC-98-002-EET-Add.1*, CERN, Geneva (**1998**). Addendum to CERN-LHC-98-002-EET.

[63] *D. Attié, et al.* "A Piggyback resistive Micromegas". *Journal of Instrumentation*, **8** (05); pp. P05019–P05019 (**2013**). doi:10.1088/1748-0221/8/05/p05019.

[64] *M. Chefdeville, et al.* "An electron-multiplying 'Micromegas' grid made in silicon wafer post-processing technology". *Nucl. Instrum. Meth.*, **A556** (2); pp. 490–494 (**2006**). doi:10.1016/j.nima.2005.11.065.

[65] *J. N. Marx and D. R. Nygren*. "The Time Projection Chamber". *Phys. Today*, **31N10**; pp. 46–53 (**1978**). doi:10.1063/1.2994775.

[66] *S. Platchkov, et al.* "A large size MICROMEGAS detector for the COMPASS experiment at CERN". **1**; pp. 292–296 vol.1 (**2002**). doi:10.1109/NSSMIC.2002.1239319.

[67] *S. D. Drell and T.-M. Yan*. "Massive Lepton-Pair Production in Hadron-Hadron Collisions at High Energies". *Phys. Rev. Lett.*, **25**; pp. 316–320 (**1970**). doi:10.1103/PhysRevLett.25.316.

[68] *D. Thers, et al.* "Micromegas as a large microstrip detector for the COMPASS experiment". *Nucl. Instrum. Meth.*, **A469** (2); pp. 133–146 (**2001**). doi:10.1016/S0168-9002(01)00769-0.

[69] *D. Neyret, et al.* "New pixelized Micromegas detector for the COMPASS experiment". *JINST*, **4** (arXiv:0909.5402); p. P12004. 11 p (**2010**). doi:10.1088/1748-0221/4/12/P12004.

[70] "ATLAS muon spectrometer: Technical Design Report". *Tech. Rep. CERN-LHCC-97-022*, CERN, Geneva (**1997**).

[71] *E. Perez Codina*. "Small-Strip Thin Gap Chambers for the Muon Spectrometer Upgrade of the ATLAS Experiment". *Tech. Rep. ATL-MUON-PROC-2015-004*, CERN, Geneva (**2015**). doi:10.1016/j.nima.2015.11.095.

[72] *T. Alexopoulos, et al.* "A spark-resistant bulk-micromegas chamber for high-rate applications". *Nucl. Instrum. Meth.*, **A640** (1); pp. 110–118 (**2011**). doi:10.1016/j.nima.2011.03.025.

[73] *K. Morishima, et al.* "Discovery of a big void in Khufu's Pyramid by observation of cosmic-ray muons". *Nature*, **552** (7685); pp. 386–390 (**2017**). doi:10.1038/nature24647.

[74] *S. Procureur, et al.* "Why do we flush gas in gaseous detectors?" *Nucl. Instrum. Meth.*, **A955**; p. 163290 (**2020**). doi:10.1016/j.nima.2019.163290.

[75] *S. Andriamonje, et al.* "Development and performance of Microbulk Micromegas detectors". *Journal of Instrumentation*, **5** (02); pp. P02001–P02001 (**2010**). doi:10.1088/1748-0221/5/02/p02001.

[76] *T. Kajita*. "The JHF-Kamioka Neutrino Project". *Neutrino Oscillations and Their Origin*, (pp. 239–248). doi:10.1142/9789812776488_0026.

[77] *J. Nieves, J. E. Amaro, and M. Valverde*. "Inclusive quasi-elastic neutrino reactions". *Phys. Rev. C*, **70**; p. 055503 (**2004**). doi:10.1103/PhysRevC.70.055503. [Erratum: Phys.Rev.C 72, 019902 (2005)].

[78] *N. Abgrall, et al.* "Time Projection Chambers for the T2K Near Detectors". *Nucl. Instrum. Meth. A*, **637**; pp. 25–46 (**2011**). doi:10.1016/j.nima.2011.02.036.

[79] *A. Obertelli, et al.* "MINOS: A vertex tracker coupled to a thick liquid-hydrogen target for in-beam spectroscopy of exotic nuclei". *The European Physical Journal A*, **50** (1); p. 8 (**2014**). doi:10.1140/epja/i2014-14008-y.

[80] *T. Behnke, et al.* "The International Linear Collider Technical Design Report - Volume 1: Executive Summary" (**2013**).

[81] *R. Diener*. "Development of a TPC for an ILC Detector". *Phys. Procedia*, **37**; pp. 456–463 (**2012**). doi:10.1016/j.phpro.2012.02.393.

[82] *N. Colonna et al.* "The fission experimental programme at the CERN n_TOF facility: status and perspectives". *Eur. Phys. J. A*, **56** (2); p. 48 (**2020**). doi:10.1140/epja/s10050-020-00037-8.

[83] *S. Andriamonje, et al.* "The MICROMEGAS neutron detector for CERN n-TOF". *Advanced Technology and Particle Physics*, (pp. 633–638) (**2002**). doi:10.1142/9789812776464_0091.

[84] *F. Belloni, et al.* "Neutron beam imaging with micromegas detectors in combination with neutron time-of-flight at the nTOF facility at CERN". *4th International Conference on Current Problems in Nuclear Physics and Atomic Energy, NPAE 2012*, (pp. 366–368) (**2013**).

[85] *T. Papaevangelou, et al.* "ESS nBLM: Beam Loss Monitors based on Fast Neutron Detection". (p. THA1WE04) (**2018**). doi:10.18429/JACoW-HB2018-THA1WE04.

[86] *J. Derré, et al.* "Fast signals and single electron detection with a MICROMEGAS photodetector". *Nucl. Instrum. Meth.*, **A449** (1); pp. 314–321 (**2000**). doi:10.1016/S0168-9002(99)01452-7.

[87] *G. Charpak and F. Sauli*. "Use of Tmae in a Multistep Proportional Chamber for Cherenkov Ring Imaging and Other Applications". *Nucl. Instrum. Meth.*, **A225**; p. 627 (**1984**). doi:10.1016/0167-5087(84)90116-9.

[88] *S. Majewski, et al.* "Low-pressure ultraviolet photon detector with TMAE gas photocathode". *Nucl. Instrum. Meth.*, **A264** (2); pp. 235–250 (**1988**). doi:10.1016/0168-9002(88)90913-8.

[89] *A. Peyaud, et al.* "The ForFire photodetector". *Nucl. Instrum. Meth.*, **A787**; pp. 102–104 (**2015**). doi:10.1016/j.nima.2014.11.044.

[90] *L. Sohl*. "Beam Measurements of PICOSEC Gaseous Detectors for Fast-Timing Applications". Master's thesis, Ruhr-Univesität Bochum, Germany (**2018**).

[91] *P. Colas, et al.* "Electron drift velocity measurements at high electric fields". *Nucl. Instrum. Methods Phys. Res.,*, **A478** (DAPNIA-2001-09. 1-2); pp. 215–219. 10 p (**2001**).

[92] *J. V. Jelley*. Cerenkov Radiation and Its Applications. Pergamon Press (**1958**). doi:10.1088/0508-3443/6/7/301.

[93] CIVIDEC. C2-HV - Broadband Amplifier, 2 GHz, 40 dB Product Information Sheet (**2017**).

[94] Teledyne LeCroy. WaveRunner 8000 Series Datasheet (**2018**).

[95] *K. Paraschou*. "Study of the PICOSEC-Micromegas Detector with Test Beam Data and Phenomenological Modelling of its Response". Master's thesis, Aristotle University of Thessaloniki, Greece (**2018**).

[96] *K. Kordas, et al.* "Progress on the PICOSEC-Micromegas Detector Development: Towards a precise timing, radiation hard, large-scale particle detector with segmented readout". *Nucl. Instrum. Meth.*, **A958**; p. 162877 (**2020**). doi:10.1016/j.nima.2019.162877.

[97] *J. Bortfeldt et al.* "Modeling the Timing Characteristics of the PICOSEC Micromegas Detector". *Preprint at arXiv* (**2019**). e-print: 1901.10779 [physics.ins-det].

[98] *H. Schindler and R. Veenhof.* "Garfield++ - simulation of tracking detectors". `http://garfieldpp.web.cern.ch/garfieldpp/`.

[99] *J. R. Leslie*. "The Inverse Gaussian Distribution: Theory, Methodology, and Applications". *Journal of the Royal Statistical Society Series C*, **39** (2); pp. 259–260 (**1990**). doi:10.2307/2347765.

[100] Coherent. Mira Optima 900 F Data Sheet (**2002**).

[101] Coherent. Verdi Family Data Sheet (**2011**).

[102] *W. Koechner*. Solid State Laser Engineering. Springer series in optical sciences. Springer-Verlag (**1976**).

[103] Coherent. Mira OPO-X Data Sheet (**2015**).

[104] Coherent. Pulse Picker Model 9200 Data Sheet (**2009**).

[105] *E. W. J. Mitchell, J. W. Mitchell, and N. F. Mott*. "The work functions of copper, silver and aluminium". *Proceedings of the Royal Society of London. Series A. Mathematical and Physical Sciences*, **210** (1100); pp. 70–84 (**1951**). doi:10.1098/rspa.1951.0231.

[106] *L. Sohl, et al.* "Single photoelectron time resolution studies of the PICOSEC-Micromegas detector". *Journal of Instrumentation*, **15** (04); pp. C04053–C04053 (**2020**). doi:10.1088/1748-0221/15/04/c04053.

[107] *Y. Giomataris*. "Development and prospects of the new gaseous detector "Micromegas"". *Nucl. Instrum. Meth.*, **A419** (2); pp. 239–250 (**1998**). doi:10.1016/S0168-9002(98)00865-1.

[108] *T. Zerguerras, et al.* "Understanding avalanches in a Micromegas from single-electron response measurement". *Nucl. Instrum. Meth.*, **772**; pp. 76–82 (**2015**). doi:10.1016/j.nima.2014.11.014.

[109] *D. Attié, et al.* "Towards smaller gap microbulks". *Journal of Instrumentation*, **9** (04); pp. C04013–C04013 (**2014**). doi:10.1088/1748-0221/9/04/c04013.

[110] *B. Chauchaix*. "SPS Primary Targets". *Tech. rep.*, CERN (**2009**). `https://twiki.cern.ch/twiki/bin/view/ABATBEA/SPSPrimaryTargets`.

[111] CERN. Introduction to the use of the H4 beam (**2010**). `http://sba.web.cern.ch/sba/BeamsAndAreas/h4/H4manual.htm`.

[112] *M. C. Vignali, et al.* "Deep diffused Avalanche photodiodes for charged particles timing". *Nucl. Instrum. Meth.*, **A958**; p. 162405 (**2020**). doi:10.1016/j.nima.2019.162405.

[113] *Müller, Hans and Kaminski, Jochen.* "RD51 Working Group 5". `http://rd51-public.web.cern.ch/rd51-public/Activities/WG5.html`.

[114] *S. Bachmann, et al.* "Discharge studies and prevention in the gas electron multiplier (GEM)". *Nucl. Instrum. Meth.*, **A479** (2); pp. 294–308 (**2002**). doi:10.1016/S0168-9002(01)00931-7.

[115] *M. French, et al.* "Design and results from the APV25, a deep sub-micron CMOS front-end chip for the CMS tracker". *Nucl. Instrum. Meth.*, **A466** (2); pp. 359–365 (**2001**). doi:10.1016/S0168-9002(01)00589-7.

[116] *L. Jones*. APV25-S1: User guide version 2.2. RAL Microelectronics Design Group, Chilton (**2001**).

[117] *M. Raymond, et al.* "The APV25 0.25 mu;m CMOS readout chip for the CMS tracker". **2**; pp. 9/113–9/118 vol.2 (**2000**). doi:10.1109/NSSMIC.2000.949881.

[118] *S. Colafranceschi*. "A new Slow Control and Run Initialization Byte-wise Environment (SCRIBE) for the quality control of mass-produced CMS GEM detectors" (**2016**).

[119] CERN. ALICE DAQ and ECS Manual (**2010**). `https://ph-dep-aid.web.cern.ch/ph-dep-aid/dateUserGuide/dateUserGuide.pdf`.

[120] *J. Bortfeldt*. "Development of floating strip micromegas detectors". Ph.D. thesis, Ludwig-Maximilians-Universität München, Germany (**2014**).

[121] *R. E. Kalman*. "A New Approach to Linear Filtering and Prediction Problems". *Journal of Basic Engineering*, **82** (1); pp. 35–45 (**1960**). doi:10.1115/1.3662552.

[122] Hamamatsu PHOTONICS K. K. R3809U-50 SERIES Data Sheet (**2015**).

[123] Photek Limited. Photomultiplier & Photodiode User Guide (**2016**).

[124] "Spatial time resolution of MCP-PMTs as a t0-reference". *Nuclear Instruments and Methods in Physics Research Section A: Accelerators, Spectrometers, Detectors and Associated Equipment*, **936**; pp. 583–585 (**2019**).

[125] *D. Gonzalez-Diaz, F. Resnati, and R. Veenhof.* "RD51 Precise timing workshop" (**2017**). `https://indico.cern.ch/event/607147`.

[126] *A. Delbart, et al.* "Performance of MICROMEGAS with preamplification at high intensity hadron beams". *Nucl. Instrum. Meth.*, **A478** (1); pp. 205–209 (**2002**). doi:10.1016/S0168-9002(01)01758-2.

[127] *L. Sohl, et al.* "PICOSEC-Micromegas: Robustness measurements and study of different photocathode materials". *J. Phys. Conf. Ser.*, **1312** (1); p. 012012 (**2019**). doi:10.1088/1742-6596/1312/1/012012.

[128] *J. Wotschack*. "The development of large-area Micromegas detectors for the ATLAS upgrade". *Mod. Phys. Lett. A*, **28**; p. 1340020. 11 p (**2013**). doi:10.1142/S0217732313400208.

[129] *F. J. Iguaz Gutierrez*. personal communication.

[130] *J. Samarati, et al.* "Characterisation of the charging up effect in resistive Micromegas detectors". *Journal of Physics: Conference Series*, **1498**; p. 012030 (**2020**). doi: 10.1088/1742-6596/1498/1/012030.

[131] *P. Colas, I. Giomataris, and V. Lepeltier*. "Ion backflow in the Micromegas TPC for the future linear collider". *Nucl. Instrum. Meth.*, **A535** (1); pp. 226–230 (**2004**). doi:10.1016/j.nima.2004.07.274.

[132] *K. Nikolopoulos, et al.* "Electron transparency of a Micromegas mesh". *Journal of Instrumentation*, **6** (06); pp. P06011–P06011 (**2011**). doi:10.1088/1748-0221/6/06/p06011.

[133] *P. Bhattacharya, et al.* "Investigation of Ion Backflow in Bulk Micromegas Detectors". *JINST*, **10** (09); p. P09017 (**2015**). doi:10.1088/1748-0221/2015/9/P09017.

[134] *J. Wotschack*. "The development of large-area Micromegas detectors for the ATLAS upgrade". *Modern Physics Letters A*, **28** (13); p. 1340020 (**2013**). doi:10.1142/S0217732313400208.

[135] *M. Ariyuki, et al.* "Development of large size MgF2 single crystal grown by the CZ method". **7504**; pp. 589 – 596 (**2009**). doi:10.1117/12.836349.

[136] *F. M. Brunbauer*. personal communication.

[137] *F. Himpsel, et al.* "Quantum photoyield of diamond(111) A stable negative-affinity emitter". *Physical Review B*, **20** (2); pp. 624–627 (**1979**). doi:10.1103/PhysRevB.20.624.

[138] *C. Bandis and B. Pate*. "Photoelectric emission from negative-electron-affinity diamond (111) surfaces: Exciton breakup versus conduction-band emission". *Physical Review B*, **52** (16); pp. 12056–12071 (**1995**). doi:10.1103/PhysRevB.52.12056.

[139] *J. S. Foord, C. H. Lau, and M. Hiramatsu*. "Transmissive diamond photocathodes". *Carbon*, **43** (10); pp. 2106–2111 (**2005**). doi:10.1016/j.carbon.2005.03.025.

[140] *J. Robertson*. "Diamond-like amorphous carbon". *Materials Science and Engineering: R: Reports*, **37** (4); pp. 129–281 (**2002**). doi:10.1016/S0927-796X(02)00005-0.

[141] *T. Okada, et al.* "Formation of carbon nitride films with high N/C ratio by high-pressure radio frequency magnetron sputtering". *Journal of Applied Physics*, **78** (12); pp. 7416–7418 (**1995**). doi:10.1063/1.360397.

[142] *M. Daenen, et al.* "Seeding, growth and characterization of nanocrystalline diamond films on various substrates". *physica status solidi (a)*, **203**; pp. 3005–3010 (**2006**). doi:10.1002/pssa.200671122.

[143] *J. Arnault, et al.* "Diamond nanoseeding on silicon: Stability under H2 MPCVD exposures and early stages of growth". *Diamond and Related Materials*, **17** (7); pp. 1143–1149 (**2008**). doi:10.1016/j.diamond.2008.01.008.

[144] McPherson. 632 Deuterium Lamp Data Sheet (**2017**).

[145] *M. Lisowska and F. M. Brunbauer*. personal communication.

[146] *R. Bitter, T. Mohiuddin, and M. Nawrocki*. LabVIEW: Advanced programming techniques. Crc Press (**2006**).

[147] *K. Okano, et al.* "Characterization of Boron-Doped Diamond Film". *Japanese Journal of Applied Physics*, **28** (Part 1, No. 6); pp. 1066–1071 (**1989**). doi:10.1143/jjap.28.1066.

[148] *A. Deneuville, et al.* "Highly and heavily boron doped diamond films". *Diamond and Related Materials*, **16** (4); pp. 915–920 (**2007**). doi:10.1016/j.diamond.2006.12.057.

[149] *F. Thévenot*. "Boron carbide—A comprehensive review". *Journal of the European Ceramic Society*, **6** (4); pp. 205–225 (**1990**). doi:10.1016/0955-2219(90)90048-K.

[150] *Y. Lv, et al.* "Production and performance study of Diamond-Like Carbon resistive electrode in MPGD". *Nucl. Instrum. Meth. A*, **958**; p. 162759 (**2020**). doi:10.1016/j.nima.2019.162759.

[151] *L. Austin and H. Starke*. "Über die Reflexion der Kathodenstrahlen und eine damit verbundene neue Erscheinung secundärer Emission". *Annalen der Physik*, **314** (10); pp. 271–292 (**1902**). doi:10.1002/andp.19023141003.

[152] *J. E. Yater and A. Shih*. "Secondary electron emission characteristics of single-crystal and polycrystalline diamond". *Journal of Applied Physics*, **87** (11); pp. 8103–8112 (**2000**). doi:10.1063/1.373505.

[153] *Y. Zhang, et al.* "Research on Secondary Electron Emission Characteristics of Diamond-like Carbon Thin Films". *J. Phys. Conf. Ser.*, **1350** (1); p. 012177 (**2019**). doi:10.18429/JACoW-IPAC2019-TUPMP031.

[154] *A. Buzulutskov, A. Breskin, and R. Chechik*. "Field enhancement of the photoelectric and secondary electron emission from CsI". *Journal of Applied Physics*, **77** (5); pp. 2138–2145 (**1995**). doi:10.1063/1.358791.

[155] *G. Brunetti, et al.* "Status of the ENUBET project". *Proceeding of Science*, **NuFACT2018**; p. 122. 4 p (**2019**). doi:10.22323/1.341.0122.

[156] *A. Accardi et al.* "Electron Ion Collider: The Next QCD Frontier: Understanding the glue that binds us all". *Eur. Phys. J. A*, **52** (9); p. 268 (**2016**). doi:10.1140/epja/i2016-16268-9.

[157] *D. D. Gruttola*. "Particle IDentification with the ALICE Time-Of-Flight detector at the LHC". *Journal of Instrumentation*, **9** (10); pp. C10019–C10019 (**2014**). doi:10.1088/1748-0221/9/10/c10019.

université PARIS-SACLAY | ÉCOLE DOCTORALE PHENIICS

Titre: Développement de PICOSEC-Micromegas pour les environments à haut flux de particules

Mots clés: Precision temporelle ultra rapide, Detecteurs Micromegas, Micromegas resistives, Detecteurs gazeux à micropistes, photocathodes, haut flux de particules

Résumé: Les futures expériences de physique des particules devront être opérationnelles pour un flux de particules et une luminosité croissants. Plus particulièrement, les détecteurs proches du point d'interaction devront présenter une très bonne robustesse pour faire face à un flux de particules très élevé. De plus, une résolution temporelle de quelques dizaines de picosecondes pour les particules au minimum d'ionisation sera nécessaire pour assurer une séparation nette des vertex reconstruits et réduire l'empilement d'événements.

Ce manuscrit a pour sujet l'instrument PICOSEC-Micromegas, un détecteur de particules innovant basé sur la lecture d'un détecteur Micromegas couplé à un radiateur Cherenkov et une photocathode. Dans ce dispositif, chaque électron primaire étant produit à la surface de la photocathode, l'étalement en temps du signal est minimal, alors qu'il peut atteindre plusieurs nanosecondes lorsque les ionisations primaires ont lieu sur le passage d'une particule dans l'espace de dérive. La hauteur de ce dernier est ici du même ordre de grandeur que celle de la région d'amplification (100-200 µm) afin de minimiser l'ionisation directe du gaz. L'espace de dérive est également utilisée comme espace de pré-amplification.

Un modèle mathématique, basé sur des simulations GARFIELD++, a été développé pour décrire le développement de l'avalanche de pré-amplification. Il a permit de montrer que la longueur et la multiplication de l'avalanche dans l'espace de dérive sont les facteurs dominants dans la résolution temporelle. Le concept PICOSEC-Micromegas a été étudié avec plusieurs prototypes optimisant les champs électriques, la distance de dérive et le mélange gazeux auprès de l'installation laser du LIDYL (Laboratoire Interactions, Dynamiques et Lasers). Une résolution temporelle de ∼44 ps a été obtenue pour un photo-électron unique. Par ailleurs, des mesures effectuées en faisceau test au CERN ont permis d'obtenir une résolution temporelle de 24 ps pour des muons de 150 GeV, avec un espace de dérive de 200 µm et une photocathode en CsI (10 photoélectrons par MIP).

Afin de passer du concept de détection à un démonstrateur plusieurs prototypes ont été développés, en se concentrant sur les propriétés spécifiques nécessaires aux applications futures: segmentation de l'anode, annulation des étincelles, efficacité de la photocathode et robustesse à haut flux de particules. Un prototype à pads hexagonaux a été testé en faisceau et montré une résolution temporelle de ∼36 ps dans le pad central. Les performances à haut flux sont testées avec des détecteurs résistifs dans des faisceaux de muons et de pions. Des résolutions temporelles nettement inférieures à 100 ps et un fonctionnement stable en faisceau de pions sont obtenus avec tous les prototypes résistifs. Des matériaux de photocathode robustes, comme alternative au CsI, sont étudiés pour réduire la dégradation due au retour des ions. Les matériaux les plus prometteurs sont le "diamond-like carbon" (DLC) et le carbure de bore (B4C).

Compte tenu des résultats obtenus, deux cas d'application sont considérés pour les perspectives de ce programme de R&D. La première application considérée est l'utilisation du détecteur PICOSEC à l'intérieur d'un calorimètre comme couche de synchronisation ou de nombreuses particules secondaires sont produites dans un calorimètre électromagnétique après quelques longueurs de radiation. Une résolution temporelle de ∼5 ps est attendue avec le PICOSEC-Micromegas. La seconde application est l'identification des particules par des mesures de temps de vol (TOF) ou PICOSEC-Micromegas devrait permettre de doubler la plage d'impulsion des détecteurs TOF actuels pour la séparation π/K avec 3σ.

université PARIS-SACLAY | ÉCOLE DOCTORALE PHENIICS

Title: Development of PICOSEC-Micromegas for fast timing in high rate environments

Keywords: High precision timing, Micromegas gaseous detectors, Resistive Micromegas, MicroPattern Gaseous Detectors, Photocathodes, High particle flux

Abstract: Future particle physics experiments will face an increasing particle flux with rising beam luminosity. Detectors close to the interaction point will need to provide robustness against the high particle flux. Moreover, a time resolution of tens of picosecond for Minimum Ionising Particles will be necessary to ensure a clear vertex separation of the reconstructed secondary particles and to reduce pile-up.

This manuscript focusses on the PICOSEC-Micromegas, an innovative particle detector based on the Micromegas readout coupled to a Cherenkov radiator and a photocathode in front of the gaseous volume. In this way, each primary electron is located on the surface of the photocathode, suppressing thus the inevitable time jitter of several nanoseconds, due to the different ionisation positions created by the passage of a particle from the drift region of a gaseous detector. The drift region length is reduced to the same order of magnitude as the amplification region (100-200 µm) to minimise direct gas ionisation, and it is additionally used as a pre-amplification stage.

A mathematical model, based on GARFIELD++ simulations, is developed to describe the propagation of the pre-amplification avalanche showing that the length and multiplication of the avalanche in the drift region is the dominant factor in the timing performance. The PICOSEC-Micromegas concept is studied with several prototypes optimising the electric fields, the drift distance, and the gas mixture in the LIDYL (Laboratoire Interactions, Dynamiques et Lasers) UV laser facility. A single photoelectron time resolution of ∼44 ps is measured with the shortest tested drift region length of 119 µm and the highest stable field setting. Measurements performed in the secondary particle beam at CERN have resulted in a time resolution of 24 ps for 150 GeV muons with a drift region length of 200 µm and a CsI photocathode providing 10 photoelectrons per MIP.

In order to evolve from the detection concept to a versatile instrument, several prototypes are developed, focusing on specific properties needed for future applications: anode segmentation, spark quenching, photocathode efficiency and robustness for higher particle flux. An hexagonal segmented multi-pad prototype is tested in the beam with a time resolution of ∼36 ps in the central pad. The operation in high rate environments is studied with different resistive strip and floating strip anodes resistive detectors in muon and pion beams. Time resolutions significantly under 100 ps and stable operation in the pion beam are achieved with all resistive prototypes. Robust photocathode materials, as an alternative to CsI, are investigated to reduce degradation from the ion-backflow generated in the pre-amplification avalanche. The most promising materials are diamond-like carbon (DLC) and boron carbide (B4C).

Considering all the results achieved, two application cases are projected with the PICOSEC-Micromegas detector. The first one is the use in a calorimeter as a timing layer. Many secondary particles are produced in an electromagnetic calorimeter after few radiation lengths and a time resolution down to ∼5 ps is expected with the PICOSEC-Micromegas. The second one is particle identification through time-of-flight (TOF) measurements. The PICOSEC-Micromegas is expected to double the momentum range of current TOF detectors for π/K separation with 3σ.

Université Paris-Saclay
Espace Technologique / Immeuble Discovery
Route de l'Orme aux Merisiers RD 128 / 91190 Saint-Aubin, France